UNIVERSITÀ DEGLI STUDI DI MILANO
FACOLTÀ DI SCIENZE E TECNOLOGIE

Doctorate School in Industrial Chemistry, XXXVIII cycle
Department of Chemistry

Amphoteric Polyamidoamines as Functional Specialty Polymers

Tutor: **Professor Elisabetta RANUCCI**

Co-tutor: **Professor Jenny ALONGI**

PhD course coordinator: **Professor Laura PRATI**

PhD candidate

Sofia TRECCANI

Academic year 2024/2025

INDEX

Abbreviation list

Abbreviation	***Meaning***
MPP^+	1-methyl-4-phenylpyridinium iodide
BAC	2,2-(bis-acrylamido)acetic acid
DAPI	4′,6-Diamidino-2-phenylindole
AGM	4-aminobutylguanidine
LC_{50}	50% Lethal concentration
Bmp	Bone morphogenetic protein
CNS	Central nervous system
CYSS	Cystine
PAMAM	Dendrimeric polyamidoamines
DA	Dorsal aorta
DLAV	Dorsal longitudinal anastomotic vessel
DMEM	Dulbecco's modified Eagle medium
EGFP	Enhanced green fluorescent protein
EPR	Enhanced permeability and retention effect
EDA	Ethylenediamine
FET	Fish embryo acute toxicity
FR	Flame retardant
FITC	Fluorescein 5(6)-isothiocyanate
Fli1	Friend leukemia integration 1 transcription factor
GLY	Glycine
GAP-43	Growth associated protein 43
Hpf	Hours post-fertilization
ISV	Intersegmental vessel
ALA	L-Alanine

ARG	L-Arginine
GLU	L-Glutamic acid
HIS	L-Histidine
LPS	Lipopolysaccharide
LEU	L-Leucine
SER	L-Serine
RAW 264.7	Macrophage cell line from a male mouse
MBA or M	N,N'-methylenebisacrylamide
SH-SY5Y	Neuroblastoma cell line derived from a metastatic bone tumor from a 4-year-old cancer patient
OECD	Organization for economic co-operation and development
PFA	Paraformaldehyde
PBS	Phosphate Buffered Saline
PAA	Polyamidoamine
PEI	Polyethylenimine
PLLA	Poly-L-lactic acid
PLL	Poly-L-lysine
SEM	Scanning electron microscopy
TLR	Toll-like receptors
Tg(*Bmp*:EGFP)	Transgenic zebrafish line with the bmp marker driving EGFP
Tg(*fli1*:EGFP)	Transgenic zebrafish line with the endothelial marker *fli1* driving EGFP

PREFACE

This thesis regards the synthesis and different sets of polyamidoamines intended for different applications. It is subdivided into seven chapters.

Chapter 1 "*INTRODUCTION TO POLYAMIDOAMINES*" provides a general introduction to polyamidoamines, covering their synthesis, structural characteristics, and key physicochemical properties. The chapter also highlights their main applications, laying the groundwork for the research presented in the following sections.

Chapter 2 "*SYNTHESIS AND CHARACTERIZATIONS OF PAAs*" outlines the general methods, both synthetic procedures and characterization techniques, employed throughout the thesis, as they are consistently applicable to all synthesized PAAs, regardless of their specific applications. All synthesized PAAs were characterized with respect to their structural, thermal, and acid-base properties.

Chapter 3 "*SHORT-TERM PHYTOTOXICITY SCREENING OF PAAs BY SEED GERMINATION TEST*" explores the use of the seed germination test with *Lepidium sativum* seeds as a model to assess the phytotoxicity of six amphoteric α-amino acid-based PAAs, with particular focus on correlating phytotoxicity to polymer charge distribution.

Chapter 4 "*EVALUATION OF AQUATIC TOXICITY OF PAAs USING ZEBRAFISH AS A VERTEBRATE MODEL*" regards the assessment of the impact of different amphoteric α-amino acid-based PAAs on aquatic ecosystems using zebrafish (*Danio rerio*) embryos, a vertebrate model organism sharing several features with mammals.

Chapter 5 "*α-AMINO ACID-DERIVED PAAs AS PHOTOSTABILIZERS FOR COTTON FABRICS*" is devoted to assessing the photostability properties of PAAs derived from various α-amino acids with different UV-absorption properties, and particularly their potential as photostabilizers for cotton in accelerated photoaging tests.

Chapter 6 "*POLY-L-LACTIC ACID NANOFIBER/PAA COMPOSITE HYDROGEL AS NOVEL STRATEGY FOR IN VITRO NEUROREGENERATION AND NEUROPROTECTION*" regards the preparation of bioactive PAA-based composite hydrogels reinforced with functionalized PLLA mats, as novel biomaterials with neuroregenerative and neuroprotective properties.

Chapter 7 "*ASSESSMENT OF ACCELERATED AGING ON PAA SOLUTIONS AND SOLID FILMS*" regards the preliminary assessment of the photodegradation mechanism of M-GLY both in solution and in the solid state under different experimental conditions.

OBJECTIVE OF THE THESIS

This doctoral research centered on the synthesis and characterization of amphoteric polyamidoamines in both linear and cross-linked forms. The study is organized into two main thematic lines, each comprising multiple projects. The first one was to evaluate the potential environmental impact of amphoteric water-soluble PAAs, which may accidentally be released into ecosystems during or after their useful life. The ecotoxicity of PAAs was evaluated on the early stages of plant development using *Lepidium sativum* (watercress) seeds. In this study, the effectiveness and robustness of the seed germination test for assessing the phytotoxicity of water-soluble polymers has been investigated. Several parameters have been considered to assess the response of seeds exposed to PAA water solutions at different concentrations, including germination percentage, root and bud elongation. To extend the environmental toxicity assessment, the effects of PAAs were evaluated on aquatic ecosystems using zebrafish (*Danio rerio*) embryos, a vertebrate model organism sharing several features with mammals. Embryos development was monitored by performing the standard fish embryo acute toxicity test, evaluating the survival rate, morphological defects, organ deformities, and developmental delay compared to the control.

The second thematic line aimed at exploring PAAs versatility in diverse applications, as water solutions and as hydrogels. Linear α-amino acid-derived PAAs with varying UV-absorption characteristics were investigated as functional coatings to enhance cotton photostability in accelerated photoaging tests under UVA-UVB irradiation. To gain deeper insight into this phenomenon, the photodegradation mechanism both in solution and in the solid state was investigated during the research period at the Université Clermont Auvergne. Photodegradation was evaluated under different experimental conditions, UVA and UVC irradiation, as well as in the presence of hydrogen peroxide as an oxidative agent. PAAs were investigated also in their cross-linked form through the development of biofunctional hydrogels. Cell-adhesive PAA-based composite hydrogels reinforced with electrospun poly-L-lactic acid mats, were studied as novel biomaterials with neuroregenerative and neuroprotective properties on preneuronal and immune cell lines.

1. INTRODUCTION TO POLYAMIDOAMINES

1.1. Polyamidoamines (PAAs)

PAAs are synthetic polymers synthesized by the aza-Michael polyaddition of *prim*-monoamines and *sec*-diamines to bisacrylamides (Scheme 1.1.1)*(1)*. The synthesis occurs in aqueous medium, at room temperature, without adding catalysts. As a polyaddition reaction, PAA synthesis does not produce by-products and monomers are completely converted to polymers. Consequently, the PAA synthetic process is considered easily scalable and responds to numerous principles of green chemistry *(2)*.

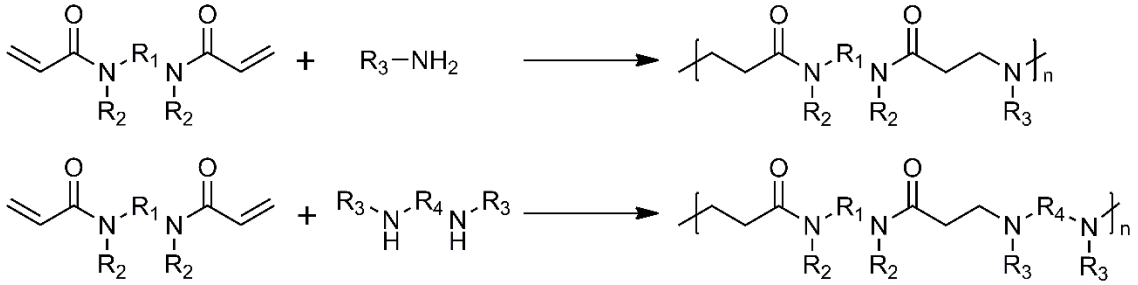

Scheme 1.1.1 General synthesis scheme of PAAs.

The Michael addition is an equilibrium reaction, therefore increasing the temperature, the polymerization rate increases, but the molecular weight tends to level off at a progressively lower limiting value. All PAAs are polyelectrolytes, since the *prim*-or *sec*-amine groups involved in polyaddition reactions, give rise to *tert*-amine groups in the polymer chain and retain their basic character. The polyelectrolytic character can be further enhanced by introducing ionizable side substituents and it is strictly dependent on the pH. PAAs are not only intrinsically functional polymers but are also amenable to further functionalization since chemical functions, such as hydroxy-, *tert*-amine-, allyl-, amide-, and ether groups if present in the monomers do not interfere in the polymerization process and remain as side substituents in the final product. Furthermore, PAAs essentially degrade into diluted aqueous solution by undergoing retro-aza-Michael reaction*(3)*. The degradation becomes evident in the pH interval 7.0–9.0, whereas it is almost negligible at pH 4.0. No spectral evidence of extensive hydrolytic degradation was found, but in several cases the kinetic curves provided clear hints that some hydrolytic cleavage of the amide bonds occurred along with the retro-aza-Michael reaction. Besides homopolymers, random or quasi-random copolymeric PAAs can be obtained starting from mixtures of monomers with no further precautions. In addition, crosslinked PAAs can be obtained by different methods, for instance by using multifunctional amines as co-monomers or by preparing PAA pre-polymers with terminal acrylamide double bonds and then triggering

their radical polymerization by conventional techniques, such as UV irradiation or the addition of radical initiators. They are usually referred to as hydrogels, insoluble materials which in aqueous media absorb large quantities of water while retaining their three-dimensional structure. Regarding biocompatibility, most PAAs exhibit LD_{50} values in vitro higher by 2 orders of magnitude than PLL, PEI, or PAMAM dendrimers *(4)*. The chemical structures of some representative PAAs are reported in Table 1.

1.2. PAAs as polyelectrolytes

PAAs can be regarded as polyelectrolytes since they possess *ter*-amino groups in the main chain. Many relevant properties of PAAs, including hydrodynamic volume, ability to form stable coordination compounds with heavy metal ions and, generally speaking, to interact with components of the biological environments including nucleic acids, proteins and living cells, are strongly dependent on their acid-base properties, hence on their ionization state. The protonation constants of polyelectrolytes are usually referred to as "apparent" constants, as opposed to the "real" constants of non-macromolecular acids and bases*(5)*. However, in most PAAs the results of the potentiometric titrations demonstrated that ionizable groups behave as if they belong to a small molecule, nearly independent of the protonation state of the rest of the macromolecule. The number of the protonation constants is always equal to the number of acid and tert-amine groups present in the repeating unit. This behavior is probably due to the relatively long distance between the amine groups belonging to different units, combined with the high charge-sheltering efficiency of the two amide groups interposed. Interestingly, when carboxyl groups are present as side substituents in PAAs, their constants tend to be "apparent". Basicity and acidity constants can be determined by titration except for PAAs with solubility constraints. The pK_a values of ionizable functions are determined as the pH values at the half-equivalent points, located in the buffer zone related to the specific function. Polyelectrolyte behavior is described by the modified Henderson-Hasselbalch equation (Equation (1.2.1)):

$$pH = pK_a - \beta \log \frac{1-\alpha}{\alpha} \quad (Eq.\ 1.2.1)$$

where β is the Katchalsky and Spitnik parameter accounting for possible interactions between ionizable groups of repeat units being spatially or topologically adjacent. Speciation diagrams are obtained by plotting the concentration fractions (α) of the different ionic species, calculated with the K_a values according to the Equations previously reported, as a function of pH *(6)*. The acid-base properties of some representative PAA are reported in Table 1.2.1.

Table 1.2.1. Structures and properties of representative PAAs.

Code	Structure of the repeating unit	pK_a values	IP[a)]	Applications
AGMA1	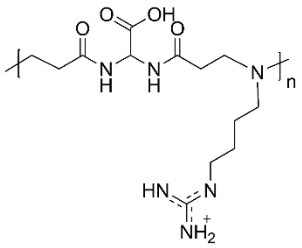	pK_{a1}= 2.30 pK_{a2}= 7.40 $pK_{a\text{-}guanidine}$ > 10	> 10	Antiviral activity, cell adhesion properties, transfection ability, drug delivery *(7–11)*
M-AGM	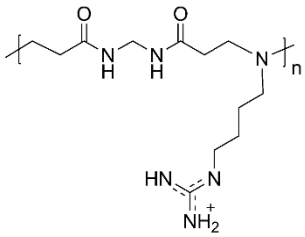	pK_{a1}= 7.1 $pK_{a\text{-}guanidine}$ > 10	-	Heavy metal ion complexation *(12)*
ISA23	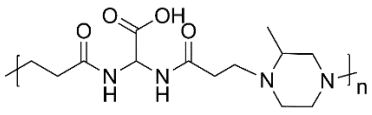	pK_{a1}= 2.31 pK_{a2}= 3.24 pK_{a3}= 7.48	5.2	Transfection ability, drug delivery and conjugation *(13,14)*

[a)] Isoelectric point

Polyamidoamines can be designed to be amphoteric, introducing acidic functions as side substituents, in most cases carboxyl groups. Most amphoteric PAAs derive either from aminoacids or from carboxylated bis-acrylamides, such as 2,2-(bis-acrylamido)acetic acid (BAC), as monomers. In both cases, a stoichiometric amount of strong base must be added to the monomer mixture. Amphoteric PAAs exhibit physico-chemical properties that are governed by their ionization state, which is obviously pH-dependent. By a proper choice of the starting monomers, the acid and basic strength of the amino and the carboxyl groups can be controlled in such a way that the polymer passes from a prevailingly anionic to a prevailingly cationic state during a relatively modest pH change. Amphoteric PAAs are generally less toxic than purely cationic PAAs of similar structure and they have proven in several instances to be highly biocompatible *(15)*. Amphoteric PAAs present a unique interest as bioactive polymers and among them, AGMA1 proved outstanding properties. It derives from BAC and 4-aminobutylguanidine (AGM) and it differs from most other PAAs because, despite having

isoelectric point > 10 and, at pH 7.4, +0.55 average positive charge per unit, proved little cytotoxic ($IC_{50} \geq 5$ mg mL^{-1} on different cell strains; MTD_{50} in mice > 0.5g kg^{-1} upon intravenous administration) and negligibly hemolytic from pH 4 to 7.4. In addition, it demonstrated to have excellent cell adhesion properties *(7,16)*.

1.3. Chiral properties of natural α-amino acid-derived PAAs

Natural α-amino acid-derived polyamidoamines are a lateral offshoot of linear amphoteric polyamidoamines synthesized by the aza-Michael polyaddition of bisacrylamides with natural α-amino acids. Oligomers with controlled molecular weights and sequence of the repeat units can be obtained by a step-by-step polyaddition process leading to homo- and copolymeric PAAs with well-defined structures*(17)*. In the synthesis, α-amino acids maintain both their chirality and their amphoteric nature. As many other chiral polymers, chiral PAAs and most of their respective copolymers are capable of assuming stable, pH-dependent conformations in aqueous media. Chirality governs fundamental recognition and replication functions in biological systems, as for instance biomaterial-cell interactions. Designing chiral synthetic polymers capable of self-assembling into stable secondary structures in water and exerting specific biorecognition represents an attractive biomimetic approach. The first chiral α-amino acid-derived polyamidoamine example investigated was L-ARGO7, which employed L-arginine and MBA as monomers. Subsequently, also the PAAs deriving from D-, and D,L arginine (D-, and D,L-ARGO7) were prepared and their structuring in aqueous media studied by circular dichroism spectroscopy (CD) and molecular modeling *(18)*. The CD spectrum of D,L-ARGO7 at 25 °C in 0.1 M NaCl and in the 2.1−12.1 pH range, gave no evidence of structuring, whereas those of D- and L-ARGO7 showed negative- or positive ellipticity, respectively, with peaks at 228 nm indicating ordered secondary structures (Figure 1.3.1). Structuring proved strongly pH-dependent. It was interesting to ascertain whether this peculiar behavior was typical of ARGO7 polymers, with their bulky and charged side substituent, or is a common feature of PAAs deriving from chiral α-amino acids. To this purpose, three novel PAAs obtained by polyaddition of MBA with natural α-amino acids carrying different hydrophobic substituents, namely L-alanine (M-ALA), L-valine (M-VAL) and L-leucine (M-LEU), were prepared and studied *(19)*. The CD spectra of all PAAs samples in 0.1 M NaCl showed clear evidence of pH-dependent structuring in the pH range 3-11 and in the wavelength interval 200-280 nm (Figure 1.3.2). It suggested that this property, already observed for D- and L-ARGO7, might be general for all chiral members of the family. Theoretical modeling studies carried out on PAA oligomers, as with L-ARGO7, showed stable folded conformations due to intramolecular interactions leading

to main chain arrangements reminding hairpin motif of proteins. Owing to the versatility of their chemical structure and their ability to assume chirality-related stable conformations in solution, α-amino acid-derived PAAs constitute a promising field for several applications, including biological applications.

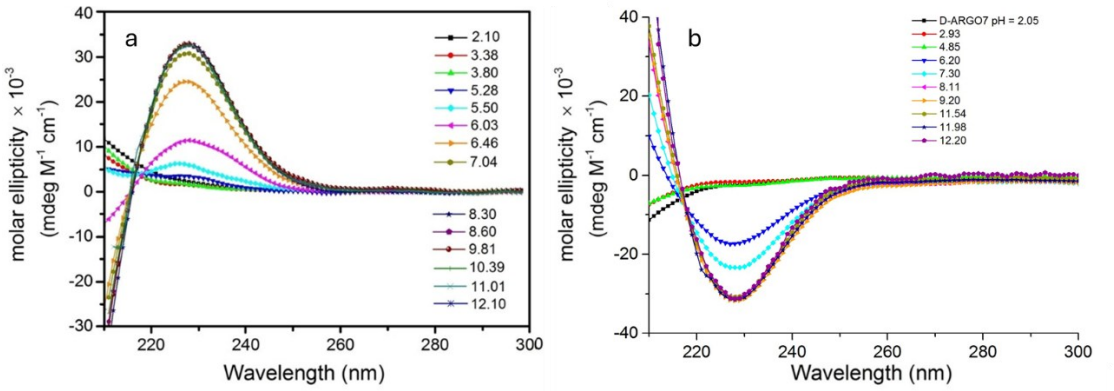

Figure 1.3.1. The CD spectra of L- (a) and D- (b) ARGO7.

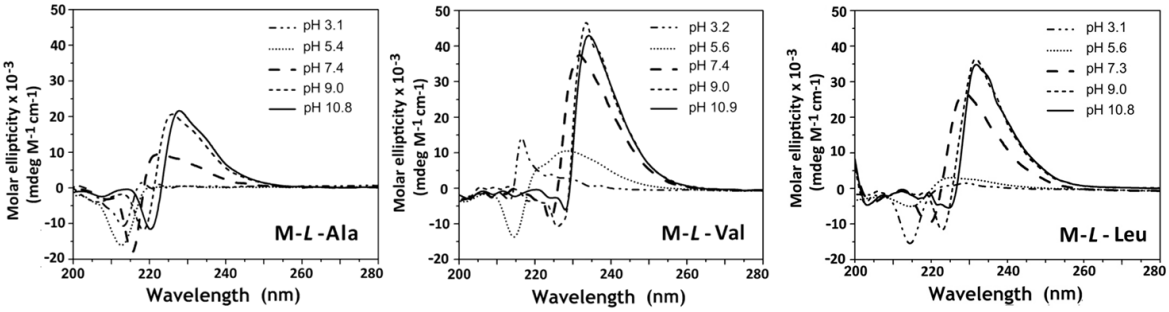

Figure 1.3.2. The CD spectra of M-ALA, M-VAL and M-LEU in 0.1 M NaCl.

1.4. PAA hydrogels

Hydrophilic polymers, which in linear form are water-soluble, if crosslinked, give rise to insoluble materials, which in aqueous media absorb large quantities of water while retaining their three-dimensional structure; these are usually referred to as hydrogels. Thanks to their high water-content, hydrogels are soft viscoelastic materials endowed with physical properties, including nutrient permeability and low interfacial tension, resembling those of soft biological tissues. If the related linear polymers are biocompatible and biodegradable, hydrogels can be considered for use as scaffolds for soft tissue engineering *(20)*. Crosslinked PAAs can be obtained by different methods, for instance by preparing PAA pre-polymers with terminal acrylamide double bonds and then triggering their radical polymerization by conventional

techniques, such as UV irradiation or the addition of radical initiators. It may be observed that, in this process, the acrylamide terminals of the oligomeric PAA precursors are still susceptible to undergoing aza-Michael addition reaction with amines. The hydrogel based on the amphoteric PAA called AGMA1 proved to have excellent cell adhesion properties *(9,21)*. When tested in vivo in a rat model, as conduit for sciatic nerve regeneration, it has been remarkably successful. An implanted AGMA1 hydrogel tube was indeed completely resorbed after 90 days implantation. The nerve function was fully restored, with no signs of inflammation or neuroma, and the rat fully recovered the function of its hind leg. However, the AGMA1 hydrogel tubes could only be fixed to the surrounding tissues with fibrin glue, because they were too soft to sew *(22)*. To overcome this issue, it is possible to prepare fiber-reinforced composite hydrogels that combine the best properties of both components and meet the strength and toughness requirements indispensable for various technological applications *(23,24)*. An essential condition to achieve this result is the existence of amine functions on the fiber surface, which facilitates grafting to the terminal acrylamide groups of the PAA soluble precursor. For instance, electrospun poly-L-lactic acid (PLLA) mats surface-functionalized with amine groups by nitrogen plasma treatment became macroscopically compatible with the AGMA1 matrix and remained securely attached to it even after prolonged incubation of the composite hydrogel in water *(25)*. Similarly, silk mats derived from degummed raw silk fibers proved efficient in this context due to the reaction of the amine groups of lysine residues *(12,26)*. In detail, impregnating a silk mat obtained from a suspension of very short silk fibers with a concentrated aqueous solution of the oligomeric PAA precursor, and subsequently exposing the resultant crude composite to UV irradiation, produced a tough silk-reinforced hydrogel. This composite hydrogel was still reversibly swellable in water, as was the corresponding unreinforced hydrogel, and remained unaffected after several water-uptake/drying cycles, showing no evidence of separation of its components after prolonged incubation in water. Moreover, the composite hydrogel showed much improved mechanical properties in the swollen state with respect to the virgin hydrogel and it was strong enough to be suturable *(12)*.

1.5. Biocompatibility and biotechnological applications

The combination of different chemical functionalities of PAA repeating units and their intrinsic polyelectrolytic nature, can lead to the design of structures mimic those of natural biomacromolecules, such as peptides, exhibiting similar chemical and physicochemical properties. Most PAAs are scarcely cytotoxic and their cytotoxicity is closely related to the net average positive charge at physiological pH (Table 1.5.1) *(27,28)*. The hemolytic activity of

PAAs follows the same trend *(13)*. The biological activity of polyelectrolytes is related to their pH-dependent ionic species distribution. Amphoteric PAAs have, on average, either a positive charge excess per repeat unit or a negative charge excess at pH 7.4. PAAs with prevailingly negative charge exhibited the so-called stealth properties, providing the opportunity for significant tumor targeting by the EPR effect (enhanced permeability and retention effect). Tumor targeting by the EPR effect occurs since circulating macromolecules (proteins or synthetic polymers) are unable to cross the walls of normal capillary vessels but can extravasate into tumor tissue due to their leaky angiogenic vasculature *(29,30)*. Amphoteric PAAs with, on average, excess positive charge per repeat unit at pH 7.4 are normally considerably less cytotoxic than cationic PAAs of similar charge. In addition, they maintain many relevant properties typical of polycations, such as the ability to form interpolyelectrolyte complexes with negatively charged biomacromolecules, including heparin and DNA, to exert membrane activity and to act as transfection promoters *(8,11,28)*. PAAs are also particularly suitable as intracytoplasmic/endosomolytic delivery vectors. They have basicity constants which can be tailored depending on the aminic monomers selected, resulting in a predictable charge distribution as a function of pH. This is particularly important in a narrow change when passing from pH 7.4 (blood) to pH 5.5 or less within the intracellular endosomal and lysosomal compartments. PAAs undergo pH-induced conformational changes *(31)* that activate latent endosomolytic properties favoring the endosomal escape into the cytosol of sensitive drugs that would be otherwise digested by the endosomal enzymes. As PAAs are degradable in the main chain[3] and are relatively non-toxic this would suggest potential for parenteral administration without risk of long-term accumulation in the body. On this basis, PAAs have been examined as antibacterial, antimethastatic and antiviral agents by their own and as polymer-drug conjugates *(7,10,32)*. The versatility in their chemical structure allows attachment of pendent drug moieties, targeting groups or diagnostic moieties and their hydrophilicity allows solubilization of hydrophobic drugs. Among the bioactive PAAs, those bearing side guanidine substituents are particularly interesting for biotechnological applications. Guanidine groups impart cell permeating properties by forming divalent hydrogen bonds with carboxylate-, sulfate- and phosphate groups of biological membranes. Their structure resembles that of synthetic polyarginines, but the internal buffering obtained by introducing carboxylated units giving zwitterionic structures, dramatically reduces toxicity. In particular, AGMA1 proved excellent properties as adhesion and proliferation promoter of primary brain cells such as microglia, as well as of hippocampal neurons and astrocytes when surface-adsorbed on cell

culturing coverslips *(7)*. It also showed antiviral activity against herpes simplex virus, human cytomegalovirus, human papillomavirus 16, and respiratory syncytial virus *(10)*. Promising results were obtained also with L-ARGO7, whose repeating unit is isomeric with that of AGMA1. It showed effective cell internalization ability combined with minimal cytotoxicity in vitro tests with mouse embryo fibroblasts balb/3T3 clone A31 *(33)*. Amphoteric PAAs proved to be biocompatible and biodegradable also in the form of hydrogels *(9)*. These hydrogels were obtained by polyaddition of 2,2-bisacrylamidoacetic acid with 2-methylpiperazine and 4-aminobutyl guanidine. Both PAA hydrogels proved noncytotoxic and adhesive to cell membranes, as ascertained by means of cytotoxicity and proliferation tests carried out on fibroblast cell lines. They underwent degradation tests under controlled conditions simulating the biological environments, that is, Dulbecco medium at pH 7.4 and 37 °C. They completely dissolved and the degradation products were completely noncytotoxic.

Table 1.5.1. Cytotoxicity of PAAs

PAA	**Cell line**	**IC_{50} (mg mL^{-1})**
ISA23 *(13)*	B16F10; Balb/3T3 Clone A31; Cos-1; HT-29; ML-1	>5.0
AGMA1 *(13)*	Cos-1, HT-29, ML-1	>5.0
L-ARGO7 *(33)*	Balb/3T3 Clone A31	>5.0

1.6. Heavy metal ion complexation

Besides biomedicine and biotechnology, PAAs have been studied for potential applications in different technical fields, including heavy metal ion complexation both as linear soluble polymers *(34)* and crosslinked resins *(35–38)*. Many PAAs have proven capable of providing stable complexes with heavy metal ions such as Cu(II), Ni(II), Co(II), and Mn(II) and their complexation ability was attributed to the numerous tertiary amine and carboxyl groups regularly distributed in their repeating units, which can act as ligands of ions. Based on the metal-ion uptake, potential environmental applications have been investigated such as pollutants elimination from contaminated groundwater. Among the heavy metal ions present in water, Cr(VI) represents a severe hazard for both biota and human health. Cr(VI) most stable species are $HCrO_4^-$ and CrO_4^{2-} oxyanions and several amine-functionalized adsorbents have been developed but proved to be not sufficiently efficient. Therefore, the preparation of an

adsorbent material with high performance towards Cr(VI) ions is desirable. The guanidinium ion can strongly bind bidentate oxyanions, thanks to its peculiar molecular geometry, charge distribution, and hydrogen bonding ability. Unsurprisingly, it showed to efficiently uptake Cr(VI) anions from aqueous solutions. The guanidine group can be inserted as pendants in PAAs by using 4-aminobutyl guanidine (agmatine) as a monomer since agmatine can be made to react with bisacrylamides only through the primary amine groups and proper adjustment of the pH of the reaction mixture *(16)*. Silk-reinforced PAA hydrogel membranes bearing guanidine pendants in the repeat units have been successfully prepared *(26)* and they have been further considered to reduce the amount of Cr(VI) in polluted water to negligible amounts (<50 ppb). The goal was achieved by ultrafiltering aqueous solutions of 1 ppm Cr(VI) on the membranes, reducing chromium content to a final concentration of 4 ppb *(12)*. These features, coupled with the easy, inexpensive, and environmentally friendly preparation of these membranes, make them an attractive tool for heavy metal ion sorption from polluted waters.

1.7. Flame retardancy

Fire accidents pose a significant global safety concern. Many fires are accidentally triggered indoor on textiles present as curtains, covers of armchairs and sofas, clothes or linens based on cotton or similar easily flammable cellulosic materials. Consequently, many efforts have been devoted to the development of safe and effective flame retardants (FR). For over five decades, phosphorylated compounds have been the most used FR for cotton fabrics but many of these products have a recognized environmental impact, due to the release of formaldehyde during manufacturing and service life. The development of new and more environmentally friendly non-toxic cotton flame retardants with performances comparable to the conventional ones has gained importance and for this purpose many biomolecules, including polysaccharides, lignin, DNA and proteins have been considered and proved effective. On these premises, PAAs suggested that they could act as FR for cotton fabrics, since their structural features and their thermal decomposition pattern, with decomposition onset temperatures > 200 °C, were comparable with those of some proteins. Some α-amino acid-derived PAAs, particularly those deriving from the polyaddition of MBA with glycine and L-arginine, were shown to be non-flammable by applying a propane flame. In fact, contact with the flame induced a superficial intumescence leaving the inner layers white and apparently unaltered *(39)*. It has long been recognized that intumescence plays a key role in providing FR properties. Therefore, a library of PAAs deriving from MBA and nine different natural α-amino acids was considered to assess their FR performance onto cotton and the influence of the amino acid α-substituent.

Thermogravimetric analysis in air showed that all samples formed a swollen porous carbonaceous structure, demonstrating their intumescent character. Interestingly, the phenomenon of the intumescence of PAAs is particularly significant at 350 °C, which corresponds precisely to the T_{max} of cotton. In these conditions, the porous crust formed by heating the PAA coating under the effect of oxygen exerts its protective action on cotton by insulating it and modifying its decomposition pattern *(40)*. Flame spread tests in different configurations (horizontal and vertical) were performed on cotton strips impregnated with PAA solutions and then dried. The morphology of the PAA-treated fabrics, analyzed by SEM, showed a regular distribution of the PAA coating over the entire fabric up to the inside of the fibers. None of the PAAs extinguished the flame in vertical configuration even at high add-ons, but all of them left a substantial residue. However, all the PAAs efficiently extinguished the flame in horizontal configuration at an add-on above 7%.

1.8. Photostability

One of the major drawbacks of cellulosic materials, such as cotton, linen, and paper, is their susceptibility to photoaging when exposed to air and light, especially ultraviolet (UV) radiation. This process leads to discoloration, embrittlement, and the loss of aesthetic properties, which poses a significant challenge both for the preservation of historical manuscripts and textiles, and in materials science, where cellulosic fibers are widely used in composite materials. It is well established that the photoinduced degradation of cellulose begins with the generation of carbon-centered radicals under UV irradiation. These radicals react with oxygen to form peroxyl radicals, which can then transform into hydroperoxides by abstracting hydrogen atoms *(41)*. Due to their high reactivity, hydroxyl radicals react nonspecifically with carbohydrates and abstract hydrogen from C-H bonds. UV exposure can introduce new functional groups, such as carbonyl and carboxyl groups, increasing the susceptibility of cellulose to degradation. Potential strategies to protect cellulose from photoaging include the incorporation of UV absorbers, reactive oxygen species (ROS) quenchers, or antioxidants *(42)*. Among photostabilizers based on UV absorption, three primary categories can be distinguished: benzophenones, benzotriazoles, and triazines. Instead, hindered amine light stabilizers (HALS) offer an alternative mechanism of protection; although they do not absorb UV radiation, they act as efficient scavengers of free radicals generated during photooxidation, thereby inhibiting cellulose degradation. Despite the high efficacy of UV stabilizers mitigating UV-induced damage, several limitations remain, particularly regarding their environmental impact, and cost-effectiveness. Particularly benzophenones and certain benzotriazoles have been associated with

potential health risks, including endocrine disruption and skin sensitization. Certain stabilizers can persist in the environment and accumulate in living organisms, raising concerns about long-term ecological effects. In this context, polymeric photostabilizers have gained interest since thanks to their size, they have lower environmental impact, reduced leaching and improved safety profile. Since thermo-oxidative decomposition of polymers proceeds through a radical mechanism, exactly as in photo-oxidative decomposition, it was hypothesized that PAAs, that proved efficient as flame retardants for cotton, could also play a role as photostabilizers. A small group of α-amino acid-derived polyamidoamines, in particular those deriving from glycine, leucine, arginine and glutamic acid, proved to be efficient as photostabilizers when deposited onto cotton. PAA-treated cotton specimens were exposed to extensive UV-A irradiation in air and their structural and color changes were monitored over time. PAAs do not normally absorb UV-A rays, unless specific chromophores are introduced in their repeat units, thus their efficacy as anti-photoaging coatings was ascribed to their radical scavenger ability, due to the presence of tert-amine groups in the main chain reacting with radicals *(43)*.

1.9. Phytotoxicity

PAAs are water-soluble polymers that are normally used as aqueous solutions. Therefore, they could end up contaminating surface water and soil during or after their useful life and their presence must be monitored and robust tests adopted to assess their ecotoxicity. The effect of PAAs was evaluated firstly on the early stages of plant development. International agencies for the protection of the environment have proposed different tests, both aquatic and terrestrial, to evaluate the eco-toxicity of potentially dangerous and noxious substances in case of accidents *(44,45)*. Among them, seed germination tests have been extensively used to evaluate the phytotoxicity of hydrocarbons in oil contaminated soils, of heavy metal ions *(46)* and drugs present in polluted water, as well as of compost for agricultural use *(47)*. Several parameters can be considered to assess the germination activity, such as the germination percentage, the root elongation and the germination index, GI, defined as the product of relative radical growth times relative seed germination *(48)*. These parameters are officially recognized by National Authorities. The scientific literature does not report information on the use of seed germination tests to evaluate the phytotoxicity of synthetic polymers. However, considering that linear PAAs, including those active as flame retardants, are very soluble in water, it was considered appropriate to use this test to evaluate their effect on the early stages of plant development. The seed germination test using watercress seeds was adopted to determine the eco-compatibility of the PAA named M-GLY that derives from the polyaddition of MBA with glycine. M-GLY

subjected to watercress seed germination test, showed a remarkable lack of phytotoxicity at all tested concentrations up to 5.0 mg mL^{-1}, that is, a concentration remarkably higher than those commonly adopted when assessing the phytotoxicity of chemicals. These results were in line with those of previous *in vitro* cytotoxicity tests on many amphoteric polyamidoamines. For some concentrations, namely 1.25 and 0.625 mg mL^{-1}, the germination index values suggested a fertilizing effect. In addition, two M-GLY water solutions, namely 5.0 and 2.5 mg mL^{-1}, aged under conditions that in previous research were found to lead to partial depolymerization and to produce from 10 to 15% acrylamide reactive terminals, proved to be comparable with freshly prepared M-GLY solutions *(49)*.

2. SYNTHESIS AND CHARACTERIZATIONS OF PAAs

In this Chapter, general methods, namely synthetic procedures and characterization techniques, are presented once since they apply uniformly across all polyamidoamines, regardless of their final application. All the synthesized polyamidoamines were characterized in terms of their structural, thermal, and acid-base properties.

2.1. Synthesis of PAAs and their ionic species distributions

A series of polyamidoamines were synthesized via aza-Michael polyaddition between N,N′-methylene bisacrylamide (MBA) and various α-amino acids, namely L-glycine, L-arginine, L-serine, L-histidine, L-alanine, L-leucine, L-glutamic acid, L-cystine, and L-tyrosine, as described in Section 2.2, *"Synthesis of linear α-amino acid-derived polyamidoamines"*. Each homopolymer was prepared in a one-step reaction conducted in aqueous solution at pH 11.0, using a 1:1 molar ratio of MBA to α-amino acid, with a solid content of 60 wt.% (Scheme 2.1.1a). Reaction times varied according to the different reactivities of the amino acids, which are influenced by steric effects of their side chains. Additionally, two copolymers were synthesized (Scheme 2.1.1b-c): one from a glycine/cystine mixture in a 1:0.5:0.5 molar ratio, and another from a tyrosine/arginine mixture in a 1:0.3:0.7 molar ratio. All final products were obtained by freeze-drying, with no further purification except for those intended for in vivo applications. These were further purified by ultrafiltration using membranes with a 3000 Da molecular weight cut-off to remove low molecular weight oligomers.

a)

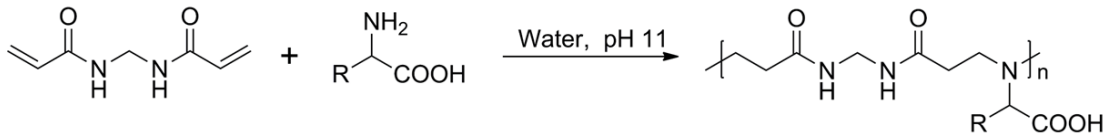

M 1 + **α-Amino acid** 1 → **PAA**

R = H	GLY	**M-GLY**
R = CH_2OH	SER	**M-SER**
R = CH_3	ALA	**M-ALA**
R = $CH_2CH(CH_3)$	LEU	**M-LEU**
R = $(CH_2)_2COOH$	GLU	**M-GLU**
R = $(CH_2)_3NHC{=}NH(NH_2)$	ARG	**M-ARG**
R = CH_2–imidazole	HIS	**M-HIS**

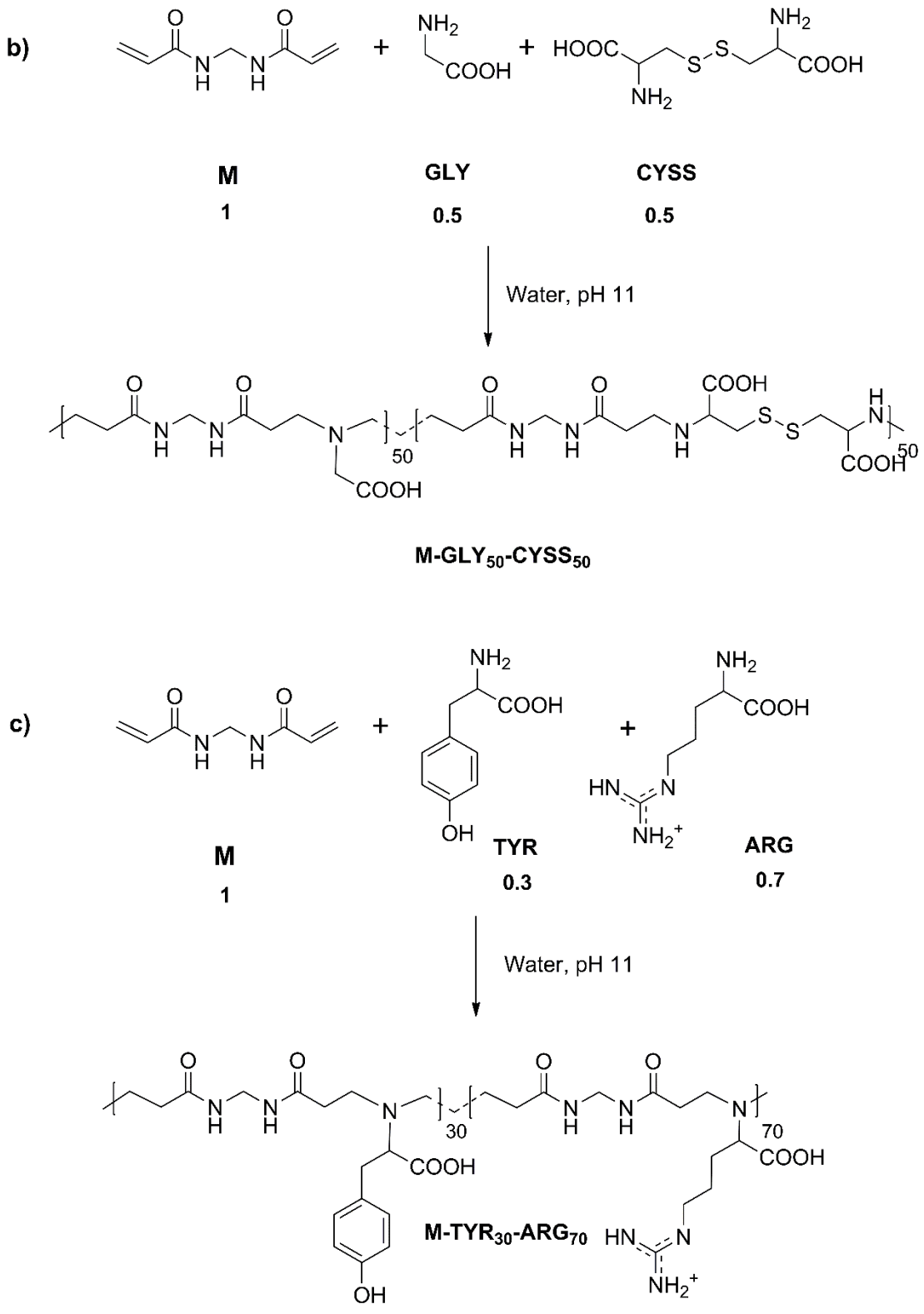

Scheme 2.1.1. Synthesis of PAA homopolymers (a) and of the glycine-cystine (b) and tyrosine-arginine-derived (c) PAA copolymers.

In addition to amino acid-based PAAs, a polyamidoamine named AGMA1 was synthesized, whose repeating unit is isomeric with that of M-ARG. The monomers used were 4-

aminobutylguanidine (AGM), an amine derived from the decarboxylation of L-arginine, and 2,2-bis(acrylamido)acetic acid (BAC), used here as an alternative to the common MBA. The aim was to obtain an α,ω-bisacrylamide-terminated oligomer, namely $AGMA_{20}$, with the same polymerization procedure developed for linear PAAs, with the addition of a 20% molar excess of BAC relative to AGM (Scheme 2.1.2). In fact, in bifunctional stepwise polymerization, the products of stoichiometrically unbalanced polymerization experiments are oligomers α,ω-terminated with the excess function.

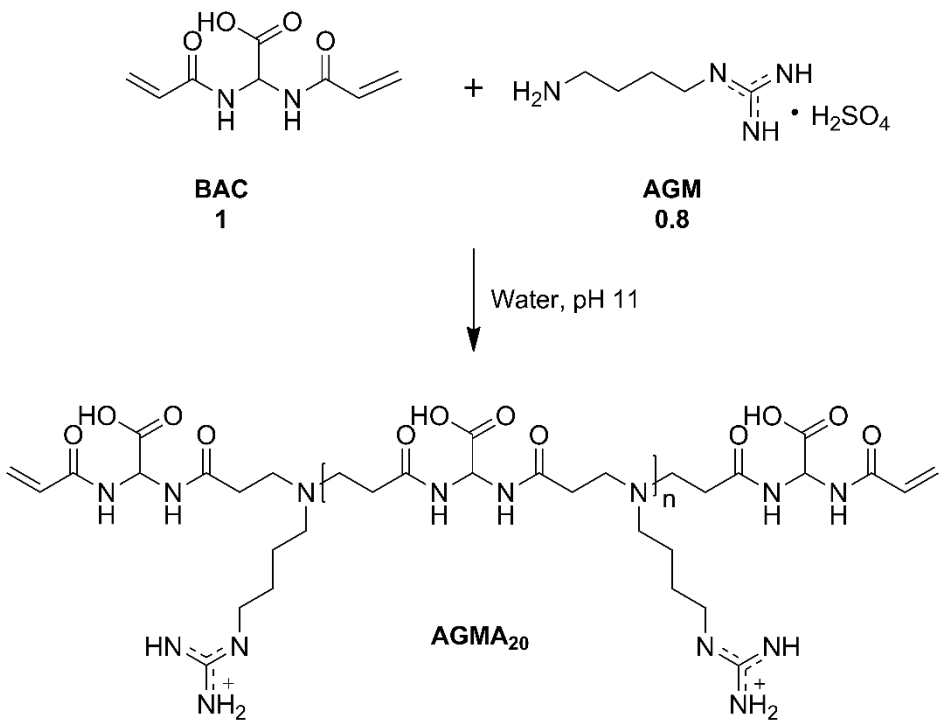

Scheme 2.1.2. Synthesis of $AGMA_{20}$ oligomer.

The chemical structures of all PAAs considered were checked by ^{1}H-NMR, ^{13}C-NMR, HSQC (Annex 1) and FT-IR/ATR spectroscopy (Annex 2). The NMR spectra of the samples display signals of residual vinyl protons from negligible unreacted MBA, typically appearing between 5.7 and 6.5 ppm. In several cases, signals of terminal groups can also be observed as minor side peaks adjacent to the main peak of the polymer backbone. Notably, M-HIS is the only polymer for which the NMR analysis indicates that histidine reacted through addition at both the primary amine and the imidazole moiety, consistent with dual-site reactivity of the monomer under the polymerization conditions. The FT-IR/ATR spectra of all samples display the characteristic absorption bands associated with PAA backbone structure: ν N-H at 3250 cm^{-1}, overtone δ N-H at 3050 cm^{-1}, ν_{as} CH_2 and ν_s CH_2 at 2950 and 2850 cm^{-1} respectively, ν N-C=O + ν_{as} COO^- overlapped at 1620 cm^{-1} and δ N-H + ν C-N at 1530 cm^{-1}. In addition, signals attributable to

the amino acid side chains can be recognized where resolution permits, although they frequently overlap with other characteristic bands, complicating their assignment.

The thermal stability was assessed by thermogravimetric analysis (Annex 3) and all PAAs presented typical degradation pattern as previously reported *(40,50)*. The corresponding $T_{onset10\%}$ (temperature at 10% weight loss), T_{max} (temperature at maximum degradation rate), and RMF (residual mass fraction at 800 °C) are summarized in Table A3.1. The TG curves in air closely resembled those in nitrogen up to 350 °C. At higher temperatures, the profiles diverged due to oxidation of the char formed during earlier decomposition. As regards homopolymers, in nitrogen, $T_{onset10\%}$ ranged from 115 to 172 °C, while in air it ranged from 101 to 177 °C. All PAAs degraded in a single main step in nitrogen (T_{max} 238–351 °C), whereas in air two main decomposition steps were observed between 230 and 350 and between 500 and 620 °C. As regards the copolymers, M-GLY_{50}-$CYSS_{50}$ and M-TYR_{30}-ARG_{70} showed complex multimodal weight-loss curves in both nitrogen and air with the lowest RMFs in nitrogen and the highest ones in air.

PAAs derived from α-amino acids are amphoteric polyelectrolytes, whose physico-chemical properties are governed by their ionization state, which is obviously pH-dependent. The ionic species distributions of PAAs (Annex 4) were calculated according to the Equations reported in Section 2.2 *"Characterization techniques"*, with the pK_a values of the ionizable groups in their repeating units listed in Table 2.1.1. pK_a values of the ionizable functions of PAAs were determined by titration as the pH values at the half-equivalent points, located in the buffer zone related to the specific function. The half-equivalent points were obtained as the half-titrant volume amounts added between consecutive inflections in the pH versus titrant volume curves. Direct determination of the pK_a values of the ionizable functions of the copolymers M-GLY_{50}-$CYSS_{50}$ and M-TYR_{30}-ARG_{70} was not possible due to their solubility constraints. The isoelectric point and the net charge reported in Table 2.1.1 were calculated considering the two repeating units separately in the selected ratio. The pK_a values of M-TYR were approximated using those of M-SER due to the similarity in their α-amino acid pK_a values while literature values were used for M-CYSS *(51)*. The speciation diagrams of M-GLY and M-ARG are reported in Figure 2.1.1.

Table 2.1.1. Average charge on PAAs' repeat units.

PAA	pK_a values	IP[a)]	Net charge at pH 7.0
M-GLY	pK_{a1}= 2.3	5.2	-0.07

	pK_{a2}= 8.1		
M-ARG	pK_{a1}= 2.4 pK_{a2}= 6.9 $pK_{a\text{-}guanidine}$ > 10	9.5	+0.29
M-SER	pK_{a1}= 2.3 pK_{a2}=7.2	4.8	-0.38
M-ALA	pK_{a1}= 2.12 pK_{a2} = 8.13	5.1	-0.09
M-LEU	pK_{a1}= 2.11 pK_{a2} = 7.37	4.8	-0.34
M-HIS	pK_{a1}= 2.1 $pK_{a\text{-}imidazole}$ = 5.1 pK_{a3}= 8.3	6.7	-0.04
M-GLU	pK_{a1}= 2.32 pK_{a2} = 4.28 pK_{a3}= 7.78	3.3	-1.14
AGMA1	pK_{a1}= 2.30 pK_{a2}= 7.40 $pK_{a\text{-}guanidine}$ > 10	9.7	+0.72
M-GLY$_{50}$-CYSS$_{50}$	-	5.1	-0.09
M-TYR$_{30}$-ARG$_{70}$	-	8.1	+0.21

[a)] Isoelectric Point

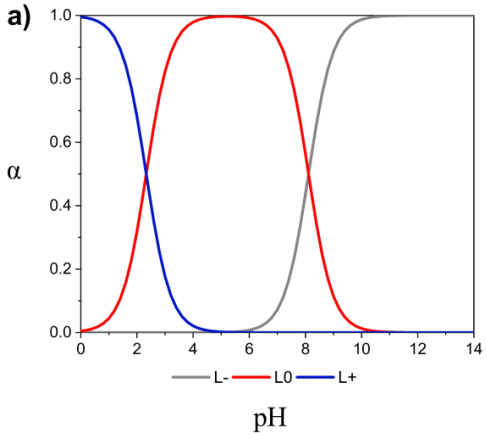

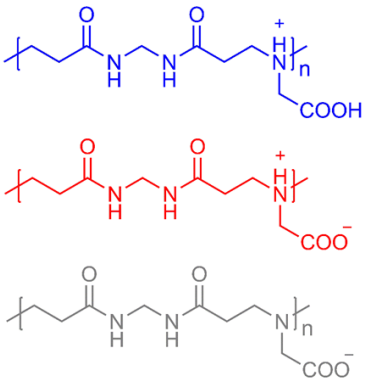

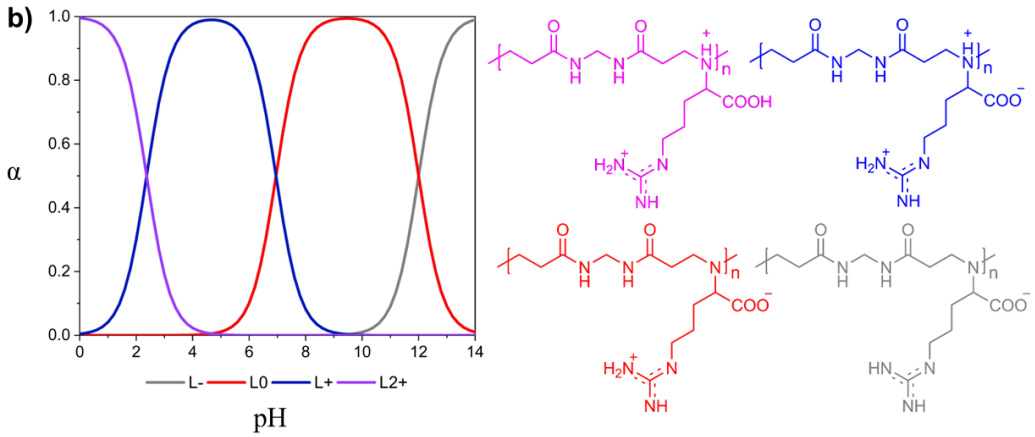

Figure 2.1.1. Speciation diagram and chemical structures of the ionized repeat units of M-GLY (a) and M-ARG (b).

2.2. Experimental part

Materials

N,N'-methylenebisacrylamide (M, 99 %), L-arginine (ARG, 99 %), L-glycine (GLY, 99 %), L-alanine (ALA, 99 %), L-leucine (LEU, 99 %), L-serine (SER, 99 %), L-histidine (HIS, 99 %), L-tyrosine (TYR, 98 %), L-glutamic acid (GLU, >98 %), L-cystine (CYSS, >98 %), lithium hydroxide monohydrate (98 %), hydrochloric acid (HCl, 37 %), D_2O (>99.9 %), glyoxylic acid (50 % w/w water solution), sulfuric acid (97 %), Phosphate Buffered Saline (PBS), lipopolysaccharide (LPS) from Escherichia coli (O111:B4), Griess reagent and 1-methyl-4-phenylpyridinium iodide (MPP^+) were purchased from Sigma-Aldrich (Milan, Italy) and used as received; 4-aminobutylguanidine sulphate (AGM, 95 %) was purchased from Enamine (Riga, Latvia); acrylonitrile (99.5 %) and ethylenediamine (EDA) (≥98 %) were supplied by Fluka (Charlotte, NC).

Synthesis of linear α-amino acid-derived polyamidoamines

PAAs were synthesized according to a well-established procedure *(39)* and the conditions adjusted depending on the different amino acid reactivity.

Synthesis of M-GLY: N,N'-methylenebisacrylamide (M), glycine (GLY) and lithium hydroxide monohydrate were dissolved in ultrapure water in 1:1:1 molar ratio and 60 wt% concentration. The reaction mixture was heated to 50 °C under stirring for 5 days in the dark under nitrogen. After this time, it was diluted with ultrapure water and acidified with 6 M HCl. The product was retrieved by freeze-drying the retained portion. All other α-aminoacid-derived PAAs were

synthesized following the same procedure adopted for M-GLY, using reagent quantities and conditions shown in Table 2.2.1.

Table 2.2.1. Experimental conditions adopted in the synthesis of PAAs.

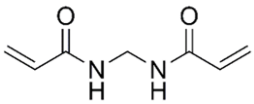

PAA code[a)]	α-Amino acid	α-Amino acid amount (g; mmol)	$LiOH \cdot H_2O$ (g; mmol)	T (°C)	t (days)
M-GLY	Glycine	2.4; 32	1.4; 32	50	5
M-ARG	Arginine	5.6; 32	-	50	9
M-SER	Serine	3.4; 32	1.4; 32	-	5
M-HIS	Histidine	5.0; 32	1.4; 32	50	9
M-ALA	Alanine	2.9; 32	1.4; 32	50	5
M-LEU	Leucine	4.3; 32	1.4; 32	50	10
M-GLU	Glutamic acid	4.8; 32	2.8; 64	50	9
$M\text{-}GLY_{50}\text{-}CYSS_{50}$	Glycine	1.2; 16	4.1; 48	50	2
	Cystine	3.9; 16			
$M\text{-}TYR_{30}\text{-}ARG_{70}$	Arginine	4.0; 22.4	-	75	8
	Tyrosine	1.8; 9.6	0.4; 9.6		

[a)]All preparations were performed using 5.0 g (32 mmol) of N,N'-methylenebisacrylamide.

The synthesis of α,ω-bisacrylamide-terminated oligomers $AGMA_{20}$ follows the same procedure adopted for linear PAAs previously reported, using a fixed molar excess of bisacrylamide respect to the amine. The selected bisacrylamide was 2,2-bis(acrylamido)acetic acid (BAC) and it synthesized according to a well-established procedure. A mixture of glyoxylic acid (25.2 g, 50 wt% water solution, 0.17 mol) and sulfuric acid (69.1 g, 0.68 mol) was prepared by dropwise addition the latter while maintained cooled in an ice bath. The cold acid mixture was then dropped very slowly under vigorous stirring in a three-necked glass flask containing acrylonitrile (26.4, 0.50 mol) and copper acetate (10 mg) at -4 °C. During the reaction, the temperature was maintained between 0-10 °C. After the addition (2 h), the temperature was allowed to gradually adjust to room temperature and the mixture was maintained under stirring for a further 2.5 h. The resulting yellowish, viscous solution was slowly poured in cold water (120 mL) to give a white precipitate which was left at 4 °C overnight. After this time, the raw

solid was recovered by filtration. The product was washed by pouring into 50 mL cold water for 20 min (3 x 50 mL) and filtered. The white precipitate was dried to constant weight at 25 ° C under reduced pressure. Yield = 72 %, purity = 100%. The conditions for the synthesis of α,ω-bisacrylamide-terminated AGMA1 oligomer coded $AGMA_{20}$ are reported in Table 2.2.2 and the preparation was performed using 5.0 g (25 mmol) of 2,2-bis(acrylamido)acetic acid (BAC).

Table 2.2.2. Experimental conditions adopted in the synthesis of $AGMA_{20}$.

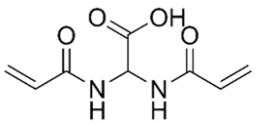

PAA	Amine	Amine (g; mmol)	$LiOH \cdot H_2O$ (g; mmol)	T (°C)	t (days)
$AGMA_{20}$	4-aminobutylguanidine	4.9; 20	1.9; 45	50	4

Characterization techniques

PAAs were analyzed by nuclear magnetic resonance, namely, ^{1}H-NMR and ^{13}C-NMR, by FT-IR/ATR spectroscopy and thermogravimetric analysis.

Nuclear Magnetic Resonance (NMR): the chemical structure of PAAs was assessed by ^{1}H-NMR, collecting spectra in D_2O at pH 4.5 and at 25 °C using a Bruker Avance NEO-400 NMR spectrometer (Milan, Italy) operating at 400.13 MHz. Parameters: scan number 32, relaxation delay, d1, 10.0 s. PAAs were also characterized by ^{13}C-NMR and Heteronuclear Single Quantum Coherence (HSQC) NMR (Annex 1). Deuterium oxide (D_2O, >99.9%), and deuterium chloride solution (DCl, 35% in D_2O) were supplied by Sigma-Aldrich (Milan, Italy) and used as received.

FT-IR/ATR Spectroscopy: synthesized PAAs were analyzed by Attenuated Total Reflectance (ATR) Fourier Transform Infrared spectroscopy (FT-IR). FT-IR/ATR spectra were recorded at room temperature, in the 4000 - 600 cm^{-1} wavenumber range, with 256 scans and 4 cm^{-1} resolution, using a Jasco FT-IR/FIR spectrophotometer (Milano, Italy), equipped with a diamond crystal (Annex 2).

Thermogravimetric Analysis (TGA): the thermal stability of PAAs was assessed by thermogravimetric analysis in nitrogen and air from 30 to 800 °C range, at 10 °C min^{-1} heating rate, with a 50 mL min^{-1} gas flow, using a TGA 2 Star System (Mettler-Toledo, Milan, Italy). All samples were dried in isothermal conditions at 100 °C for 3 min prior to the heating run (Annex 3).

Ionic species distributions: the ionic species distributions of PAAs were calculated based on the pK_a values of the ionizable groups in their repeating units. pK_a values were determined as the pH values at the half-equivalent points, located in the buffer zone related to the specific function following the De Levie approach *(52)*. The half-equivalent points were obtained as the half-titrant volume amounts added between consecutive inflections in the pH versus titrant volume curves. Speciation diagrams (Annex 4) were obtained by plotting the concentration fractions (α) of the different ionic species as a function of pH.

In this thesis, two types of repeating units differing in the number of ionizable functional groups were considered: one is characterized by three ionizable groups and one by two ionizable groups, each with distinct pK_a values.

The concentration fractions of a species with three pK_a, as M-ARG ($pK_{a\text{-}COOH}$, $pK_{a\text{-}NR3}$ and $pK_{a\text{-}guanidine}$), M-HIS ($pK_{a\text{-}COOH}$, $pK_{a\text{-}NR3}$ and $pK_{a\text{-}imidazole}$) M-GLU ($pK_{a1\text{-}COOH}$, $pK_{a2\text{-}COOH}$ and $pK_{a\text{-}NR3}$) and AGMA1 ($pK_{a\text{-}COOH}$, $pK_{a\text{-}NR3}$ and $pK_{a\text{-}guanidine}$) were calculated according to the following Equations in which *L* is the species with a defined net charge (e.g *L2+* is the species with charge +2):

- Mass balance: $C_{\mathrm{T}} = C_{\mathrm{L2+}} + C_{\mathrm{L+}} + C_{\mathrm{L0}} + C_{\mathrm{L-}}$
- Equilibrium constants: $K_{\text{a-COOH}} = \frac{C_{\mathrm{L+}}\, C_{\mathrm{H+}}}{C_{\mathrm{L2+}}} = K_{a1}$; $K_{\text{a-NR3}} = \frac{C_{\mathrm{L0}}\, C_{\mathrm{H+}}}{C_{\mathrm{L+}}} = K_{a2}$; $K_{\text{a-guanidine}} = \frac{C_{\mathrm{L-}}\, C_{\mathrm{H+}}}{C_{\mathrm{L0}}} = K_{a3}$
- Concentration fractions:

$$C_{\mathrm{L+}} = \frac{C_{\mathrm{L2+}} K_{a1}}{C_{H+}} \qquad \textit{Eq. 2.2.1}$$

$$C_{\mathrm{L0}} = \frac{C_{\mathrm{L+}} K_{a2}}{C_{H+}} = \frac{C_{\mathrm{L2+}} K_{a1} K_{a2}}{C_{H+}^2} \qquad \textit{Eq. 2.2.2}$$

$$C_{\mathrm{L-}} = \frac{C_{\mathrm{L0}} K_{a3}}{C_{H+}} = \frac{C_{\mathrm{L2+}} K_{a1} K_{a2} K_{a3}}{C_{H+}^3} \qquad \textit{Eq. 2.2.3}$$

$$C_{\mathrm{T}} = C_{L2+} + \frac{C_{\mathrm{L2+}} K_{a1}}{C_{H+}} + \frac{C_{\mathrm{L2+}} K_{a1} K_{a2}}{C_{H+}^2} + \frac{C_{\mathrm{L2+}} K_{a1} K_{a2} K_{a3}}{C_{H+}^3} \qquad \textit{Eq. 2.2.4}$$

$$= C_{L2+}\left(1 + \frac{K_{a1}}{C_{H+}} + \frac{K_{a1} K_{a2}}{C_{H+}^2} + \frac{K_{a1} K_{a2} K_{a3}}{C_{H+}^3}\right)$$

$$\boldsymbol{\alpha_{L2+}} = \frac{C_{\mathrm{L2+}}}{C_{\mathrm{T}}} = \frac{1}{1 + \frac{K_{a1}}{C_{H+}} + \frac{K_{a1} K_{a2}}{C_{H+}^2} + \frac{K_{a1} K_{a2} K_{a3}}{C_{H+}^3}} \qquad \textit{Eq. 2.2.5}$$

$$= \frac{C_{H+}^3}{C_{H+}^3 + K_{\mathrm{a1}} C_{H+}^2 + K_{\mathrm{a1}} K_{\mathrm{a2}}\, C_{H+} + K_{a1} K_{a2} K_{a3}} = \frac{C_{H+}^3}{D}$$

$$\boldsymbol{\alpha_{L+}} = \frac{C_{L+}}{C_T} = \frac{K_{a1}}{C_{H+}(1 + \frac{K_{a1}}{C_{H+}} + \frac{K_{a1}K_{a2}}{C_{H+}^2} + \frac{K_{a1}K_{a2}K_{a3}}{C_{H+}^3})} \qquad \textit{Eq. 2.2.6}$$

$$= \frac{K_{a1}C_{H+}^2}{C_{H+}^3 + K_{a1}C_{H+}^2 + K_{a1}K_{a2}C_{H+} + K_{a1}K_{a2}K_{a3}} = \frac{K_{a1}C_{H+}^2}{D}$$

$$\boldsymbol{\alpha_{L0}} = \frac{C_{L0}}{C_T} = \frac{K_{a1}K_{a2}}{C_{H+}^2(1 + \frac{K_{a1}}{C_{H+}} + \frac{K_{a1}K_{a2}}{C_{H+}^2} + \frac{K_{a1}K_{a2}K_{a3}}{C_{H+}^3})} = \frac{K_{a1}K_{a2}C_{H+}}{D} \qquad \textit{Eq. 2.2.7}$$

$$\boldsymbol{\alpha_{L-}} = \frac{C_{L-}}{C_T} = \frac{K_{a1}K_{a2}K_{a3}}{C_{H+}^3\left(1 + \frac{K_{a1}}{C_{H+}} + \frac{K_{a1}K_{a2}}{C_{H+}^2} + \frac{K_{a1}K_{a2}K_{a3}}{C_{H+}^3}\right)} = \frac{K_{a1}K_{a2}K_{a3}}{D} \qquad \textit{Eq. 2.2.8}$$

The case involving a species with two pK_a values, as M-GLY ($pK_{a\text{-}COOH}$, $pK_{a\text{-}NR3}$), M-SER ($pK_{a\text{-}COOH}$, $pK_{a\text{-}NR3}$), M-LEU ($pK_{a\text{-}COOH}$, $pK_{a\text{-}NR3}$) and M-ALA ($pK_{a\text{-}COOH}$, $pK_{a\text{-}NR3}$), represents a simplified version of the previously discussed system with three ionizable groups. The concentration fractions were calculated according to the following Equations:

- Mass balance: $C_T = C_{L+} + C_{L0} + C_{L-}$
- Equilibrium constants: $K_{a\text{-}COOH} = \frac{C_{L0}\,C_{H+}}{C_{L+}} = K_{a1}$; $K_{a\text{-}NR3} = \frac{C_{L-}\,C_{H+}}{C_{L0}} = K_{a2}$
- Concentration fractions:

$$C_{L0} = \frac{C_{L+}K_{a1}}{C_{H+}} \qquad \textit{Eq. 2.2.9}$$

$$C_{L-} = \frac{C_{L0}K_{a2}}{C_{H+}} \rightarrow C_{L-} = \frac{C_{L+}K_{a1}K_{a2}}{C_{H+}^2} \qquad \textit{Eq. 2.2.10}$$

$$C_T = C_{L+} + \frac{C_{L+}K_{a1}}{C_{H+}} + \frac{C_{L+}K_{a1}K_{a2}}{C_{H+}^2} = C_{L+}(1 + \frac{K_{a1}}{C_{H+}} + \frac{K_{a1}K_{a2}}{C_{H+}^2}) \qquad \textit{Eq. 2.2.11}$$

$$\boldsymbol{\alpha_{L+}} = \frac{C_{L+}}{C_T} = \frac{1}{1 + \frac{K_{a1}}{C_{H+}} + \frac{K_{a1}K_{a2}}{C_{H+}^2}} = \frac{C_{H+}^2}{C_{H+}^2 + K_{a1}C_{H+} + K_{a1}K_{a2}} = \frac{C_{H+}^2}{D} \qquad \textit{Eq. 2.2.12}$$

$$\boldsymbol{\alpha_{L0}} = \frac{C_{L0}}{C_T} = \frac{C_{L+}K_{a1}}{C_{H+}C_{L+}(1 + \frac{K_{a1}}{C_{H+}} + \frac{K_{a1}K_{a2}}{C_{H+}^2})} = \frac{K_{a1}C_{H+}}{C_{H+}^2 + K_{a1}C_{H+} + K_{a1}K_{a2}} = \frac{K_{a1}\,C_{H+}}{D} \qquad \textit{Eq. 2.2.13}$$

$$\boldsymbol{\alpha_{L-}} = \frac{C_{L-}}{C_T} = \frac{C_{L+}K_{a1}K_{a2}}{C_{H+}^2C_{L+}(1 + \frac{K_{a1}}{C_{H+}} + \frac{K_{a1}K_{a2}}{C_{H+}^2})} = \frac{K_{a1}K_{a2}}{C_{H+}^2 + K_{a1}C_{H+} + K_{a1}K_{a2}} = \frac{K_{a1}K_{a2}}{D} \qquad \textit{Eq. 2.2.14}$$

The first part of the thesis was focused on the evaluation of the potential environmental impact of water-soluble α-amino-acid-derived PAAs, which may accidentally be released into ecosystems during or after their useful life. In the first project, described in Chapter 3, their effects were assessed at early stages of plant development using *Lepidium sativum* (watercress) seeds, with particular focus on correlating phytotoxicity to polymer charge distribution. In the second project, described in Chapter 4, their impact was evaluated on aquatic ecosystems using zebrafish (*Danio rerio*) embryos, a vertebrate model organism sharing several features with mammals.

3. ECOTOXICITY ASSESSMENT OF PAAs: SHORT-TERM PHYTOTOXICITY SCREENING OF PAAS BY SEED GERMINATION TEST

In this study, the effectiveness and robustness of the seed germination test for assessing the phytotoxicity of water-soluble polymers has been investigated using *Lepidium sativum* seeds as a viable model. The test was applied to six amphoteric a-amino acid-derived PAAs, which proved efficient flame retardants for cotton. Several parameters have been considered to assess the response of seeds exposed to PAA water solutions at different concentrations, including germination percentage, root and bud elongation, and germination index. A large set of raw data and an accurate statistical analysis allowed us to critically analyze the different test parameters and to demonstrate their versatility and usefulness in evaluating the phytotoxicity of water-soluble polymers.

All results are presented in detail in a dedicated publication:

Ranucci, E.; Treccani, S.; Ferruti, P.; Alongi, J. The Seed Germination Test as a Valuable Tool for the Short-Term Phytotoxicity Screening of Water-Soluble Polyamidoamines. Polymers ***2024****, 16,1744. https://doi.org/10.3390/polym16121744*

3.1. Introduction

Water-soluble polymers are extensively used across a wide range of consumer product formulations, including personal care products, detergents, pharmaceuticals, and agricultural fertilizers *(53,54)*. Following their use, these polymers are typically disposed of in landfills, incinerated, or released into aquatic environments. Due to their water solubility, they can migrate through filtration processes and eventually reach aquifers, making them widespread environmental contaminants. Once present in aquatic systems, water-soluble polymers may modify the physico-chemical properties of the water matrix *(55)*. For example, their interaction

with persistent organic pollutants can increase the bioavailability of these pollutants, facilitating their entry into the food chain *(56)*. Polyelectrolytes, which carry charged groups, can also aggregate with organic matter *(57)* and minerals, forming floating composites that may sink. These materials may exert toxic effects depending on their charge density and the ratio of positive to negative charges. Despite their ubiquity, the environmental risks posed by water-soluble polymers, especially those carrying charges, are often underestimated. This is evident from their exclusion, to date, from European circular economy action plans. Given their potential ecological impact, it is essential to monitor their concentration in water systems and apply rigorous testing methods to assess their ecotoxicity *(58)*. Various short-term toxicity screening protocols for hazardous substances have been developed by international environmental agencies *(44,59)*. These tests are useful for determining whether contaminants are bioavailable, a necessary condition for them to exert toxic effects. Among them, the seed germination test has proven to be a rapid and reliable method. Commonly used to assess compost quality in agriculture *(47,60)*, it is also effective in evaluating the phytotoxicity of diverse environmental contaminants, such as heavy metals *(46,61)*, pharmaceuticals, hydrocarbons *(62)*, herbicides, and microplastics *(63)*. In a recent study *(49)*, this method was applied to evaluate the phytotoxicity of a water-soluble amphoteric glycine-derived polyamidoamine, namely M-GLY, which proved to be an efficient flame retardant for cotton fabrics *(40)*. Aqueous solutions of M-GLY at concentrations ranging from 0.156 to 5.0 mg mL^{-1} were tested, alongside oligomeric forms of M-GLY containing 20-30% acrylamide terminal groups considered potentially more toxic than the corresponding high molecular weight polymers. M-GLY exhibited no inhibitory effects on the germination or seedling elongation of *Lepidium sativum* (watercress), as indicated by germination index (GI) values, where GI is defined as the product of relative radicle growth and relative seed germination. In contrast, acrylamide-terminated M-GLY oligomers showed inhibitory effects on root elongation, but only at the highest tested concentration of 5.0 mg mL^{-1}.

3.2. Results and discussion

The aim of this study was to validate the robustness and applicability of the seed germination test as a reliable tool for assessing the environmental compatibility of water-soluble amphoteric polymers. These polymers are currently of significant interest due to their potential environmental impact, which may be comparable to that of microplastics *(56)*. In this context, six water-soluble PAAs that proved flame retardant properties, namely M-ALA, M-LEU, M-ARG, M-SER, M-GLU and the copolymer M-GLY_{50}-$CYSS_{50}$, were investigated. Since these

polymers are amphoteric polyelectrolytes with well-defined pH-dependent distributions of ionic species, one of the key objectives of the research was to investigate the correlation between the test outcomes and the ratio of positive to negative charges within the repeat units of the PAAs. The ionic species distributions shown in Figure 3.2.1 were determined from the speciation curves shown in Annex 4.

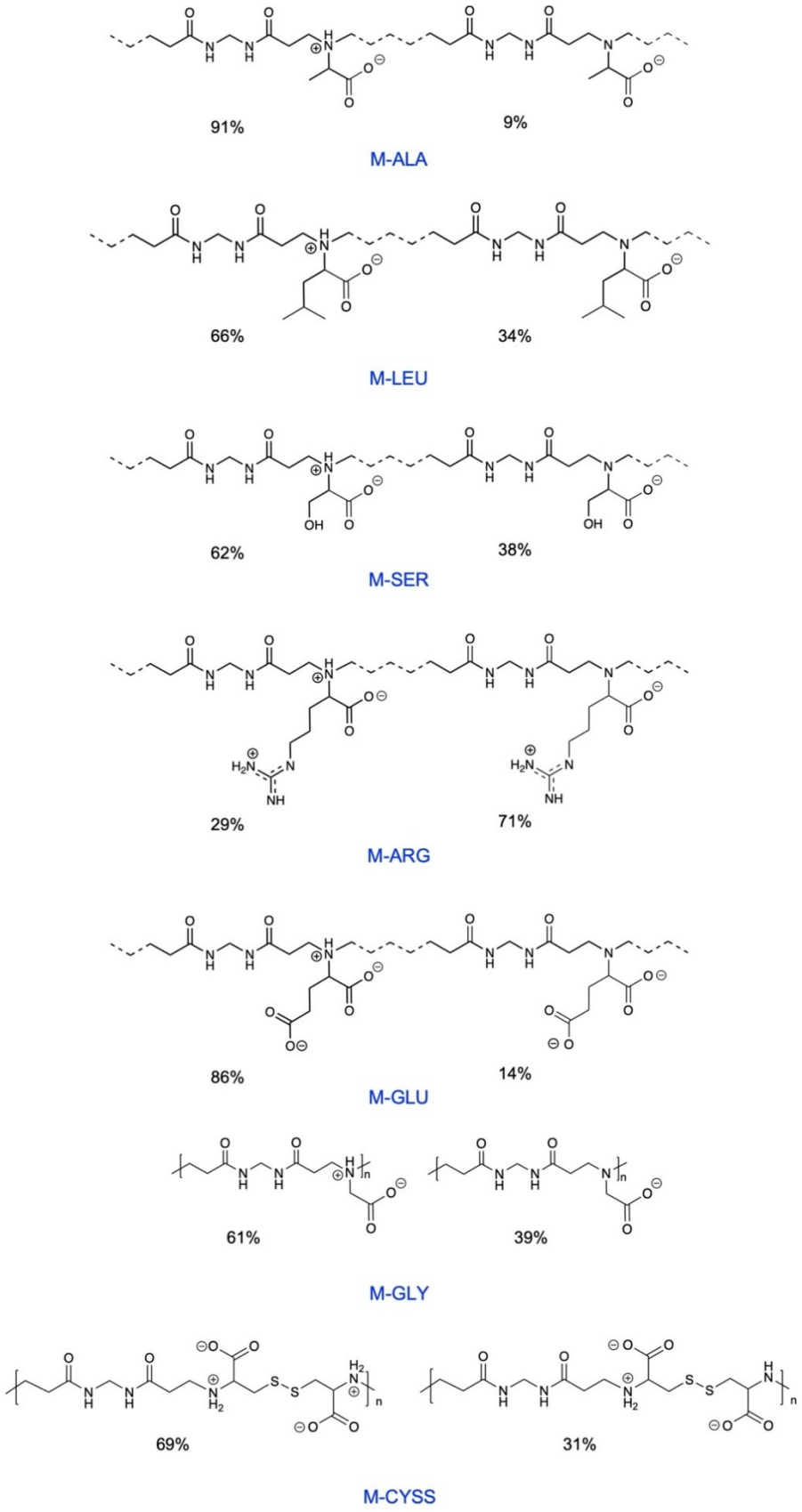

Figure 3.2.1. Ionic species distribution of PAAs at pH 7. 0, and at pH 7.5 in the case of M-GLY_{50}-$CYSS_{50}$, of which the two repeating units (M-GLY and M-CYSS) are considered separately.

The calculated isoelectric points indicate that all PAAs, except M-ARG, carry a net negative charge at pH 7.0 (pH 7.5 for M-GLY_{50}-$CYSS_{50}$). M-ALA is weakly anionic, with 9% of repeat units bearing a single negative charge and the remaining being zwitterionic (net average charge −0.09; +/− charge ratio 0.91). M-LEU, M-SER, and M-GLY_{50}-$CYSS_{50}$ are moderately anionic, with 34%, 38%, and 35% of repeat units carrying a single negative charge, respectively (net average charges −0.33, −0.38, and −0.35; +/− charge ratios 0.66, 0.62, and 0.72). M-GLU is highly anionic, containing 14% of units with two negative charges and the rest with two negative and one positive charge (net average charge −1.14; +/− charge ratio 0.43). In contrast, M-ARG is predominantly cationic, with 29% of repeat units carrying two positive charges and the remaining being zwitterionic (net charge +0.29; +/− charge ratio 1.29).

Effect of PAAs on the early stages of seed germination

To better define the endpoints of standard germination rates, the early germination kinetics of *Lepidium sativum* seeds were examined. Germination is a complex process involving several biochemical, physiological, and morphological changes. It begins with water absorption through the micropyles on the *testa* tegument of the dry seed and concludes with radicle protrusion (≥ 2 mm), marking the completion of germination *(64)*.

This process is classically divided into three phases (Figure 3.2.2a) *(64,65)*. Phase I (imbibition) is characterized by rapid water uptake, leading to seed coat softening and the activation of metabolic pathways, including respiration and hormone activity. Phase II (lag phase) features minimal water uptake but intense metabolic activity, including enzyme activation (from both stored and newly synthesized enzymes) and reserve mobilization. Radicle protrusion occurs at the end of this phase, once its growth force exceeds the mechanical resistance of seed tissues. In *Lepidium sativum*, as in many species, germination includes sequential rupture of the *testa* and endosperm *(66)*. Phase III (post-germination) marks the beginning of seedling development. In dicotyledonous seeds like *Lepidium sativum*, the radicle is the first organ to emerge, while in monocotyledonous seeds, this role is taken by the coleorhiza *(67)*.

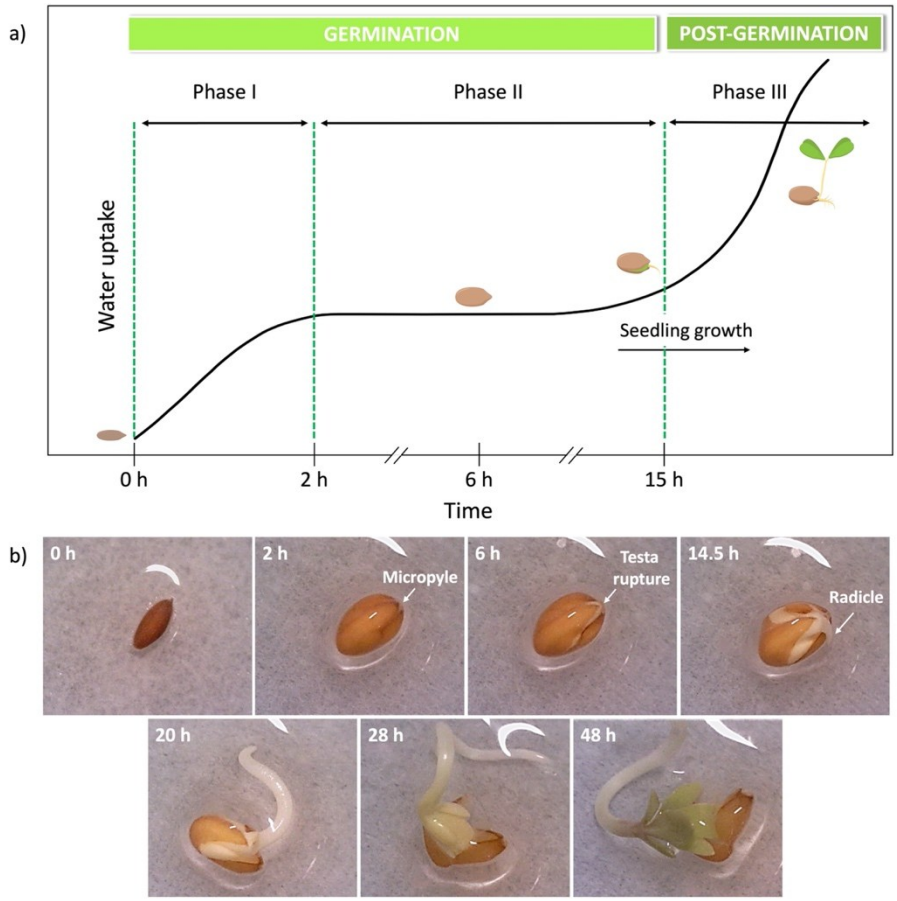

Figure 3.2.2. Phases of seed germination (a). Morphology of *Lepidium sativum* seeds at different stages of the germination process (b).

The early stages of *Lepidium sativum* seed germination in water and in PAA solutions (2.5 mg mL^{-1}, the maximum concentration used in germination tests, Section 3.3) were monitored by optical microscopy (Figure 3.2.2b) to assess potential interference of PAAs with embryo (seed) development. Key events, as complete imbibition, *testa* rupture, and radicle protrusion (≥ 2 mm), were recorded. Imbibition was completed within 2 h ± 0.5 in both water and PAA solutions and germination times did not significantly differ (Figure 3.2.3b). However, *testa* rupture was delayed in the presence of M-ARG (Figure 3.2.3a), the only predominantly cationic PAA, indicating a strong interaction with the biochemical processes involved in embryo maturation. Notably, M-ARG also showed the highest phytotoxicity, as discussed in subsequent sections. These findings suggest that early germination analysis can serve as a sensitive bioindicator and confirm that, under the tested conditions, the initial phases of germination are not affected by the presence of PAAs.

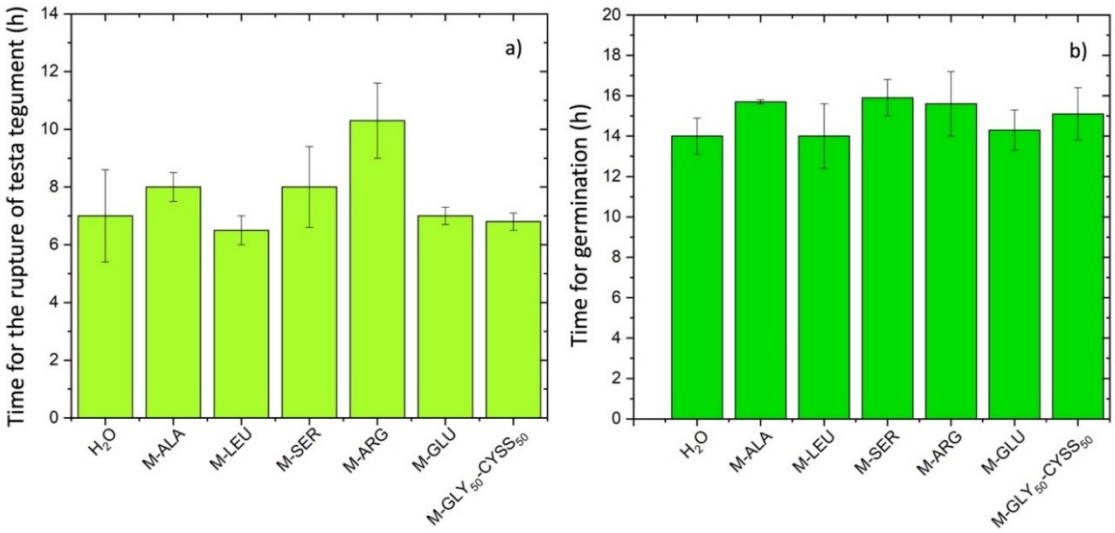

Figure 3.2.3. Germination kinetics of *Lepidium sativum* seeds exposed to 2.5 mg mL^{-1} PAA solutions for 120 h (a). Rupture of the *testa* tegument (b). Seed germination identified as the protrusion of 2 mm radicle.

Effect of PAAs on seed germination, root, and bud elongation

The seed germination test offers multiple layers of insight, with one of the primary aspects being the evaluation of acute toxicity. This is determined by identifying the EC_{50} value, the concentration at which seed germination is reduced by 50% compared to the negative control after exposure to a chemical over a set period. Sublethal effects of water-soluble compounds absorbed by seedlings are typically assessed by measuring changes in root elongation *(45)*.

In this study, the experimental protocol was designed in accordance with the guidelines of the US Environmental Protection Agency, covering general test conditions such as water type, temperature, duration, darkness, and concentration range *(44)*. *Lepidium sativum* seeds were selected as the model organism due to their rapid and consistent germination. As described in Section 3.3, the seeds were exposed to PAA aqueous solutions at concentrations of 0.156, 0.313, 0.625, 1.25, and 2.5 mg L^{-1} for 120 hours, in darkness, at 25°C and pH 7.0, except for the M-GLY_{50}-$MCYSS_{50}$ test, which was conducted at pH 7.5. Notably, the highest tested concentration exceeded the 1 mg L^{-1} limit recommended by the reference protocol *(68)*, as the goal was to challenge the system and evaluate its robustness.

Each concentration was tested in quadruplicate, and an additional quadruplicate of seeds was incubated in distilled water as a control, for a total amount of 1200 seeds tested. This large sample size enabled a statistically robust analysis of the data. According to EPA guidelines, test results were considered invalid if the average germination rate in the negative control fell below 90%. In this study, the average values for the negative control were: SG% = 98 ± 2%, total

seedling length = 12 ± 2 cm, bud length = 3.2 ± 0.4 cm, and radicle length = 8 ± 2 cm. Figure 3.2.4 displays the appearance of seeds at the beginning and after 120 hours in a single Petri dish for both negative (Figures 3.2.4a-b) and positive controls (Figures 3.2.4d-e) while Figure 3.2.4c provides a closer view of seedlings from the same experiment, highlighting the bud and radicle morphology and their respective lengths. Figure 3.2.5 illustrates seed germination and seedling development after exposure to 2.5 mg mL^{-1} PAA for 120 hours.

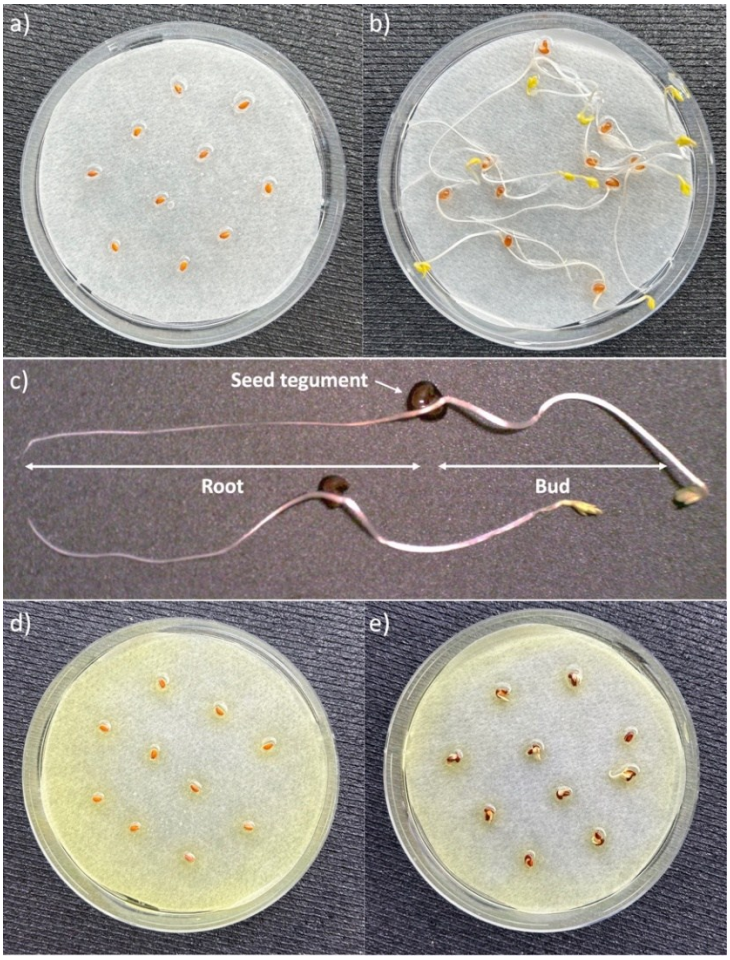

Figure 3.2.4. *Lepidium sativum* seedling growth after seed exposure to ultrapure water at 0 (a) and 120 h (b). Optical microscope image of seedlings grown in ultrapure water (c). Effect of seed exposure to the positive control (0.1% $K_2Cr_2O_7$) at 0 (d) and 120 h (e).

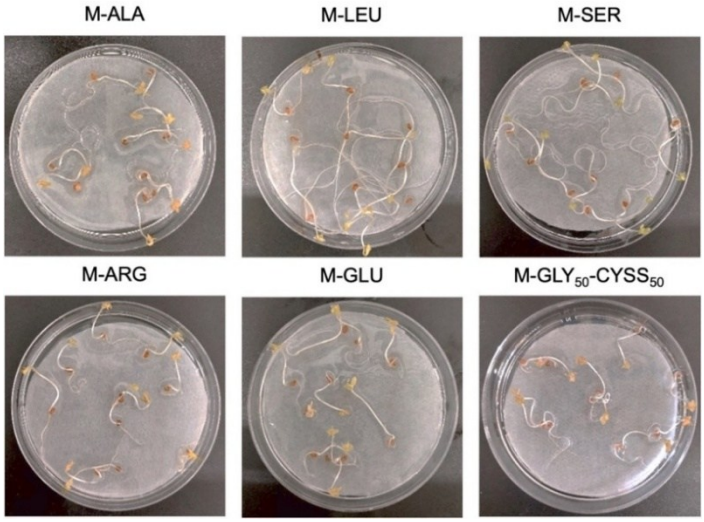

Figure 3.2.5. *Lepidium sativum* seedling growth after seed exposure to 2.5 mg mL^{-1} PAA solutions for 120 h.

The concentration dependence of the seed germination percentage (SG%) observed when *Lepidium Sativum* seeds were exposed to PAA water solutions is shown in Figure 3.2.6. Each PAA test was paired with a control using an equal number of seeds incubated in ultrapure water. SG%, calculated as the ratio of germinated seeds to total seeds (Eq. 3.3.1, Section 3.3), serves as an indicator of acute toxicity, with non-germination considered equivalent to mortality *(44)*. Substances with SG% ≥ 83% are generally classified as non-phytotoxic *(47)*. In this study, all PAA treatments consistently showed SG% values above 95%, comparable to the negative control. Therefore, the tested PAAs did not exhibit acute phytotoxicity regardless of their structure, charge, and concentration, and no EC_{50} value could be determined.

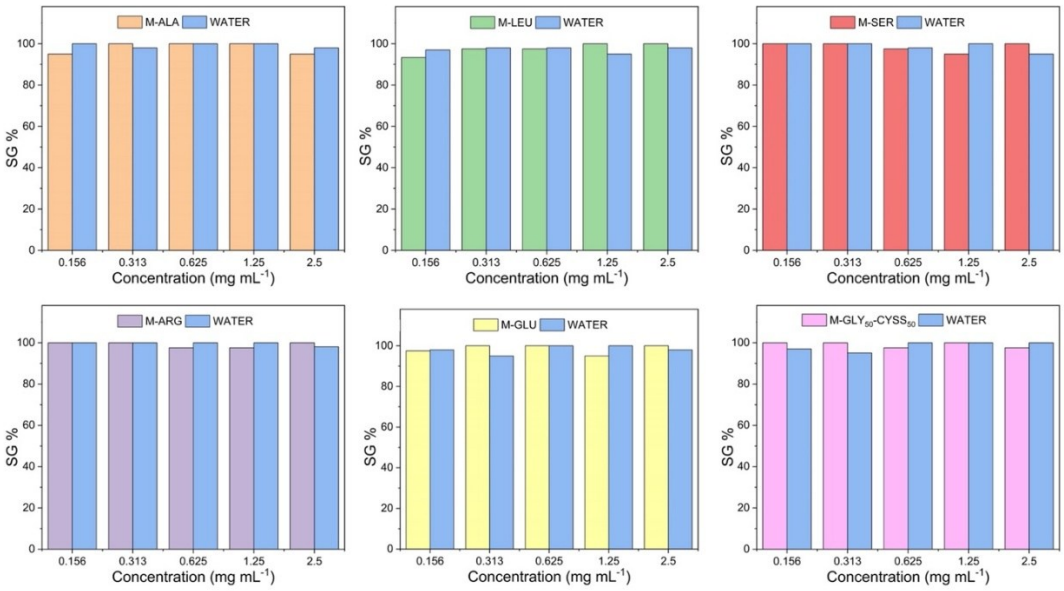

Figure 3.2.6. Concentration dependence of the seed germination percentage, SG%, of *Lepidium sativum* seeds exposed to PAA solutions for 120 h.

Relative Seed Germination (RSG) calculated using Eq. 3.3.2 (Section 3.3), compares the number of seeds germinated in PAA solutions to those in the negative control. As shown in Figure 3.2.7, all PAAs yielded RSG values near 1 (ranging from 0.95 to 1.05) across all concentrations. Consistent with SG% results, this confirms the absence of acute toxicity and any concentration-dependent effects.

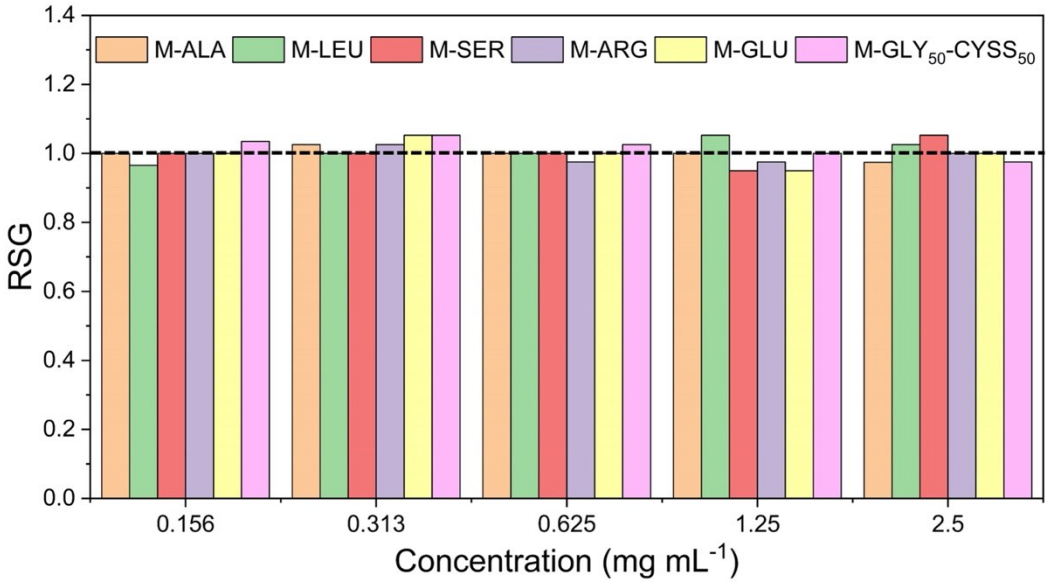

Figure 3.2.7. Concentration dependence of the relative seed germination (RSG) of *Lepidium sativum* seeds exposed to PAA solutions for 120 h.

Germination is largely driven by cotyledon energy reserves and may be less sensitive to sublethal stress. Therefore, seedling growth parameters, particularly root and bud length, are better indicators of chronic phytotoxicity *(69)*. In this study, both were assessed as sublethal endpoints. Root length reflects the development of the root system, essential for nutrient uptake, water absorption, and anchorage. As the root is the first part exposed to contaminants, it serves as a sensitive biomonitoring target *(70)* . The concentration-dependent effects of PAA exposure on *Lepidium sativum* root length after 120 hours are shown in Figure 3.2.8. Average root lengths were analyzed statistically via *t-test* (*$p < 0.05$).

Results indicate varied responses depending on PAA type and concentration. M-SER, with a moderate negative charge (-0.38 net average charge), showed minimal toxicity. Root length was slightly reduced compared to the control at the highest (2.5 mg L^{-1}) and lowest (0.156 mg L^{-1}) concentrations, while intermediate levels (0.313 and 1.5 mg L^{-1}) showed a significant stimulating effect. In contrast, M-ARG consistently and significantly inhibited root elongation across all concentrations. This was attributed to its strong positive charge (+0.29 net average), consistent with the known phytotoxicity of cationic polymers *(71–73)*. M-GLU, the most negatively charged PAA (-1.14 net average), significantly inhibited root growth only at 0.625

and 1.5 mg L^{-1}. M-ALA and M-GLY_{50}-$CYSS_{50}$ showed significant root inhibition at concentrations ≥ 1.25 and ≥ 0.625 mg L^{-1} respectively, and strongly so at 2.5 mg L^{-1}.

M-LEU, despite having a similar charge profile to M-SER, exhibited stronger inhibition at concentrations ≥ 0.625 mg L^{-1}. This difference may be due to its lipophilic side chain (-$CH_2CH(CH_3)_2$) compared to the hydrophilic -OH in M-SER, suggesting that factors beyond charge, such as side-chain chemistry, also influence PAA phytotoxicity.

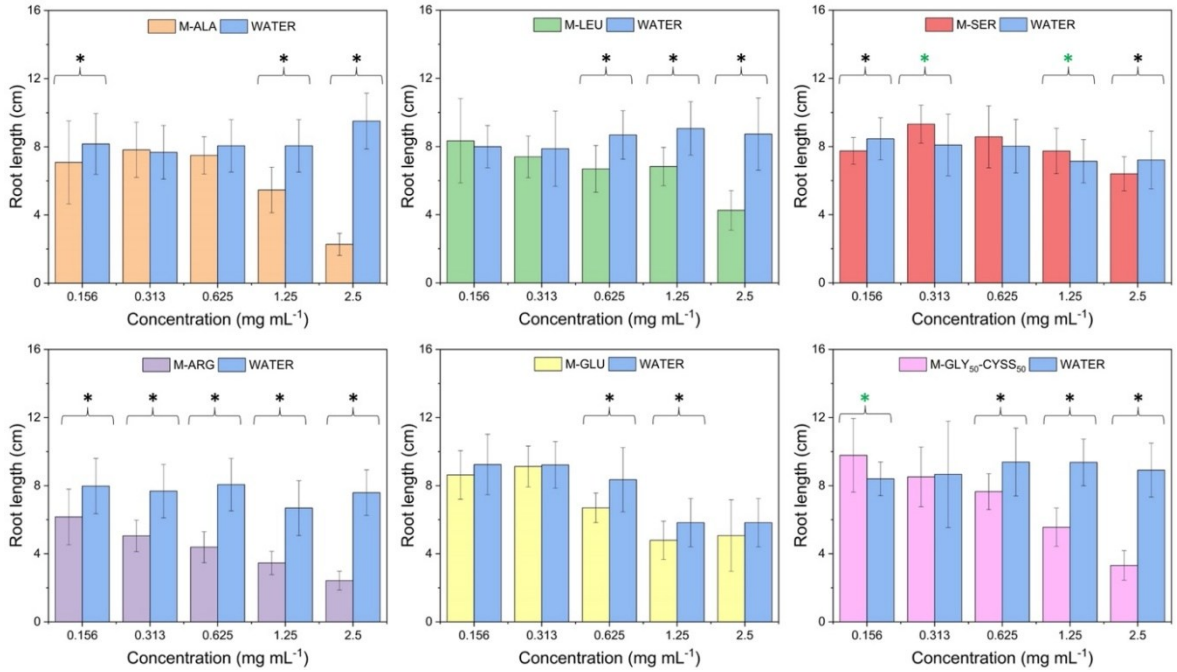

Figure 3.2.8. Concentration dependence of the length of *Lepidum sativum* roots after seed incubation in PAA aqueous solutions for 120 h. Results are reported as the mean ± confidence. Asterisks indicate significant differences (*p < 0.05) compared to the control; black asterisks indicate greater length in water, the green asterisk greater length in the PAA solution.

The concentration-dependent effects of PAA solutions on *Lepidium sativum* bud length after 120 hours is shown in Figure 3.2.9. Overall, bud growth was largely unaffected by PAA exposure. Significant inhibition was observed only at the highest concentration (2.5 mg L^{-1}), except for M-GLU, which showed effects at 1.25 mg L^{-1}. Notably, M-ARG, despite its strong root inhibition, stimulated bud growth at concentrations from 0.156 to 1.25 mg L^{-1}. These findings support previous reports highlighting that root and bud development can respond differently to toxic substances *(74)*.

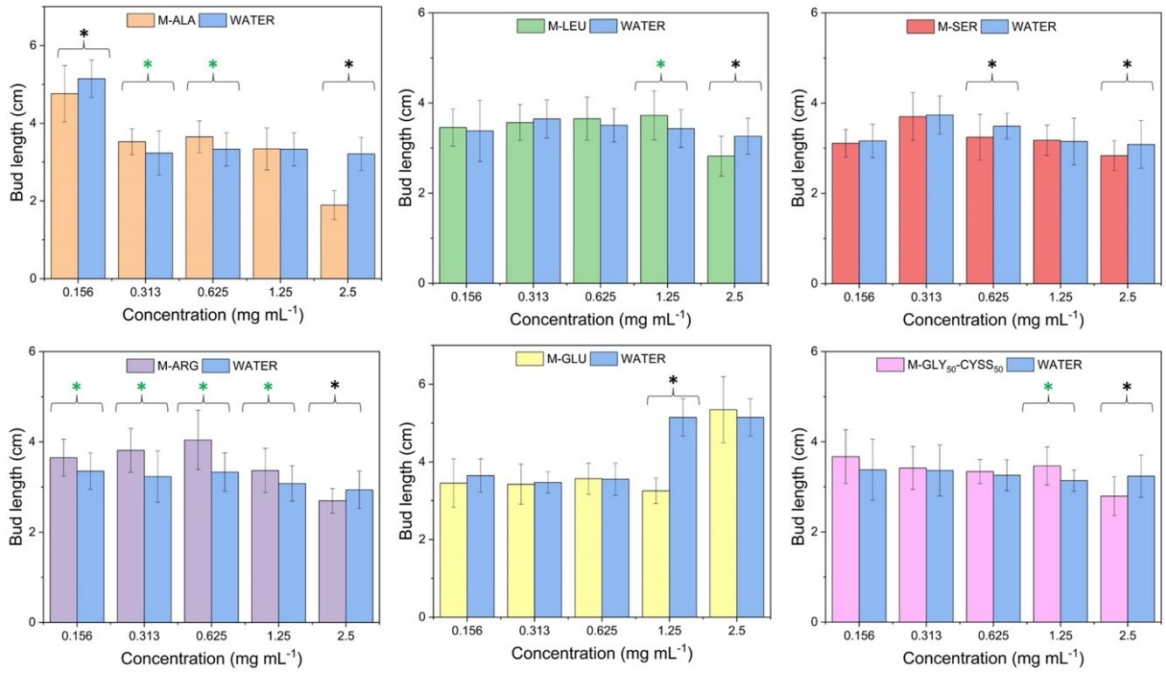

Figure 3.2.9. Concentration dependence of the length of *Lepidum sativum* buds after seed incubation in PAA aqueous solutions for 120 h. Results are reported as the mean ± confidence. Asterisks indicate significant differences (*$p < 0.05$) compared to the control; black asterisks indicate greater length in water, green asterisks greater length in the PAA solution.

To assess the impact of PAAs on *Lepidium sativum* root growth, Relative Root Growth (RRG) was calculated as the ratio of root length in PAA solutions to that in water (Eq. 3.3.3, Section 3.3). Compounds with RRG ≥ 1 are considered stimulants, while those with RRG < 1 act as inhibitors. Figure 3.2.10 presents RRG values after 120 hours of exposure. All PAAs showed inhibitory effects at 2.5 mg L^{-1}, except for M-SER and M-GLU that maintained RRG values above 0.9. M-SER stimulated root growth between 0.156 and 1.25 mg L^{-1}, while M-GLY_{50}-$CYSS_{50}$ and M-ALA showed slight stimulation at 0.156 mg L^{-1}. M-ALA, M-LEU, M-ARG, and M-GLY_{50}-$CYSS_{50}$ exhibited a clear dose-dependent inhibition, with M-ARG consistently suppressing root growth at all concentrations, consistent with direct root length measurements.

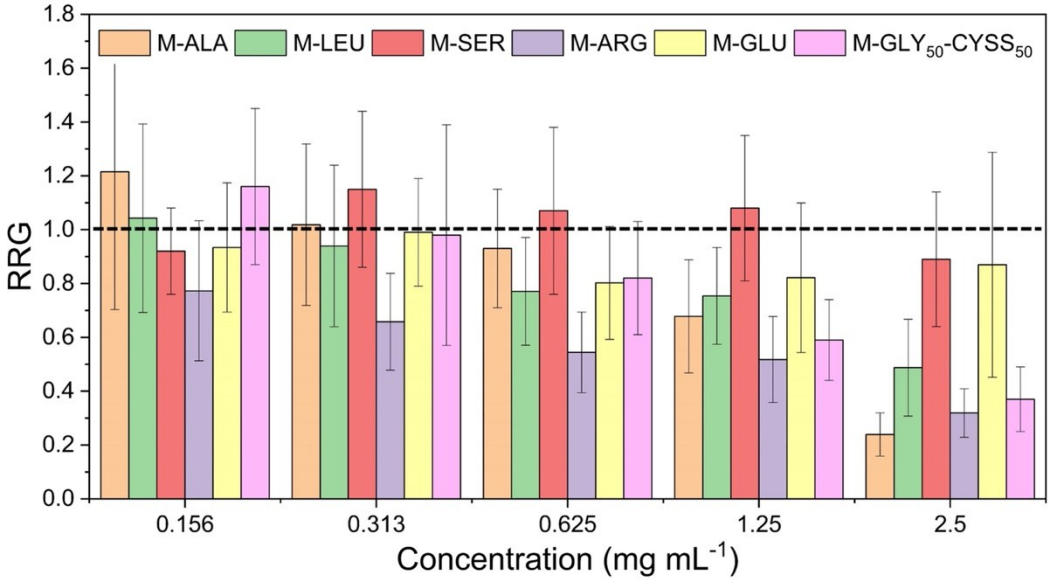

Figure 3.2.10. Concentration dependence of the relative radicle growth of *Lepidium sativum* seedlings in PAA water solutions after 120 h. Results are reported as the mean ± confidence.

The Germination Index (GI), calculated using Eq. 3.3.4 (Section 3.3), integrates seed germination and root elongation to assess overall plant response to a chemical. GI values classify compounds as highly phytotoxic (GI < 0.5), moderately phytotoxic (0.5 < GI < 0.8), mildly inhibitory (0.8 < GI < 1), or as phytostimulants (GI > 1) *(75)*. In Figure 3.2.11 GI values after 120 hours of PAA exposure are shown. Most PAAs were phytotoxic at 2.5 mg L^{-1}, except M-SER and M-GLU, which showed only mild inhibition. Consistent with RRG data, M-SER demonstrated a stimulatory effect between 0.313 and 1.25 mg L^{-1}. M-ARG, the most cationic PAA, was the most toxic, with GI < 0.8 at all concentrations and ≤ 0.5 above 0.625 mg L^{-1}. In contrast, M-GLU, the most anionic, was non-phytotoxic and slightly stimulatory at 0.313 mg L^{-1}. M-LEU showed borderline toxicity at 0.625 and 1.25 mg L^{-1}, while M-ALA and M-GLY_{50}-$CYSS_{50}$, both featuring a medium-high positive/negative charge value per repeat unit, were phytotoxic above 1.25 mg L^{-1} and followed similar trends across concentrations.

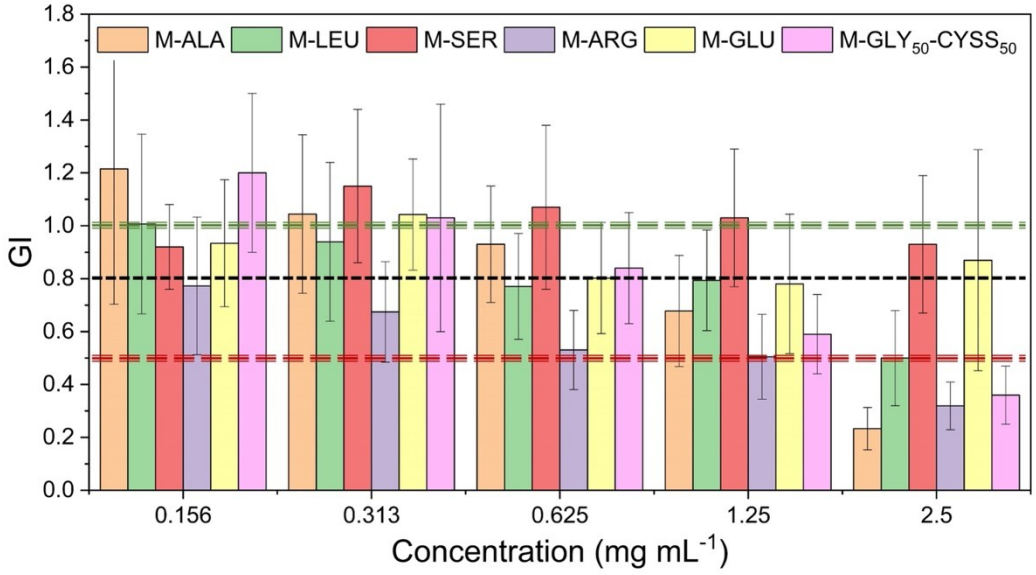

Figure 3.2.11. Concentration dependence of the germination index of *Lepidium sativum* seeds exposed to PAA water solutions for 120 h.

3.3. Experimental part

Different PAAs, namely M-ALA, M-LEU, M-ARG, M-SER, M-GLU and the copolymer M-GLY_{50}-$CYSS_{50}$ were synthesized and characterized following procedures reported in Chapter 2 and ultrafiltered using an Amicon® system equipped with a regenerated cellulose membrane having 3000 molecular weight cut-off. *Lepidium sativum* (watercress) seeds, top quality line, were purchased from Germisem Sementes (Oliveira do Hospital, Portugal) and stored in a dry location. Only seeds less than 6 months old were tested, discarding those that showed imperfections upon visual analysis. The average seed length and width, measured using a Dino-Lite Edge digital microscope (Dino-Lite Europe, Almere, The Netherlands), were 2.7 ± 0.2 mm and 1.4 ± 0.2 mm, respectively.

Seed germination test

Seed germination assay was conducted using *Lepidium sativum* seeds, following the guidelines established by the U.S. Environmental Protection Agency (EPA) *(44)*.

Test solutions of PAAs at concentrations of 0.156, 0.313, 0.625, 1.25, and 2.5 mg mL^{-1} were prepared by serial dilution of a 2.5 mg mL^{-1} stock solution. The stock solution was obtained by dissolving 250 mg of PAA in 100 mL of ultrapure water, with the pH adjusted to 7.0 for all formulations except M-GLY_{50}-$CYSS_{50}$, which required adjustment to pH 7.5 due to solubility constraints. The selected concentration range was designed in accordance with EPA guidelines, which advise the use of at least six concentrations in a geometric progression with a ratio

between 1.5 and 2.0 *(68)*. Ultrapure water and 0.1% $K_2Cr_2O_7$ served as negative and positive controls, respectively. For each condition, 10 seeds were placed on an 85 mm diameter filter paper within a 90 mm diameter polystyrene Petri dish. Each dish received 4 mL of the corresponding test solution (or ultrapure water), sealed with Parafilm M®, and incubated in darkness inside a black plastic bag at 25 ± 1 °C. All treatments were performed in quadruplicate (4 dishes per condition, 10 seeds per dish). After 120 hours, germination was assessed by counting the germinated seeds, and measuring seedling, bud, and root lengths using a Dino-Lite Edge digital microscope equipped with DinoXcope software. The results of the seed germination test were reported as: seed germination percentage (SG%), relative seed germination (RSG), relative radicle growth (RRG) and germination index (GI), obtained using the following Equations *(47)*:

$$SG\% = \frac{Number\ of\ germinated\ seeds}{Number\ of\ tested\ seeds} x100 \qquad \textit{Eq. 3.3.1}$$

$$RSG = \frac{Number\ of\ germinated\ seeds\ exposed\ to\ test\ sample}{Number\ of\ germinated\ seeds\ in\ water} \qquad \textit{Eq. 3.3.2}$$

$$RRG = \frac{Average\ radicle\ length\ in\ test\ sample}{Average\ radicle\ length\ in\ water} \qquad \textit{Eq. 3.3.3}$$

$$GI = RSG\ x\ RRG \qquad \textit{Eq. 3.3.4}$$

Seed germination kinetics

Two *Lepidium sativum* seeds were incubated in 2.5 mg mL^{-1} PAA test solution (0.5 mL) inside a quartz cuvette and visually inspected for 24 h using a Dino-Lite Edge digital microscope operating at 50X magnification. The analysis of one Lepidium sativum seed exposed to ultrapure water (0.5 mL) inside a quartz cuvette was performed as negative control. Video recording and processing were performed using the DinoXcope software.

Statistical analysis

In this study, the *t-test* was used as a statistical model to compare the response of *Lepidium sativum* seeds exposed to each PAA concentration with the response of seeds exposed in parallel to the negative control. The unequal variances *t-test*, also called the Welch's t-test, was applied and the *p-value* was calculated as the two-tailed probability of the *t*-distribution and compared referring to a chosen significance level of 0.05.

3.4. Conclusions

This study evaluated the effectiveness of the seed germination test as a rapid, low-cost method for assessing the phytotoxicity of water-soluble polymers. A series of α-amino acid-derived PAAs, under investigation as cotton flame retardants, were tested using *Lepidium sativum* seeds exposed to concentrations ranging from 0.156 to 2.5 mg mL^{-1} for 120 hours. Despite exceeding the EPA's recommended concentration limit, no acute toxicity was observed, as seed germination rates remained unaffected, even at the highest concentrations. Microscopic observations confirmed normal germination kinetics across all samples. Multiple phytotoxicity endpoints were analyzed, including seed germination percentage, relative seed germination, root and bud length, relative root growth, and germination index (GI). Among these, root length proved the most sensitive indicator. GI values enabled ranking of PAAs by phytotoxicity: serine- and glutamic acid-based PAAs, predominantly anionic, were consistently non-toxic, while the arginine-based PAA, predominantly cationic, showed increasing inhibition from 0.313 mg mL^{-1}. Notably, delayed testa rupture was observed only with M-ARG exposure. Overall, results demonstrate that the seed germination test is a reliable tool for evaluating the phytotoxicity of water-soluble polymers and linking biological effects to polymer structure, particularly charge distribution.

4. ECOTOXICITY ASSESSMENT OF PAAs: EVALUATION OF AQUATIC TOXICITY OF PAAS USING ZEBRAFISH AS A VERTEBRATE MODEL

In this study, the aquatic ecotoxicity of a small group of water-soluble amphoteric PAAs that are currently studied as flame-retardants for cotton was assessed using zebrafish (*Danio rerio*) embryos as a vertebrate model. Zebrafish represents indeed a useful model organism which shares several features with mammals. A series of tests were performed using different polymer concentrations, including the assessment of embryo viability, the evaluation of morphological macroscopic and microscopic phenotype abnormalities, the detection of change in mobility as indication of developmental neurotoxicity. To our knowledge, this is the first *in vivo* study assessing the aquatic eco-compatibility of this PAA family, with a focus on correlating charge distribution to observed biological effects.

All results are presented in detail in a dedicated publication:

Treccani, S.; Ferruti, P.; Alongi, J.; Monti, E.; Zizioli, D.; Ranucci, E. Ecotoxicity Assessment of α-Amino Acid-Derived Polyamidoamines Using Zebrafish as a Vertebrate Model. Polymers ***2024****, 16, 2087, https://doi.org/10.3390/polym16142087*

4.1. Introduction

Water-soluble polymers present in aquatic environments are currently of particular concern since may alter the physico-chemical properties of the aqueous matrix *(55)*. PAAs that have proved to be efficient flame-retardants for cotton are water-soluble polymers thus it is essential to evaluate their environmental impact, as they could be accidentally released into the environment during or after their useful life. In fact, they rapidly impregnate the soil and dissolve quantitatively in surface and groundwater, may increasing the bioavailability of pollutants or exhibiting intrinsic toxicity due to their polyelectrolytic nature. However, their environmental impact remains poorly understood and their ecological risks are often underestimated. To address this gap, the aquatic ecotoxicity of three water-soluble, amphoteric, and predominantly anionic PAAs was evaluated using zebrafish (*Danio rerio*) embryos, recommended *in vivo* model by the European Experimental Substitution Research Center *(76)*. Zebrafish represents a useful viable vertebrate model organism which shares several biochemical pathways, anatomical and physiological features with mammals and humans *(77–79)*. Moreover, the combination of their large-scale embryo production and rapid development allows for short-term evaluation of potential adverse effects resulting from early-life exposure to environmental contaminants. This approach has been especially valuable in the field of

flame-retardant technology, where zebrafish embryos have been widely used to assess the toxicity of numerous flame-retardant chemicals found in consumer products such as plastics, textiles, protective clothing, furniture, automotive components, and electronic devices *(80–84)*. One of the aims of the study was to explore potential correlations between the charge profile of PAAs and the effects observed in zebrafish embryos exposed to their aqueous solutions at varying concentrations. To achieve this, a series of tests were conducted, including assessments of embryo viability, evaluation of both macroscopic and microscopic morphological abnormalities, analysis of mobility changes in response to light/dark transitions as indicators of developmental neurotoxicity, and examination of responses to tactile stimuli to assess the integration of sensory and motor functions.

4.2. Results and discussion

The purpose of this study was to evaluate the environmental compatibility of a select group of amphoteric α-amino acid-derived PAAs, which have recently demonstrated effectiveness as flame retardants for cotton. These PAAs, namely M-GLY, M-GLU, and M-GLY_{50}-$CYSS_{50}$, are polyelectrolytes with distinctive ionic charge distributions. A key objective of this research was to investigate whether the effects of these PAAs on zebrafish embryos are in any way linked to their charge distributions. M-GLY and M-GLY_{50}-$CYSS_{50}$ are moderately anionic and feature a net average charge per repeat unit of -0.39 and -0.35 respectively. M-GLU is highly anionic and possesses a net average charge per repeat unit of -1.14 (Annex 4).

The sets of experiments conducted in this work on zebrafish embryos is shown in Figure 4.2.1, in which the temporal sequence of the tests and the endpoints considered is summarized.

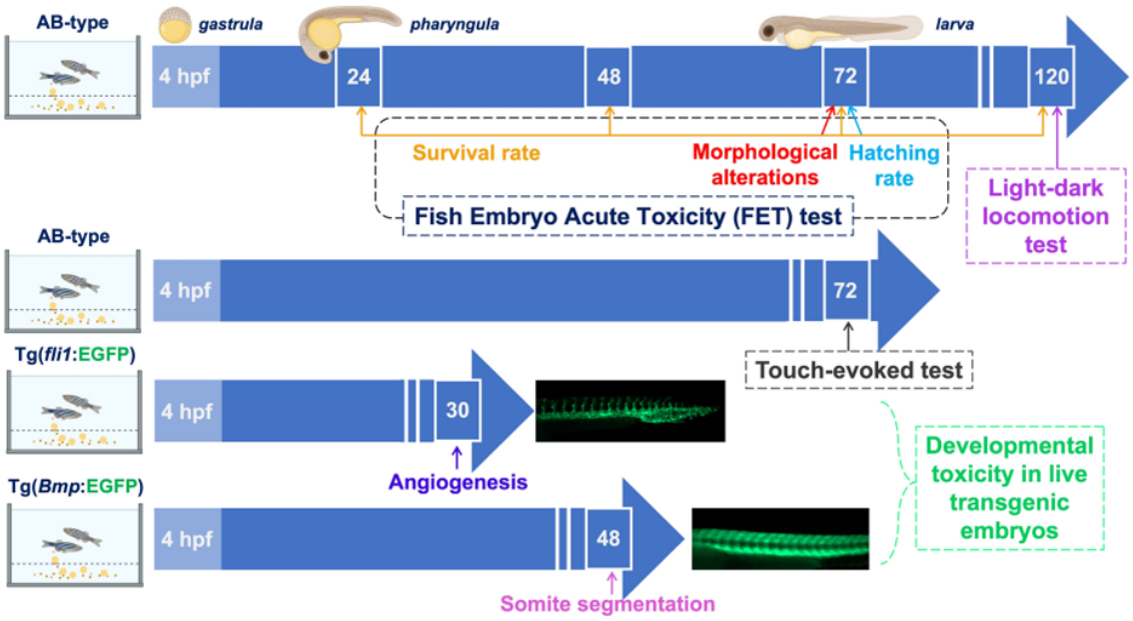

Figure 4.2.1. Timeline of ecotoxicity tests on PAA-exposed zebrafish embryos. White frames indicate execution times (hpf). *Row 1*: AB wild-type embryos considered in FET test (survival, morphology, hatching) and light/dark locomotion test. *Row 2*: AB wild-type larvae considered in touch-evoked response test. *Row 3*: Tg(*fli1*:EGFP) embryos considered for angiogenesis assessment via intersegmental vessel development. Row 4: Tg(*Bmp*:EGFP) embryos considered for somite segmentation assessment via V-shaped somite pattern.

Fish Embryo Acute Toxicity Test

The acute toxicity of M-GLY, M-GLU, and M-GLY_{50}-$CYSS_{50}$ was assessed using the FET test in accordance with OECD guideline 236 *(85)*. Lethal and sub-lethal endpoints, such as survival rate, morphological abnormalities, and hatching rate, were monitored at 48, 72, and 120 hours post fertilization (hpf) (Figure 4.2.1). Indicators of lethality included embryo coagulation (milky white under visual inspection, dark under bright-field microscopy) and absence of heartbeat. Survival rates were calculated as the percentage of live embryos out of the total tested across a concentration range of 1.5-500 mg L^{-1}. Mortality at each concentration and time point was compared to the negative control (fish water), which maintained ≥ 90% survival rate along the concentration range, in compliance with OECD standards. At 120 hpf, M-GLU and M-GLY_{50}-$CYSS_{50}$ showed a survival rate ≥ 90% at all concentrations. M-GLY showed a slight, non-significant increase in mortality above 50 mg L^{-1}. According to OECD guidelines *(85,86)*, different toxicity levels have been set to categorize substances, namely dangerous (10 mg L^{-1} < LC_{50} < 100 mg L^{-1}), toxic (1 mg L^{-1} < LC_{50} < 10 mg L^{-1}), and carcinogenic (LC_{50} < 1 mg L^{-1}). Based on this classification, all tested PAAs could be classified as non-dangerous, non-toxic, and non-carcinogenic, since their survival rate was much greater than 50% even at 500 mg L^{-1},

i.e. up to a level which could only be found in the environment in the event of a massive spill. Results are presented in Figure 4.2.2a. According to OECD guideline 236, hatching rate should be monitored from 48 to 72 hpf to ensure effective chemical exposure and avoid chorion shielding. Reduced hatchability may indicate delayed embryo development, while premature hatching, potentially triggered by chemical exposure, can impair larval swimming *(86,87)*. Under the tested conditions, no early or delayed hatching was observed. As shown in Figure 4.2.2b, hatching rates at 72 hpf remained comparable to the negative control and PAA exposure had no significant effect on hatching across all concentrations.

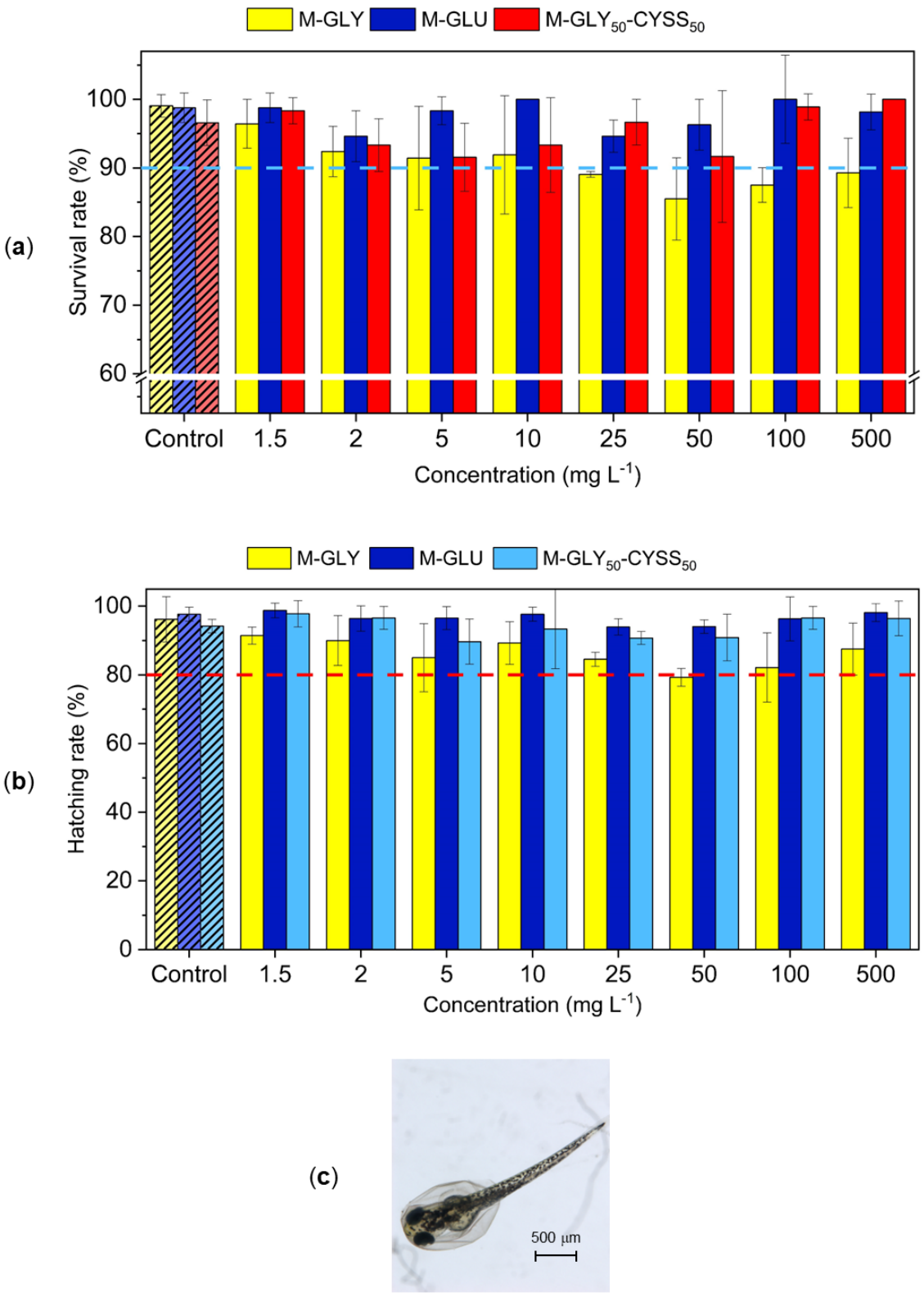

Figure 4.2.2. a) Survival rate of AB wild-type larvae after exposure to different PAA concentrations for 120 hpf. The blue dotted line represents the threshold value for the negative control indicated by the OECD guideline 236; b) hatching rate of AB wild-type larvae after exposure to different PAA concentrations for 72 hpf; c) bright field microscopic image of a hatching zebrafish larva at 72 hpf. Results are reported as the mean ± SD of three independent experiments.

Additional sub-lethal endpoints were assessed at 72 hpf and included spinal malformations, pericardial edema, growth retardation, missing pigmentation, and yolk deformation. The latter two were not observed in any treatment. Representative morphological alterations after 72 h of M-GLU exposure at selected concentrations are shown in Figure 4.2.3. The incidence of abnormalities across M-GLY, M-GLU, and M-GLY_{50}-$CYSS_{50}$ treatments is summarized in Figures 4.2.4a-c, based on three independent experiments. Morphological alterations following M-GLY treatment (Figure 4.2.4a) showed no clear dose dependence. At 1.5 mg L^{-1}, 7% of larvae were affected, comparable to 8% in the control (91 larvae tested). At 500 mg L^{-1}, only 3 out of 56 larvae showed growth retardation. The highest incidence occurred at 10 mg L^{-1}, with 14 larvae affected (spinal distortion, pericardial edema, and growth retardation). Similarly, M-GLU exposure (Figure 4.2.4b) showed no dose-dependent trend. At 1.5 mg L^{-1}, 13% of larvae showed abnormalities compared to 14% control (84 larvae tested). Only the 25 mg L^{-1} treatment showed a noticeably higher response, with 14 affected larvae. At 500 mg L^{-1}, just 1 larva out of 54 had growth retardation. For M-GLY_{50}-$CYSS_{50}$ (Figure 4.2.4c), 3% of larvae showed alterations at 1.5 mg L^{-1} compared to 5% in the control (86 larvae tested). Significant effects appeared only at 25 mg L^{-1} and 500 mg L^{-1}, without a consistent trend. Overall, morphological effects at 72 hpf were minimal and largely dose-independent. Isolated responses at certain concentrations likely reflect natural variability in the zebrafish model.

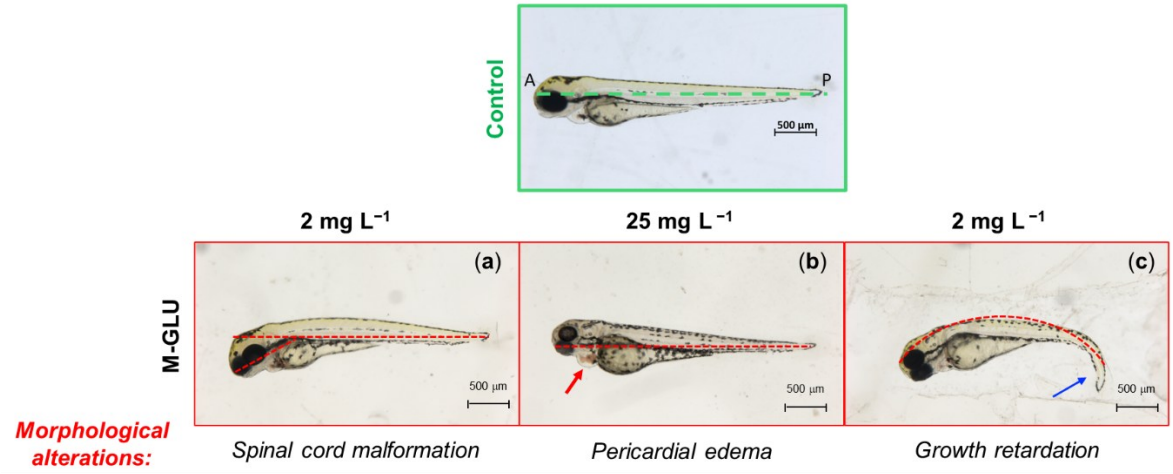

Figure 4.2.3. Representative bright field microscopic images of morphological alterations by FET test observed in zebrafish larvae after 72 hpf exposure to M-GLU solutions. The dashed green line in the control represents the anterior-posterior A-P axis. All pictures are lateral views with dorsal at the top (magnification 32X).

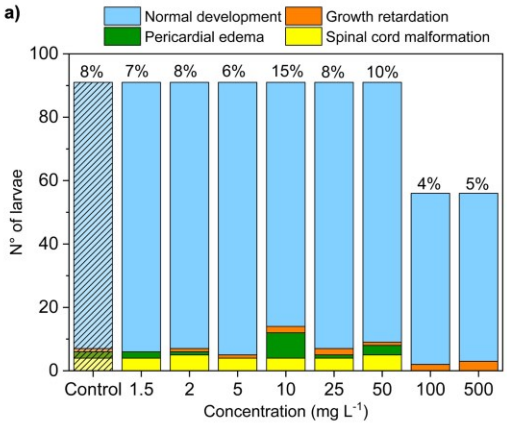

M-GLY toxicity by FET test

Concentration (mg L^{-1})	0*	1.5	2	5	10	25	50	100	500
Total n° of embryos	91	91	91	91	91	91	91	56	56
Lethal endpoints at 72 hpf									
Embryo coagulation	1	3	7	8	6	10	11	7	6
Sub-lethal endpoints at 72 hpf									
Spinal cord malformation	4	4	5	4	4	4	5	0	0
Pericardial edema	2	2	1	0	8	1	3	0	0
Growth retardation	1	0	1	1	2	2	1	2	3

** Control*

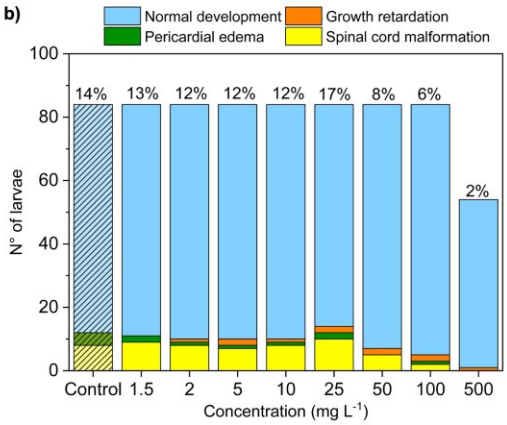

M-GLU toxicity by FET test

Concentration (mg L^{-1})	0*	1.5	2	5	10	25	50	100	500
Total n° of embryos	84	84	84	84	84	84	84	84	54
Lethal endpoints at 72 hpf									
Embryo coagulation	1	1	3	2	0	5	3	3	2
Sub-lethal endpoints at 72 hpf									
Spinal cord malformation	8	9	8	7	8	10	5	2	0
Pericardial edema	4	2	1	1	1	2	0	1	0
Growth retardation	0	0	1	2	1	2	2	2	1

** Control*

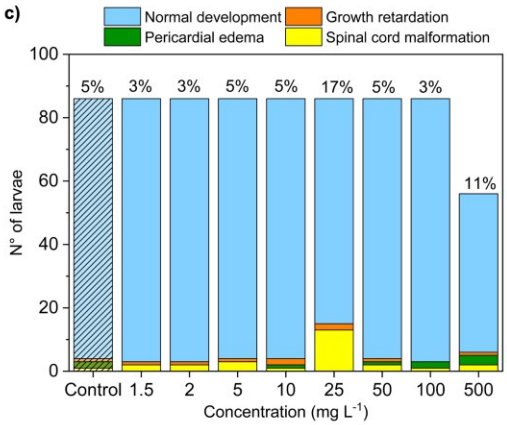

M-GLY$_{50}$-CYSS$_{50}$ toxicity by FET test

Concentration (mg L^{-1})	0*	1.5	2	5	10	25	50	100	500
Total n° of embryos	86	86	86	86	86	86	86	86	56
Lethal endpoints at 72 hpf									
Embryo coagulation	4	2	2	8	7	4	5	2	0
Sub-lethal endpoints at 72 hpf									
Spinal cord malformation	1	2	2	3	1	13	2	1	2
Pericardial edema	2	0	0	0	1	0	1	2	3
Growth retardation	1	1	1	1	2	2	1	0	1

** Control*

Figure 4.2.4. Morphological alterations of zebrafish larvae observed in the FET test at 72 hpf after exposure to: a) M-GLY, b) M-GLU and c) M-GLY$_{50}$-CYSS$_{50}$. For each PAA concentration, the total number of embryos is the sum of embryos tested in three independent experiments. Control represents zebrafish embryos exposed to fish water.

Early developmental assessment of angiogenesis using Tg(fli1:EGFP)

Due to their small size and transparency, zebrafish embryos allow real-time, in vivo imaging of specific tissues using transgenic fluorescent lines *(88,89)*. Among the 8960 GFP-expressing lines listed by ZFIN in 2021 *(90)*, Tg(*fli1*:EGFP) embryos were chosen to assess the impact of

PAA exposure on early angiogenesis. In this line, EGFP is expressed in endothelial cells under control of the *fli1* promoter, highlighting vasculature development. Angiogenesis begins around 16 hpf with intersegmental vessel (ISV) sprouting, which continues through 48 hpf to form the trunk vasculature (Figure 4.2.5b). Embryos were treated with 2 and 10 mg L^{-1} PAA solutions at 4 hpf, dechorionated at 30 hpf, and examined via fluorescence microscopy. Given the chorion pore size (0.5-0.7 μm) and the small hydrodynamic radii of PAAs (1-4 nm) *(91–95)*, PAAs likely penetrated by 24 hpf, enabling detection of effects by 30 hpf. Figure 4.2.5a shows the average number of ISV alterations observed at 30 hpf. Although embryos exposed to 10 mg L^{-1} PAAs showed more ISV abnormalities than those treated with 2 mg L^{-1}, differences were not statistically significant. Overall, none of the treatments notably disrupted angiogenesis compared to controls.

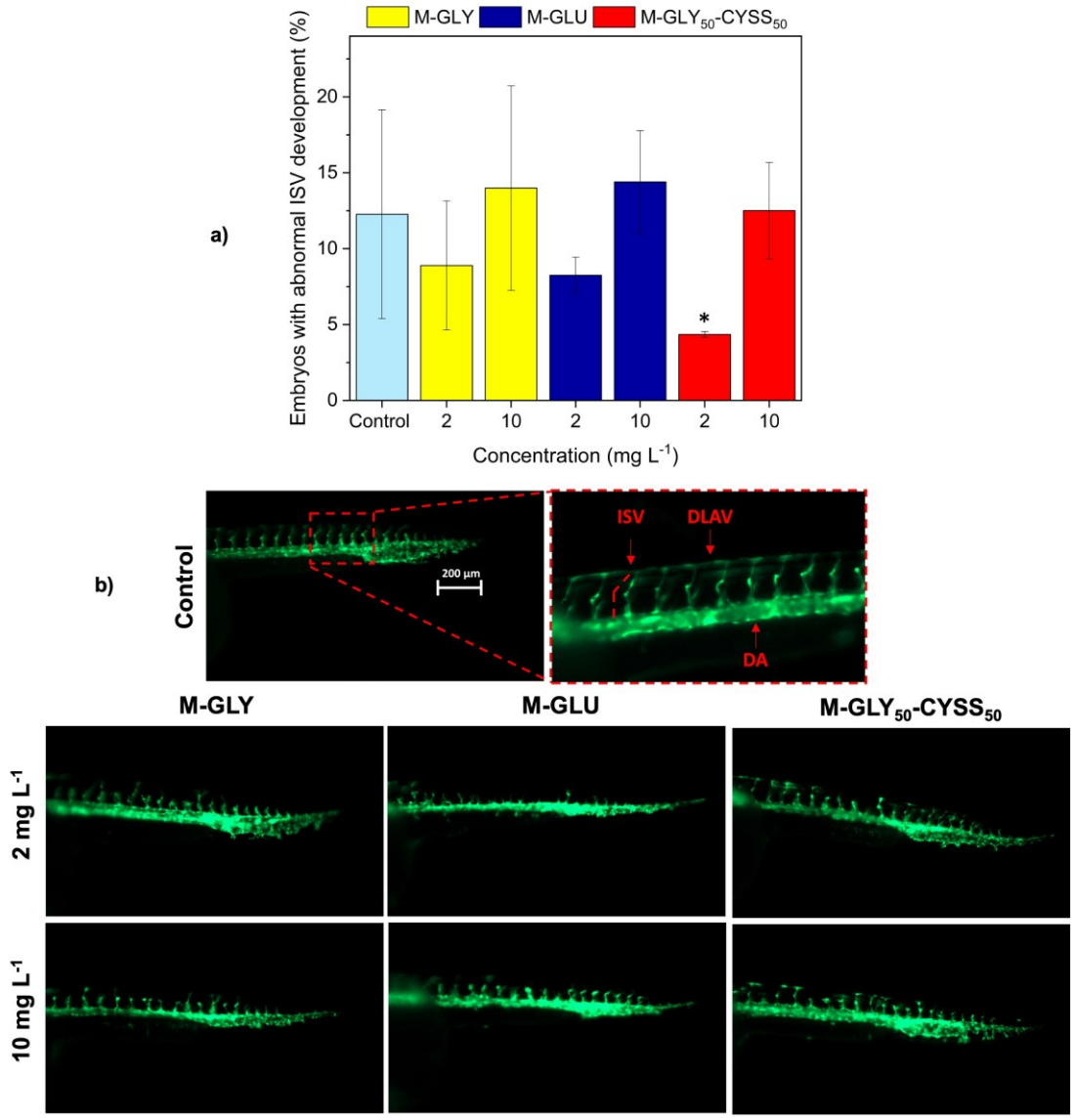

Figure 4.2.5. Intersegmental vessel (ISV) alteration in PAA-treated Tg(*fli1*:EGFP) embryos: a)

average number of zebrafish embryos exposed for 30 hpf to 2 and 10 mg L^{-1} of M-GLY (yellow), M-GLU (blue) and M-GLY_{50}-$CYSS_{50}$ (red) having ISV alterations. For each PAA dose, the average number with SD was obtained from three independent experiments. The asterisk indicates significant differences ($p < 0.05$) compared to control. b) Representative lateral views of control and PAA-treated embryos with ISV alterations (magnification 63X). ISV are labelled with a green fluorescent marker. Brightness of images was increased by 40%. DLAV = dorsal longitudinal anastomotic vessel; DA = dorsal aorta.

Somite segmentation assessment in Tg(BMP:EGFP)

Tg(*Bmp*:EGFP) transgenic zebrafish embryos express EGFP under the control of BMP-responsive elements, allowing visualization of BMP gene activity involved in tissue differentiation, tail bud and brain development, cardiovascular formation, and somite segmentation *(96,97)*. Somites in zebrafish develop into a bilaterally symmetrical V-shaped sequence in an anterior to posterior direction, starting around 10.5 hpf and completing by 24 hpf, ultimately giving rise to axial skeleton and trunk muscles *(98)*. In this study, embryos were exposed to 2 and 10 mg L^{-1} PAA solutions and examined at 48 hpf, when BMP expression is at its maximum, for somite patterning and axial structure integrity (Figure 4.2.6). Embryos in all groups, including controls, developed around 30 well-formed V-shaped somites with no abnormalities in notochord alignment or trunk morphology. In contrast, severe malformations such as notochord bending and swelling have been reported at 24 hpf following exposure to highly toxic substances like 100 mM cadmium *(99)*.

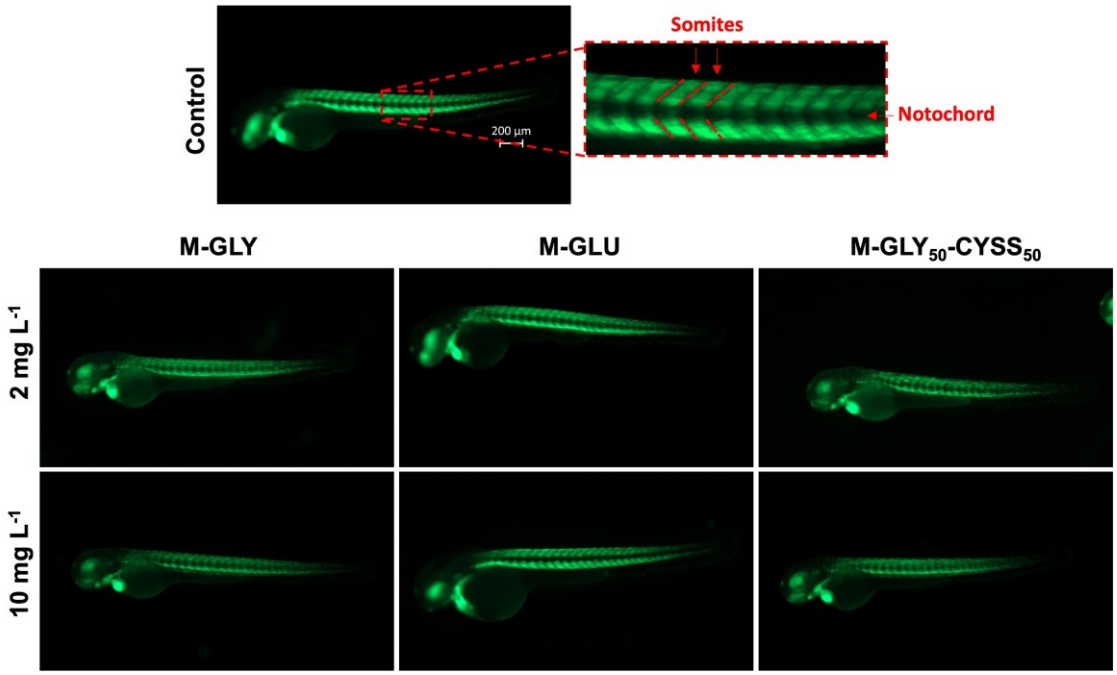

Figure 4.2.6. Representative lateral views of control and PAA-treated Tg(*Bmp*:EGFP) embryos (magnification 40X). Somites are labelled with a green fluorescent marker. Brightness of images was increased by 40%.

Neurobehavioral effects of PAAs

To evaluate neurobehavioral effects of PAAs, two complementary tests were performed: the light/dark locomotion test and the touch-evoked response assay (see Section 4.3). Locomotor behavior, an important indicator of neurological development *(100,101)*, was assessed at 120 hpf when larvae exhibit mature swimming behavior *(102)*. In the light/dark test, zebrafish typically increase movement in darkness and reduce it in light due to stress-related responses *(102–104)*. Figures 4.2.7a-c show the distance travelled during dark periods: M-GLY slightly but significantly reduced swimming distance at most concentrations (except 25 mg L^{-1}), while M-GLY_{50}-$CYSS_{50}$ had a similar effect at 1.5, 2, 50, and 100 mg L^{-1}. M-GLU showed no significant impact across the tested range. No dose-dependent trends were observed.

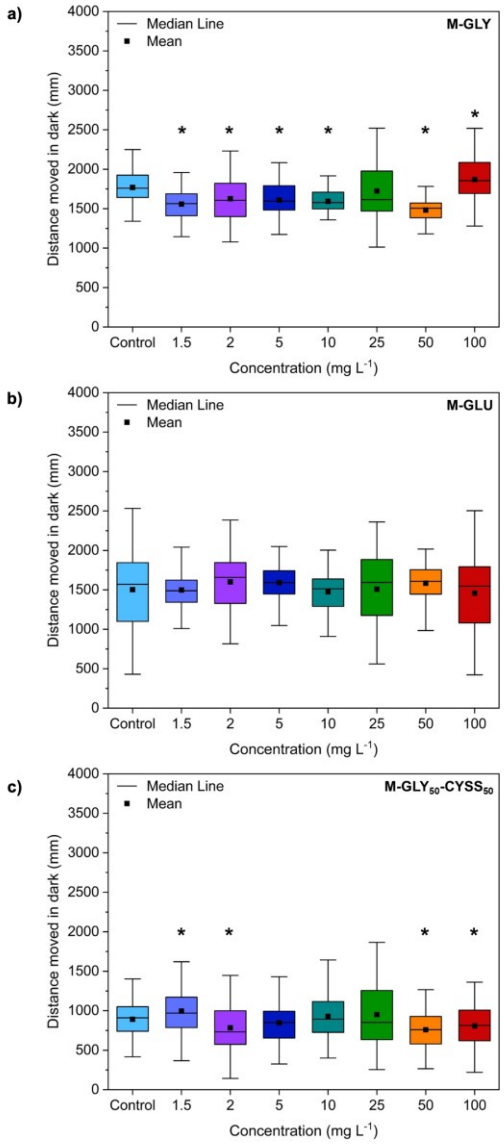

Figure 4.2.7. Results of the locomotion tests performed using AB-wild type embryos at 120 hpf. Distance moved by zebrafish larvae exposed to different M-GLY (a), M-GLU (b) and M-GLY_{50}-

$CYSS_{50}$ (c) concentrations during dark periods. Data were collected with n=36 larvae per concentration. Asterisks indicate significant differences ($p < 0.05$) compared to control.

Sensorimotor function was further assessed using the touch-evoked response test, where embryos at 48 hpf were exposed to a sudden tail stimulus *(105,106)*. The tactile startle response starts within approximately 5 ms from the stimulus onset. During the startle, the fish bends so that the head touches the tail (C-start response) in approximately 15 ms and then moves several body lengths away from its starting location in 100 ms. The correct development of the spinal cord plays a critical role in mediating touch-evoked responses by integrating sensory inputs and generating appropriate motor outputs. In healthy embryos, the rapid "C-start" escape reflex indicates intact neural circuitry. Figure 4.2.8 presents the results of this study, comparing the number of larvae that traveled various distances with those that remained immobile for each PAA concentration and control. Larvae exposed to M-GLY solutions exhibited behavior like the control up to 25 mg L^{-1}, with 81% crossing the outer 20 mm diameter circle and none remaining inside the inner 10 mm diameter circle. At greater doses, the percentage of larvae that crossed the outer circle slightly reduced to 76%. In M-GLU solutions, a few larvae did not move at the highest concentration of 100 mg L^{-1}. The percentage of larvae that crossed the outer circle reduced to 73% at 10 mg L^{-1}, compared to 80% in the control. In M-GLY_{50}-$CYSS_{50}$ solutions, the number of larvae that remained immobile at 100 mg L^{-1} increased to around 9%. Meanwhile, the percentage of larvae that crossed the outer circle reduced to 76% at 10 mg L^{-1}, compared to 81% in the control. Overall, the results of the touch-evoked response test suggest that none of the PAAs caused marked neurotoxicity at concentrations up to 10 mg L^{-1}. Moderate motility reductions were observed at higher doses for M-GLU and M-GLY_{50}-$CYSS_{50}$, while M-GLY induced only mild effects above 50 mg L^{-1}. These findings align with known toxicity patterns: highly cationic polymers are generally more toxic, while the tested PAAs are primarily anionic. Notably, M-GLY, showing the least inhibition, has a modest negative net charge at pH 7.0, whereas M-GLU has higher charge density and greater inhibitory effects. The incorporation of 50% M-CYSS units in the copolymer likely increased toxicity due to the cystine moiety, whose disulfide groups can participate in redox reactions and generate reactive thiyl radicals *(107)*, potentially interfering with embryo development.

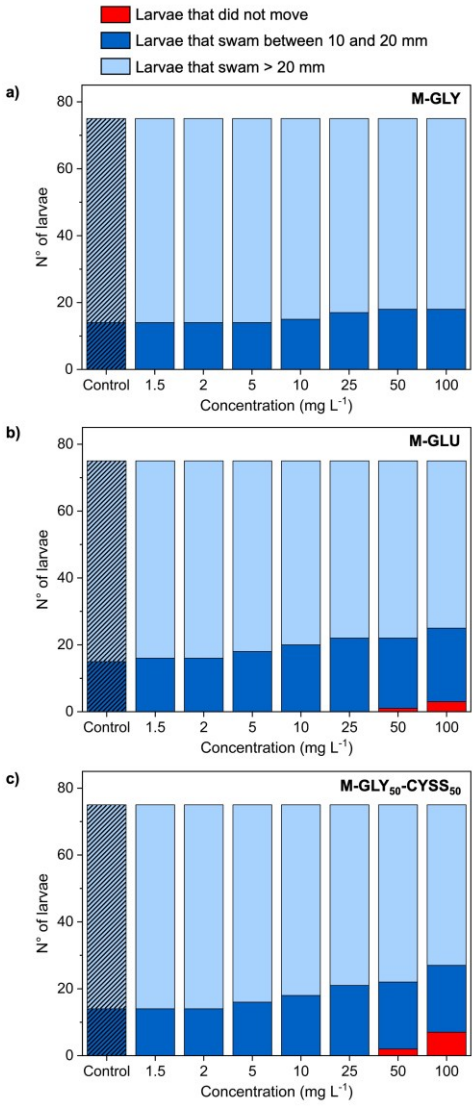

Figure 4.2.8. Results of the touch-evoked test performed on zebrafish larvae exposed at 4 hpf to different: a) M-GLY, b) M-GLU and c) M-GLY$_{50}$-CYSS$_{50}$ concentrations. Results derived from three independent experiments performed using 25 embryos.

4.3. Experimental part

Different PAAs, namely M-GLY, M-GLU and the copolymer M-GLY$_{50}$-CYSS$_{50}$ were synthesized and characterized following the procedures reported in Chapter 2. After the reaction time, the pH was adjusted to 7.0 (7.5 for the copolymer) with 6 M HCl and the products ultrafiltered using an Amicon® system equipped with a regenerated cellulose membrane having 3000 molecular weight cut-off.

Experiments took place at the Zebrafish Facility, Department of Molecular and Translational Medicine, University of Brescia, Italy. All animal experiments were conducted in accordance with the Italian and European regulations on animal care and the standard rules defined by the

Local Committee for Animal Health (OPBA) and authorized by the Italian Ministry of Health (Authorization Number 585/2018).

Zebrafish maintenance and egg collection

Zebrafish (*Danio rerio*) embryos were obtained from the AB wild-type line and two transgenic lines: Tg(*fli1*:EGFP) and Tg(*Bmp*:EGFP). Adult zebrafish were housed under standard laboratory conditions *(108)* in a recirculating aquaculture system (Techniplast ZebTEC, Italy) at 27 ± 1°C with a 14:10 h light-dark cycle. The housing system guarantees fish water (0.1 g L^{-1} Instant Ocean Sea Salts, 0.1 g L^{-1} sodium bicarbonate, 0.19 g L^{-1} calcium sulphate) at constant pH and conductivity values; ammonia, nitrite and nitrate were kept below detection limits (0-5, 0.025-1, and 0-140 mg L^{-1}, respectively). Adult males and females were mated overnight, and eggs were collected the following morning. Only batches with ≥80% fertilization were used. Embryos were maintained at 28°C in Petri dishes with fresh fish water and exposed to test substances at the onset of gastrulation (4 hours post-fertilization) *(109)*.

Fish embryo acute toxicity (FET) test

The Fish Embryo Acute Toxicity (FET) test was conducted in accordance with OECD Guideline 236 *(85)* using AB wild-type zebrafish embryos. This assay evaluates the acute or lethal toxicity of chemical substances. Stock solutions of PAAs were prepared at 1 g L^{-1} in fish water. Working solutions were freshly prepared at eight concentrations: 1.5, 2, 5, 10, 25, 50, 100, and 500 mg L^{-1}. As no significant toxicity was observed below 100 mg L^{-1}, the highest concentration was extended to 500 mg L^{-1} to enhance detection of potential effects. Each concentration was tested in triplicate with 25-30 viable embryos per replicate, exposed via static immersion in Petri dishes starting at 4 hours post-fertilization (hpf) *(110)*. Fish water served as a negative control (embryonic mortality ≤ 10%), while 3.7 mg L^{-1} 3,4-dichloroaniline was used as a positive control (mortality ≥ 90%).

Given that embryos remain enclosed within the chorion membrane, a semi-permeable barrier to high molecular weight compounds, until approximately 48 hpf *(91,111–113)*, exposure duration was extended to 120 hpf, in line with OECD recommendations for maximizing the uptake *(114)*. Embryo viability was monitored at 48, 72, and 120 hpf, using coagulation and absence of heartbeat as lethality indicators. Dead embryos were removed at each time point. Survival rate was calculated using the following Equation:

$$\text{Survival rate} = \frac{\text{survived fish}}{\text{total fish}} \times 100 \qquad \textit{Eq. 4.3.1}$$

Spontaneous dechorionation (hatching), which typically occurs between 48 and 72 hpf, was assessed at 72 hpf using the following Equation:

$$\text{Hatching rate} = \frac{\text{hatched embryos}}{\text{total exposed eggs}} \times 100 \qquad \textit{Eq. 4.3.2}$$

At 72 hpf, hatched embryos were anesthetized with 0.4% tricaine (Merck, Milan, Italy), mounted laterally in 1% agarose, and examined under a Zeiss Axiozoom V13 microscope (Carl Zeiss AG, Germany) with a PlanNeoFluar Z 1x/0.25 FWD 56 mm lens. After morphological assessment, embryos were returned to their respective exposure solutions. The incidence of malformations, such as spinal curvature, pericardial edema, and growth retardation, was compared to that in the negative control group.

Angiogenesis and somite segmentation assessment

Angiogenesis and somite segmentation were assessed in transgenic zebrafish lines Tg(*fli1*:EGFP) and Tg(*Bmp*:EGFP), respectively. In Tg(*fli1*:EGFP), EGFP is expressed in endothelial cells under the control of the *fli1* promoter, which are related to blood vessel growth and vasculature formation during embryogenesis *(115,116)*. In Tg(*Bmp*:EGFP), EGFP expression is driven by the BMP Response Element, a family of signaling proteins involved in several key processes as tissue differentiation, development of tail bud, cardiovascular system, and somite formation *(117,118)*. Embryos were exposed at 4 hpf to PAA solutions at 2 and 10 mg L^{-1}, with each concentration tested in triplicate using 25-30 viable embryos. For angiogenesis analysis, intersegmental vessel (ISV) formation, a key early marker, was evaluated at 30 hpf in Tg(*fli1*:EGFP) embryos. For musculoskeletal development, somite segmentation was examined at 48 hpf in Tg(*Bmp*:EGFP) embryos. In both cases, embryos were manually dechorionated prior to imaging using watchmakers' forceps *(119)*, anesthetized with 0.4% tricaine, and observed under a Zeiss Axiozoom V13 fluorescence microscope (Carl Zeiss AG, Germany) equipped with a PlanNeoFluar Z 1x/0.25 FWD 56 mm lens. Fluorescent images were captured laterally at different magnifications and processed using Zen 3.5 software.

Locomotor behavior assessment

Locomotor behavior was evaluated using the light-dark locomotion test *(100)*. AB-strain zebrafish embryos were exposed via static immersion to various PAA concentrations (1.5, 2, 5,

10, 25, 50, and 100 mg L^{-1}) or fish water as a control, starting at 4 hpf and continuing until 120 hpf. At the end of the exposure, individual larvae were transferred to a 96-well plate, with one larva per well in 200 µL of fish water. Behavioral testing followed the protocol outlined in Zebrafish Protocols for Neurobehavioral Research *(120)*, with 36 larvae tested per concentration. The plate was placed in a DanioVision observation chamber (Noldus, Wageningen, The Netherlands) maintained at 28 °C in a sound-isolated room. Larval movement was recorded via video tracking during a 30-minute light acclimation phase followed by three alternating 10-minute dark/light cycles (Figure 4.3.1). Locomotor activity was quantified using EthoVision software (Noldus), expressed as total distance traveled (mm) and compared to that in the negative control group.

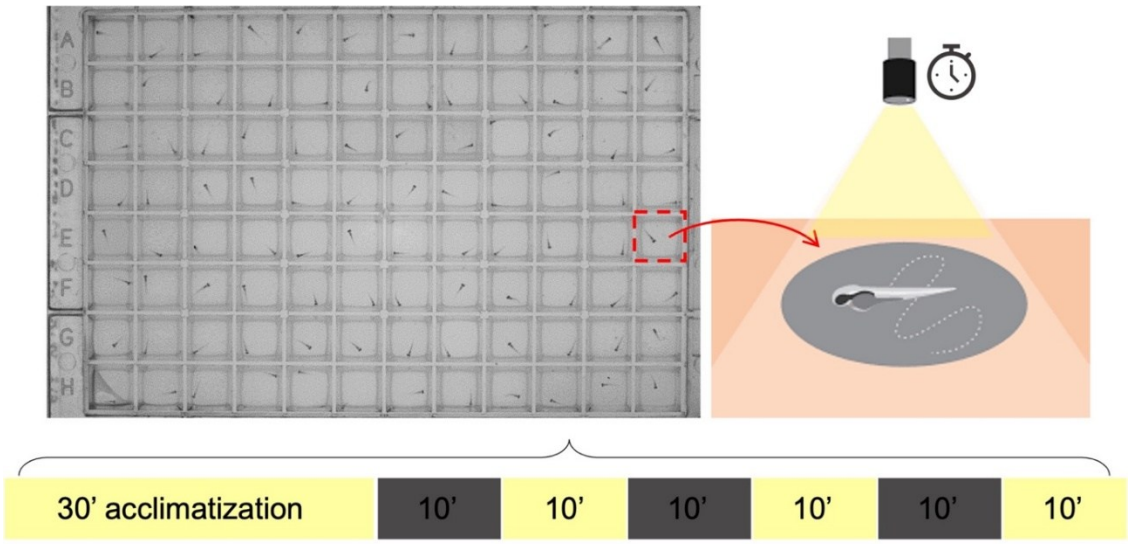

Figure 4.3.1. Scheme of the light/dark locomotion test. The test lasted 90 min, of which 30 min light acclimatization followed by 3 cycles of alternating dark/light cycles lasting 10 min per type of exposure.

Touch-evoked response test

AB-strain zebrafish embryos were exposed via static immersion to various PAA concentrations (1.5, 2, 5, 10, 25, 50, and 100 mg L^{-1}) or fish water as a control, starting at 4 hpf until 72 hpf. For each concentration, tests were conducted in triplicate using 25 larvae per replicate, totaling 75 larvae per treatment. After exposure, individual larvae were transferred to the center of a Petri dish containing the corresponding test solution. A motility wheel with two concentric circles (10 mm and 20 mm diameter) was placed beneath the dish, and a microscope was aligned above. The larva's tail was gently touched with a smooth pipette tip, and the response was categorized into three groups: (1) no movement or swimming less than 10 mm; (2) swimming between 10 and 20 mm; and (3) swimming more than 20 mm.

Statistical analysis

Each experiment was repeated in triplicate for both the control and the treated groups. Data were expressed as mean ± SD and for all comparisons a significance level of $p < 0.05$ was considered. The data distribution was evaluated for normality by the Shapiro-Wilk test. Data from survival rate and hatching rate were analyzed with one-way analysis of variance (ANOVA) followed by Bonferroni *post-hoc* test. Pairwise comparisons between each treated group and the control group of light-dark locomotion test were performed by the unequal variances *Welch's t-test*. The OriginPro 2019 software (Adalta, Arezzo, Italy) was used for statistical analysis.

4.4. Conclusions

The eco-compatibility of three α-amino acid-derived PAAs, namely M-GLY, M-GLU, and M-GLY_{50}-$CYSS_{50}$, effective flame retardants for cotton, was evaluated using the zebrafish (*Danio rerio*) embryo toxicity model. The early stage of the embryo development was studied using the fish embryo acute toxicity (FET) test according to the OECD guidelines. Embryos exposed to 1.5-500 mg L^{-1} PAA solutions from 4 hpf to 120 hpf showed < 10% mortality across all concentrations. Since LC_{50} values could not be determined, all PAAs were classified as non-toxic, non-carcinogenic, and non-dangerous. At 72 hpf, sub-lethal morphological abnormalities (e.g., spinal defects, edema, growth delay) were infrequent, dose-independent, and comparable to controls. Microscopic evaluation of vascular and musculoskeletal systems using fluorescent transgenic zebrafish revealed only minor, non-significant alterations at 2 and 10 mg L^{-1}.
Neurotoxicity was assessed at 120 hpf through light/dark locomotion and touch-evoked response tests. M-GLY caused slight activity reduction at intermediate doses, while M-GLU and M-GLY_{50}-$CYSS_{50}$ showed mild motility impairments only at higher concentrations. Among the three, M-GLY had the least impact on neuromotor function. Overall, the tested PAAs demonstrated low aquatic toxicity, supporting their potential as eco-friendly flame retardants. The zebrafish model proved valuable not only for toxicity screening but also for linking polymer structure to biological effects.

The following part of the thesis is focused on exploring different PAAs applications, both in

their linear and cross-linked form. Specifically, Chapter 5 is devoted to assessing the photostability properties of these polymers, and particularly their potential as photostabilizers for cotton in accelerated photoaging tests. Chapter 6 regards the preparation of bioactive PAA-based composite hydrogels reinforced with PLLA mats, as novel biomaterials with neuroregenerative and neuroprotective properties.

5. α-AMINO ACID-DERIVED PAAs AS PHOTOSTABILIZERS FOR COTTON FABRICS

This chapter explores the use of PAAs derived from various α-amino acids with different UV-absorption properties as photostabilizers for cotton fabrics. Cotton samples underwent accelerated UV aging in a solar chamber, with changes monitored through colorimetric, structural and morphological analyses. One of the primary goals of this research was to determine whether UV-absorbing chromophores influence PAAs effectiveness as photostabilizers.

All results are presented in detail in a dedicated publication:

Treccani S.; Alongi, J.; Ferruti, P.; Ranucci, E. α-amino acid-derived polyamidoamines as photostabilizers for cotton. Polymer Degradation and Stability ***2025****, 239, 111430, https://doi.org/10.1016/j.polymdegradstab.2025.111430*

5.1. Introduction

Cellulose-based materials are highly susceptible to UV-induced photoaging, primarily due to the formation of reactive radicals and oxidized groups that initiate degradation *(41,121–123)*. UV exposure leads to the generation of hydroperoxides, hydroxyl radicals and additional carbonyl-containing groups, ultimately compromising the structural and aesthetic integrity of materials like paper, textiles, and wood. This poses challenges for material durability but also for cultural heritage preservation. To limit UV damage, various photostabilizers, such as UV absorbers, radical scavengers, and antioxidants, have been employed. Commercially, benzophenones (BP-3, oxybenzone, BP-4), benzotriazoles, and triazines are the most common UV absorbers, often used in combination with hindered amine light stabilizers (HALS) *(124)* that do not absorb UV radiation but function as radical scavengers, for synergistic protection. However, concerns regarding their environmental impact, safety, and cost have prompted interest in alternative solutions *(125–128)*. PAAs are emerging as promising polymeric photostabilizers (see Section 1.8) due to their radical-scavenging activity from their tertiary

amine groups. Previous studies have shown the effectiveness of glycine-, arginine-, leucine-, and glutamic acid-derived PAAs in protecting cotton from UVA damage *(43)*. Building on this, the present work investigates a new series of PAAs with structural variations among the α-amino acid residues, including UV-absorbing and radical-scavenging functionalities *(129–132)* to understand their influence on the photostabilization efficiency of these polymers under combined UVA-UVB exposure.

5.2. Results and discussion

Five water-soluble PAAs, namely M-GLY, M-ARG, M-SER, M-HIS and the copolymer M-TYR_{30}-ARG_{70} were investigated for their potential as photostabilizers of cotton fabrics. PAAs derived from α-amino acids are amphoteric polyelectrolytes and their radical scavenging activity may also be influenced by the charge distribution. In this study, the ionic species distributions of PAAs are reported in Figure 5.2.1 and were calculated as reported in Chapter 2. The isoelectric points are consistent with the presence of an overall negative charge in the repeat units of M-GLY, M-SER, M-HIS at pH 7.0, and of M-TYR_{30}-ARG_{70} at the working pH of 7.5, while M-ARG exhibits an overall positive charge under the same conditions.

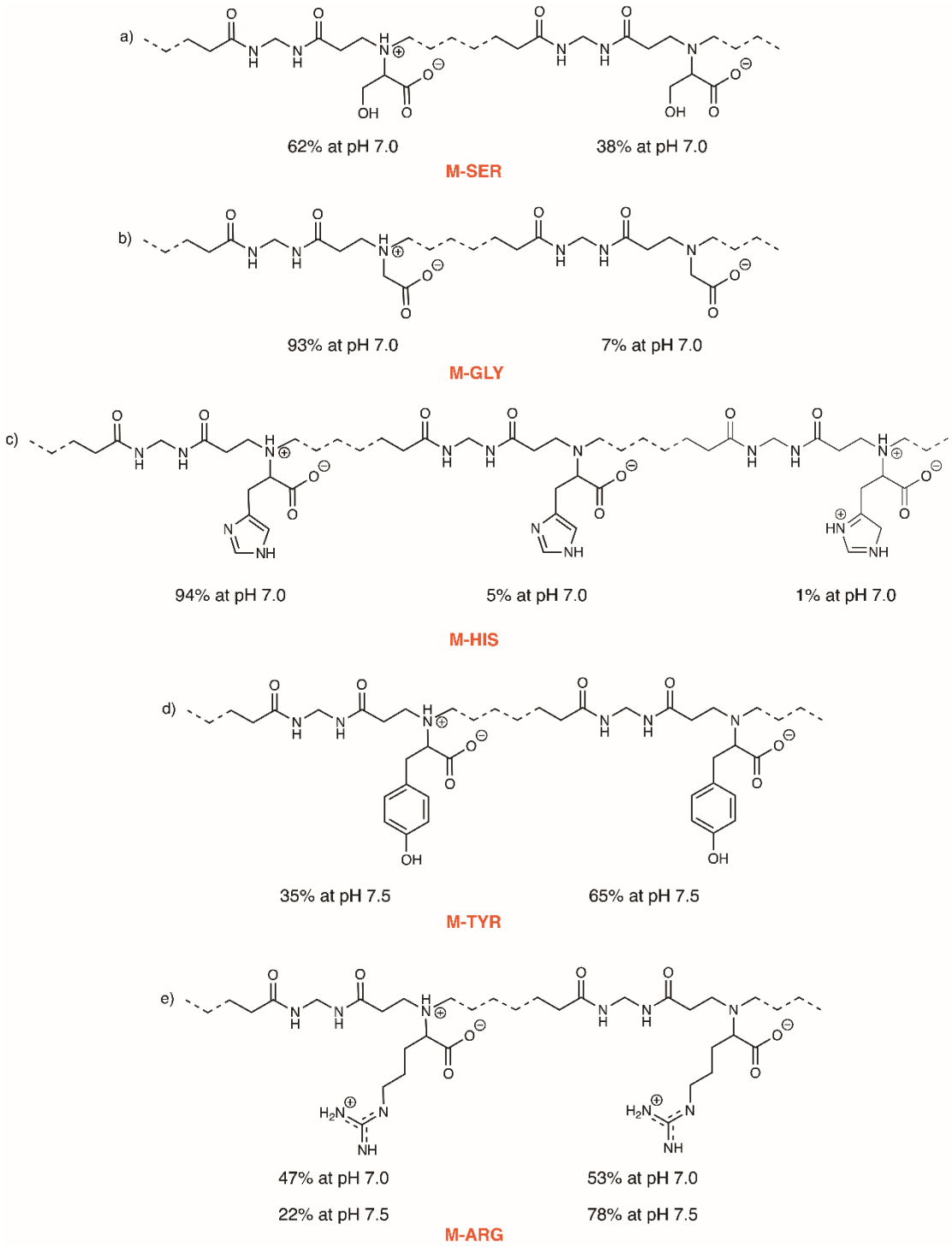

Figure 5.2.1. Distribution of ionic species in PAA repeat units at pH 7.0 and, specifically for the M-TYR and M-ARG units, at pH 7.5.

The UV absorption properties of PAAs were examined to assess the impact of chromophoric groups in their repeating units on radical scavenging activity. Figure 5.2.2 presents the UV spectra of PAAs at pH 7.0 (pH 7.5 for M-TYR$_{30}$-ARG$_{70}$ due to solubility limitations), along with those of their parent α-amino acids. All PAAs exhibit characteristic amide group absorption: a strong $\pi \rightarrow \pi^*$ transition at 190-220 nm and a weaker $n \rightarrow \pi^*$ transition at 210-

240 nm. M-GLY, M-SER, and M-ARG show no additional bands, as their side chains absorb only below 230 nm. In contrast, M-HIS and M-TYR_{30}-ARG_{70} display extended absorption due to aromatic side chains. M-HIS shows a strong band at 200-230 nm ($\pi \rightarrow \pi^*$ of the imidazole ring) and a weak band at 250-280 nm ($n \rightarrow \pi^*$). M-TYR_{30}-ARG_{70} shows strong absorption at 190-230 nm from $\pi \rightarrow \pi^*$ transitions of the benzene ring, and weaker absorption at 270-280 nm from $n \rightarrow \pi^*$ transitions of phenolic oxygen.

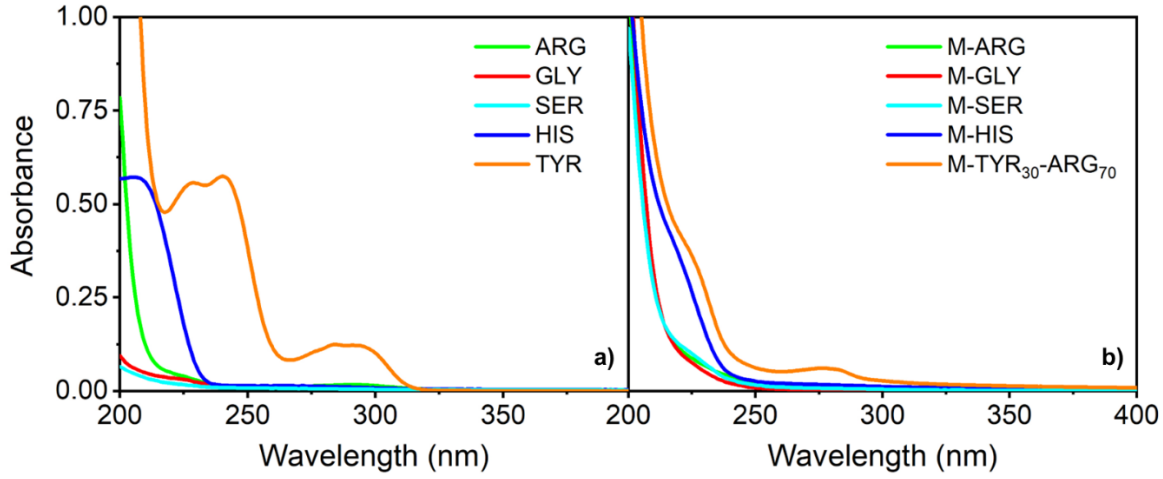

Figure 5.2.2. UV absorption spectra of PAAs (b) and parent α-amino acids (a) recorded at concentration 0.025 mg mL^{-1} and pH 7.0, except for M-TYR_{30}-ARG_{70}, whose spectrum was recorded at pH 7.5.

Photoaging tests

Accelerated photoaging tests were performed on cotton fabrics treated with 6 wt.% PAAs. Samples were exposed to UV light (280-400 nm) in air at 30-35 °C and 40% relative humidity. Each cycle included 15 minutes of irradiation followed by a 30-minute pause during which FT-IR and colorimetric measurements were performed, with samples aligned along the same axis. After daily testing, samples were stored in the dark. The total irradiation time was 14 hours. Figure 5.2.3 compares untreated and PAA-treated fabrics before and after aging. Visibly, all COT/PAA samples retained their original color after the deposition, except for COT/M-TYR_{30}-ARG_{70}. Following 14 h of irradiation, untreated cotton showed marked yellowing, while PAA-treated fabrics exhibited significantly less discoloration, except for COT/M-TYR_{30}-ARG_{70}, which showed a yellowing like that of unprotected cotton.

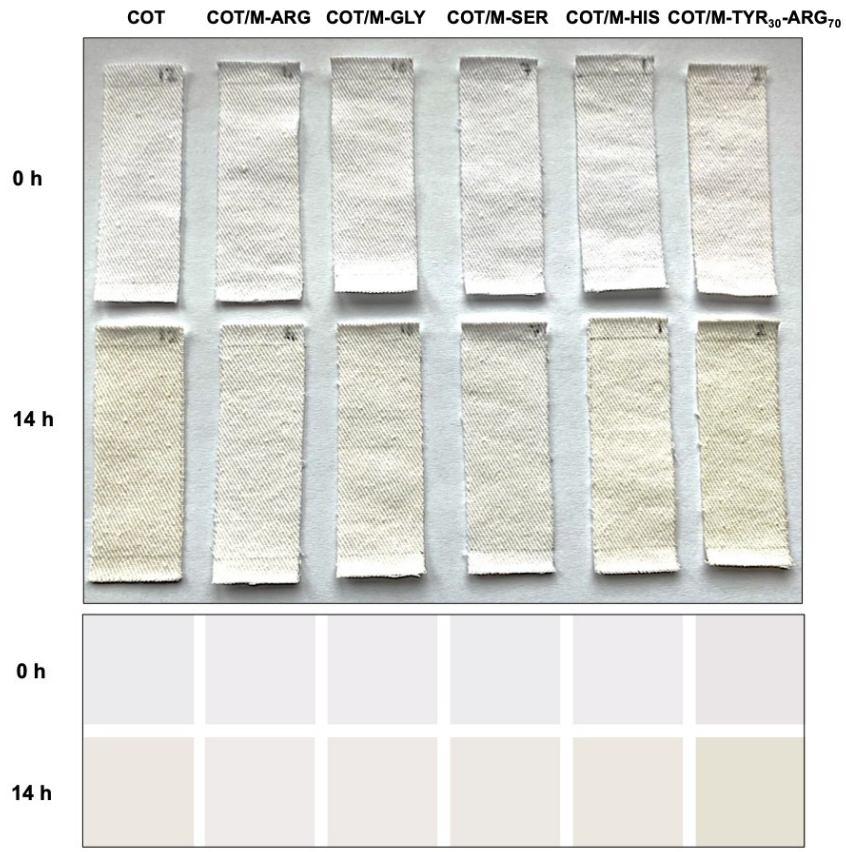

Figure 5.2.3. Digital pictures of untreated and PAA-treated cotton fabrics after 0 and 14 h photoaging (upper panel); simulated colors of cotton samples based on the determined colorimetric parameters (lower panel).

The FT-IR spectra of the PAA-treated cotton fabrics showed no significant changes after 14 hours of irradiation (Figure 5.2.4), indicating that no major structural alterations occurred during photoaging under the applied experimental conditions.

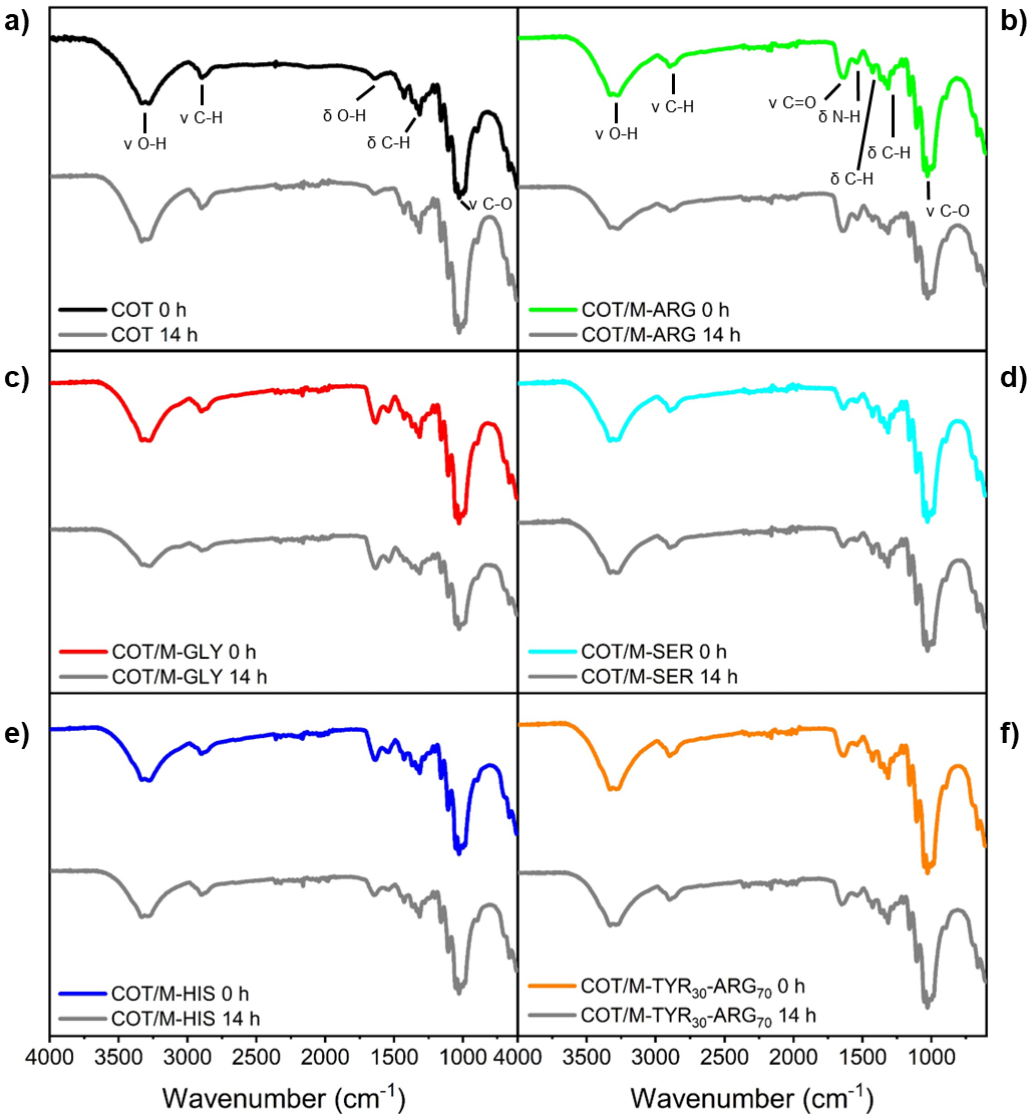

Figure 5.2.4. FT-IR/ATR spectra of COT (a), COT/M-ARG (b), COT/M-GLY (c), COT/M-SER (d), COT/M-HIS (e) and COT/M-TYR$_{30}$-ARG$_{70}$ (f) analyzed at 0 and 14 h UV irradiation.

Representative spectrophotometric data collected at different irradiation times (0, 1, 10, and 14 hours) are shown in Figure 5.2.5. A marked decrease in the maximum reflectance of untreated cotton at 450 nm was observed throughout the experiment. The reflectance began to stabilize after 9 hours, with a total reduction of 11% recorded by 14 hours. In contrast, the COT/PAA samples exhibited a slower decline in reflectance at 450 nm, with reductions of only 4%, 5%, 7%, and 8% for COT/M-ARG, COT/M-GLY, COT/M-SER, and COT/M-HIS, respectively. The COT/M-TYR$_{30}$-ARG$_{70}$ sample showed a 17% reduction, greater than virgin cotton, indicating more intense coloration under irradiation (Figure 5.2.5). Based on these results, the photoaging resistance of the cotton samples can be ranked as follows: COT/M-ARG > COT/M-GLY > COT/M-SER > COT/M-HIS > COT > COT/M-TYR$_{30}$-ARG$_{70}$.

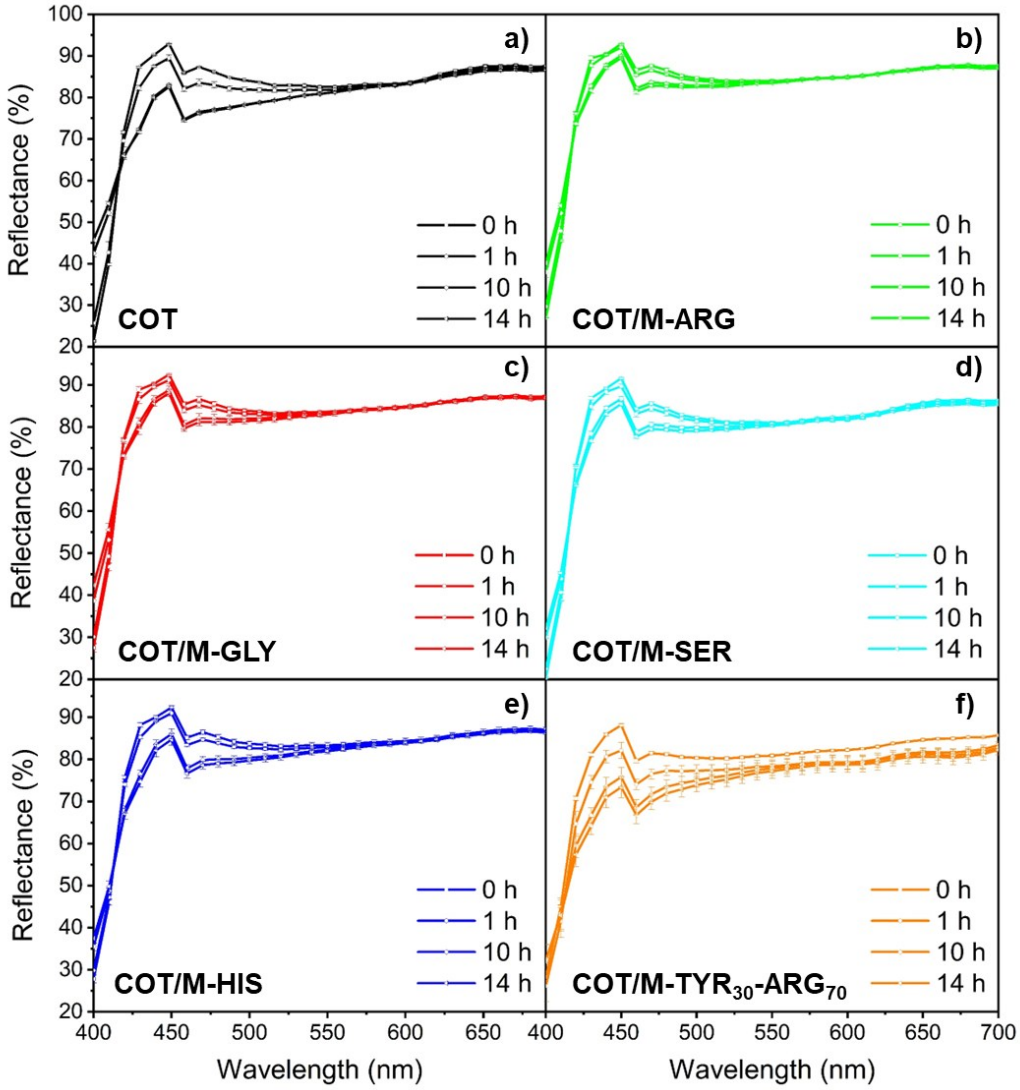

Figure 5.2.5. Reflectance spectra of untreated and PAA-treated cotton at different photoaging stages.

The color changes in photoaged cotton fabrics were more accurately assessed by tracking the CIELAB color space parameters: ΔE^* (overall color change), C^* (chroma), L^* (lightness), and the chromatic coordinates a^* (green–red axis), b^* (blue–yellow axis), as well as hue angle, h, calculated as described in Equations 5.3.2-4 (Section 5.3). For reference, an ideal pure white has values of $L^* = 100$, $a^* = 0$, $b^* = 0$, and $C^* = 0$. Figure 5.2.6 and Table 5.2.1 present the results for both untreated and PAA-treated cotton fabrics. The L^* value showed only a slight decrease over the irradiation period, with the largest decline observed for COT/M-TYR$_{30}$-ARG$_{70}$ (Figure 5.2.6a). The a* coordinate followed a similar trend in all samples, except for COT/M-TYR$_{30}$-ARG$_{70}$, which exhibited a steady decrease during the first 3 hours of irradiation, stabilizing afterward. The b* coordinate, indicating yellowness when positive, showed a distinct behavior. In untreated cotton, b* increased rapidly from -1.37 to +3.9 over

the course of irradiation, indicating pronounced yellowing. After 9 hours, this yellowing reached a plateau (Figure 5.2.6e). In contrast, PAA-treated cotton showed a more gradual and linear increase in b*, except for COT/M-TYR_{30}-ARG_{70}, which followed a trend closer to that of untreated cotton. Maximum b* values observed were 0.9, 1.4, 1.8, and 3.3 for COT/M-ARG, COT/M-GLY, COT/M-SER, and COT/M-HIS, respectively, corresponding to Δb^* values between 2.1 and 4.4. For comparison, untreated cotton and COT/M-TYR_{30}-ARG_{70} had higher Δb^* values of 5.3 and 6.8, respectively.

Similar trends were seen in the C^* (chroma) and ΔE^* (total color change) parameters, as shown in Figures 5.2.6b and 5.2.6d. Two notable markers help assess the performance of the photostabilizers: a sharp decline in the h (hue) parameter (Figure 5.2.6c), associated with a change in the sign of the b^* value and the crossover point between the a^* and b^* curves (Figures 5.2.6e-f, inlets), indicating a shift in the dominant yellow color component thus when $b^*/a^* > 1$, corresponding to h reaching 45° (i.e., $\arctan(b^*/a^*) = 1$) (Figure 5.2.6c). The ΔE^* parameter proved especially useful in quantifying overall color change due to photoaging in both untreated and treated fabrics. Based on the colorimetric analysis summarized in Table 5.2.1, the effectiveness of the PAA photostabilizers can be ranked as follows: M-ARG > M-GLY > M-SER > M-HIS > M-TYR_{30}-ARG_{70}. A clear performance gap separates the top three polymers from the rest, with COT/M-TYR_{30}-ARG_{70} consistently performing worse than untreated cotton.

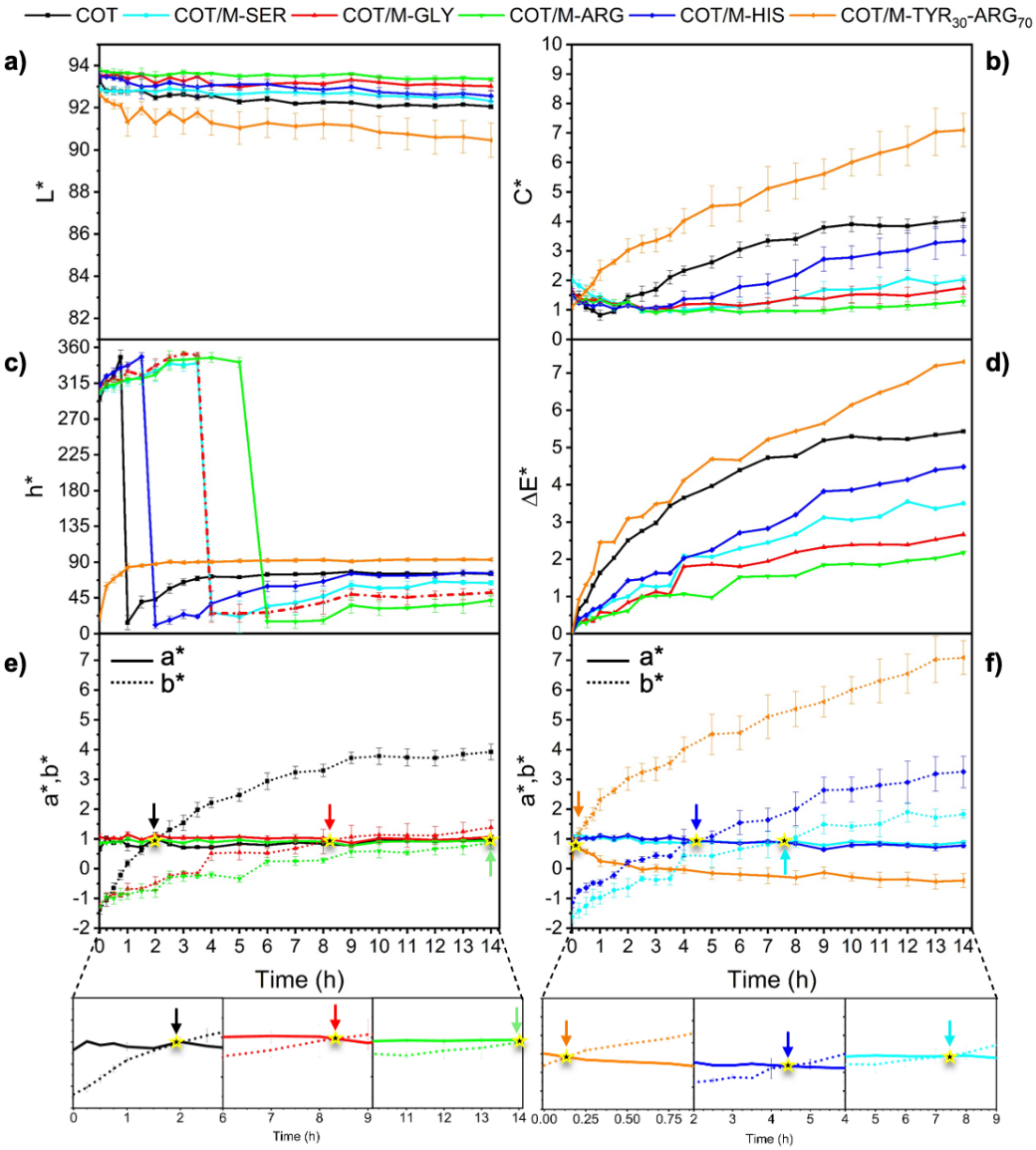

Figure 5.2.6. Change of the color parameters of untreated and PAA-treated cotton during accelerated photoaging tests.

Table 5.2.1. Colorimetric parameters of photoaged cotton samples.

	Maximum reflectance reduction at 14 h (%)	**$b^*_{14\ h}$**	**$\Delta b^*_{14\ h}$**	**$t_{hue\ drop}$ [a)] (h)**	**$t_{crossover}$ [b)] (h)**	**$\Delta E^*_{14\ h}$**
COT	11	3.9 ± 0.3	5.3	1	2	5.4
COT/M-ARG	4	0.9 ± 0.2	2.1	6	14	2.2
COT/M-GLY	5	1.4 ± 0.3	2.6	4	8.5	2.7
COT/M-SER	7	1.8 ± 0.1	3.5	4	7.5	3.5
COT/M-HIS	8	3.3 ± 0.5	4.4	2	4.5	4.5
COT/M-TYR_{30}-ARG_{70}	17	7.1 ± 0.6	6.8	0.25	0.25	7.3

[a)] Time at which a sudden decrease of h^* is observed, corresponding to the sign change of the b^* coordinate; [b)] Time at which the a^* and b^* curves intersect.

Efficacy of PAAs as photostabilizers for cotton

The photostabilizing effectiveness of PAA coatings on cotton arises from several key factors. An essential factor is their UV stability that depends on efficient deexcitation mechanisms with rapid internal conversion to the ground state and vibrational cooling occurring faster than bond dissociation. In addition, their antioxidant and radical-scavenging properties play a major role, as they neutralize reactive oxygen species (ROS) generated during cellulose photooxidation, preventing further damage *(133)*. All PAAs studied share structural features: two amide groups, a tertiary amine in the backbone, and a carboxyl group in the side chain. While amide and carboxyl groups are stable against oxidation, the radical-scavenging activity of M-ARG, M-GLY, M-SER, and M-HIS is primarily due to the tertiary amines, which donate electron pairs to neutralize radicals *(134)*. The extent of this activity is pH-dependent: at pH 7.0, the deprotonation levels of the tertiary amines are 53% (M-ARG), 7% (M-GLY), 38% (M-SER), and 5% (M-HIS) (Figure 5.2.1). Differences in photostability are also influenced by the side-chain structure derived from α-amino acid residues. PAAs with UV-absorbing side groups, M-HIS (UVC range) and M-TYR_{30}-ARG_{70} (UVB range), are less effective. In particular, M-TYR_{30}-ARG_{70} failed to protect cotton from photoaging. Their vulnerability derived from inefficient energy dissipation and the stabilization of radicals via resonance in imidazole (M-HIS) and phenol (M-TYR) groups. In contrast, PAAs lacking chromophores (M-ARG, M-GLY, M-SER) are inherently more photostable. M-GLY proved slightly more efficient than M-SER due to the absence of tertiary hydrogens, which are more prone to radical attack. M-ARG shows

the highest stability, thanks to its guanidine groups, which participate in electron transfer with radicals, forming stable radical cations.

Morphological analysis cotton specimens

Field-emission scanning electron microscopy (FE-SEM) was used to assess the effects of UV irradiation on the surface morphology of untreated and PAA-treated cotton fabrics. Virgin cotton fibers exhibited their typical elongated, ribbon-like shape with natural twists and a flat, smooth surface (Figure 5.2.7) *(135)*. At high magnification (10000X), cellulose microfibrils forming the primary wall were visible, along with occasional natural inhomogeneities. All PAA-treated samples showed similar morphology regardless of the polymer type. Due to the hydrophilic nature of both cotton and PAAs, a thin, continuous, and uniform coating formed on the fiber surfaces. Importantly, PAAs also penetrated the cotton weave and reached the microfibrils, as seen in Figures 5.2.7a,c,e,g,i,m (inlets), ensuring close contact between the photostabilizer and cellulose and enhancing protection against photooxidation.

After 14 hours of UV exposure, untreated cotton displayed clear surface erosion and structural damage (Figure 5.2.7b, inlet). In contrast, PAA-treated fibers remained intact and coated. Minor defects such as cracking or partial delamination appeared in some samples, specifically COT/M-GLY, COT/M-SER, COT/M-HIS, and COT/M-TYR_{30}-ARG_{70} (Figures 5.2.7f,h,n, and inlets). Notably, COT/M-ARG showed no visible damage, with a smooth, unbroken coating (Figure 5.2.7d).

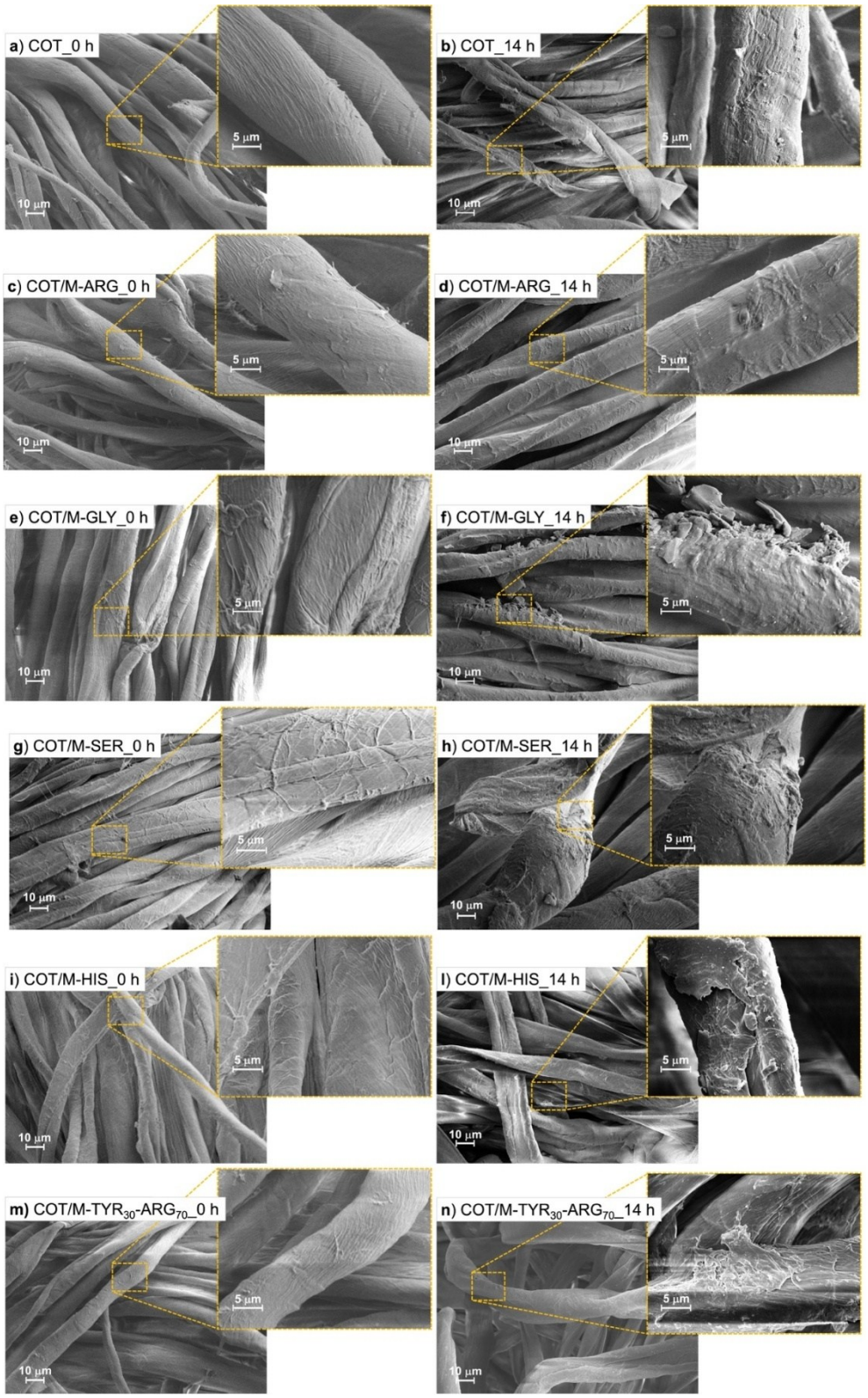

Figure 5.2.7. FE-SEM micrographs in secondary electron mode (2500X) of untreated cotton (COT) and cotton fabrics treated with 6% add-on after 0 h and 14 h UV irradiation. Inlet magnification: 10000X.

Effect of photoaging on the crystallinity of cotton fabrics

X-ray diffraction (XRD) was used to assess the effects of photoaging on the crystalline structure of cellulose in untreated and PAA-treated cotton. Figure 5.2.8 shows the XRD patterns before and after 14 hours of UV exposure, as well as after PAA extraction post-photoaging. Crystallinity data for the unirradiated samples are summarized in Table 5.2.2. In untreated cotton, the XRD pattern prior to irradiation displays characteristic broad peaks at 15.19°, 16.73°, and 23.08°, corresponding to the (100), (010), and (110) planes of cellulose. A shoulder near 20° is linked to the (012)/(102) facets, and a weaker peak around 35.10° corresponds to the (2-1-1)/(210)/(201) planes *(136)*. Overall, the degree of crystallinity remained largely unchanged after irradiation, indicating that the crystalline structure of cellulose was preserved.

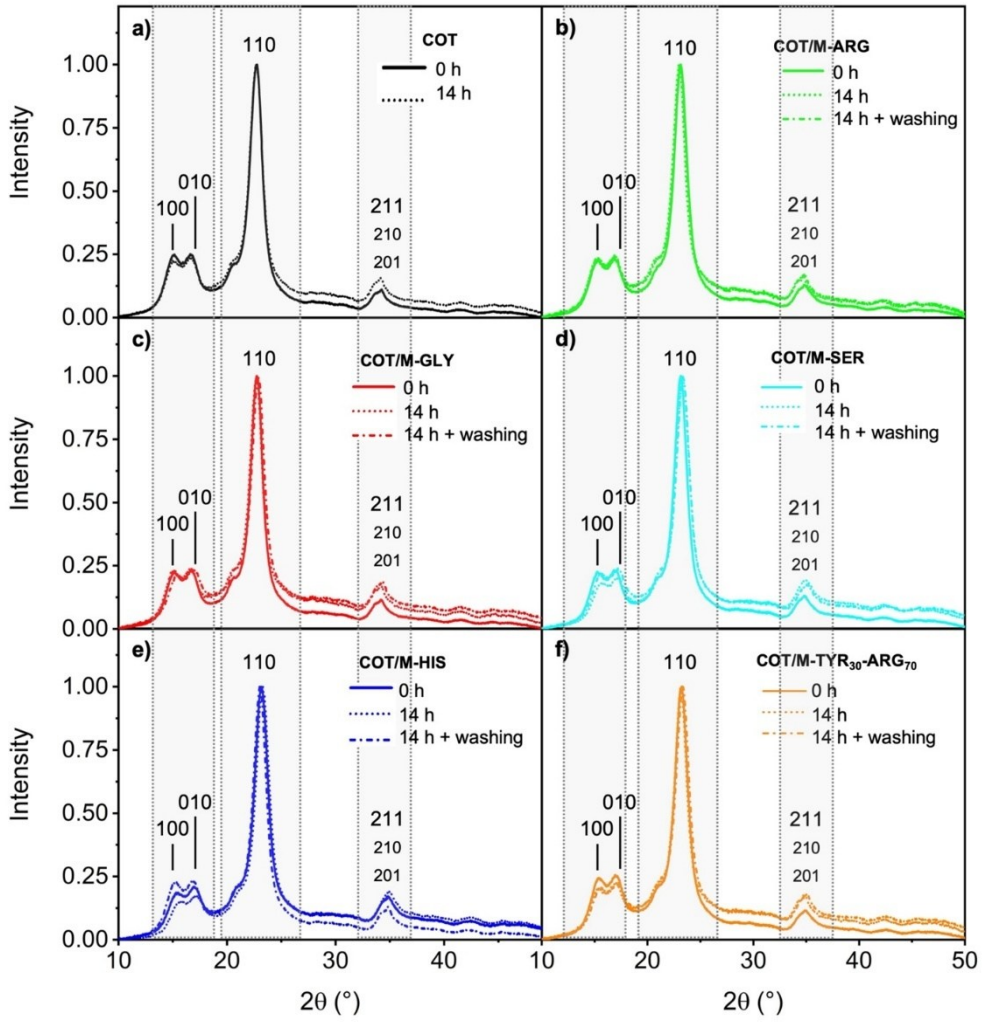

Figure 5.2.8. XRD spectra of untreated cotton (COT, a) and cotton fabrics treated with 6% add-on M-ARG (b), M-GLY (c), M-SER (d), M-HIS (e), and M-TYR_{30}-ARG_{70} (f) after 0 and 14 h irradiation and after washing with water at the end of irradiation.

Table 5.2.2. Position of XRD signals and crystallographic parameters of photoaged cotton samples.

Sample	**2θ**			**d (nm)**		
Assignment	**100**	**010**	**110**	**100**	**010**	**110**
COT	15.19	16.73	23.08	0.294	0.268	0.196
COT/M-ARG	15.25	16.82	23.09	0.293	0.266	0.196
COT/M-GLY	15.25	16.80	23.08	0.293	0.266	0.196
COT/M-SER	15.33	17.00	23.27	0.291	0.263	0.195
COT/M-HIS	15.24	16.88	23.23	0.293	0.265	0.195
COT/M-TYR_{30}-ARG_{70}	15.40	17.00	23.27	0.290	0.263	0.195

Extraction of PAA coatings and analysis of cotton fabrics

At the end of the photoaging tests, PAA coatings were extracted from the treated cotton strips using deuterated water and analyzed by ^{1}H-NMR. The spectra of the photoaged PAAs closely matched those of the original, unirradiated polymers, confirming that no degradation occurred and no cellulose-derived residues were present. The washed cotton samples were then evaluated colorimetrically. As shown in Table 5.2.3, cotton from COT/M-ARG, COT/M-GLY, and COT/M-SER recovered most of their original color, with ΔE^* values between 1.7 and 2.2, indicating only slight, barely perceptible color changes. In contrast, greater color shifts were observed in samples from COT/M-HIS and COT/M-TYR_{30}-ARG_{70}, with ΔE^* values of 3.2 and 4.2, respectively.

Table 5.2.3. Colorimetric parameters of photoaged COT/PAA samples after washing with water.

	L*	**a***	**b***	**ΔE*** [a)]	**Simulated colors** [b)]
COT_{t0} [c)]	93.3 ± 0.1	0.65 ± 0.02	-1.37 ± 0.15	-	
Post extraction					
COT/M-ARG	93.4 ± 0.2	0.98 ± 0.09	0.44 ± 0.09	1.8	
COT/M-GLY	93.1 ± 0.1	1.09 ± 0.02	0.95 ± 0.15	2.4	
COT/M-SER	92.8 ± 0.1	0.92 ± 0.04	0.63 ± 0.13	2.1	
COT/M-HIS	92.5 ± 0.6	1.04 ± 0.20	1.93 ± 0.52	3.4	
COT/M-TYR_{30}-ARG_{70}	90.7 ± 0.3	0.88 ± 0.21	3.97 ± 0.48	5.9	

[a)] Color change with respect to virgin cotton before irradiation; [b)] simulated colors of photoaged cotton samples after water extraction based on the determined colorimetric parameters; [c)] virgin cotton.

5.3. Experimental part

Different PAAs, namely M-GLY, M-ARG, M-SER, M-HIS and the copolymer M-TYR_{30}-ARG_{70} were synthesized and characterized following the procedures reported in Chapter 2. After the reaction time, the pH was adjusted to 7.0 (7.5 for the copolymer) with 6 M HCl and the product was retrieved by freeze-drying.

Treatment of cotton fabrics

Cotton fabric strips (20 mm × 60 mm) were first dried at 100 °C for 4 minutes and weighed. Each strip was then treated with 300 μL of a 6 wt.% aqueous PAA solution using an electronic micropipette, followed by another drying step at 100 °C for 4 minutes. The dry solid add-on (*Add-on*, wt.%) was calculated by measuring the sample weight before (W_i) and after (W_f) treatment, according to the following Equation:

$$Add-on\% = \frac{W_f - W_i}{W_i} \times 100 \qquad \textit{Eq. 5.3.1}$$

For all PAAs, the final add-on percentage was established at 6%. Cotton fabrics treated with PAAs were labeled using the following format: COT/M-GLY denotes a cotton sample treated with M-GLY.

Accelerated photodegradation tests

Accelerated photodegradation tests were performed in a closed solar chamber lined with aluminum foil. Untreated and PAA-treated cotton strips were mounted on a rotating stand (250 rpm) and exposed to a 500 W UV lamp (280-400 nm), positioned 45 cm from the samples. A 40% relative humidity was maintained using a saturated potassium carbonate solution. To prevent overheating, irradiation was paused every 15 minutes for 30 minutes. Sample temperatures reached up to 50 °C, measured at a 15 cm distance using a Tilswall digital thermometer. After each irradiation cycle, samples underwent colorimetric and FT-IR analyses. At the end of each day, they were stored in the dark. All tests were conducted in duplicate. Following exposure, PAA-treated samples were extracted with 1 mL D_2O at room temperature for 1 hour under stirring, and the extracts were analyzed by ^{1}H-NMR.

Characterization techniques

UV-vis spectroscopy: the UV absorption spectra of PAAs and their parent α-amino acids were obtained from 0.025 mg mL^{-1} water solutions at pH 7.0 using a Lambda 4 Perkin Elmer spectrophotometer (Milan, Italy) operating in the wavelength range 200-800 nm, except for the

M-TYR$_{30}$-ARG$_{70}$ copolymer, which was analyzed at pH 7.5 due to solubility constrains. *Scanning Electron Microscopy (SEM)*: the morphology of untreated (COT) and PAA-treated (COT/PAA) cotton samples was examined before and after 14 h of UV irradiation. Fabric surfaces (5 mm × 5 mm) were gold-coated and analyzed using a Zeiss SIGMA 300 field-emission scanning electron microscope (FE-SEM) operating at a 5 kV beam voltage and 8.5 mm working distance (Zeiss, Ramsey, NJ, USA).

Colorimetric analysis: the surfaces of untreated and PAA-treated cotton strips were spectrophotometrically analyzed following the ISO11664 standard *(137)* using a YS3010 Handheld Spectrophotometer (3nh Global, Guangzhou, China) equipped with the SQCX software. The chromaticity coordinates of the samples L^*, a^*, b^*, where L^* is the sample brightness ranging from 0 (black) to 100 (white), a^* (green-red axis) and b^* (blue-yellow axis) were obtained directly from the software. Based on these values, the following CIELAB color space parameters were calculated to assess visual changes: total color difference (ΔE^*), chroma (C^*), and hue angle (h), as defined by following Equations:

$$\Delta E^* = \sqrt{(\Delta L^*)^2 + (\Delta a^*)^2 + (\Delta b^*)^2} \qquad \textit{Eq. 5.3.2}$$

$$C^* = \sqrt{a^{*2} + b^{*2}} \qquad \textit{Eq. 5.3.3}$$

$$h = arctg\frac{b^*}{a^*} \qquad \textit{Eq. 5.3.4}$$

These coordinates and the derived parameters are unitless, expressing perceptual color characteristics. ΔE^* quantifies overall color change referring to human color perception, with higher values indicating more pronounced aging effects. C^* reflects color intensity or saturation, and h describes hue direction in the a^*-b^* plane, expressed in degrees. Color differences were categorized as follows: not present ($\Delta E^* = 0$); imperceptible to the human eye ($0 < \Delta E^* \leq 1$); perceptible under close observation ($1 < \Delta E^* \leq 2$); immediately noticeable ($2 < \Delta E^* \leq 10$); highly distinct ($11 < \Delta E^* \leq 49$); and extremely distinct ($\Delta E^* \geq 50$) *(138)*.

X-ray Diffraction (XRD): The X-ray diffraction spectra of COT and COT/PAA samples were recorded using a Miniflex 600 diffractometer with Cu $K_{\alpha 1}$ radiation at 1.5405 Å, at 40 kV voltage and 15 mA current (Rigaku Europe SE, Germany).

5.4. Conclusions

A series of α-amino acid-derived PAAs was tested as photostabilizers for cotton fabrics. Among them, M-ARG, M-GLY, and M-SER effectively reduced UV-induced yellowing, while M-HIS and M-TYR_{30}-ARG_{70} were less effective. UVA/UVB irradiation over 14 hours showed that only COT/M-TYR_{30}-ARG_{70} degraded more than untreated cotton. FT-IR analysis did not reveal any structural changes on the cotton surface during irradiation. Colorimetric parameters were used to rank the efficacy of the PAA photostabilizers as follows: M-ARG > M-GLY > M-SER > M-HIS> M-TYR_{30}-ARG_{70}. Only the COT/M-TYR_{30}-ARG_{70} samples photodegraded to a larger extent than virgin cotton. Morphological analysis revealed meaningful insights. FE-SEM analysis showed that PAAs formed a uniform and continuous coating on the cotton fibers and after photoaging, the PAA coatings occasionally developed wrinkles and surface fractures, suggesting localized embrittlement. At the end of the photoaging tests, PAAs were extracted from the aged PAA-treated cotton fabrics using deuterated water and analyzed by ^{1}H-NMR spectrometry. Spectral analysis revealed no significant structural changes caused by UV exposure. Meanwhile, the extracted cotton strips largely regained their original color, except for M-HIS and M-TYR_{30}-ARG_{70} that exhibited residual yellowing. The photostabilizing effectiveness of PAA coatings on cotton results from multiple factors. The least effective PAAs were those bearing UV absorbing aromatic or heteroaromatic groups in the side chains (M-HIS and M-TYR_{30}-ARG_{70}) due to the structural destabilization deriving from the mobility of the α-hydrogens in radical reactions. PAAs lacking chromophores in the side chains (M-ARG, M-GLY and M-SER) are intrinsically photostable. Their effectiveness can be ascribed to the radical scavenging activity of the tertiary amine groups in the main chain. The exceptional performance of M-ARG is ascribed to its guanidine residues, which engage in electron transfer reactions with radicals, forming radical cations. Overall, these findings confirm the potential of α-amino acid-derived PAAs as anti-photoaging additives for cotton, especially those with side residues possessing radical scavenging ability, such as the guanidine residue.

6. POLY-L-LACTIC ACID NANOFIBER/PAA COMPOSITE HYDROGEL AS NOVEL STRATEGY FOR IN VITRO NEUROREGENERATION AND NEUROPROTECTION

This chapter explores the development and characterization of a novel composite hydrogel designed for neuroregenerative and neuroprotective applications. The material combines a poly-L-lactic acid (PLLA) electrospun mat with a cell-adhesive polyamidoamine hydrogel (H-$AGMA_{20}$), forming a soft, pliable PLLA/H-$AGMA_{20}$ composite. The PLLA mat was chemically modified to enable covalent grafting of the hydrogel onto the PLLA fibers, resulting in a stable composite structure. *In vitro* studies using preneuronal and immune cell lines revealed that the composite supports neuronal cell proliferation and differentiation, providing protection against neuroinflammatory damage.

All results are presented in detail in a dedicated publication:

Treccani, S.; Bonadies, I.; Ferruti, P.; Alongi, J.; Scarpa, E.; Laurienzo, P.; Raucci, M.G.; Fasolino, I.; Ranucci, E. Poly-L-lactic acid nanofiber/polyamidoamine composite hydrogel as novel strategy for in vitro neuroregeneration and neuroprotection. Biomaterials Advances ***2025****, 177, 214415, https://doi.org/10.1016/j.bioadv.2025.214415*

6.1. Introduction

Understanding neurotoxicity requires reliable *in vitro* models capable of replicating complex cellular and molecular interactions that are difficult to study *in vivo (139)*. Hydrogels have gained importance in this context due to their biocompatibility, chemical versatility, and tissue-like properties. Their porous structure promotes nutrient exchange and waste removal, while their high water content and viscoelasticity mimic the native extracellular matrix, supporting cell viability and differentiation *(140,141)*. Among hydrogel-forming materials, PAAs stand out as biodegradable, functional polymers. In particular, AGMA1, an amphoteric PAA, has demonstrated high bioactivity and biocompatibility in both linear and crosslinked forms (see Section 1.4-1.5). AGMA1 hydrogels have shown therapeutic potential *in vivo* but their intrinsic softness limits the applicability *(22)* thus fiber-reinforced hydrogels have been widely studied as a strategy to enhance mechanical strength while preserving biocompatibility *(142–144)*. AGMA1 has been reinforced with fibers with surface amine groups that allow grafting to the terminal acrylamide groups of the soluble precursor (see Section 1.4). Among them, electrospun poly-L-lactic acid (PLLA) mats were functionalized with amine groups by nitrogen plasma treatment but, despite its efficacy, the physical treatment proved complex, and the resulting

functionalization was not sufficiently durable, reproducible, or easily scalable for broader production needs *(25)*. Electrospun PLLA scaffolds are widely used in neural tissue engineering due to their biodegradability, tunable architecture, and capacity to support neuronal differentiation, particularly in SH-SY5Y preneuronal cell models. Functionalizing PLLA with bioactive molecules further enhances its role in guiding neuronal behavior *(145–148)*. Building on these properties, a composite hydrogel, PLLA/H-AGMA$_{20}$, was prepared by reinforcing AGMA1 hydrogel with an electrospun PLLA mat functionalized via ethylenediamine vapor-induced aminolysis *(149,150)*. This strategy enabled the formation of a robust, homogeneous composite with covalent bonds between components. The composite was designed to support neuronal development and withstand *in vitro* testing under both physiological and pathological conditions. To assess its neuroregenerative and neuroprotective potential, the PLLA/H-AGMA$_{20}$ composite was tested *in vitro* with SH-SY5Y preneuronal cells and RAW 264.7 immune cells. Its effects on neuronal maturation, as well as its ability to mitigate damage from the neurotoxin 1-methyl-4-phenylpyridinium iodide (MPP^+) and the proinflammatory agent lipopolysaccharide (LPS), were evaluated.

6.2. Results and discussion

For comparison, a plain H-AGMA$_{20}$ hydrogel was prepared using the same curing conditions as the PLLA/H-AGMA$_{20}$ composite. The synthesis of H-AGMA$_{20}$ involved two steps. First, an α,ω-acrylamide-terminated oligomer, named AGMA$_{20}$, was synthesized by reacting 2,2'-bis(acrylamido)acetic acid with 4-aminobutylguanidine in a 1.2:1 molar ratio (see Chapter 2). The resulting AGMA$_{20}$ oligomer was obtained as a 50 wt.% aqueous solution, and its structure was confirmed by ^{1}H-NMR spectroscopy (Annex 1). In the second step, AGMA$_{20}$ underwent UV-initiated radical polymerization at pH 7 (Scheme 6.2.1), resulting in a soft, fragile hydrogel sheet approximately 420 µm thick (Figure 6.2.1).

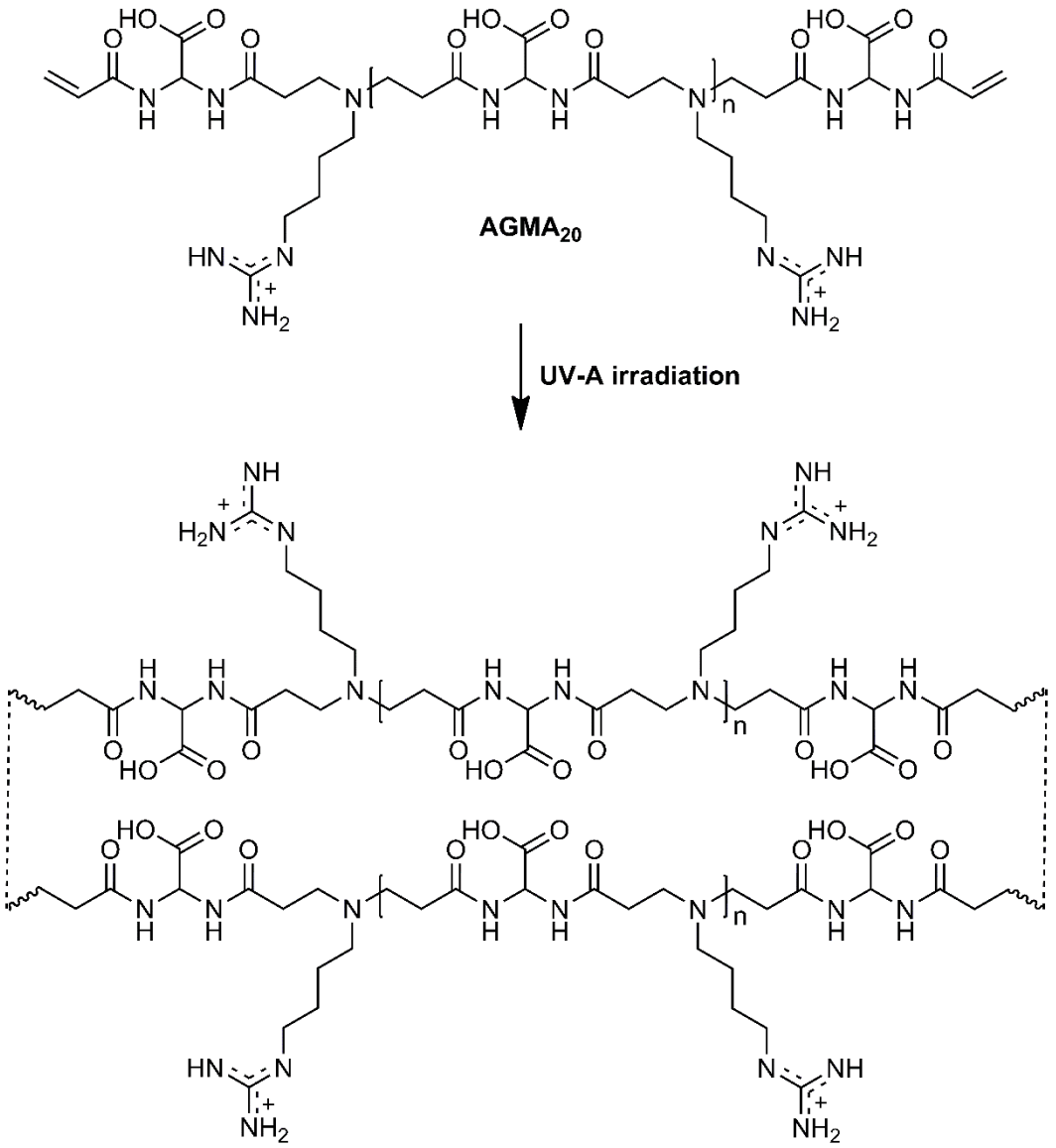

Scheme 6.2.1. Synthesis of the H-AGMA$_{20}$ hydrogel: cross-linking of the AGMA$_{20}$ oligomer. Number of the repeat units, n = 6, from ^{1}H-NMR.

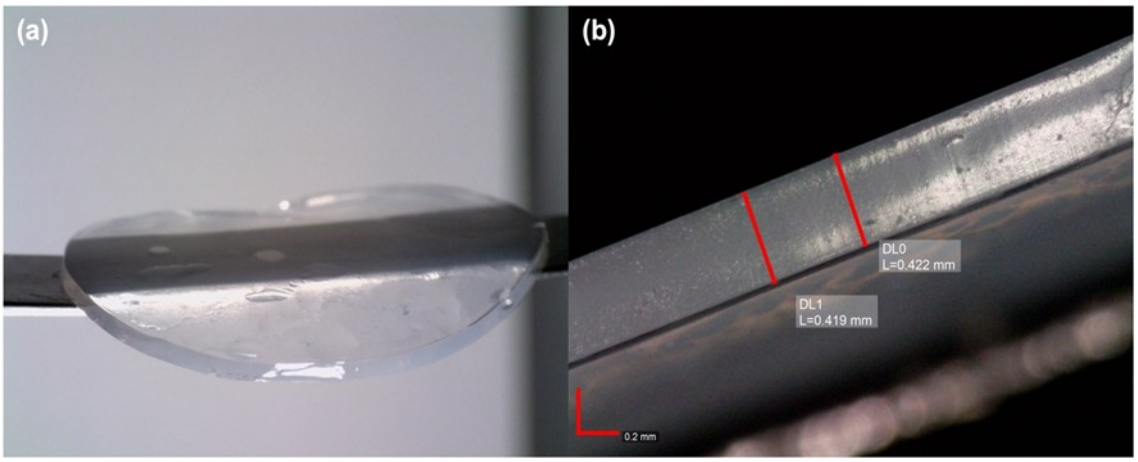

Figure 6.2.1. Optical micrographs of a fully hydrated H-AGMA$_{20}$ hydrogel.

Functionalization and characterization of PLLA nanofibers

PLLA mats with a thickness of 100 µm were fabricated via electrospinning, following optimization of processing parameters. In their native form, the mats were hydrophobic and incompatible with the aqueous $AGMA_{20}$ oligomer solution, preventing effective impregnation. To overcome this, the mats were exposed to EDA vapors to introduce amine groups onto the PLLA surface through aminolysis, a common method for surface functionalization of polyesters *(151)*. The success of the aminolysis reaction was confirmed using a ninhydrin staining test *(152)*. Spectrophotometric analysis of the resulting color change provided CIELAB chromatic parameters. As shown in Figures 6.2.2d, EDA-treated PLLA exhibited a decrease in brightness (L*), a notable increase in the yellow-blue coordinate (b*, from –0.19 to 0.39), and a pronounced increase in the red-green coordinate (a*, from 0.56 to +5.52), indicating the presence of surface amines. Following EDA treatment, the water wettability of the mats improved significantly. While untreated PLLA showed a contact angle of approximately 132°*(153)* (Figure 6.2.2a, inlet), the EDA-treated mats became rapidly wettable, with a near-zero contact angle. The treated mats also appeared transparent (Figure 6.2.2b), as demonstrated by the visibility of blue tweezers behind them, unlike the opaque, untreated mats (Figure 6.2.2a). SEM was used to assess the impact of EDA exposure on surface morphology. Figures 6.2.2e-f show that both untreated and EDA-treated mats consisted of randomly oriented fibers with uniform size and smooth surfaces. EDA treatment did not noticeably alter the structure. Statistical analysis of 50 fibers from each sample revealed no significant differences in average diameter: 1.31 ± 0.25 µm for untreated and 1.17 ± 0.33 µm for EDA-treated fibers.

Energy Dispersive X-ray Spectroscopy (EDX) analysis of the treated mats confirmed the presence of carbon and oxygen, elements naturally present in PLLA, but failed to detect nitrogen (Figure 6.2.2g). This likely reflects the low surface concentration of amine groups and the low energy (0.392 keV) of nitrogen's Kα X-ray, which limits its detectability via EDX.

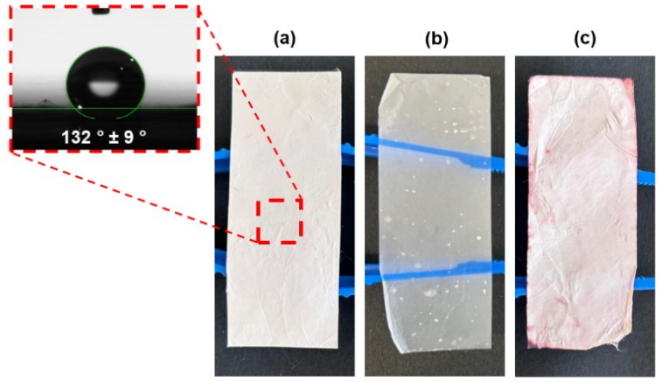

(d)

	PLLA (a)	EDA-treated PLLA after ninhydrin staining (c)
L*	95.04	90.68
a*	0.56	**5.52**
b*	-0.19	0.39
Simulated color		
ΔE*	6.63	

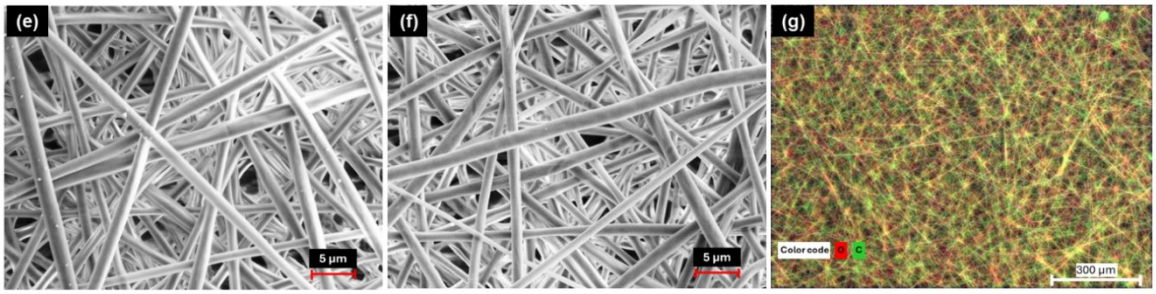

Figure 6.2.2. Untreated PLLA mat (a); EDA-treated PLLA mat after washing with water before (b) and after (c) ninhydrin staining; CIELAB chromatic parameters (d). Insert to (a) shows the contact angle of untreated PLLA mat. SEM micrographs of untreated PLLA mat (e) and EDA-exposed PLLA mat after washing (f). SEM micrograph with EDX color analysis of EDA-exposed PLLA mat after washing (g).

Synthesis and characterization of the PLLA/H-AGMA$_{20}$ composite hydrogel

The multistep synthesis process described in Section 7.2 yielded a flexible, pliable, and macroscopically uniform PLLA/H-AGMA$_{20}$ composite hydrogel approximately 490 µm thick (Figure 6.2.3).

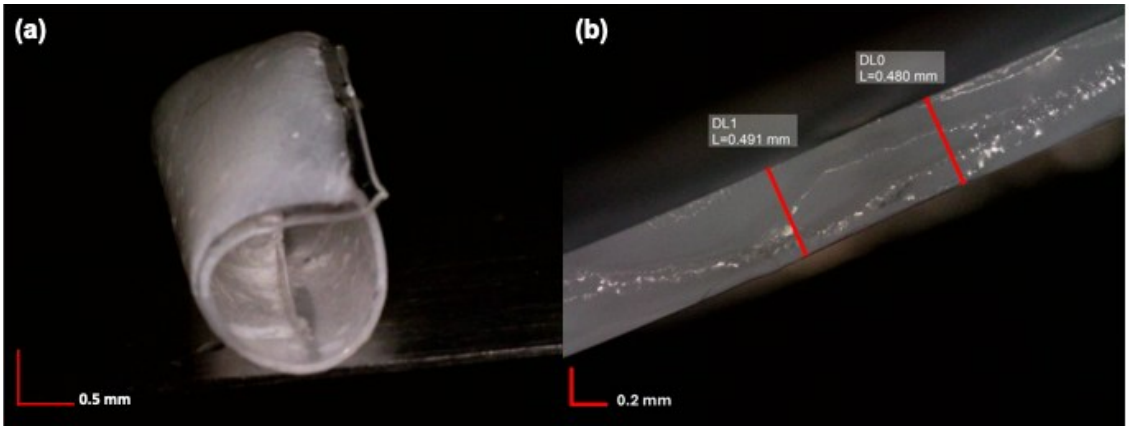

Figure 6.2.3. Optical micrographs of water-swollen PLLA/H-AGMA$_{20}$ composites prepared from EDA-treated PLLA (a and b).

In its dry state, the composite consisted of 8 wt.% PLLA and 92 wt.% H-AGMA$_{20}$. As a result, its water uptake capacity was comparable to that of pure H-AGMA$_{20}$, reaching nearly 200%

(Figure 6.2.4a). Like H-AGMA$_{20}$, the composite demonstrated complete reversibility through multiple swelling and drying cycles (Figure 6.2.4b-c), showing strong resistance to osmotic stress. Notably, PLLA/H-AGMA$_{20}$ samples remained stable in water for several weeks, with no visible detachment of PLLA fibers from the hydrogel matrix.

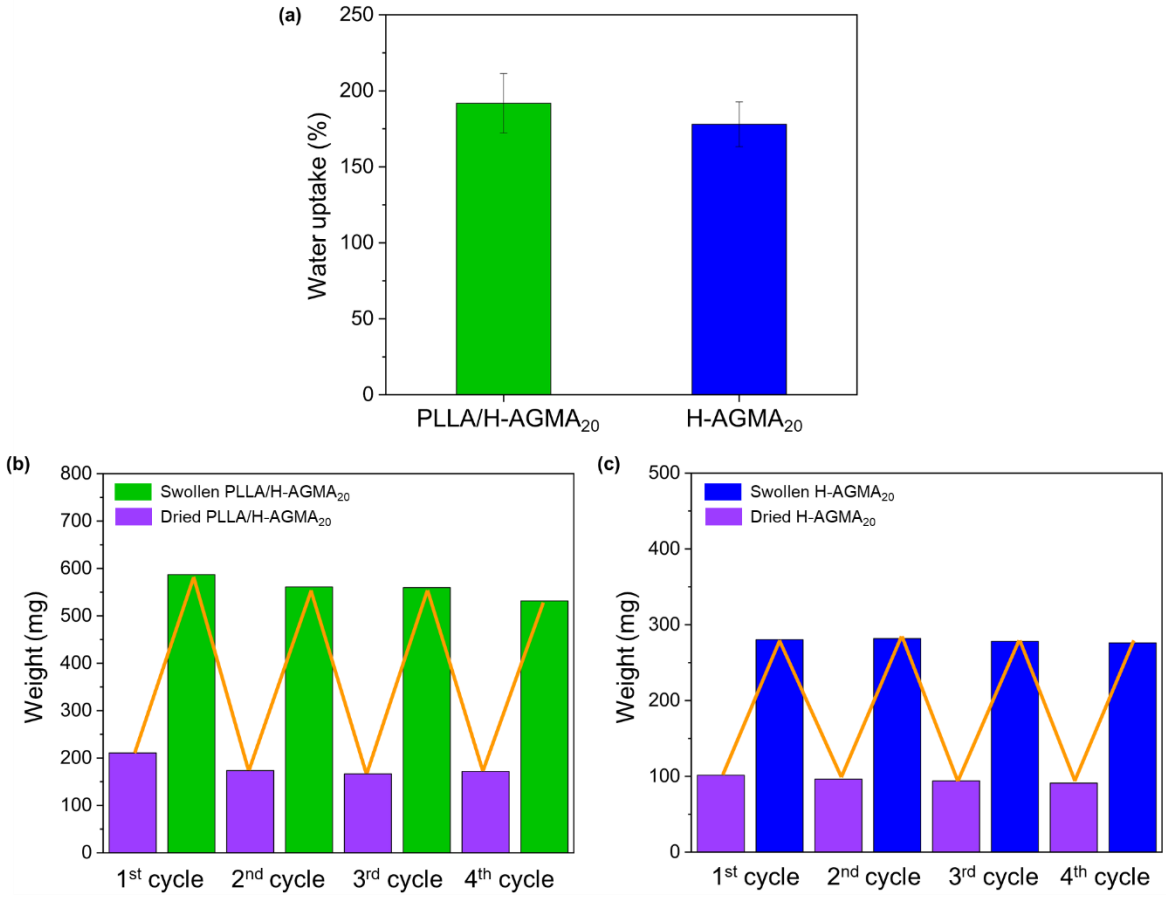

Figure 6.2.4. Water absorption ability of PLLA/H-AGMA$_{20}$ and H-AGMA$_{20}$ (a). Reversible water uptake in absorbing/drying cycles (b) and (c).

SEM analysis of the fracture surface (Figure 6.2.5a) revealed that PLLA fibers were well-integrated within the H-AGMA$_{20}$ matrix, with no signs of separation. This observation supports the formation of covalent bonds between the fibers and the hydrogel, which likely contribute to the composite's mechanical integrity. To confirm the role of surface functionalization in fiber-hydrogel bonding, a control sample was prepared by impregnating a non-functionalized (untreated) PLLA mat with AGMA$_{20}$ and curing it under the same conditions. The resulting material was structurally inconsistent and, upon swelling in water, exhibited complete separation between the hydrogel and fiber layers, as shown by optical (Figure 6.2.5b) and SEM imaging (Figure 6.2.5c).

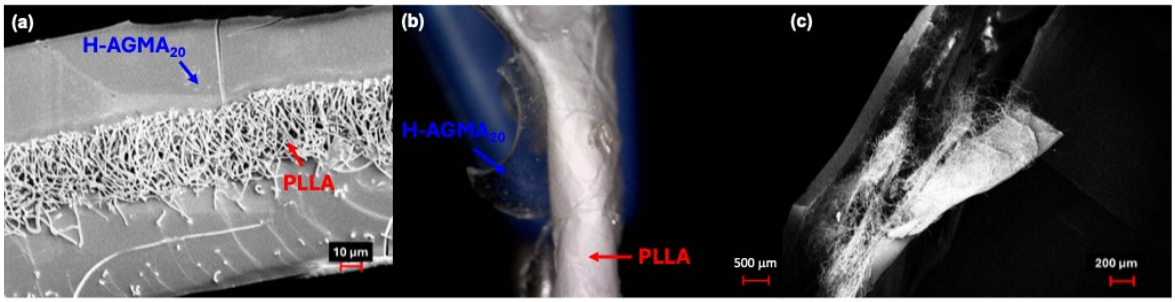

Figure 6.2.5. SEM micrographs of fragile fracture surfaces of PLLA/H-AGMA$_{20}$ (a). Optical microscope (b) and SEM (c) micrographs of an H-AGMA$_{20}$ hydrogel with an embedded PLLA mat, not previously exposed to EDA vapors.

The PLLA/H-AGMA$_{20}$ composite hydrogel was analyzed by FT/IR-ATR spectroscopy and compared to its individual components (Figure 6.2.6). Only the characteristic absorption bands of the hydrogel matrix were observed, consistent with its predominance in the dry composite (92 wt.% H-AGMA$_{20}$, 8 wt.% PLLA).

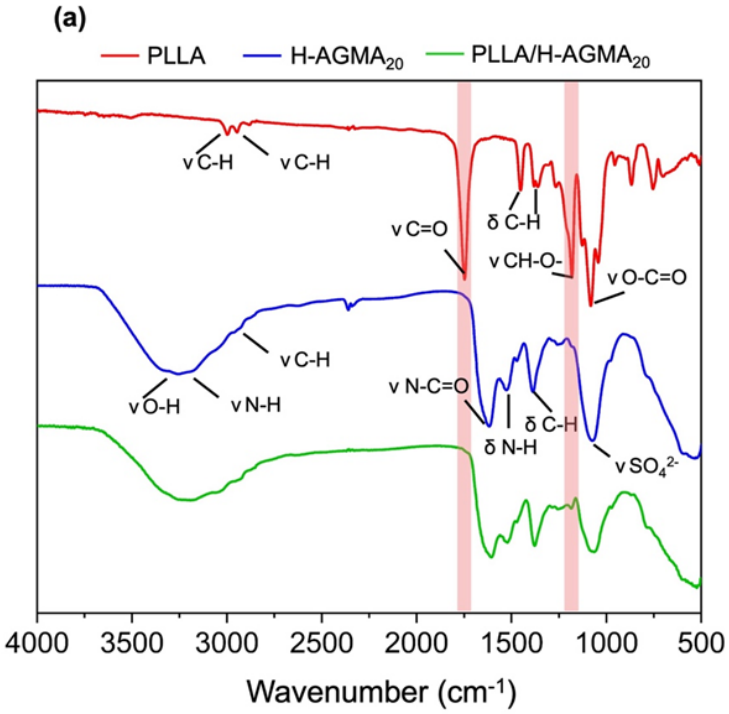

(b)

Wavenumber (cm^{-1})	Assignment
H-AGMA$_{20}$	
3400	ν OH
3296	ν N-H
2972-2880	ν C-H
1680-1590	ν C=O, ν C=C
1528	δ N-H
1386	δ C-H
1080	ν SO_4^{2-}
PLLA	
2997	ν C-H
2945	ν C-H
1748	ν C=O
1183	ν CH-O-

Figure 6.2.6. FT-IR/ATR spectra of PLLA mat (red), H-AGMA$_{20}$ (blue), and PLLA/H-AGMA$_{20}$ (green).

Mechanical properties, including Young's modulus, maximum stress, and strain at break, were assessed through tensile testing and compared across the composite, the pure H-AGMA$_{20}$ hydrogel, and the PLLA mat. Results in Table 6.2.1 confirm that the PLLA mat reinforces the hydrogel via covalent bonding, improving structural cohesion. Although H-AGMA$_{20}$ alone is relatively rigid, it shows low elasticity (Young's modulus: 0.3 MPa), with an ultimate tensile strength of 0.10 N and a maximum stress of 0.04 MPa before failure. However, incorporating

PLLA fibers into the hydrogel led to a reduction in the composite's overall tensile performance, particularly in strain at break. This decrease is mainly due to the low PLLA content (8 wt.% dry, 4 wt.% hydrated), and to the strong interfacial bonding with the matrix, which restricts fiber realignment under stress, as confirmed by SEM (Figure 7.3.5). Stress-strain curves (Figure 6.2.7) show that both the composite and the PLLA mat exhibit an initial linear elastic region with limited deformation, due to the tight, interwoven structure of the mat. In the composite, once inter-fiber junctions begin to rupture, deformation becomes irreversible. Following the elastic region, the PLLA/H-AGMA$_{20}$ composite extends uniformly without necking until failure. In contrast, the pure PLLA mat displays higher elongation and significant narrowing as fibers slide and align along the tensile direction, eventually leading to complete failure *(154)*.

Table 6.2.1. Tensile parameters of PLLA/H-AGMA$_{20}$ and its constituents. [a)]

Sample	Young modulus (MPa) ± SD	Stress max (MPa) ± SD	Strain at break (%) ± SD
H-AGMA$_{20}$	0.3± 0.1	0.04± 0.01	0.01± 0.06
PLLA	88.52 ± 31.96	3.89 ± 0.49	215.78 ± 23.58
PLLA/H-AGMA$_{20}$	47.82 ± 17.89	2.2 ± 0.38	39.96 ± 9.03

[a)] All values are reported as the average of five measurements ± standard deviation (SD).

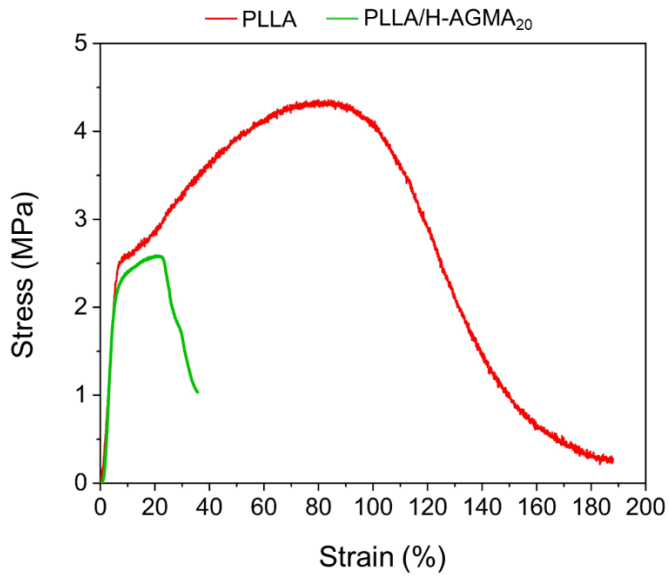

Figure 6.2.7. Representative stress-strain curves of PLLA/H-AGMA$_{20}$ (green line) and PLLA (red line).

SH-SY5Y viability, adhesion and differentiation

Traditionally, neurodegenerative research has relied on two-dimensional (2D) cell culture models. These models are convenient and widely used but they fail to replicate the complexity of *in vivo* environment. In contrast, biologically inspired scaffolds, such as hydrogel matrices, offer a more physiologically relevant alternative by mimicking the extracellular matrix and supporting neuronal behavior. These scaffolds enhance the differentiation of preneuronal cells into dopaminergic-like neurons (DLNs) and help regulate cell proliferation, an essential factor in neuroregeneration *(145,155)*. Since proliferation and differentiation are inversely related (with cell division preceding differentiation), balancing this interplay is critical for proper neuronal development *(156)*. Scaffolds that can modulate this relationship are therefore key to effective neuroregenerative strategies. Among promising materials, AGMA1-based hydrogels exhibit favorable biological properties but suffer from poor mechanical stability due to their softness. To address this, composite hydrogel systems, such as PLLA/H-AGMA$_{20}$, have been developed to provide both structural support and biochemical cues in three-dimensional (3D) culture systems. Initial analyses of SH-SY5Y preneuronal cells showed that while cell viability on PLLA/H-AGMA$_{20}$ was lower than on controls (tissue culture surface and PLLA alone) at day 1, it increased steadily over 14 days, confirming the composite's biocompatibility and support for cell adhesion and survival (Figures 6.2.8A-B). Over time, PLLA/H-AGMA$_{20}$ also promoted neuronal differentiation and moderated cell proliferation.

Fluorescence analysis (Figures 6.2.8C-D) revealed that GAP-43 expression, a marker of neuronal maturation, peaked in cells cultured on PLLA/H-AGMA$_{20}$ after 7 days and remained sustained until 14 days compared to controls. No GAP-43 expression was detected in cells on neat PLLA, emphasizing the critical role of the H-AGMA$_{20}$ in inducing neuronal differentiation. These results are consistent with previous findings showing strong adhesion and proliferation of primary brain cells on linear analogues of H-AGMA$_{20}$ *(7)*.

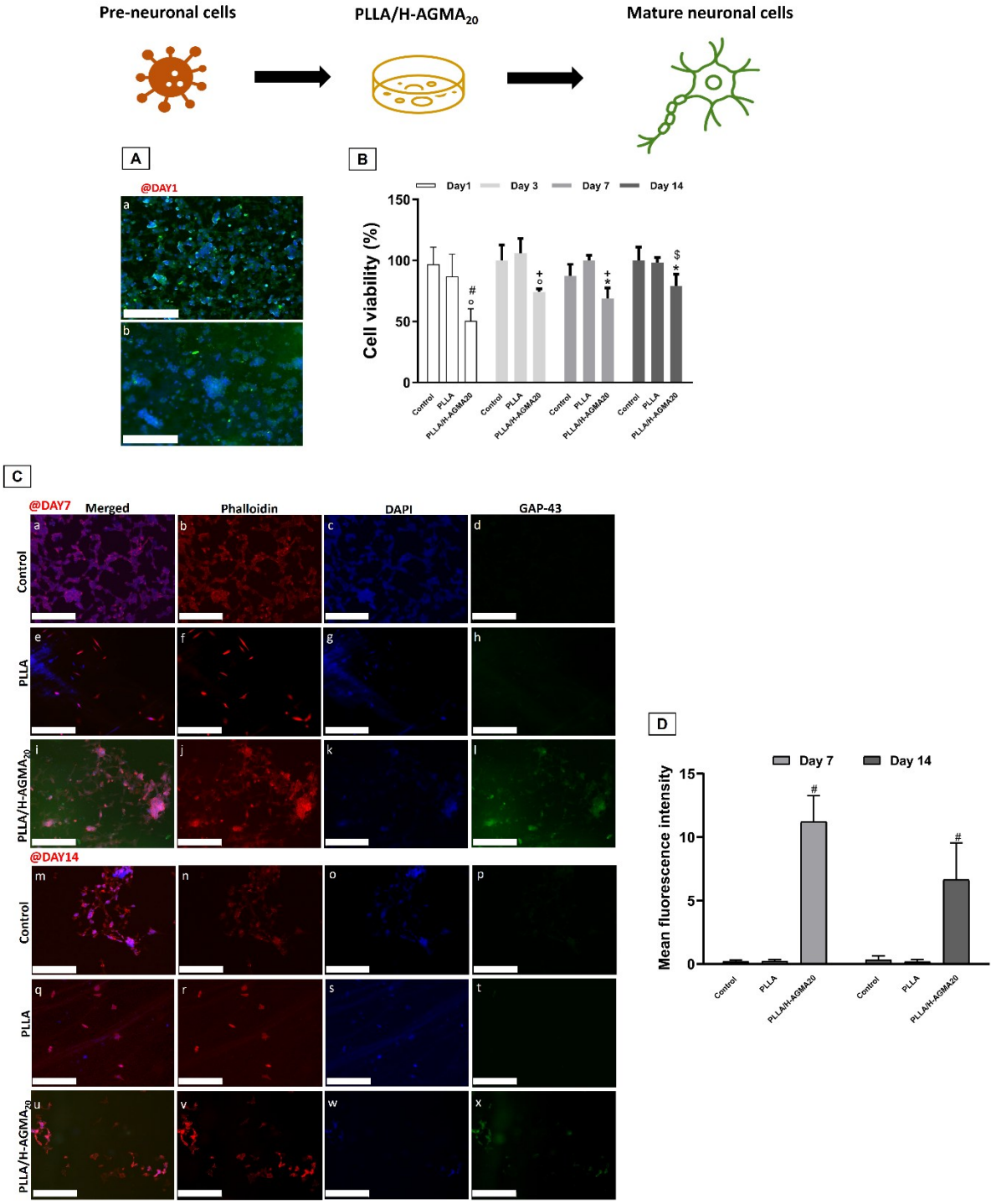

Figure 6.2.8. Effect of PLLA/H-AGMA$_{20}$ on SH-SY5Y cell adhesion, viability and differentiation. marker (GAP-43) Qualitative SH-SY5Y cell adhesion after 1 day of cell culture was tested through fluorescence analysis in the absence (a) and in the presence (b) of PLLA/H-AGMA$_{20}$ (merged images of FITC-Phalloidin for cytoskeleton in green and DAPI staining for nuclei in blue) (A). Cell viability was assessed using the AlamarBlue® assay (B). (*p≤0.05 and °p≤0.001 vs Control; $^{\$}$p 0,05, $^{+}$p 0,001 and $^{\#}$p 0,0001vs PLLA). Fluorescence analysis on cell differentiation was performed using the GAP-43 marker expression (C). (a,e,i,m,q,u= merged; b,f,j,n,r,v=cytoskeleton; c,g,k,o,s,w=nuclei; d,h,l,p,t,x= GAP-43. Magnification 10X, scale bar: 250 µm, $^{\#}$p≤0.0001 vs Controls). The fluorescence intensity was normalized to the number of cells per surface. Results are mean ± SD and the images are representative of 3 independent experiments (D).

SH-SY5Y cell response to MPP^+ stimulation

To assess the neuroprotective potential of PLLA/H-$AGMA_{20}$, SH-SY5Y cells were differentiated on the composite for 7 days and then exposed to the neurotoxin MPP^+ for 24 hours. Cell viability analysis showed that MPP^+ significantly reduced survival on control surfaces (tissue culture plate and neat PLLA), while no significant reduction was observed in cells cultured on PLLA/H-$AGMA_{20}$, indicating a protective effect (Figure 6.2.9A). MPP^+ is known to induce overexpression of Toll-like receptor 4 (TLR-4) in SH-SY5Y cells *(157,158)*. Consistent with this, MPP^+ exposure upregulated TLR-4 expression in control groups. However, PLLA/H-$AGMA_{20}$ inhibited both basal and MPP^+-induced TLR-4 expression after 7 days of culture and 24 hours of toxin exposure (Figure 6.2.9B), as further confirmed by image analysis (Figure 6.2.9C).

These findings suggest that PLLA/H-$AGMA_{20}$ not only preserves cell viability under neurotoxic conditions but also suppresses inflammatory signaling, supporting its promise as a neuroprotective scaffold for neurodegenerative disease models.

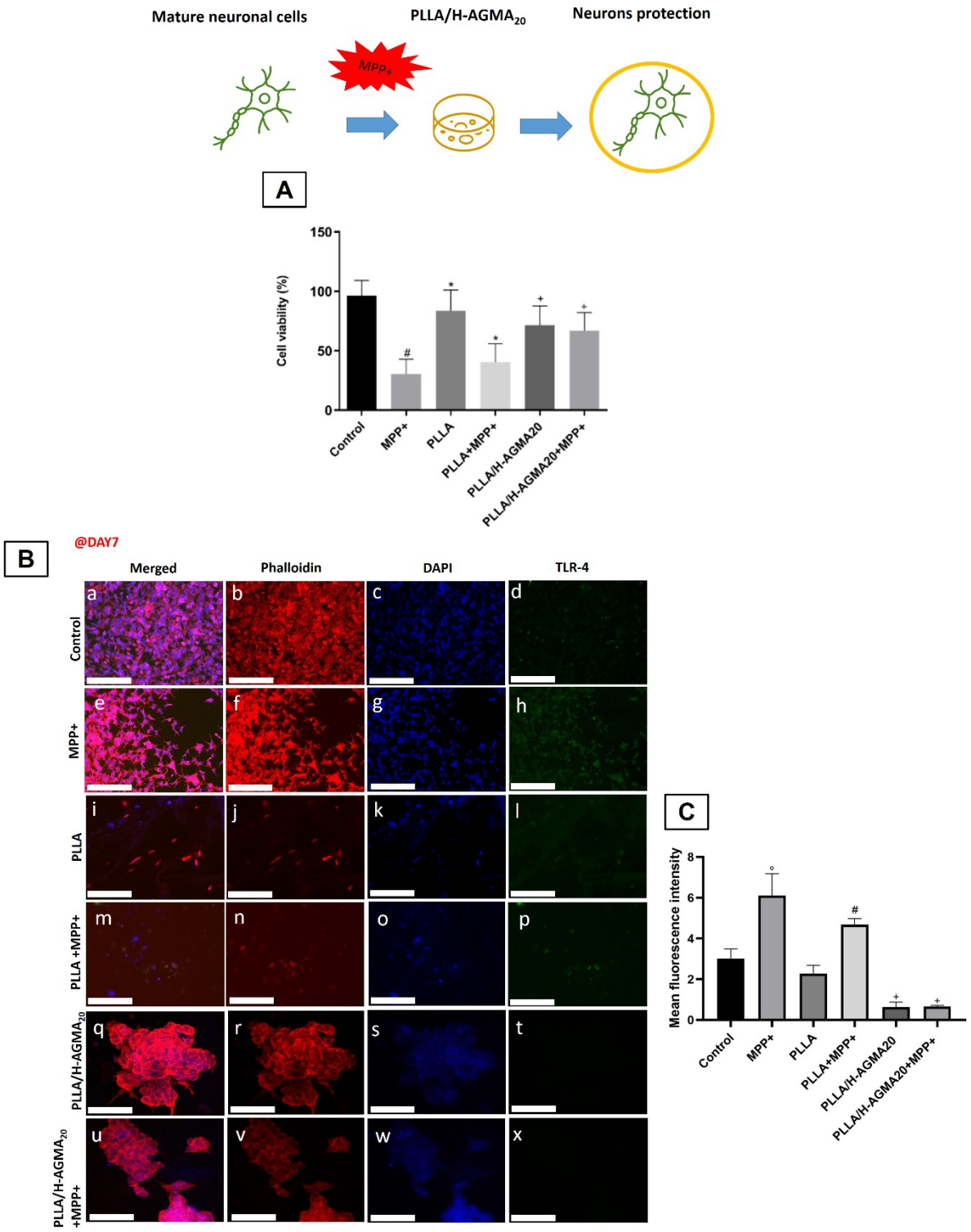

Figure 6.2.9. Effect of PLLA/H-AGMA$_{20}$ on *in vitro* MPP$^+$ stimulation of SH-SY5Y cells. Cell viability evaluated using the AlamarBlue® assay. (*p≤0.05 and $^{\#}$p≤0.0001 vs Control; $^{+}$p≤0.0001 vs MPP$^+$) (A). Fluorescence analysis on TLR-4 expression was performed after 7 days of cell culture and after 24 h MPP$^+$ exposure (B). (a,e,i,m,q,u=merged; b,f,j,n,r,v=cytoskeleton; c,g,k,o,s,w=nuclei; d,h,l,p,t,x=TLR-4. Magnification 10X, scale bar: 250 µm). °p≤0.001 vs Control; #p≤0.0001 vs PLLA and +p≤0.001 vs MPP$^+$. The fluorescence intensity was normalized to the number of cells per surface. Results are mean ± SD and the images are representative of 3 independent experiments (C).

Effect of PLLA/H-AGMA$_{20}$ on the Inflammatory Response

LPS is known to selectively activate the TLR-4 pathway in microglia, triggering the release of inflammatory mediators. Eumelanin-functionalized PLLA has previously been shown to downregulate this pathway, even under non-stimulated conditions *(148)*. In the CNS, elevated inflammation leads to increased production of proinflammatory cytokines like IL-1β and nitric oxide (NO), key drivers of neuroinflammation and oxidative stress, ultimately contributing to neuronal damage. To evaluate the anti-inflammatory properties of PLLA/H-AGMA$_{20}$, we tested its effects on MPP^+-stimulated SH-SY5Y cells and LPS-stimulated RAW 264.7 macrophages. PLLA alone was not included due to its limited ability to regulate inflammation *(148)*. In SH-SY5Y cells, MPP^+ significantly increased nitrite and IL-1β levels. However, these markers were significantly reduced when cells were cultured on PLLA/H-AGMA$_{20}$ (Figures 6.2.10a-b), indicating a strong anti-inflammatory effect. Interestingly, MPP^+ alone induced an anti-inflammatory response, as evidenced by IL-10 production, with no significant differences observed in the presence of PLLA/H-AGMA$_{20}$ (Figure 6.2.10c). A more pronounced effect was seen in RAW 264.7 macrophages. PLLA/H-AGMA$_{20}$ supported cell viability after 7 days of culture, even following 24 hours of LPS exposure (Figure 6.2.10d). Importantly, the composite significantly lowered LPS-induced nitrite and IL-1β levels (Figures 6.2.10e-f), while restoring IL-10 production, which was otherwise suppressed by LPS (Figure 6.2.10g).

These results highlight the dual functionality of PLLA/H-AGMA$_{20}$ as a neuroprotective and anti-inflammatory material, promoting cell survival and effectively modulating inflammatory responses.

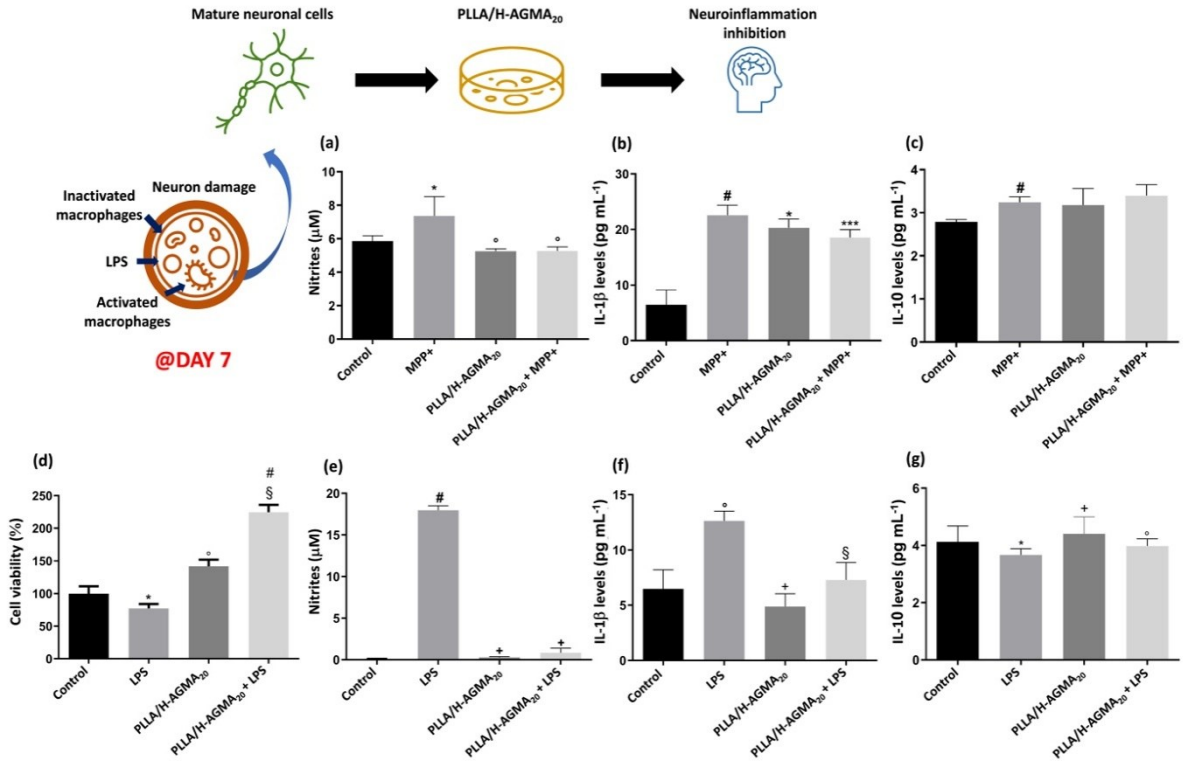

Figure 6.2.10. Effect of PLLA/H-AGMA$_{20}$ on SH-SY5Y and RAW 264.7 *in vitro* inflammatory response. Nitrite production after the exposure of SH-SY5Y cells to MPP$^+$ and of RAW 264.7 cells to LPS for 24 h after 7 days cell culture (a, e). (*p≤0.05 and $^{\#}$p≤0.0001 vs Control; °p≤0.001 vs MPP$^+$ and $^+$p≤0.0001 vs LPS).

IL-1β levels in SH-SY5Y cells and RAW 264.7 cells exposed to MPP$^+$ and LPS, respectively, for 24 h (b,f). (*p≤0.05 and ***p≤0.0001 vs MPP$^+$; §p≤0.001 and +p≤0.0001 vs LPS; °p≤0.001 and $^{\#}$p≤0.0001 vs Control).

RAW 264.7 cell viability after 24 h LPS exposure was evaluated using the AlamarBlue® assay (d). (*p≤0.05; °p≤0.001 vs Control; §p≤0.001 vs PLLA/H-AGMA$_{20}$ and $^{\#}$p≤0.0001 vs LPS).

IL-10 levels in SH-SY5Y cells and RAW 264.7 cells exposed to MPP$^+$ and LPS, respectively, for 24 h (c,g). ($^{\#}$p≤0.0001 vs Control; °p≤0.001 and $^+$p≤0.0001 vs LPS). Results are mean ± SD of 3 independent experiments.

Mechanism of action of the PLLA/H-AGMA$_{20}$ composite hydrogel

To further elucidate the mechanisms underlying the neuroprotective and neuroregenerative properties of PLLA/H-AGMA$_{20}$, the molecular pathways modulated by the composite hydrogel were investigated. In particular, inflammatory signaling cascades such as Caspase-1 and the neurotrophic factor β-nerve growth factor (β-NGF) were analyzed through fluorescence imaging. Previous studies have identified the caspase family as a key mediator of neuronal apoptosis, thus playing a pivotal role in the progression of neurodegeneration *(159)*. Among them, Caspase-1, a component of the NLRP3 (NOD-like receptor pyrin domain-containing 3)

inflammasome complex, contributes significantly to neuroinflammation by activating microglia. Moreover, it is well established that MPP^+ exposure in SH-SY5Y cells induces Caspase-1 activation, leading to Caspase-7 cleavage, nuclear translocation of poly(ADP-ribose) polymerase 1 (PARP1), and increased release of apoptosis-inducing factor (AIF). In the present study, PLLA/H-$AGMA_{20}$ markedly suppressed Caspase-1 expression in SH-SY5Y cells following MPP^+ stimulation after 7 days of cell–material interaction (Figure 6.2.11a). This downregulation was associated with protection against apoptosis via the Caspase-7/PARP1/AIF pathway (Figure 6.2.11b), confirming the neuroprotective capacity of PLLA/H-$AGMA_{20}$ against MPP^+-induced cytotoxicity. Importantly, PLLA alone failed to attenuate MPP^+-induced Caspase-1 expression, indicating that the hydrogel component predominantly mediates this protective response. These qualitative observations were corroborated by image analysis (Figure 6.2.11c). In addition, PLLA/H-$AGMA_{20}$ preserved high levels of β-NGF expression in SHSY5Y cells, a factor essential for neuronal survival and differentiation *(160)*. Collectively, these findings demonstrate that H-$AGMA_{20}$ not only enhances cell adhesion and differentiation but also modulates inflammatory signaling pathways such as the Caspase-1 cascade and promotes β-NGF production. Thus, the PLLA/H-$AGMA_{20}$ composite not only maintains structural stability over time but also fosters a regenerative and neuroprotective microenvironment, offering a significant advantage over conventional single-component biomaterials. This dual functionality highlights PLLA/H-$AGMA_{20}$ as a promising candidate for advanced neuroregenerative applications.

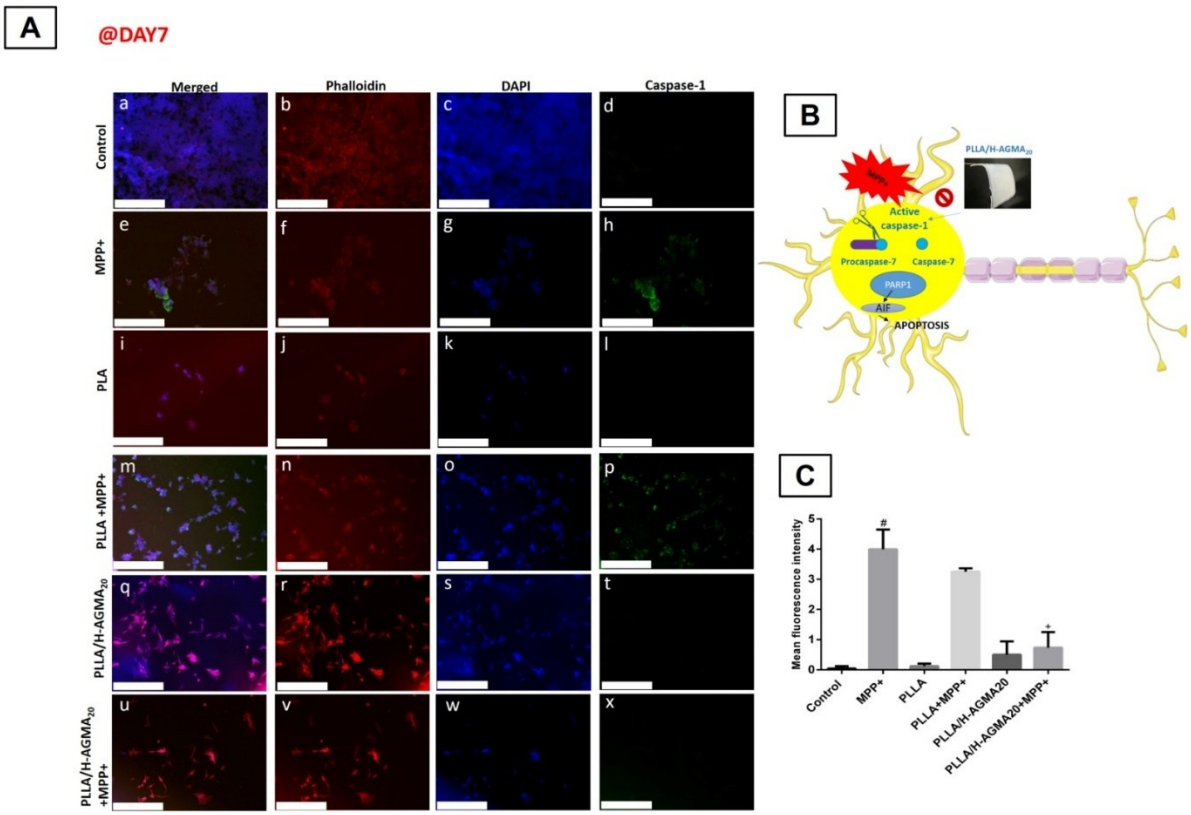

Figure 6.2.11. Fluorescence analysis of Caspase-1 expression was conducted on day 7 of cell culture following 24 h exposure to MPP^+. Cells were fixed and immunostained using specific antibodies: anti-Caspase-1 (green), anti-Phalloidin-ATTO 594 for F-actin (red), and DAPI for nuclei (blue). Panels represent: merged images (a,e,i,m,q,u), cytoskeleton (b,f,j,n,r,v), nuclei (c,g,k,o,s,w), and Caspase-1 (d,h,l,p,t,x). Magnification: 10×; scale bar: 250 μm. Data are presented as mean ± SD from three independent experiments (A).

Schematic illustration of the inhibitory effect of PLLA/H-$AGMA_{20}$ on the Caspase-1 signaling pathway. MPP^+ activates Caspase-1, leading to the cleavage of pro-Caspase-7 into active Caspase-7, which promotes nuclear translocation of PARP1 and cytoplasmic release of AIF, resulting in neuronal apoptosis (B). Image quantification of Caspase-1 expression is shown (#p ≤ 0.0001 vs Control; +p ≤ 0.0001 vs PLLA+MPP^+). Fluorescence intensity was normalized to the number of cells per area. Data are expressed as mean ± SD and are representative of three independent experiments (C).

6.3. Experimental part

The synthesis of the soluble α,ω-bisacrylamide-terminated precursor, namely $AGMA_{20}$, is reported in Chapter 2.

Synthesis of the H-$AGMA_{20}$ hydrogel

H-$AGMA_{20}$ hydrogel sheets were prepared using a mold composed of two 2 mm thick silanized glass plates, separated by a 0.5 mm silicone spacer defining an internal volume of 25 mm ×

50 mm × 0.5 mm. Prior to use, the glass plates were silanized with methyltrichlorosilane. A 0.5 mL $AGMA_{20}$ solution was injected into the mold and polymerized by UV irradiation (30 min per side) using a 250 W HG200 Ultra UV lamp (Jelosil S.r.l., Milan, Italy; 315-400 nm) at 15 cm distance. The resulting hydrogel sheets had an average thickness of 0.42 ± 0.02 mm, measured with a Dino-Lite Edge digital microscope (Dino-Lite Europe, Almere, The Netherlands) and DinoXcope software.

Electrospinning of PLLA fibers

PLLA (Ingeo™ 4032D; 0.7 mol% L-isomer, molar mass = 2.1×10^5 g mol^{-1}, PDI = 1.7) was obtained from NatureWorks LLC (Minneapolis, MN, USA), and all solvents used were of reagent grade. A 10% w/v PLLA solution in chloroform/dimethylformamide (90:10) was electrospun using a NF103 setup (MECC Co., Ltd., Fukuoka, Japan) with a 0.55 mm inner diameter needle and a flat plate collector. Electrospinning was performed at room temperature and 30% relative humidity, with a flow rate of 3 mL h^{-1}, an applied voltage of 30 kV, and a 25 cm tip-to-collector distance. Fibers were collected for at least 2 hours, producing mats approximately 100 μm thick, as measured by a digital micrometer.

Functionalization of the PLLA surface

Ethylenediamine (EDA, 10 mL) was placed in an open 100 mL beaker, and a 100 μm thick PLLA mat was suspended 50 mm above the liquid on a metal grid, exposing each side to EDA vapors for 1 minute. The mat was then rinsed with ultrapure water to remove residual EDA. To confirm surface amination, a PLLA strip (12 mg) was treated with 0.4% w/w aqueous ninhydrin solution and incubated at 55 °C for 1 hour 29. Ninhydrin reacts with surface amines, forming a purple chromophore (Ruhemann's purple), allowing qualitative visualization. Colorimetric analysis was performed using a YS3010 Handheld Spectrophotometer (3nh Global, Guangzhou, China) and SQCX software, following the ISO11664 standard. CIELAB parameters, L^* (brightness), a^* (green-red), b^* (blue-yellow), and color change ΔE^* (see Equation 5.3.2, Chapter 5), were assessed.

Synthesis of the PLLA/H-$AGMA_{20}$ composite hydrogel

PLLA/H-$AGMA_{20}$ composites were prepared using the same glass mold as for the H-$AGMA_{20}$ hydrogels. Initially, 0.3 mL of $AGMA_{20}$ solution was injected into the open mold to fill the frame. A functionalized PLLA mat (25 mm × 50 mm × 0.1 mm; 24 mg) was then placed inside and gently pressed to promote impregnation. An additional 0.3 mL of $AGMA_{20}$ solution was

added, and the mold was sealed with a second glass plate. UV curing was carried out as described for plain H-AGMA$_{20}$. After polymerization, the composite was carefully removed and soaked in water for 2 hours. The final hydrogels had an average thickness of 0.49 ± 0.02 mm, measured with a digital microscope, and were stored in fresh water. The synthesis procedure is illustrated in Figure 6.3.1.

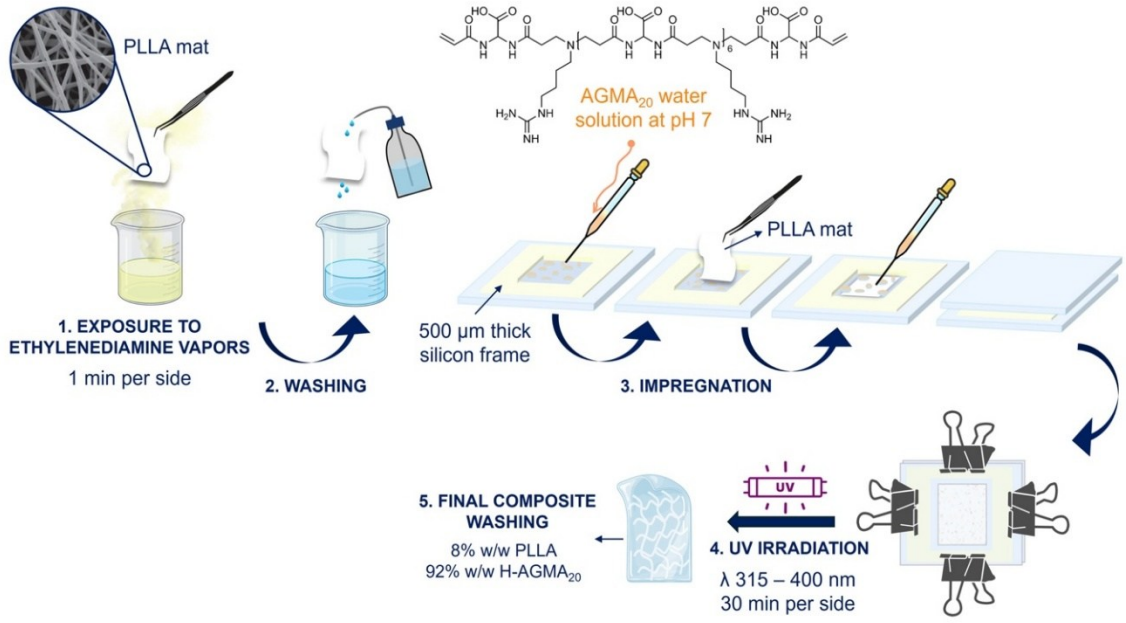

Figure 6.3.1. PLLA/H-AGMA$_{20}$ preparation steps: exposure of PLLA mat to EDA vapors (1); washing with water (2); impregnation of PLLA mat with a 50% AGMA$_{20}$ water solution (3); UV irradiation (4); final composite washing (5).

Characterization techniques

FT-IR/ATR spectroscopy: unfunctionalized and EDA-functionalized PLLA mats, both before and after washing, were characterized by FT-IR/ATR spectroscopy. Spectra were collected at room temperature using a Jasco FT-IR/FIR spectrophotometer (Milan, Italy) equipped with a ZnSe crystal, over the 4000-600 cm^{-1} range, with 256 scans and 4 cm^{-1} resolution.

Scanning Electron Microscopy (SEM): the morphology of PLLA mats and PLLA/H-AGMA$_{20}$ composites was examined by field-emission scanning electron microscopy (FE-SEM) using a ZEISS-SIGMA 300 microscope, operated at 5 kV and 10.8 mm working distance. Samples (5 mm × 5 mm), coated with a 4 nm platinum layer, were imaged on both the surface and cross-section, the latter obtained via brittle fracture.

Tensile tests

Tensile tests were conducted at room temperature to evaluate the mechanical properties of

PLLA/H-AGMA$_{20}$ composite hydrogels and PLLA mats. Measurements were performed using an Instron 5564 testing machine (Turin, Italy) with a 100 N load cell and a crosshead speed of 5 mm min^{-1}. Five hydrated specimens were tested immediately after removal from water. Samples, cut into 50 mm-wide strips, had a gauge length of 10 mm, and thickness was measured using a digital micrometer. Mechanical behavior was reported in terms of nominal stress (force divided by initial cross-sectional area) and nominal strain (change in grip separation relative to initial length).

In vitro biological tests: cell culture

To evaluate the neuroprotective and anti-inflammatory properties of PLLA/H-AGMA$_{20}$, two cell lines were used: SH-SY5Y (a human neuroblastoma line derived from a pediatric metastatic tumor) and RAW 264.7 (a mouse macrophage line), both obtained from Sigma Aldrich (Milan, Italy). Cells were cultured in Dulbecco's Modified Eagle Medium (DMEM) supplemented with 10% fetal bovine serum (GIBCO), 2 mM L-glutamine, and antibiotics (100 µg mL^{-1} streptomycin and 100 U mL^{-1} penicillin, Sigma Chem. Co). PLLA/H-AGMA$_{20}$ substrates were sterilized under UV light for 2 hours and pre-incubated in antibiotic solution to ensure sterility. Cells were seeded onto the composites and maintained for up to 14 days, with medium changes every 3 days. Cells cultured on standard flat plates served as controls. Neuronal responses to PLLA fibers alone were also considered, based on findings from prior studies *(145,147,148)*.

SH-SY5Y cell viability and adhesion

SH-SY5Y cells were seeded onto PLLA/H-AGMA$_{20}$ composites at a density of 1.5 × 10^4 cells/well in a 48-well plate and incubated at 37 °C with 5% CO_2. Cell viability was assessed at 1, 3, 7, and 14 days using the AlamarBlue® assay (Bio-Rad, Italy), which measures metabolic activity as an indicator of cell vitality and proliferation. At each time point, culture medium was replaced with a 10% (v/v) AlamarBlue® solution, followed by 3 hours of incubation at 37 °C. The reduction of resazurin to resorufin by metabolically active cells was quantified via absorbance measurements at 570 and 600 nm using a UV-Visible spectrophotometer Victor X3 plate reader (Perkin Elmer, Milan, Italy) *(161)*. Cell adhesion on PLLA/H-AGMA$_{20}$ was also evaluated qualitatively via fluorescence imaging. SH-SY5Y cells (2 × 10^4 cells/well) were seeded in 24-well plates onto the composites or flat control surfaces. After 24 hours, cells were fixed in 4% paraformaldehyde (PFA, Sigma-Aldrich) at 4 °C for 24 hours, washed with PBS, and permeabilized using 0.1% Triton X-100 in 0.1% BSA for 1 hour. Actin filaments were stained with FITC-conjugated phalloidin (Thermo Fisher Scientific), samples were washed, and

later nuclei were counterstained with 10 μg mL^{-1} 4′,6-diamidino-2-phenylindole (DAPI) (Molecular Probes®, Thermo Fisher Scientific). After washing, fluorescence images were acquired using a JuLI™ Stage microscope (NanoEntek) at 10x magnification.

SH-SY5Y cells differentiation

Neuronal differentiation of SH-SY5Y cells was assessed via immunofluorescence using FITC-conjugated GAP-43 (Growth Associated Protein 43) antibody (Thermo Fisher Scientific), a marker of neuronal maturation. Cells (2×10^4 cells/well) were seeded on PLLA and PLLA/H-$AGMA_{20}$ substrates in 24-well plates and cultured in basal medium for 7 and 14 days. Fixation and permeabilization were performed as previously described for the cell adhesion assay. Following this, samples were incubated overnight at 4 °C with FITC-conjugated GAP-43 antibody (1:100 dilution). After three PBS washes, the cytoskeleton was stained with Phalloidin-ATTO 594 (1:200, Sigma Aldrich) for 1 hour. Nuclei were then counterstained with DAPI (10 μg mL^{-1}) for 10 minutes at 37 °C. After final PBS washes, fluorescence images were acquired at 10x magnification using a JuLI™ Stage (NanoEntek) and a Leica TCS SP8 confocal microscope. Fluorescence intensity was quantified using ImageJ software (v1.44, Java 1.6, 64-bit) and it was normalized to the number of cells per surface by subtracting the background intensity from the cell intensity.

SH-SY5Y-response to MPP^+ stimulation

To assess the neuroprotective effects of PLLA/H-$AGMA_{20}$ against MPP^+-induced toxicity, SH-SY5Y cells (1.5×10^4 cells/well) were cultured on the composite in 48-well plates for 7 days. Cells were then exposed to 1.5 mM MPP^+ for 24 hours to induce neurotoxic damage. Cell viability was evaluated using the AlamarBlue® assay, as previously described. MPP^+ is known to induce dopaminergic neuron death, with Toll-like receptor 4 (TLR-4) signaling recognized as a key pathway involved in the inflammatory response triggered by MPP^+ exposure *(162)*. To investigate the anti-inflammatory potential of PLLA/H-$AGMA_{20}$, TLR-4 expression was analyzed by immunofluorescence. SH-SY5Y cells (2×10^4 cells/well) were fixed and permeabilized, then incubated overnight at 4 °C with a FITC-conjugated rabbit anti-TLR-4 polyclonal antibody (1:200, Thermo Fisher Scientific). The cytoskeleton was stained with Phalloidin-ATTO 594 (1:200, Sigma Aldrich) for 1 hour, and nuclei were counterstained with DAPI (10 μg mL^{-1}) for 10 minutes at 37 °C. Fluorescence imaging was performed using a Leica TCS SP8 confocal microscope at 10x magnification, and TLR-4 expression was quantified using ImageJ, following the same protocol used for GAP-43 analysis in cell differentiation

assay.

SH-SY5Y and RAW 264.7 inflammatory response

RAW 264.7 cell viability was assessed after 7 days of culture on PLLA/H-AGMA$_{20}$, followed by 24 hours of stimulation with the inflammatory agent lipopolysaccharide (LPS, 10 μg mL^{-1}), using the AlamarBlue® assay (Bio-Rad, Italy). To evaluate inflammatory responses, both SH-SY5Y and RAW 264.7 cells were seeded onto PLLA/H-AGMA$_{20}$ at a density of 5 × 10^4 cells/well in 12-well plates and cultured for 7 days. Cells were then exposed for 24 hours to MPP$^+$ (1.5 mM) or LPS (10 μg mL^{-1}), respectively, in the presence or absence of the composite. After stimulation, cell supernatants were collected for analysis. Nitrite production, an indicator of nitric oxide release, was measured by mixing 100 μL of supernatant with 100 μL of Griess reagent (Sigma Aldrich, Milan, Italy) in a 96-well plate. After 1 hour of incubation at room temperature, absorbance was read at 550 nm using a fluorescent microplate reader VICTOR X3 (PerkinElmer, Milan, Italy). Additionally, IL-1β and IL-10 cytokine levels were quantified using commercial ELISA kits (Elabioscience), following the manufacturer's instructions.

Inhibition of neuroinflammatory pathways in SH-SY5Y cells

The inhibition of inflammatory signaling in SH-SY5Y cells was evaluated by analyzing specific pathways, including the Caspase-1 cascade and the expression of the neurotrophic factor β-nerve growth factor (β-NGF), through fluorescence imaging. For this purpose, SH-SY5Y cells (2 × 10^4 cells/well) were seeded on PLLA/H-AGMA$_{20}$ composites or PLLA alone in 48-well plates and cultured for 7 days. After incubation, cells with or without stimulation by 1.5 mM MPP$^+$ for 24 h, were fixed and permeabilized as previously described. Subsequently, cells were incubated overnight at 4 °C with rabbit polyclonal anti-Caspase-1 antibody (Proteintech, 1:50) or rabbit polyclonal anti-β-NGF antibody (Arigo Biolaboratories Corp., 1:500). This was followed by a 1 h incubation at room temperature with FITC-conjugated goat anti-rabbit IgG secondary antibody (1:80, Sigma Aldrich, Milan, Italy). The cytoskeleton was stained with Phalloidin-ATTO 594 (1:200, Sigma Aldrich) for 1 h, and nuclei were counterstained with DAPI (10 μg mL^{-1}) for 10 min at 37 °C. After staining, samples were washed three times with PBS. Fluorescence images were acquired using a JuLI™ Stage microscope (NanoEntek) at 10x magnification, and image analysis was performed with ImageJ software (version 1.44, Java 1.6, 64-bit), as previously described.

Statistical analysis

Statistical analyses were performed using GraphPad Prism®, version 8.00 (GraphPad Software, La Jolla, California, USA). Data were analyzed using a Student's *t-test*, two-way ANOVA and Sidak's multiple comparisons test as appropriate. The results are expressed as mean ± standard deviation (SD). Values of $p < 0.05$ were considered significant.

6.4. Conclusions

In this study, a 490 µm-thick PLLA/H-AGMA$_{20}$ composite hydrogel was fabricated combining a PLLA electrospun mat with a cell-adhesive polyamidoamine hydrogel H-AGMA$_{20}$. The PLLA mat was chemically modified via aminolysis by EDA vapors to enable covalent grafting of the hydrogel onto the PLLA fibers, resulting in a stable composite structure.

The resulting composite hydrogel retained the water absorption capacity of native H-AGMA$_{20}$, remaining soft and flexible when hydrated but with improved mechanical toughness. Importantly, PLLA/H-AGMA$_{20}$ supported SH-SY5Y neuronal cell growth and maturation without added differentiation factors. It also conferred neuroprotection against MPP^+-induced toxicity and reduced inflammation in both SH-SY5Y and RAW 264.7 macrophage cell lines.

Together, these findings highlight PLLA/H-AGMA$_{20}$ as a promising scaffold for *in vitro* neurodegenerative disease models, offering both neuroprotective and anti-inflammatory benefits.

7. ASSESSMENT OF ACCELERATED AGING ON PAA SOLUTIONS AND SOLID FILMS

This chapter describes the project carried out during the research period at the photochemistry department of the Université Clermont Auvergne. The study was focused on the preliminary assessment of the photodegradation mechanism of M-GLY both in solution and in the solid state under different experimental conditions, including UVA and UVC irradiation, as well as in the presence of hydrogen peroxide as an oxidative agent.

7.1. Introduction

One major problem associated with the applications of polymers is their instability to weathering *(163–165)*. The behavior of these polymers under use conditions is generally predicted by artificial ageing, induced by devices that provide an accelerated simulation of the various environmental stresses, such as light, oxygen, water, pollution, and mechanical stresses. The ageing methods are often standardized and the property deterioration is followed by several analytical techniques to characterize the degradation of the polymer matrix. Since most of the degradation results from chemical changes in the polymer, the reliability of the observed phenomena has to be controlled at the molecular level through the recognition of the chemical reactions of the macromolecules *(166,167)*. Usually, the most important route involves an oxidative mechanism whose products are formed in concentrations high enough to be observed by vibrational spectroscopy.

7.2. Results and discussion

M-GLY films were prepared on CaF_2 support by drop-casting but it was challenging to obtain homogeneous and continuous films probably because of polymer's average molecular weight. M-GLY films were subjected to combined UVA/UVB exposure for 400 h in a SEPAP 12/24 unit as reported in Section 7.3. The FT-IR spectrum of the M-GLY film was recorded every 24 h and spectra at different times are reported in Figure 7.2.1. After 17 days of irradiation, no additional peaks or marked differences were observed compared to the initial spectrum, suggesting negligible photodegradation under the applied conditions. A very weak band appeared at around 1720 cm^{-1} after 12 days (see Figure 7.2.1c), which can likely be attributed to carbonyl-containing oxidation products, such as carboxylic acids. Overall, these results confirm that M-GLY is photostable under UVA/UVB irradiation.

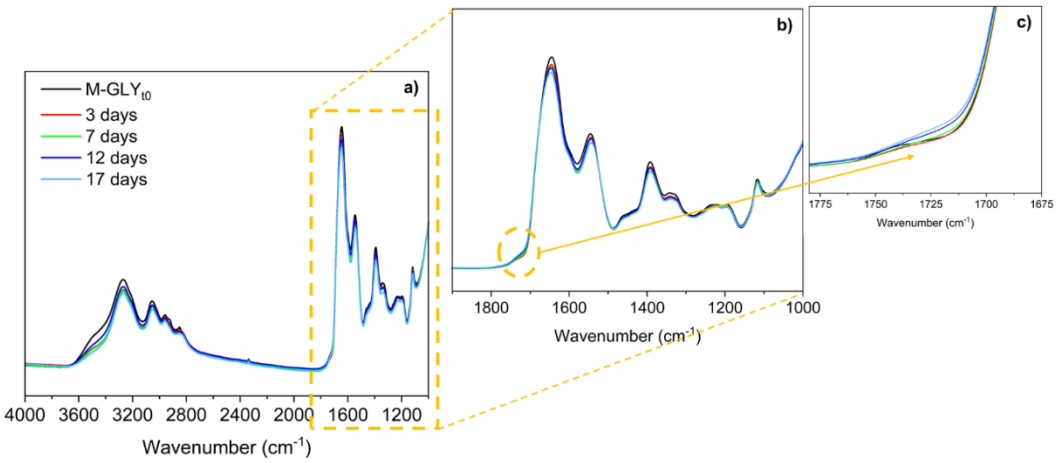

Figure 7.2.1. FT-IR spectra of M-GLY films before and after photoaging under UVA/UVB irradiation.

M-GLY films were subjected also to 254 nm irradiation for 300 h in a SEPAP 253 unit as reported in Section 7.3. These irradiation conditions do not mimic real environmental exposure but can provide valuable insights into the degradation mechanism. The FT-IR spectrum of the M-GLY film was recorded every 24 h and spectra at different times are reported in Figure 7.2.2. Up to 7 days of irradiation, the FT-IR spectrum was very similar to that at time zero, with only the appearance of a weak new band at 1590 cm^{-1}. After 13 days of irradiation, the spectrum showed a marked change, with a well-defined new peak at 1590 cm^{-1} that can be reasonably attributed to photooxidation products. To confirm this, the film was treated with SF_4 vapors to perform a derivatization reaction (Figure 7.2.2c-d) according to the procedure reported in Section 7.3. The result expected from derivatization reactions is a simplification in the interpretation of the infrared spectrum, resulting from the disappearance of specific bands and the appearance of the absorption bands of the derived products. SF_4 derivatization is very informative, and it implies the conversion of carboxyl acids to acyl fluorides with an important shift between their corresponding carbonyl bands (C=O stretching vibration). Since native M-GLY is characterized by the carboxylic acid group of glycine, it was essential to analyze its spectrum after SF_4 treatment (Figure 7.2.2d) in order to clearly distinguish the band corresponding to the newly formed oxidation product.

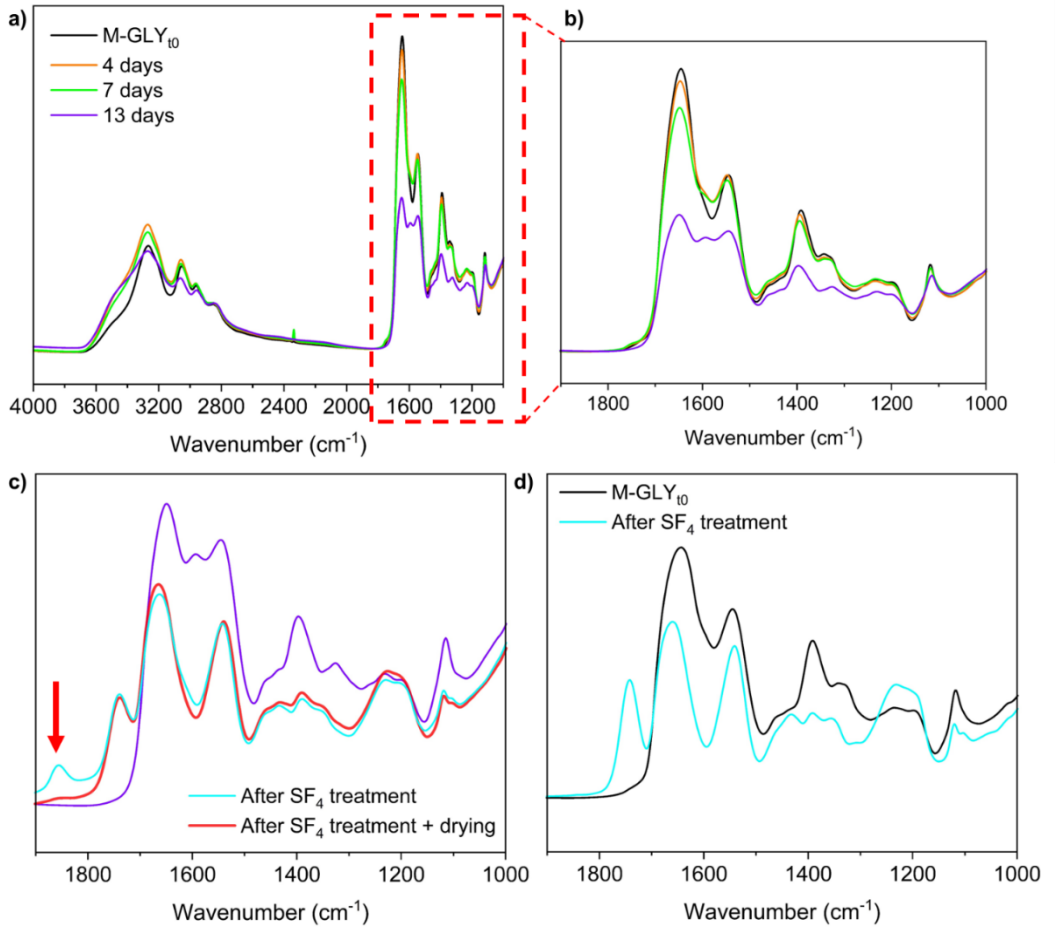

Figure 7.2.2. FT-IR spectra of M-GLY films before and after photoaging under UVC irradiation (a,b). FT-IR spectra of 13 day-photoaged M-GLY before and after SF_4 treatment (c). Native M-GLY before and after SF_4 treatment (d).

Aqueous solutions of M-GLY (4 g L^{-1}) were subjected to different irradiation conditions as reported in Section 7.3 and analyzed by SEC that revealed distinct degradation behaviors (Figure 7.2.3).

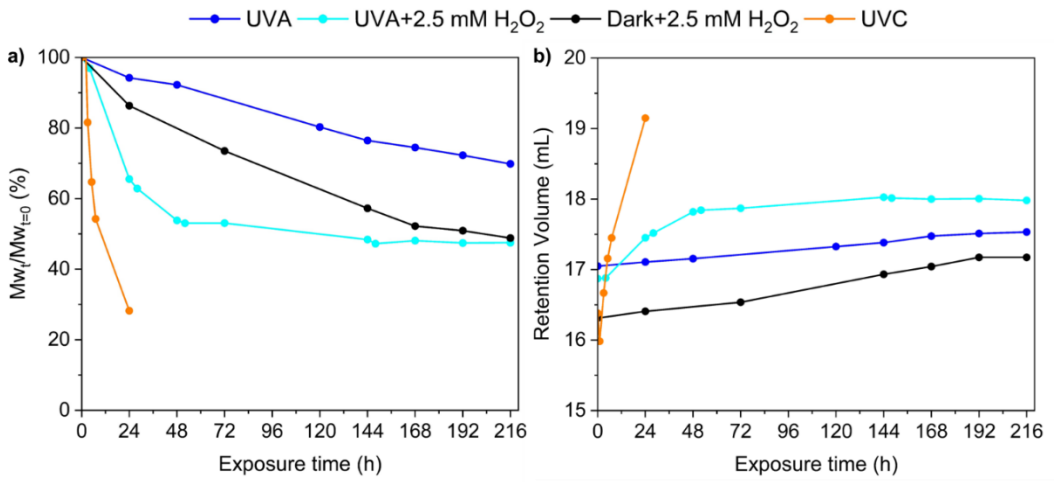

Figure 7.2.3. SEC analysis during time of M-GLY solutions irradiated in different conditions.

Under UVC irradiation, photodegradation was particularly pronounced: within 24 hours the molecular weight of the polymer decreased by nearly 70%, reaching the detection limit of the SEC column (Figure 7.2.3 orange line). As confirmation of the degradation, it was observed that the solution turned yellow during irradiation. By contrast, UVA irradiation alone induced only a slow degradation process (Figure 7.2.3 blue line), with less than a 20% reduction in the molecular weight even after 9 days, thereby confirming the intrinsic photostability of M-GLY. The addition of 2.5 mM H_2O_2 significantly altered this trend. When irradiated with UVA, the M-GLY/H_2O_2 solution exhibited a much faster degradation rate, especially during the first 48 hours, after which the process reached a plateau. Interestingly, even in the absence of irradiation, the M-GLY solution containing 2.5 mM H_2O_2 underwent a marked degradation compared to the UVA-irradiated solution without oxidant, highlighting the strong contribution of the oxidizing agent to the overall degradation pathway (Figure 7.2.3 cyan and black lines). The behavior of the M-GLY solutions containing H_2O_2, whether irradiated or kept in the dark, is closely correlated with the amount of H_2O_2 still present in solution at a given time. In the case of the solution irradiated under UVA, the degradation profile showed a rapid decrease in the average molecular weight during the first 48 hours, followed by a plateau. This can be explained by the spectrofluorimetric analysis of the aliquots at different irradiation times, performed according to the procedure reported in Section 7.3 (see Figure 7.2.4b,c). Fluorescence measures revealed that after 48 hours no detectable H_2O_2 remained in solution (Figure 7.2.4a,b). Since the oxidant was completely consumed within this time frame, the degradation process significantly slowed down, confirming the central role of H_2O_2 in accelerating the photodegradation mechanism. In the case of the M-GLY solution with H_2O_2 kept in the dark, the degradation was less rapid. Fluorescence analysis revealed that even after 9 days approximately 60% of the initial H_2O_2 was still present in solution (Figure 7.2.4a,c), indicating a reduced consumption of the oxidant and a correspondingly slower degradation pathway compared to the irradiated samples.

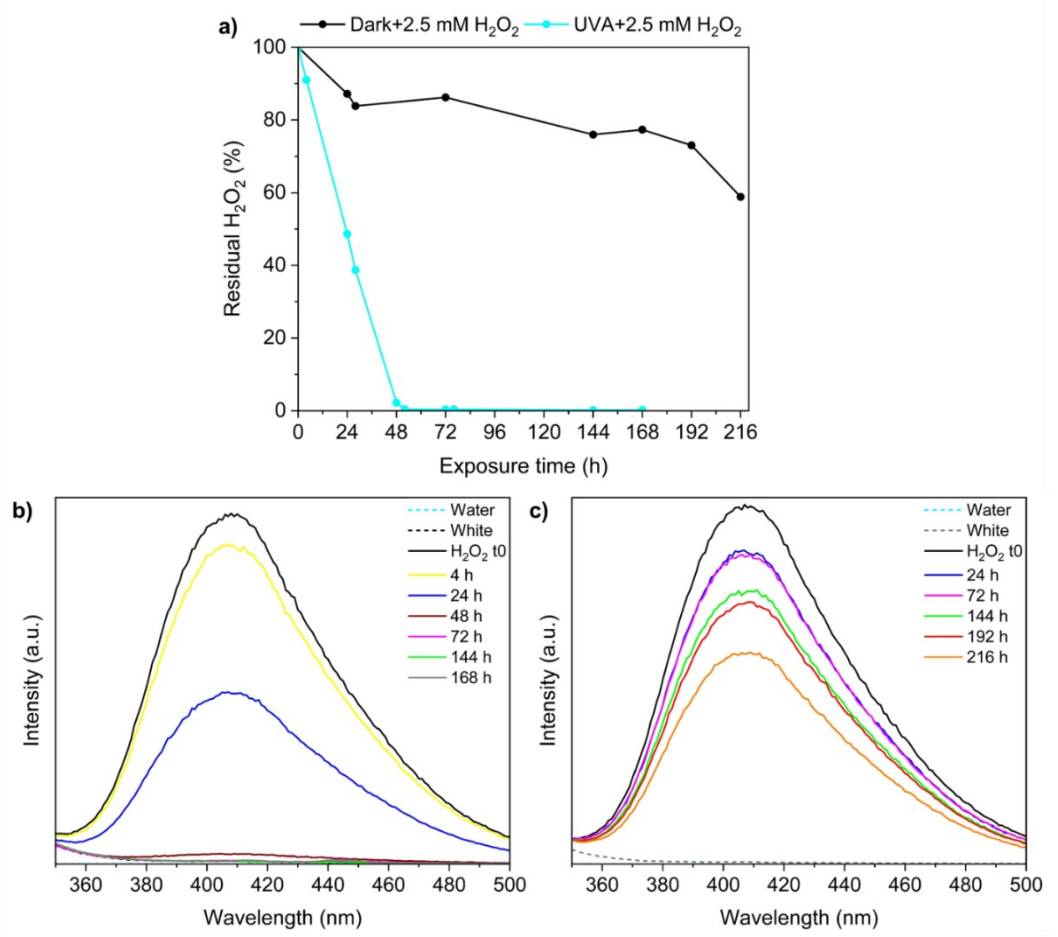

Figure 7.2.4. Spectrofluorimetric analysis at different time points of M-GLY solutions with 2.5 mM H_2O_2 UVA-irradiated (b) and in the dark (c).

7.3. Experimental part

M-GLY was synthesized and characterized following the procedures reported in Chapter 2. The product was purified by ultrafiltration using membranes with a 3000 Da molecular weight cut-off to remove low molecular weight oligomers and retrieved by freeze-drying.

Preparation of samples for photoaging experiments

Photoaging of M-GLY was assessed both on solid films and on aqueous solutions.

Films were prepared on CaF_2 supports by drop-casting 1 mg mL^{-1} M-GLY aqueous solution at pH 7. The samples were dried overnight under nitrogen atmosphere and a second deposition was performed to increase the thickness of the film.

For liquid-phase irradiation experiments, a 4 g L^{-1} M-GLY solution was prepared in ultrapure water and filtered through a 0.45 µm membrane. To evaluate the effect of an oxidative agent, 2.5 mM H_2O_2 was added by diluting a 10 M stock solution.

Accelerated photoaging tests

Solid M-GLY films on CaF_2 were mounted on custom-made holders designed to fix them to the rotating support in the exposure chamber and to allow their infrared analysis without removing them from the holders. M-GLY films were subjected to two irradiation conditions. Combined UVA/UVB exposure was carried out for 400 h in a SEPAP 12/24 unit (Atlas) equipped with four vertically mounted medium-pressure mercury lamps (Novalamp RVC 400 W). Radiation below 295 nm was filtered by the lamp glass envelopes. During irradiation, the sample surface temperature was maintained at 60 °C and relative humidity was kept below 3%. Irradiation at 254 nm was performed for 300 h using a SEPAP 253 system (ref. G13 TL 15W TUV germicidal UVC).

In aqueous-phase experiments, M-GLY solutions were irradiated in a 150 mL Pyrex reactor, magnetically stirred and kept at 25 °C by a cooling system. The reactor was placed in a custom-made rectangular box equipped with four fluorescent tubes mounted on each side: either UVA lamps (F15W/350BL, Sylvania Blacklight, Germany) or UVC lamps (Monoline S 15W, Claude, France).

Characterization techniques

FT-IR Spectroscopy: photoaging was monitored by analyzing M-GLY films with Fourier Transform Infrared (FT-IR) spectroscopy after each 24-h irradiation cycle. FT-IR spectra were recorded at room temperature, in the 4000 - 1000 cm^{-1} wavenumber range, with 32 scans and 4 cm^{-1} resolution, using a Nicolet 6700 FT-IR spectrophotometer (Thermo Fisher Scientific, France). The resolution of infrared spectroscopy was extended by employing derivatization reactions *(168)*. M-GLY films were placed in a closed chamber and first exposed to an argon flow for 5 minutes to eliminate residual moisture. The chamber was then purged with the reactive gases SF_4 and NH_3 for 20 minutes, followed by an additional 5-minute argon purge to remove any excess. FT-IR spectra were recorded in the same conditions.

Size Exclusion Chromatography (SEC): photodegradation in liquid-phase was monitored with SEC using a PL1149-6240 aquagel-OH column (Agilent, France) in 0.5 M $NaNO_3$ aqueous solution (1.0 mL min^{-1}). Weight and number average molecular weights were determined using a Viscotek VE 3500 RI detector (Waters, France), calibrated with PEG standards.

Spectrofluorimetric analysis: H_2O_2 concentration was followed using 2.1 mM p-hydroxyphenylacetic acid (HPAA, purity > 98%) and 5 units mL^{-1} horseradish peroxidase (HRP), according to the spectrofluorimetric quantification method

(169) with a Varian Cary Eclipse fluorescence spectrophotometer setting excitation wavelengths at 320 nm and emission maximum at 420 nm. The formation of the dimer of HPAA was correlated with the concentration of H_2O_2 using standard solutions.

7.4. Conclusions

The stability of M-GLY under UVA irradiation was confirmed both in the solid state and in aqueous solution. In contrast, UVC exposure induced a much more pronounced photodegradation in both conditions, highlighting the need for further investigation into the nature of the degradation products and the degradation mechanism. The presence of an oxidizing agent such as H_2O_2 accelerated the degradation under UVA irradiation when compared to samples without the oxidant. Moreover, even in the absence of irradiation, the polymer solution containing H_2O_2 exhibited a more pronounced degradation than that observed under UVA light alone.

ANNEX 1

NMR spectra of polyamidoamines

All synthesized PAAs were analyzed by NMR spectroscopy. ^{1}H-, ^{13}C-NMR and HSQC spectra were collected in D_2O at pH 4.5 at 25 °C using a Bruker Avance NEO-400 NMR spectrometer operating at 400.13 MHz. Parameters: scan number 32, relaxation delay, d1, 10.0 s.

M-GLY

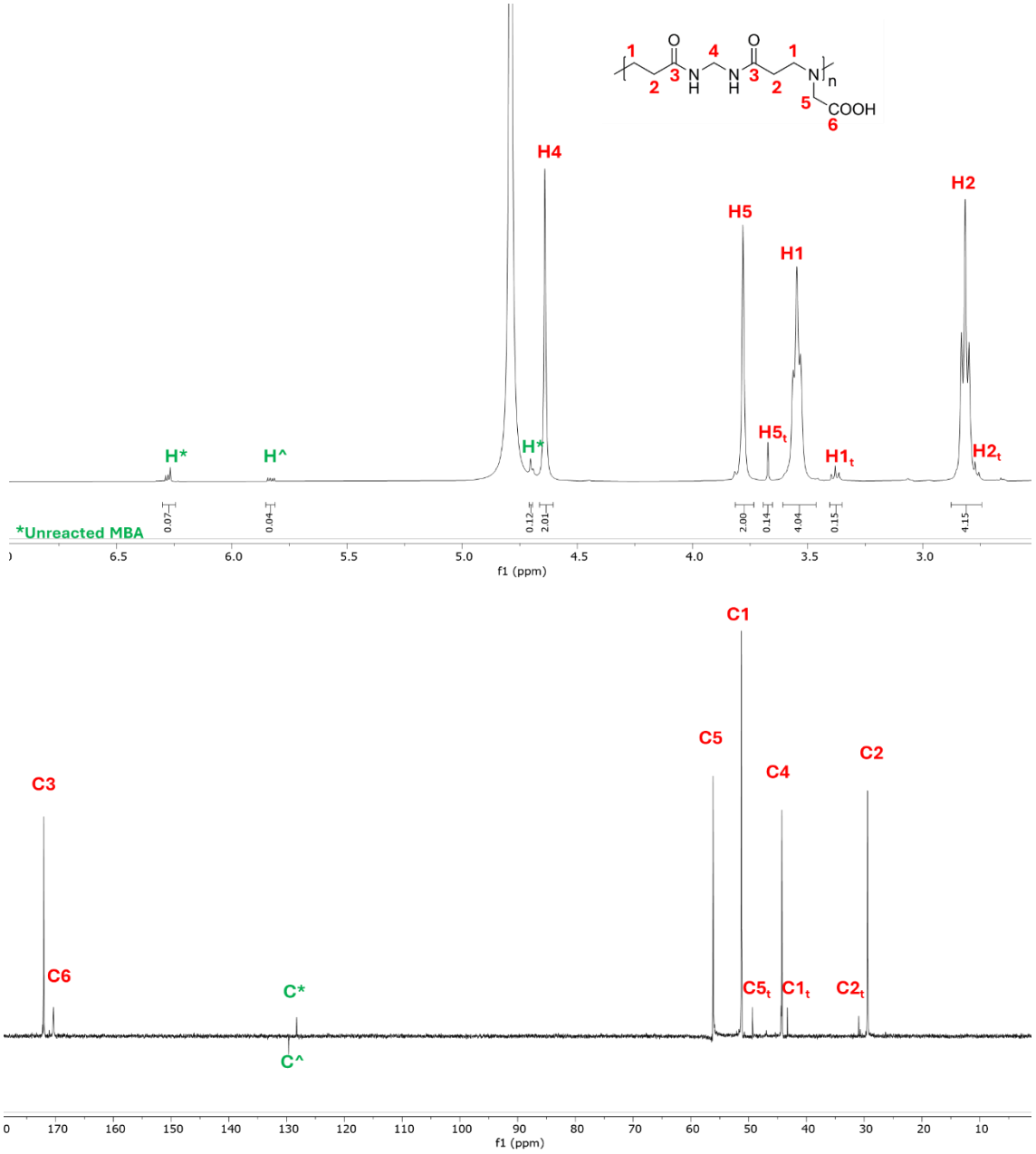

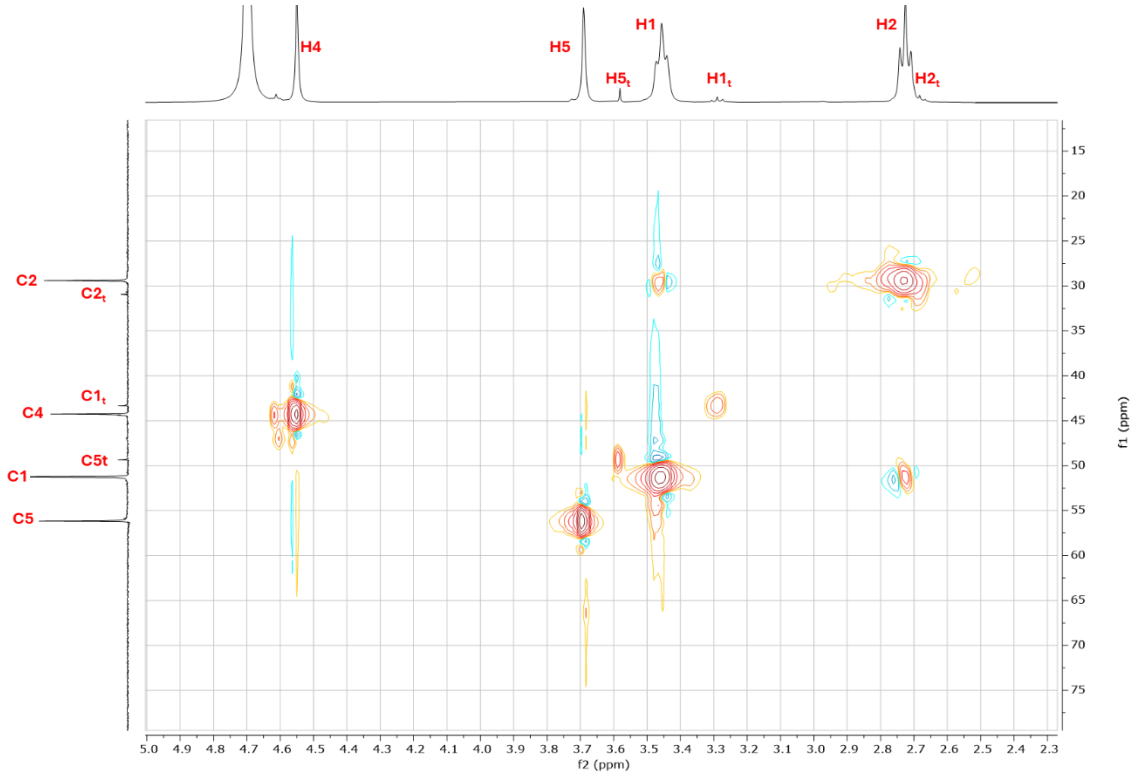
H4
H5
H5t
H1
H1t
H2
H2t
C2
C2t
C1t
C4
C5t
C1
C5
f2 (ppm)
f1 (ppm)

M-ARG

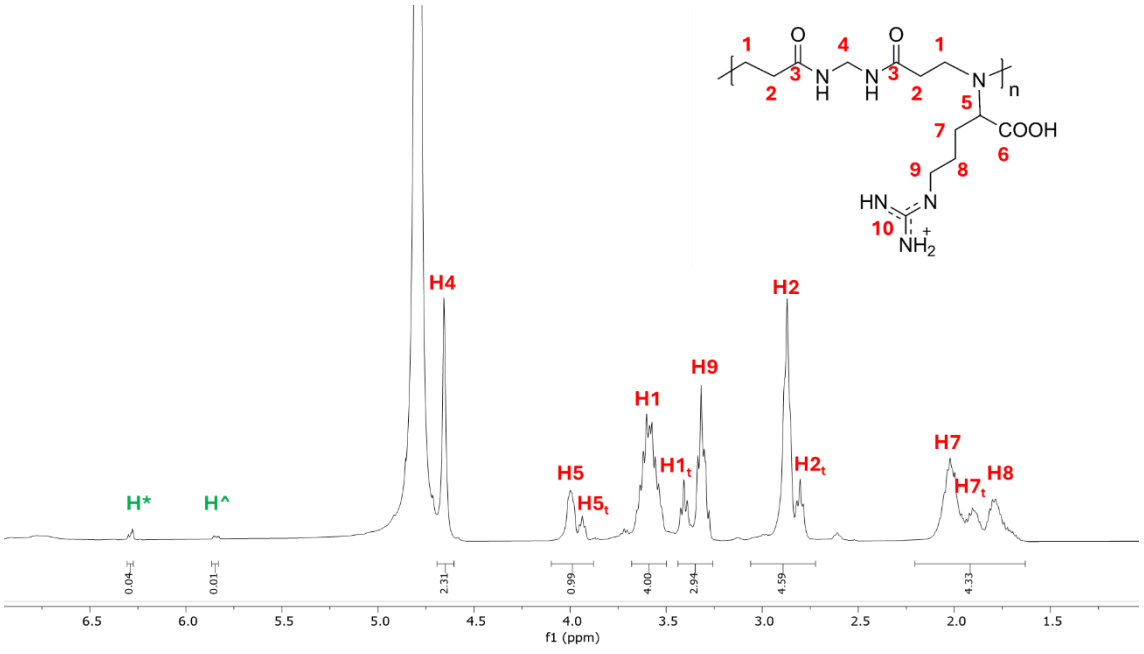
H*
H^
H4
H5
H5t
H1
H1t
H9
H2
H2t
H7
H7t
H8
COOH
NH2
f1 (ppm)

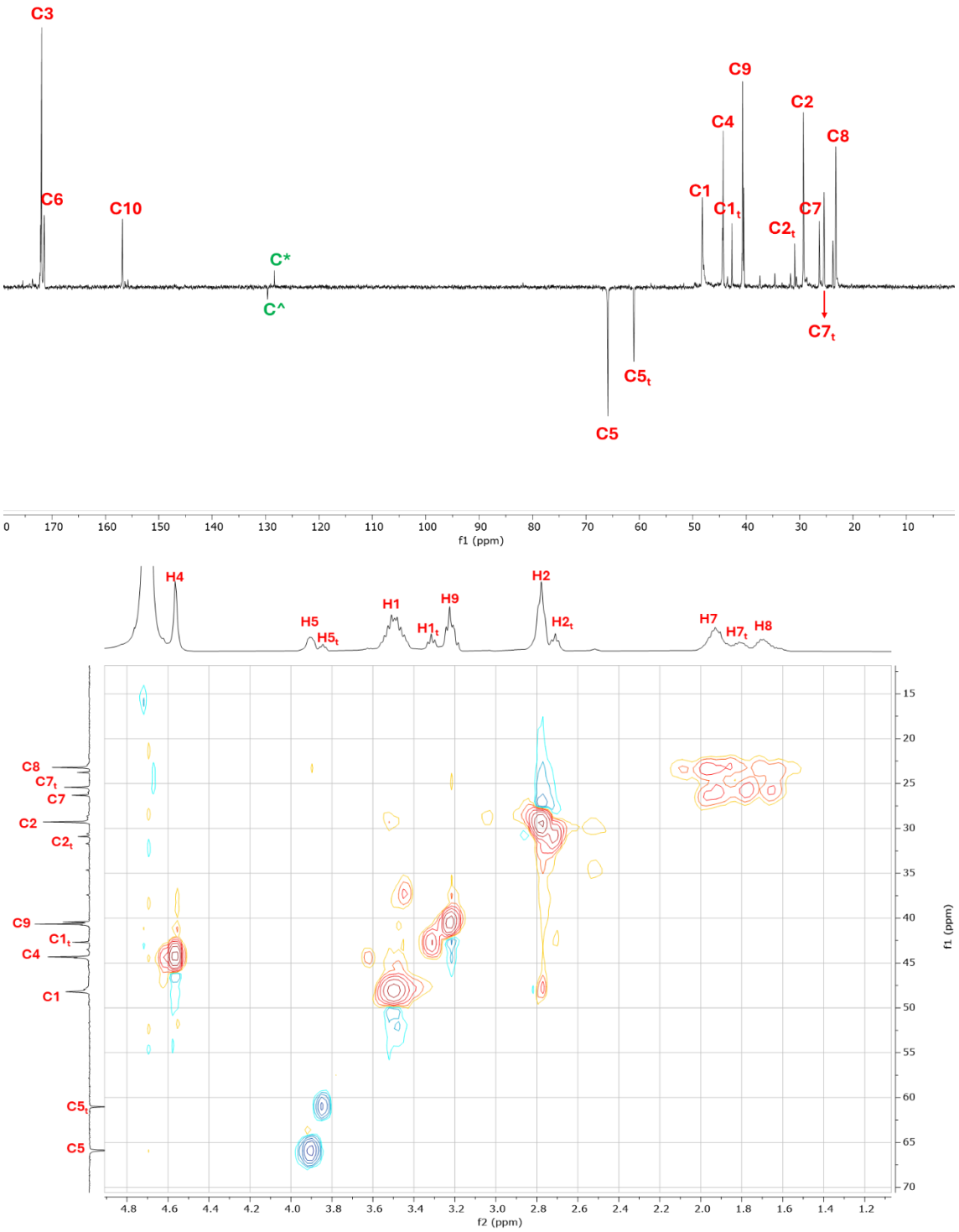
C3
C6
C10
C*
C^
C9
C4
C2
C8
C1
C1t
C7
C2t
C7t
C5t
C5
f1 (ppm)
H4
H5
H5t
H1
H1t
H9
H2
H2t
H7
H7t
H8
C8
C7t
C7
C2
C2t
C9
C1t
C4
C1
C5t
C5
f2 (ppm)
f1 (ppm)

M-SER

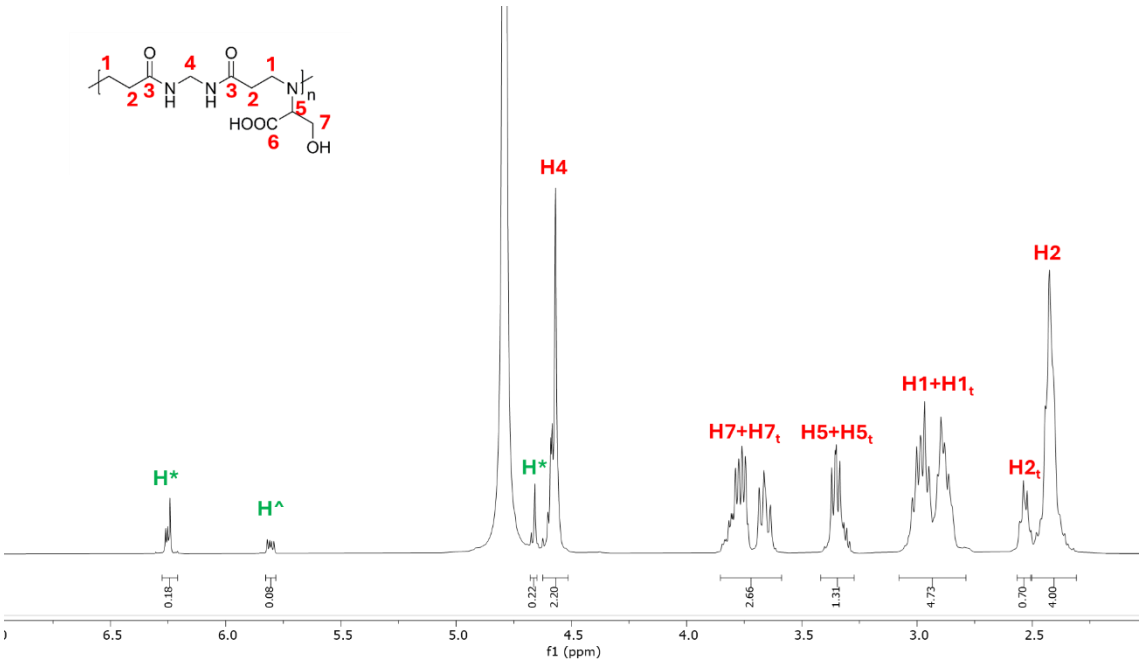
H*
H^
H*
H4
H7+H7t
H5+H5t
H1+H1t
H2t
H2
0.18
0.08
0.22
2.20
2.66
1.31
4.73
0.70
4.00
f1 (ppm)

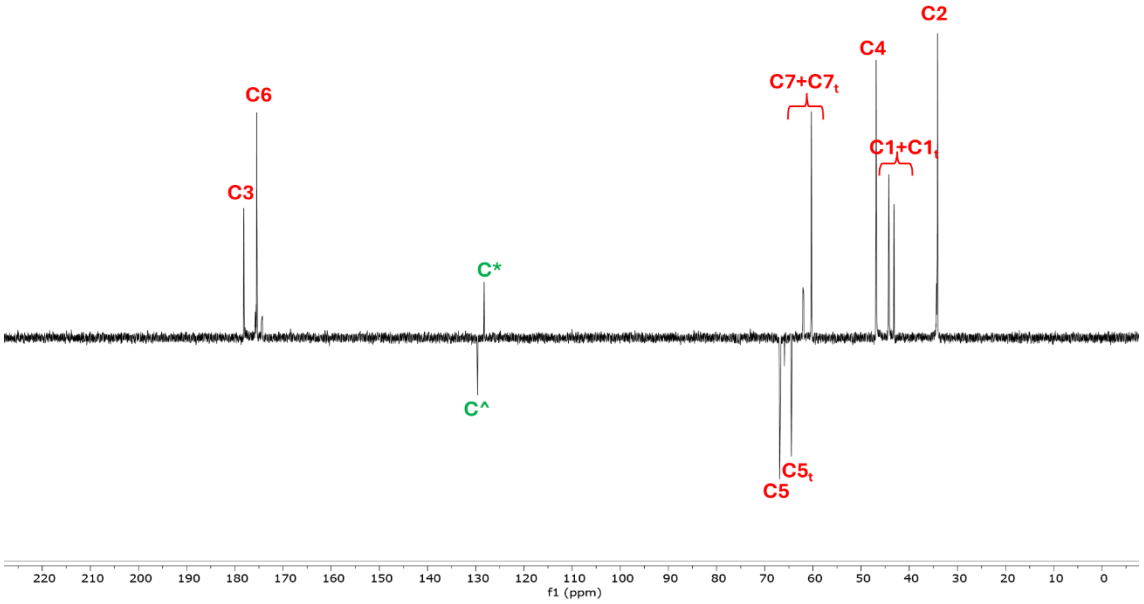
C6
C3
C*
C^
C7+C7t
C4
C2
C1+C1t
C5t
C5
f1 (ppm)

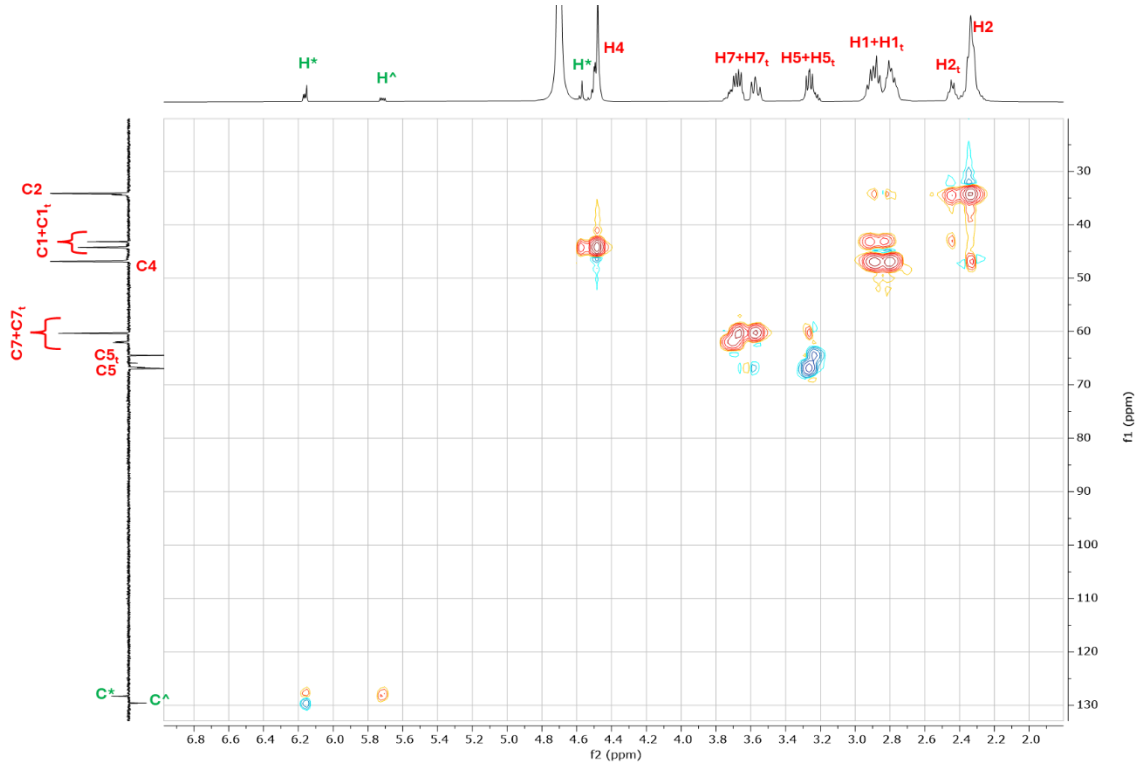
H*
H^
H*
H4
H7+H7t
H5+H5t
H1+H1t
H2t
H2
C2
C1+C1t
C4
C7+C7t
C5t
C5
C*
C^
f2 (ppm)
f1 (ppm)

M-ALA

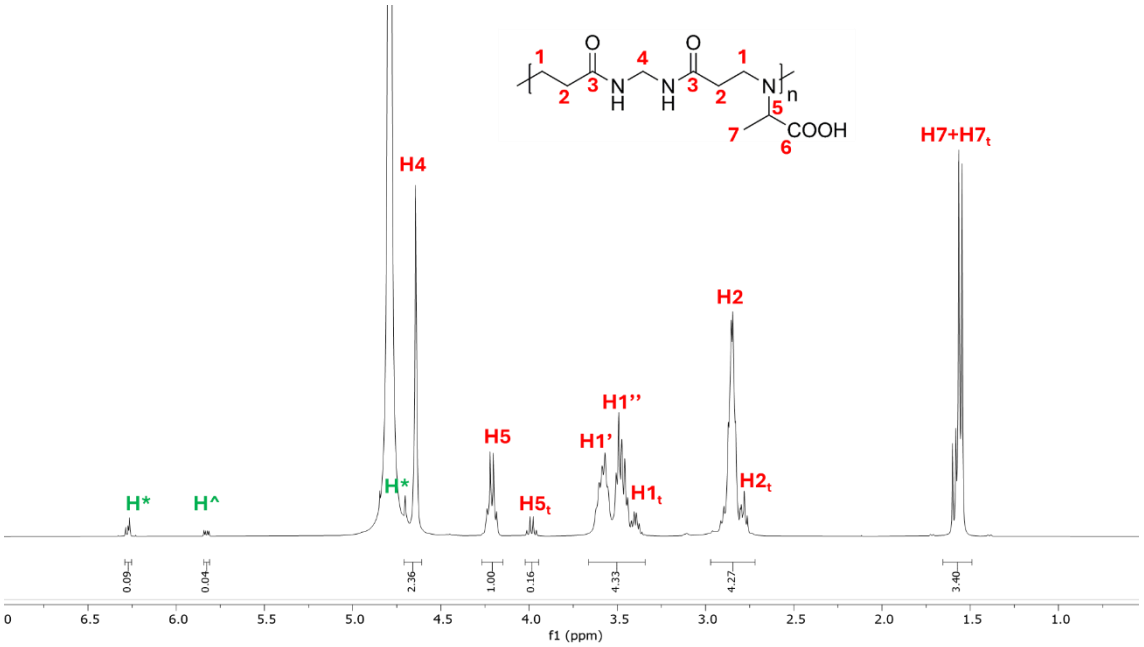
H4
H*
H^
H5
H5t
H1''
H1'
H1t
H2
H2t
H7+H7t
COOH
f1 (ppm)

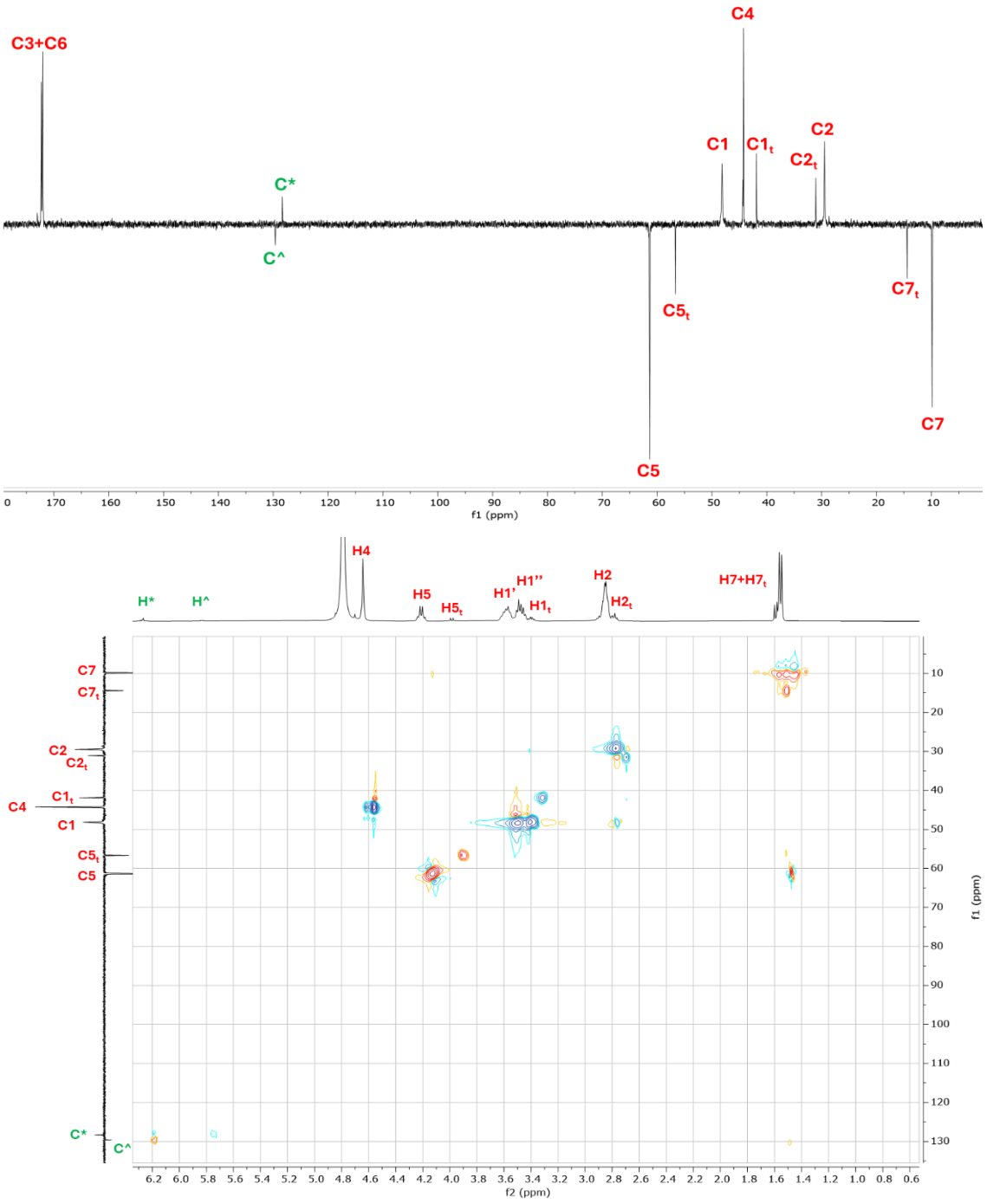
C3+C6
C4
C1
C1t
C2
C2t
C*
C^
C5t
C7t
C5
C7
f1 (ppm)
H*
H^
H4
H5
H5t
H1''
H1'
H1t
H2
H2t
H7+H7t
C7
C7t
C2
C2t
C4
C1t
C1
C5t
C5
C*
C^
f2 (ppm)
f1 (ppm)

M-LEU

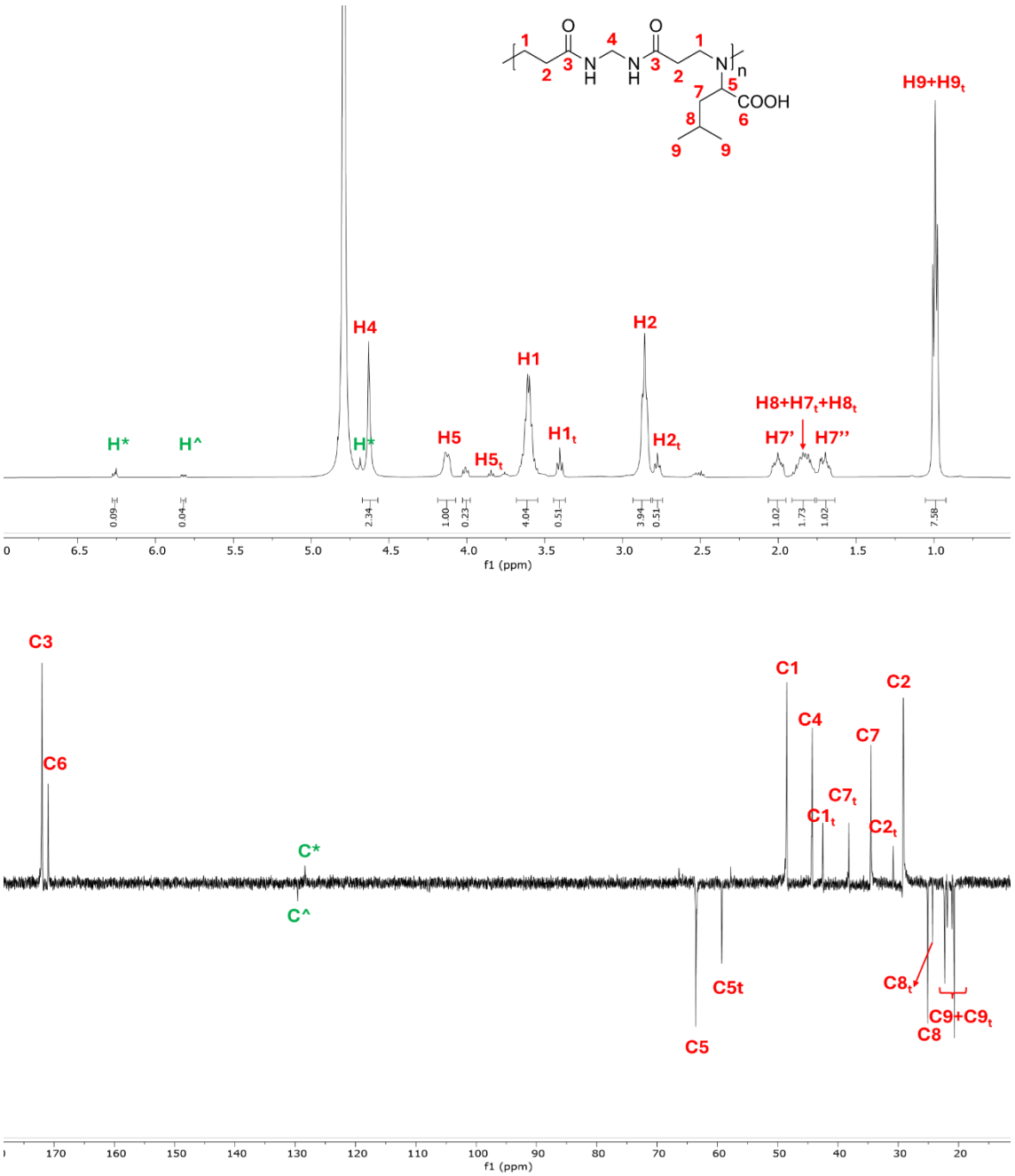
H*
H^
H4
H*
H5
H5t
H1
H1t
H2
H2t
H8+H7t+H8t
H7'
H7''
H9+H9t
f1 (ppm)
C3
C6
C*
C^
C1
C4
C7
C7t
C1t
C2t
C2
C5t
C5
C8t
C9+C9t
C8
f1 (ppm)

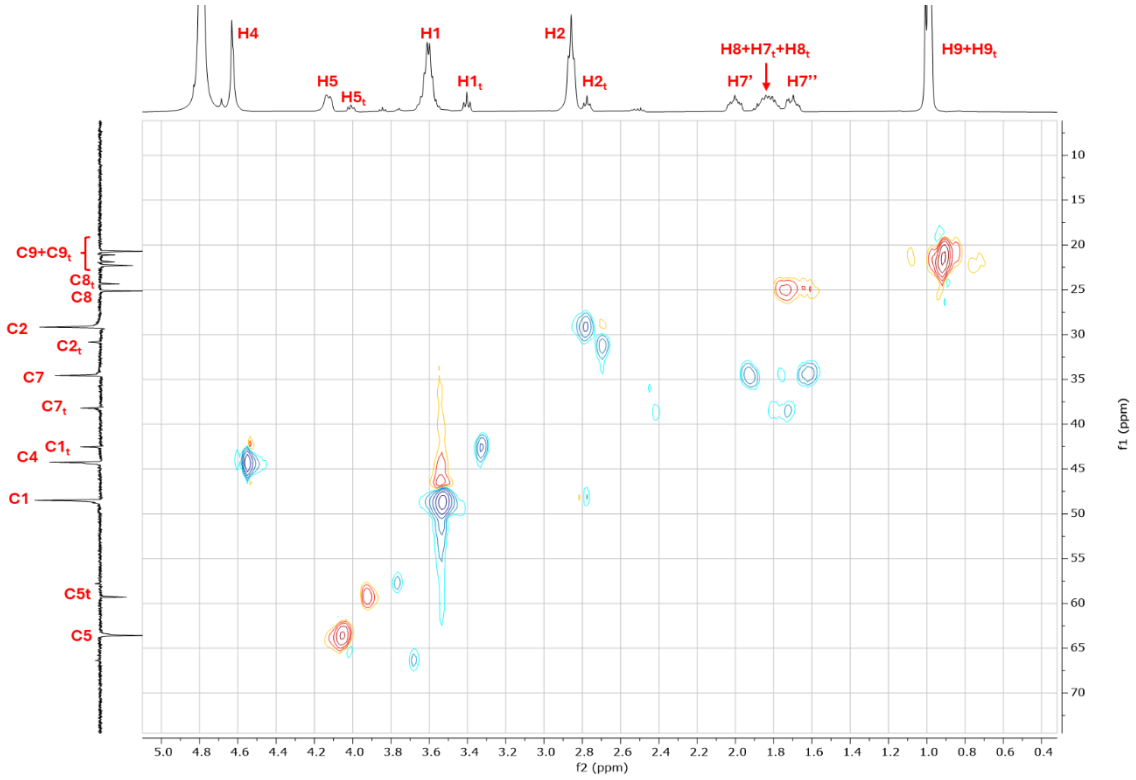
H4
H5
H5t
H1
H1t
H2
H2t
H8+H7t+H8t
H7'
H7''
H9+H9t
C9+C9t
C8t
C8
C2
C2t
C7
C7t
C1t
C4
C1
C5t
C5
f1 (ppm)
f2 (ppm)

M-HIS

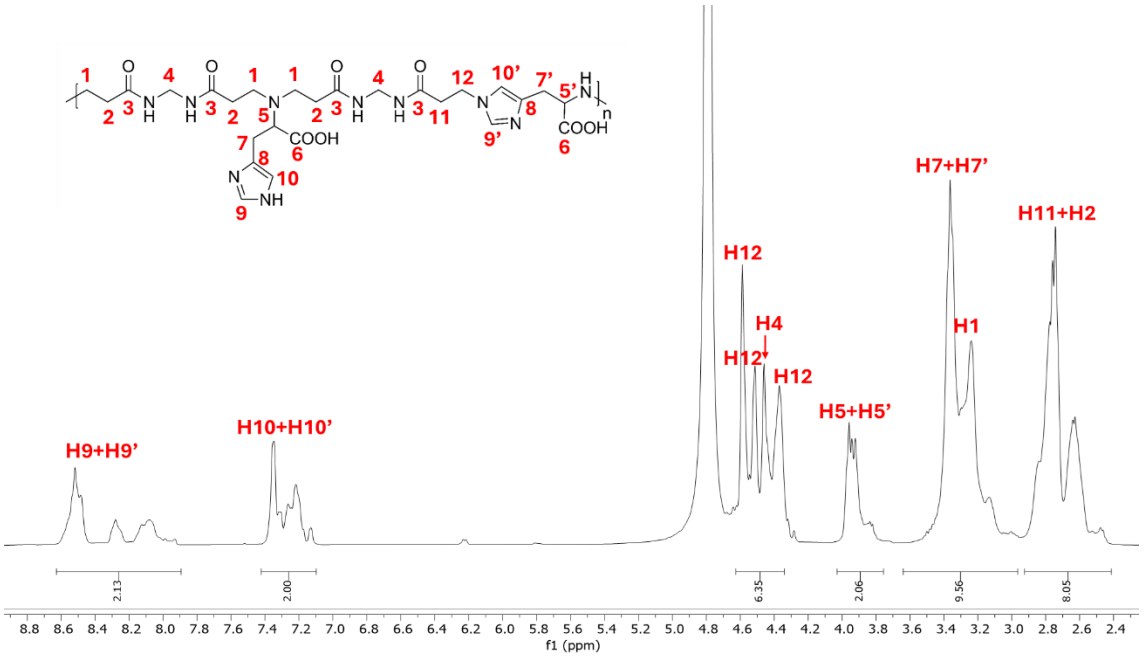
H9+H9'
H10+H10'
H12
H4
H12'
H12
H5+H5'
H7+H7'
H1
H11+H2
2.13
2.00
6.35
2.06
9.56
8.05
f1 (ppm)

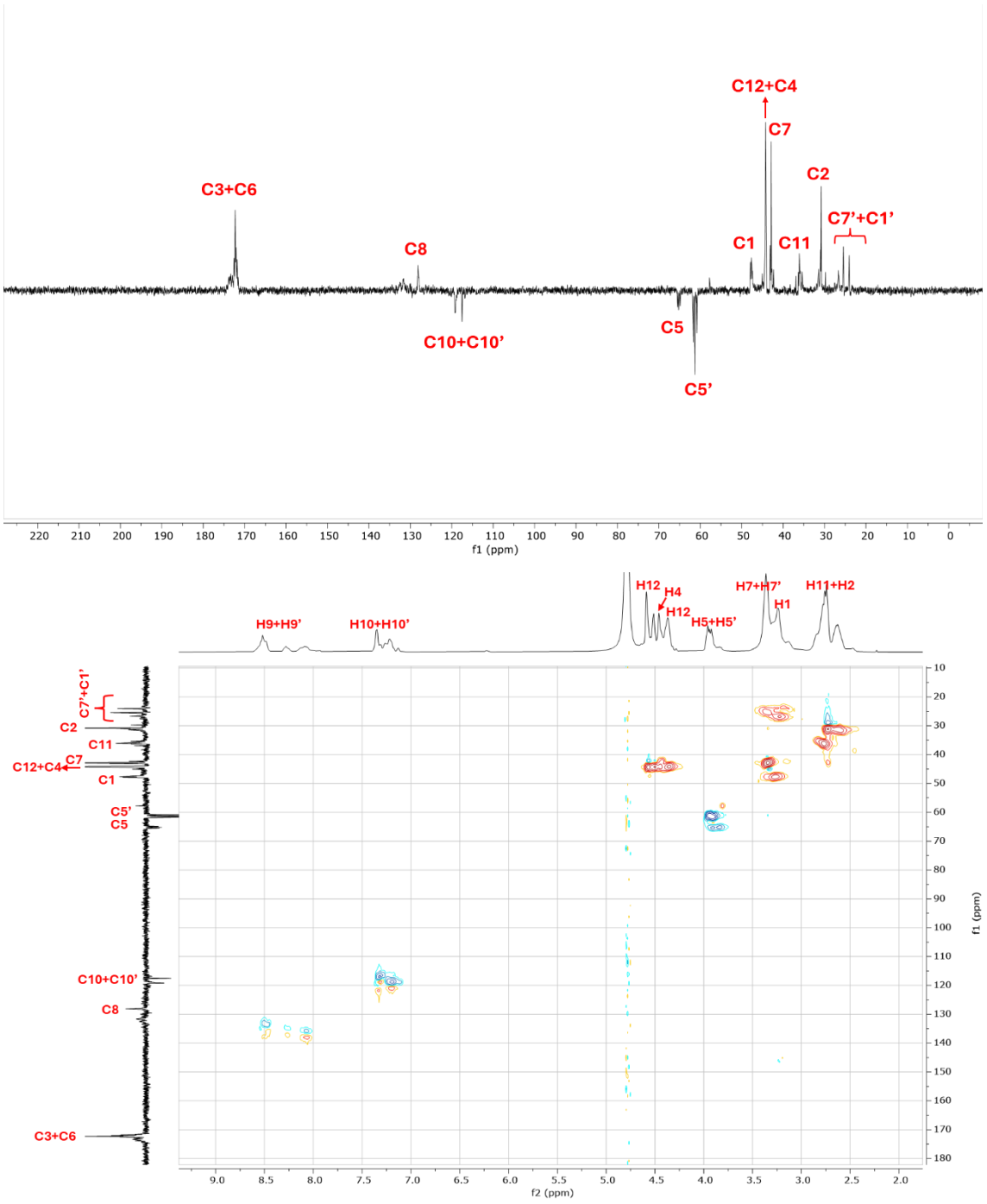
C12+C4
C7
C2
C3+C6
C7'+C1'
C1
C11
C8
C10+C10'
C5
C5'
f1 (ppm)
H12
H4
H7+H7'
H11+H2
H12
H1
H9+H9'
H10+H10'
H5+H5'
C7'+C1'
C2
C11
C12+C4
C7
C1
C5'
C5
C10+C10'
C8
C3+C6
f2 (ppm)
f1 (ppm)

M-GLU

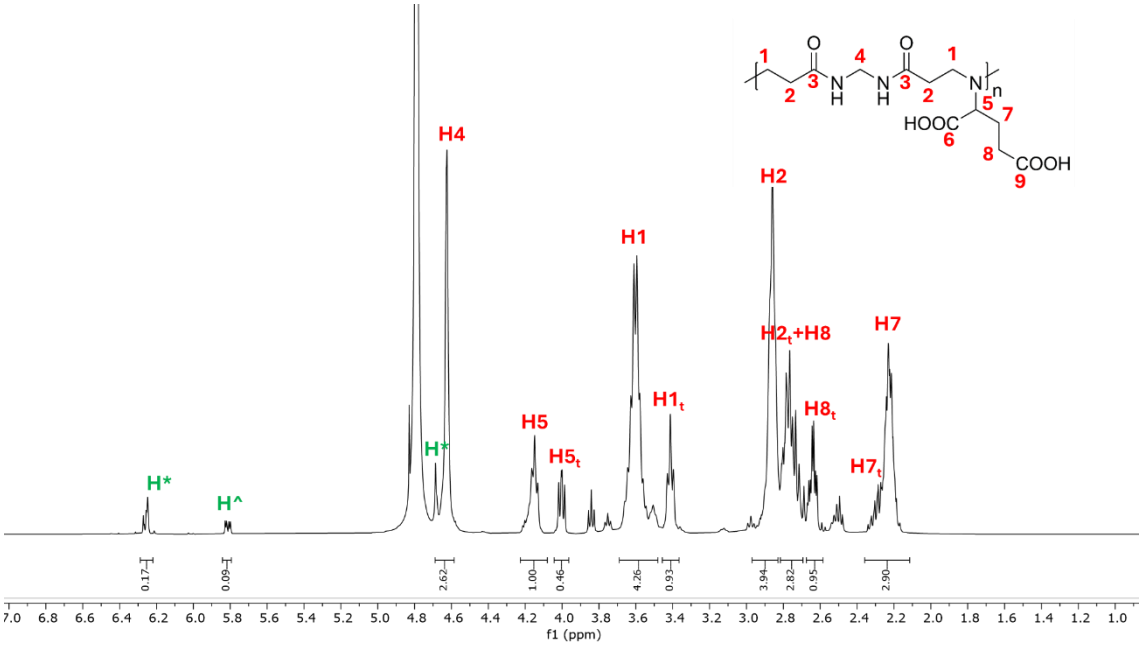
H*
H^
H4
H*
H5
H5t
H1
H1t
H2
H2t+H8
H8t
H7
H7t
0.17
0.09
2.62
1.00
0.46
4.26
0.93
3.94
2.82
0.95
2.90
f1 (ppm)

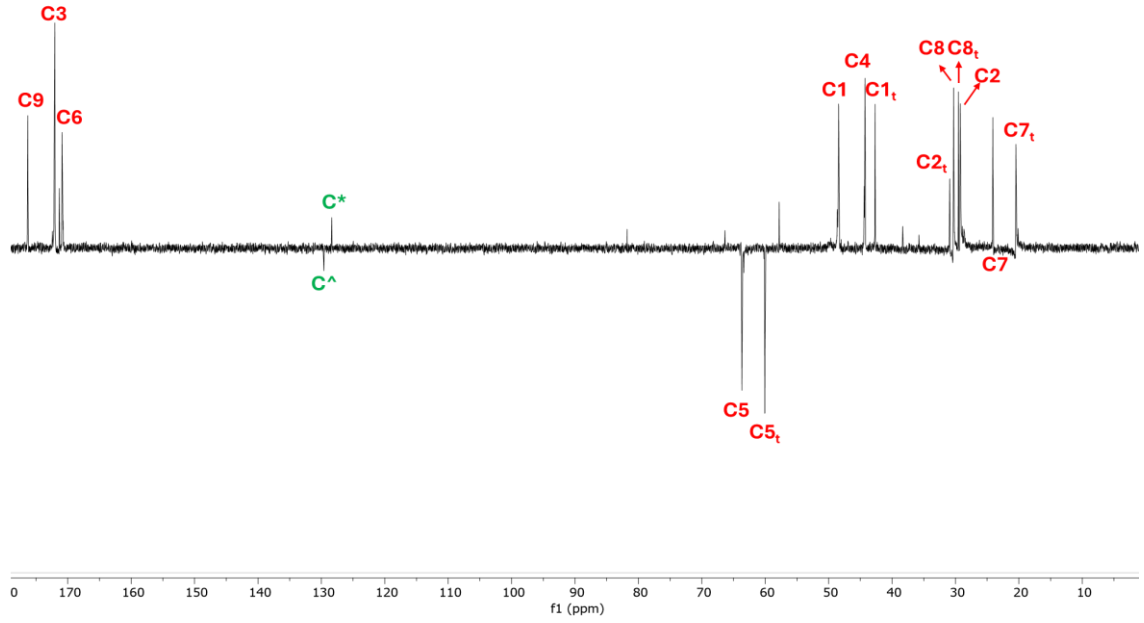
C3
C9
C6
C*
C^
C4
C1
C1t
C8
C8t
C2
C2t
C7t
C7
C5
C5t
f1 (ppm)

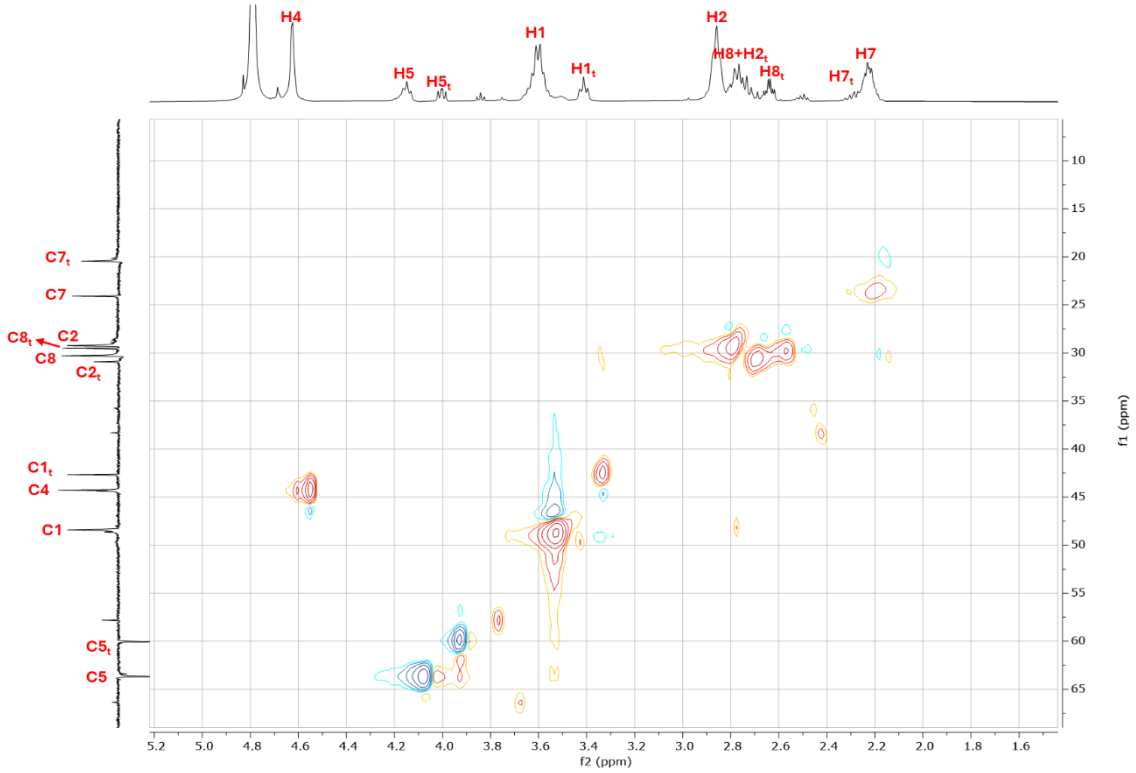

M-GLY$_{50}$-CYSS$_{50}$

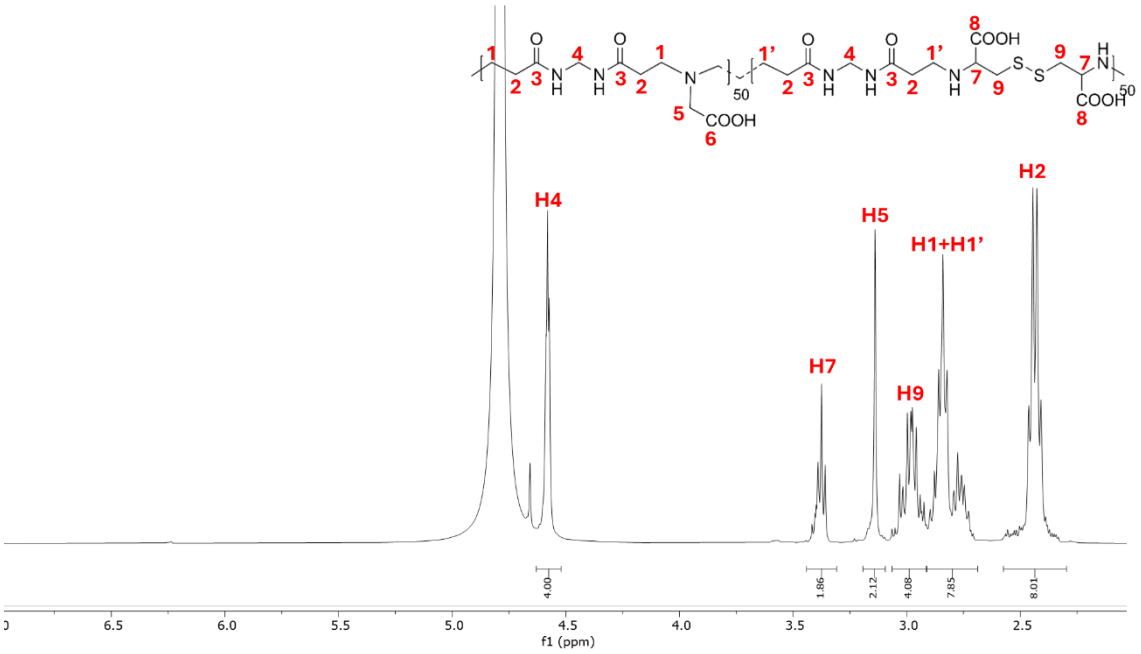

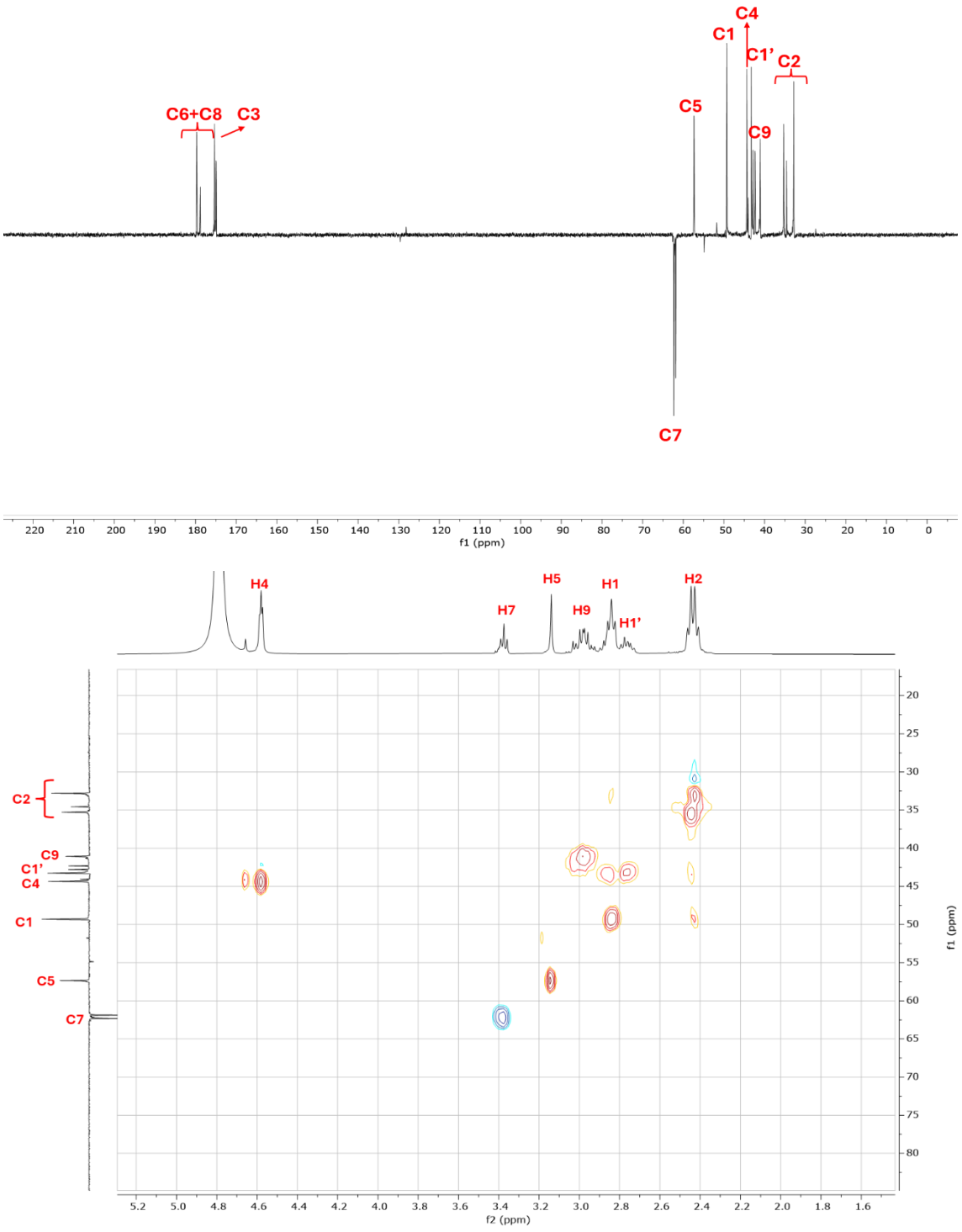
C4
C1
C1'
C2
C6+C8
C3
C5
C9
C7
f1 (ppm)
H4
H5
H1
H2
H7
H9
H1'
C2
C9
C1'
C4
C1
C5
C7
f1 (ppm)
f2 (ppm)

M-TYR$_{30}$-ARG$_{70}$

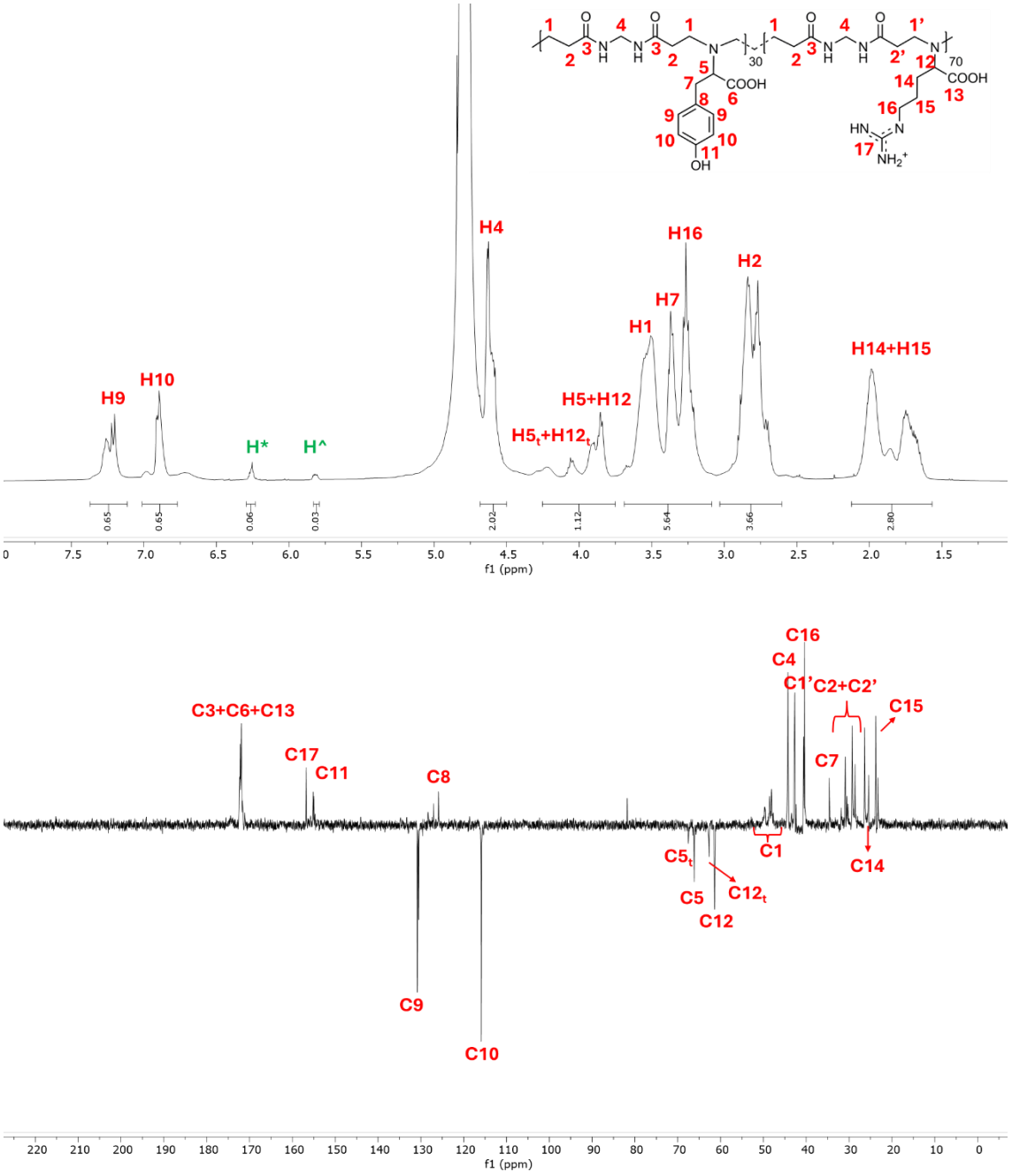

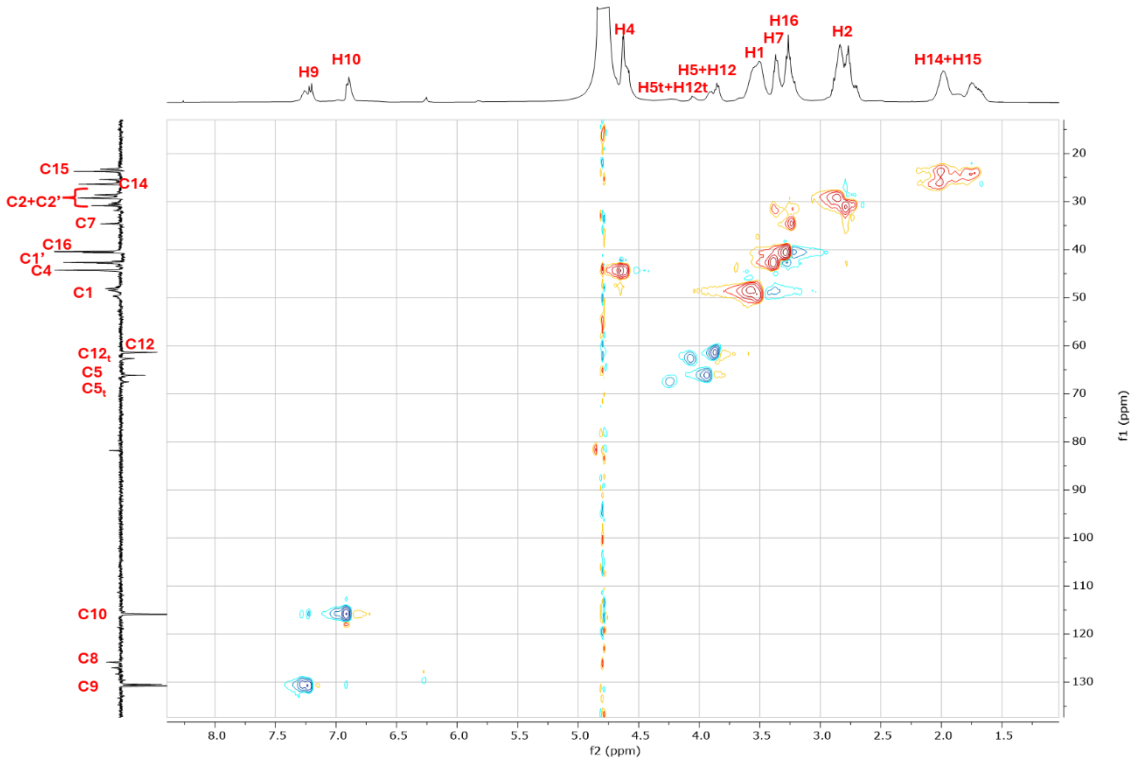
H9
H10
H4
H5+H12
H5t+H12t
H1
H16
H7
H2
H14+H15
C15
C14
C2+C2'
C7
C16
C1'
C4
C1
C12
C12t
C5
C5t
C10
C8
C9
f2 (ppm)
f1 (ppm)

AGMA1

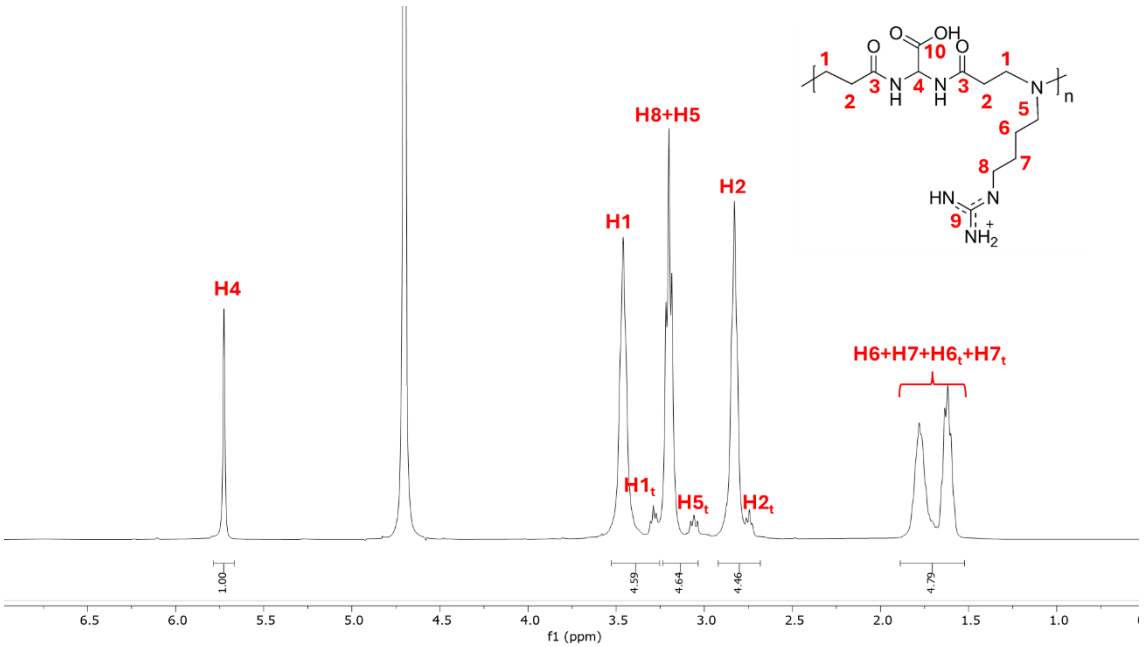
H4
H1
H8+H5
H2
H6+H7+H6t+H7t
H1t
H5t
H2t
1.00
4.59
4.64
4.46
4.79
f1 (ppm)

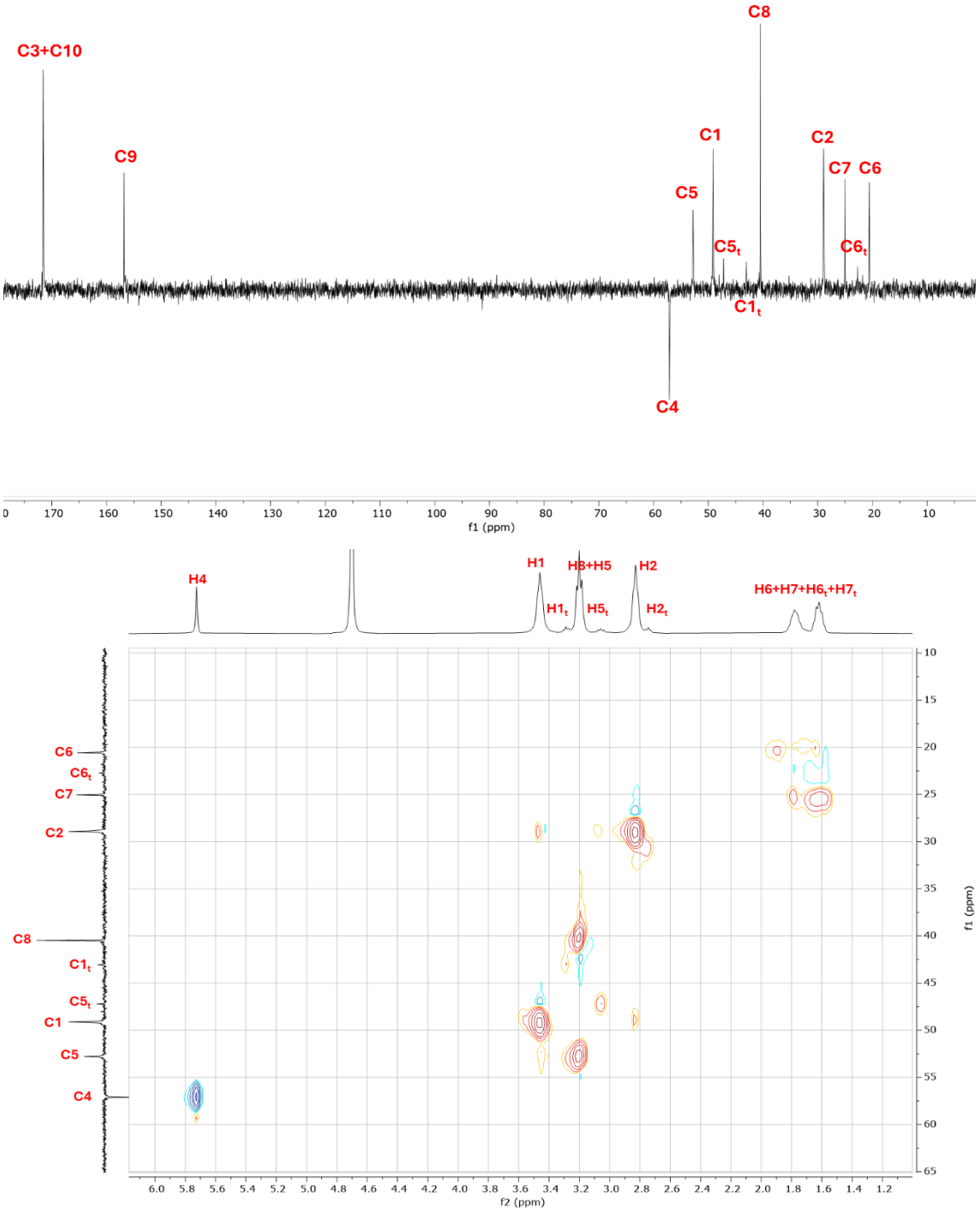
C3+C10
C9
C8
C1
C2
C7
C6
C5
C5t
C6t
C1t
C4
f1 (ppm)
H4
H1
H3+H5
H2
H1t
H5t
H2t
H6+H7+H6t+H7t
C6
C6t
C7
C2
C8
C1t
C5t
C1
C5
C4
f2 (ppm)
f1 (ppm)

ANNEX 2

Infrared spectra of polyamidoamines

All synthesized PAAs were analyzed by FT-IR spectroscopy. FT-IR/ATR spectra were recorded at room temperature in the 4000 - 600 cm^{-1} wavenumber range using a Jasco FT-IR/FIR spectrophotometer equipped with a diamond crystal. The following conditions were adopted: 256 scans and 4 cm^{-1} resolution.

M-GLY

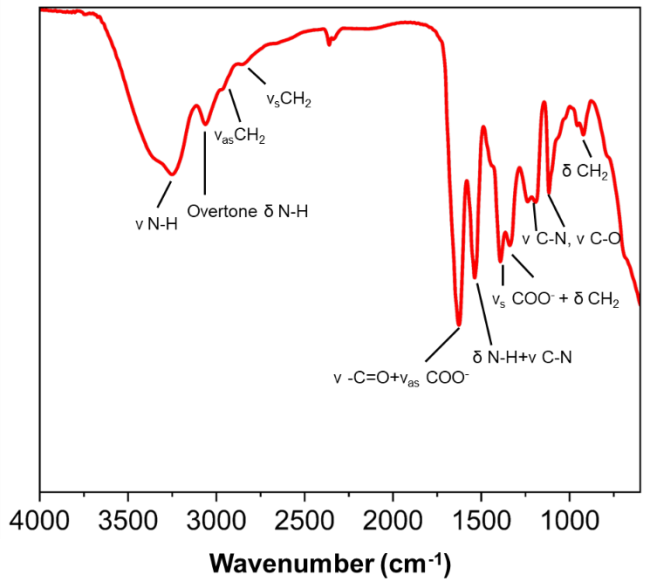

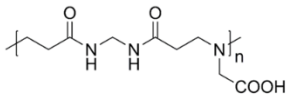

Assignments	Wavenumber (cm^{-1})	Intensity
ν N-H amide	3253	s
Overtone δ N-H	3050	w
$\nu_{as}CH_2$	2950	w
ν CH_2 amide	2920	w
ν_sCH_2	2854	w
ν N-C=O + ν_{as} COO^-	1627	s
δ N-H + ν C-N	1537	s
ν_s COO^-, $\delta_{(scissoring+wagging)}CH_2$	1386, 1336	s
ν C-N, ν C-O	1220, 1109	w
$\delta_{(rocking)}CH_2$	922	w

M-ARG

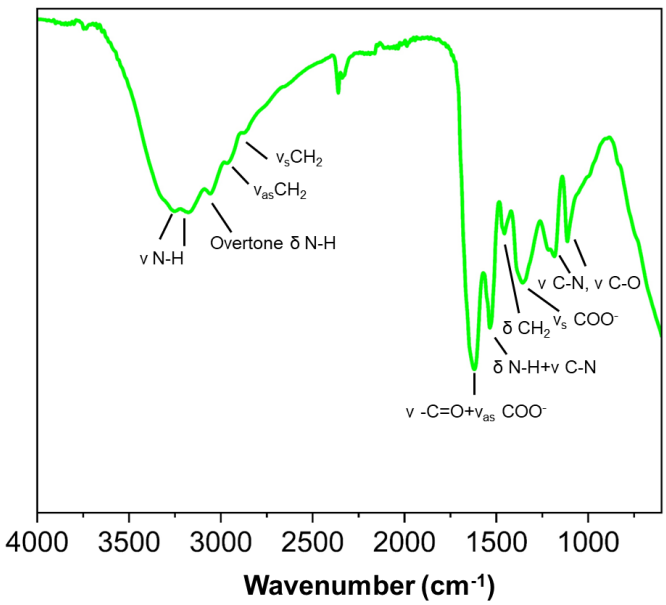

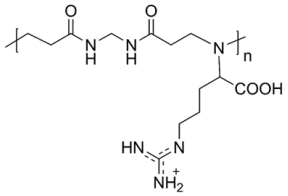

Assignments	Wavenumber (cm^{-1})	Intensity
ν N-H	3258, 3160	s
Overtone δ N-H	3050	w
$\nu_{as}CH_2$, ν_sCH_2	2951, 2867	w
ν N-C=O + ν_{as} COO^-	1624	s
δ N-H + ν C-N	1534	s
$\delta_{(scissoring)}CH_2$	1464	w
ν_s COO^-, ν C-N	1353	s
ν C-N, ν C-O	1187, 1105	w

M-SER

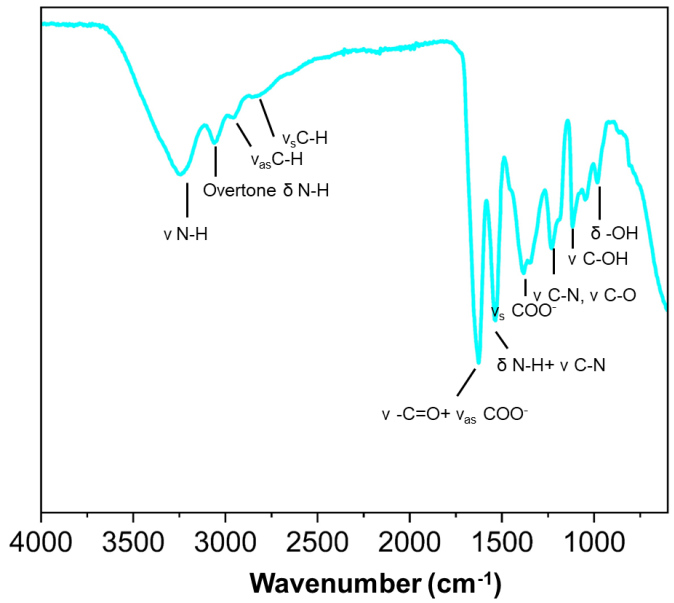

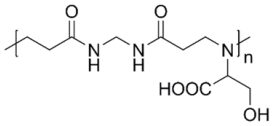

Assignments	Wavenumber (cm^{-1})	Intensity
ν N-H amide	3240	s
Overtone δ N-H	3064	w
ν_{as}C-H, ν_{s}C-H	2955, 2837	w
ν N-C=O + ν_{as} COO^-	1633	s
δ N-H + ν C-N	1542	s
ν_{s} COO^-	1379	s
ν C-N, ν C-O	1339, 1229	w
ν C-OH	1108	w
δ OH	983	w

M-ALA

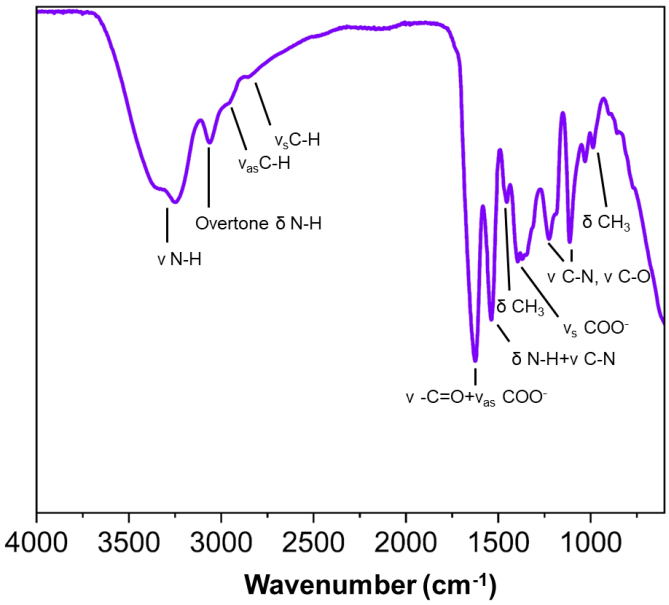

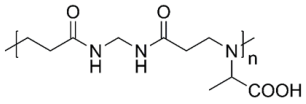

Assignments	Wavenumber (cm^{-1})	Intensity
ν N-H amide	3251	s
Overtone δ N-H	3060	w
ν_{as}C-H, ν_{s}C-H	2956, 2848	w
ν N-C=O + ν_{as} COO^-	1634	s
δ N-H + ν C-N	1544	s
$\delta_{(scissoring)}CH_3$ + ν_{s} COO^-	1450, 1368	s
ν C-N, ν C-O	1220, 1105	w
$\delta_{(rocking)}CH_3$	982	w

M-LEU

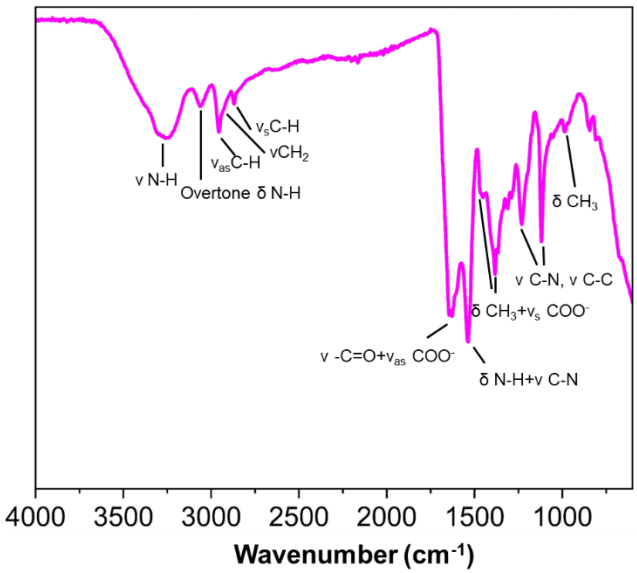

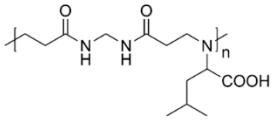

Assignments	Wavenumber (cm^{-1})	Intensity
v N-H amide	3257	s
Overtone δ N-H	3062	w
v_{as}C-H, v CH_2 amide, v_sC-H	2952, 2925, 2867	w
v N-C=O+ v_{as} COO^-	1643	s
δ N-H + v C-N	1531	s
$\delta_{(scissoring)}CH_3$ + v_s COO^-	1455, 1378	s
v C-N, v C-C	1228, 1111	w
$\delta_{(rocking)}CH_3$	980	w

M-HIS

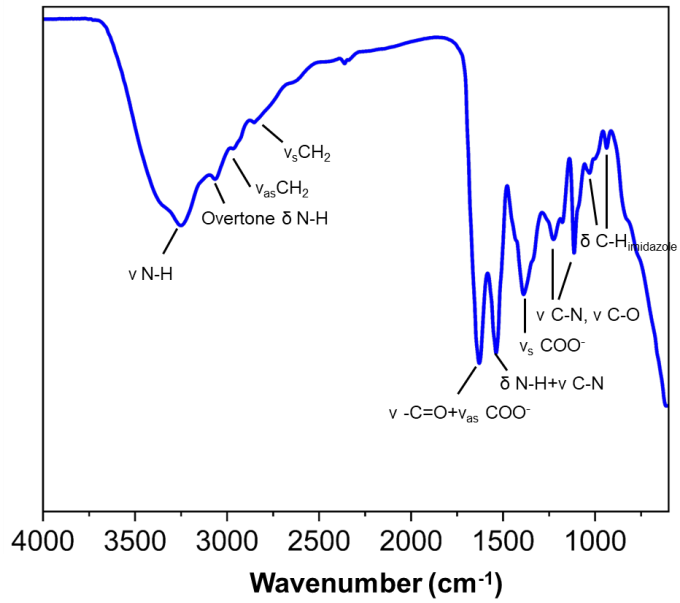

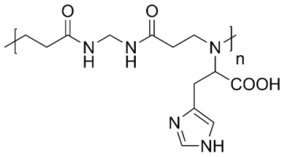

Assignments	Wavenumber (cm^{-1})	Intensity
v N-H amide	3249	s
Overtone δ N-H	3065	w
$v_{as}CH_2$, v_sCH_2	2967, 2851	w
v N-C=O + v_{as} COO^-	1625	s
δ N-H + v C-N	1535	s
v_s COO^-	1384	s
v C-N, v C-O	1228, 1115	w
δ $C\text{-}H_{imidazole}$	1025, 935	w

M-GLU

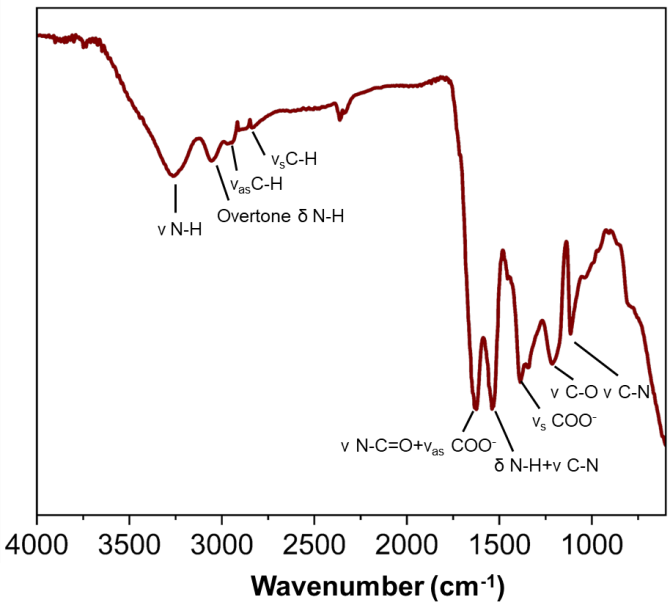

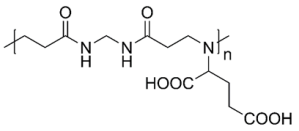

Assignments	Wavenumber (cm^{-1})	Intensity
v N-H	3263	s
Overtone δ N-H	3055	w
v_{as}C-H, v_sC-H	2962, 2870	w
v N-C=O + v_{as} COO^-	1629	s
δ N-H + v C-N	1535	s
v_s COO^-	1389	s
v C-O, v C-N	1209,1105	s

M-GLY$_{50}$-CYSS$_{50}$

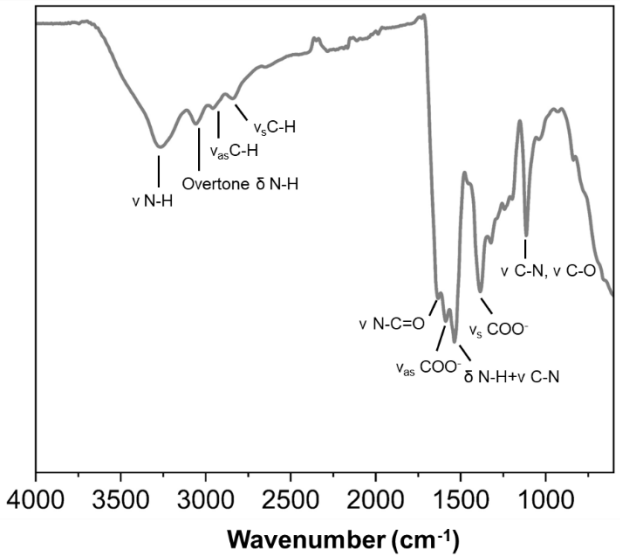

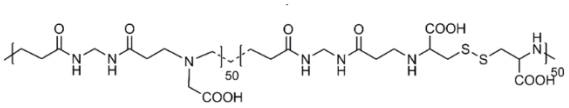

Assignments	Wavenumber (cm^{-1})	Intensity
v N-H amide	3262	s
Overtone δ N-H	3058	w
v_{as}C-H, v_sC-H	2955, 2837	w
v N-C=O	1625	s
v_{as} COO^-	1589	w
δ N-H + v C-N	1542	s
v_s COO^-	1381	s
v C-N, v C-O	1115	s

M-TYR$_{30}$-ARG$_{70}$

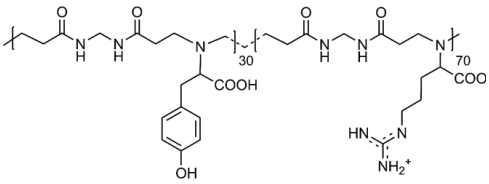

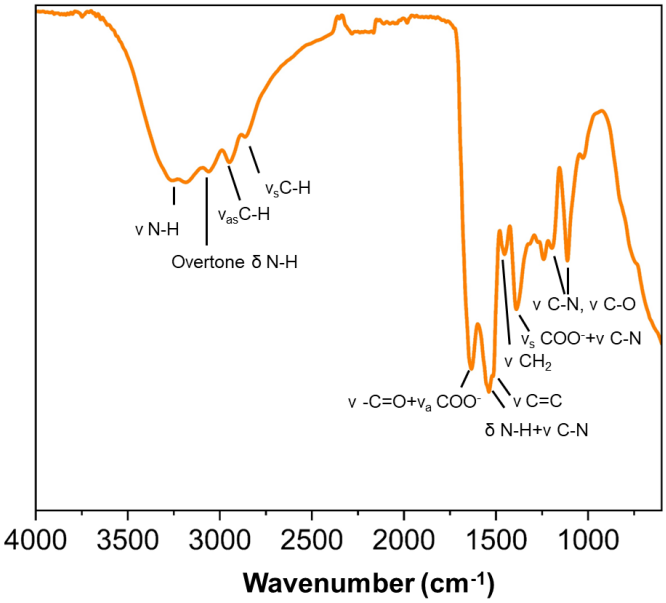

Assignments	Wavenumber (cm^{-1})	Intensity
ν N-H amide	3257	s
Overtone δ N-H	3055	w
ν_{as}C-H, ν_{s}C-H	2946, 2853	w
ν N-C=O + ν_{as} COO^-	1634	s
δ N-H + ν C-N	1534	s
ν C=C	1480	w
$\nu_{(scissoring)}$ CH_2	1449	w
ν_s COO^- + ν C-$N_{guanidine}$	1388	w
ν C-N, ν C-O	1245–1106	w

AGMA1

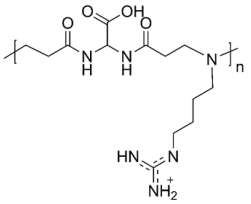

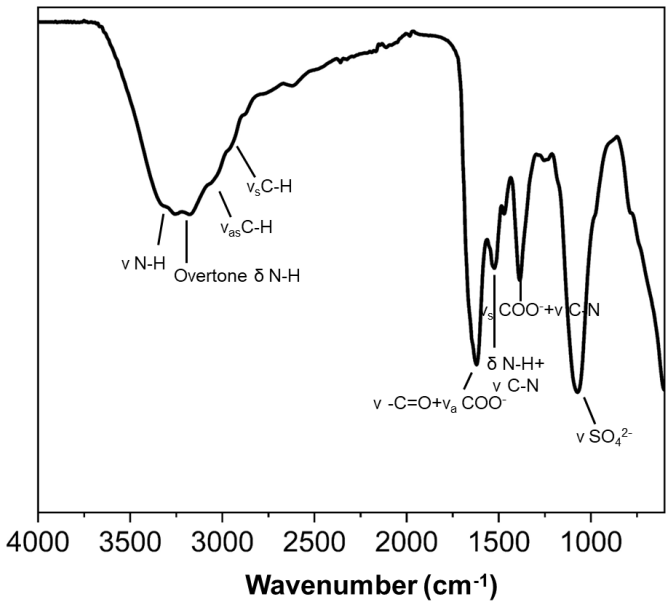

Assignments	Wavenumber (cm^{-1})	Intensity
ν N-H amide	3206	s
Overtone δ N-H	3050	w
ν_{as}C-H, ν_{s}C-H	2965, 2850	w
ν N-C=O + ν_{as} COO^-	1625	s
δ N-H + ν C-N	1526	w
ν_s COO^- + ν C-$N_{guanidine}$	1387	s
ν S-O	1069	s

ANNEX 3

Thermogravimetric profiles of polyamidoamines

The thermal stability of PAAs was assessed by thermogravimetric analysis in nitrogen and air from 30 to 800 °C range using a TGA 2 Star System. The following conditions were adopted: 10 °C min^{-1} heating rate, 50 mL min^{-1} gas flow.

AIR	N_2
M-GLY	
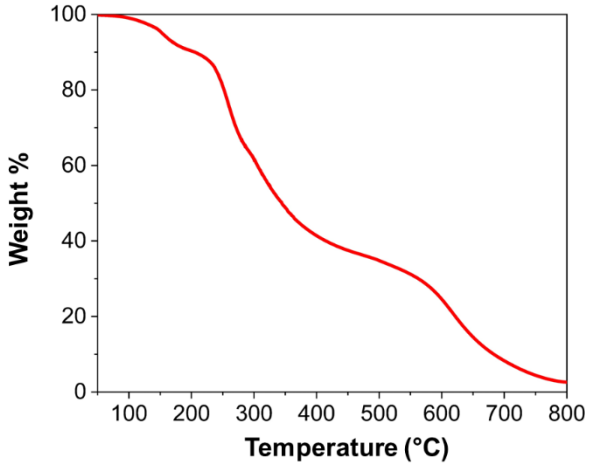	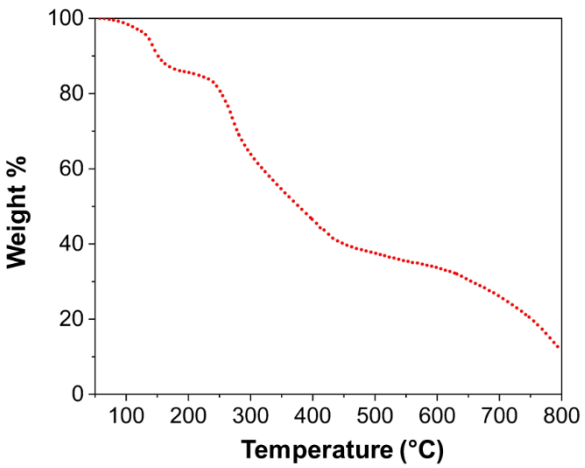
M-ARG	
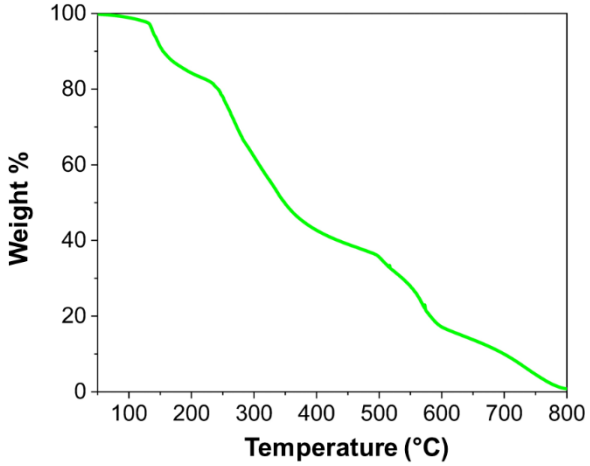	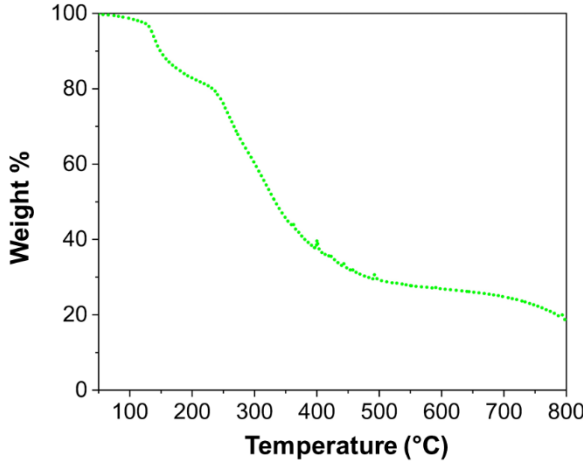

M-SER

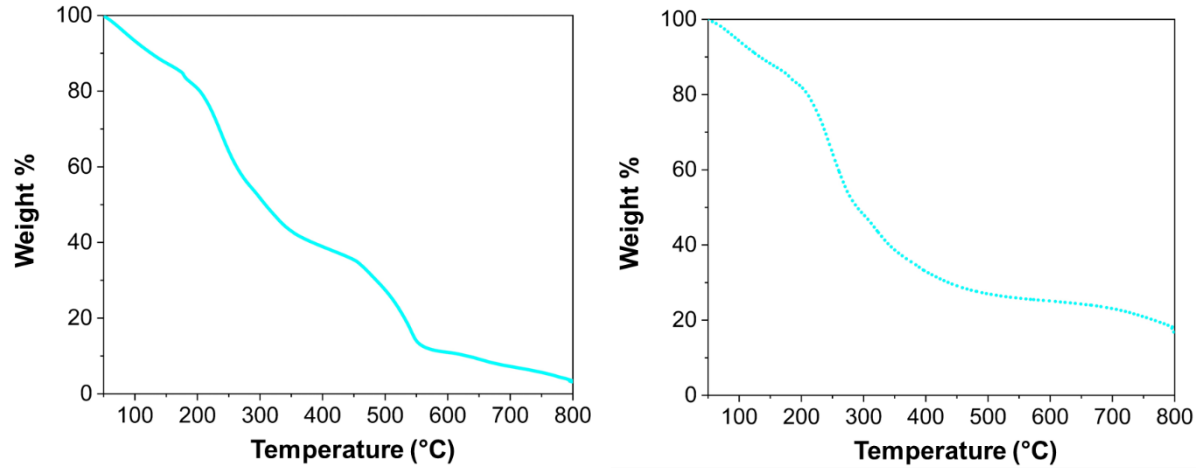

M-ALA

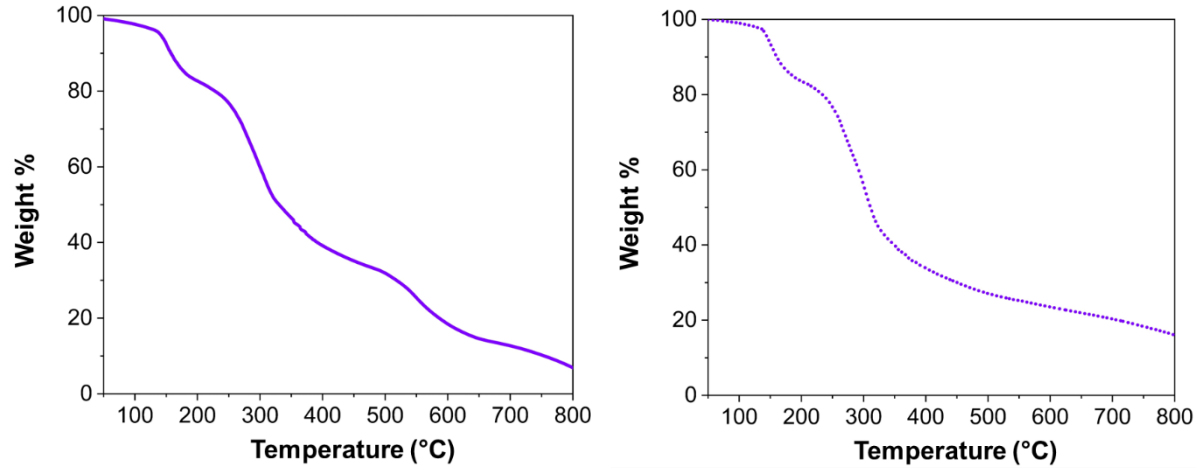

M-LEU

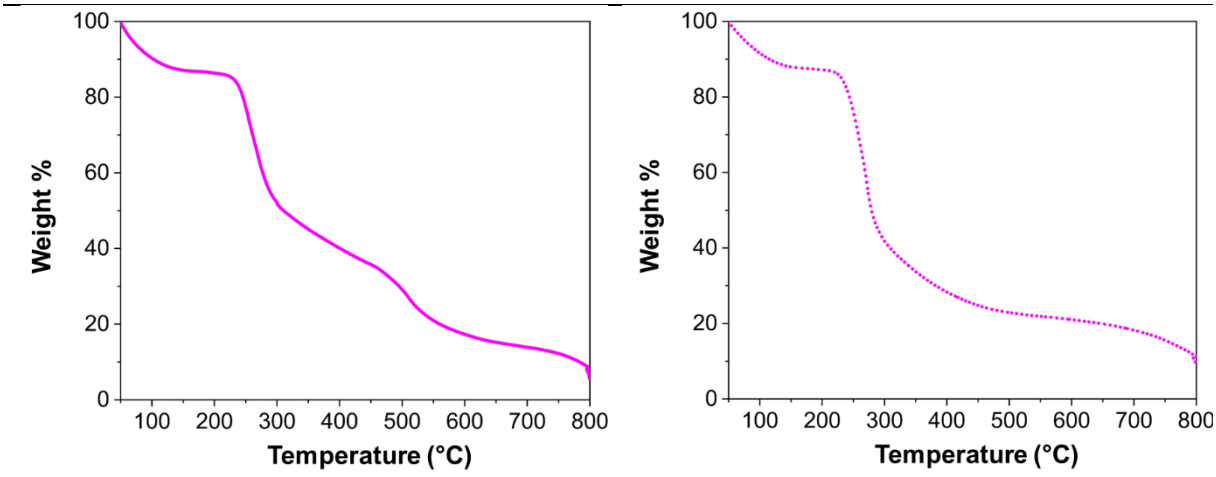

M-HIS

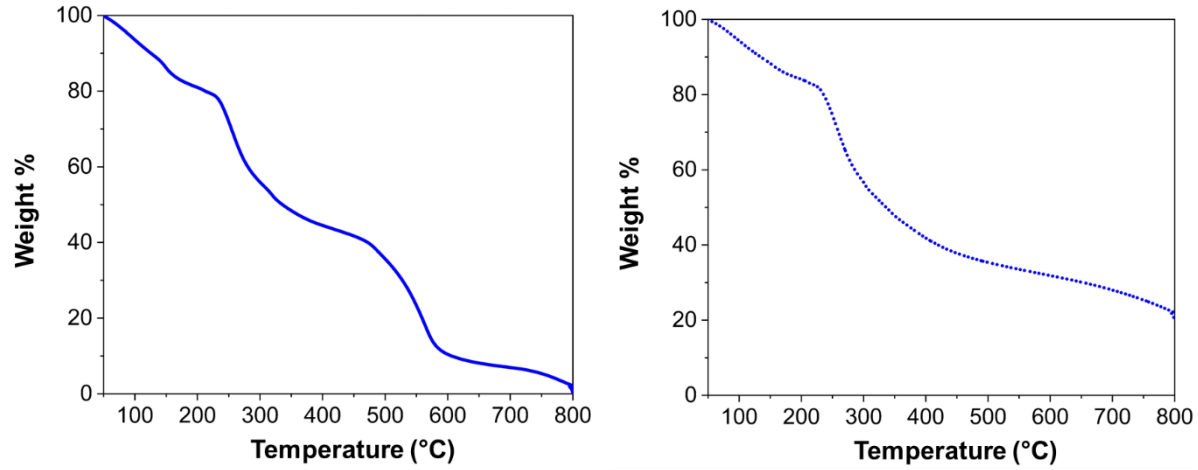

M-GLU

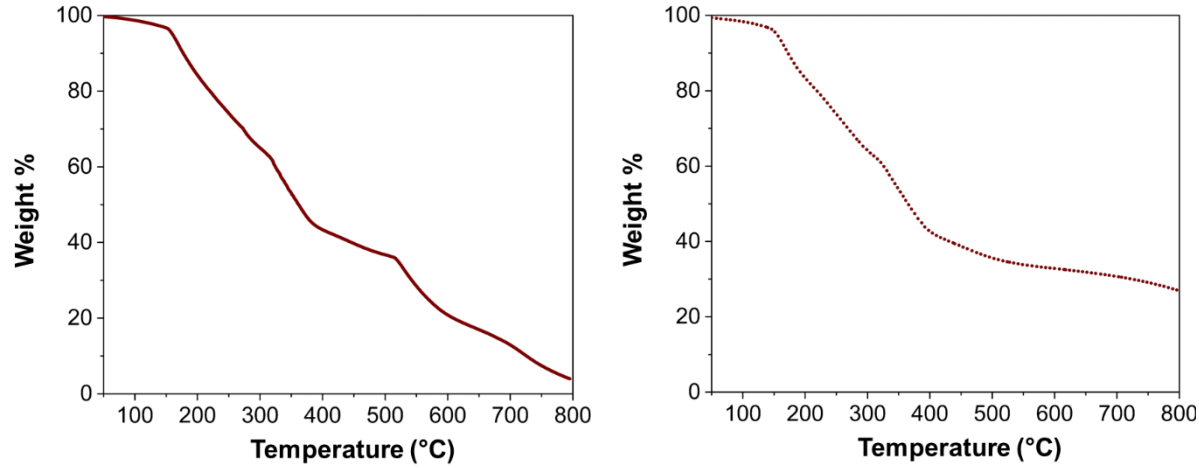

M-GLY$_{50}$-CYSS$_{50}$

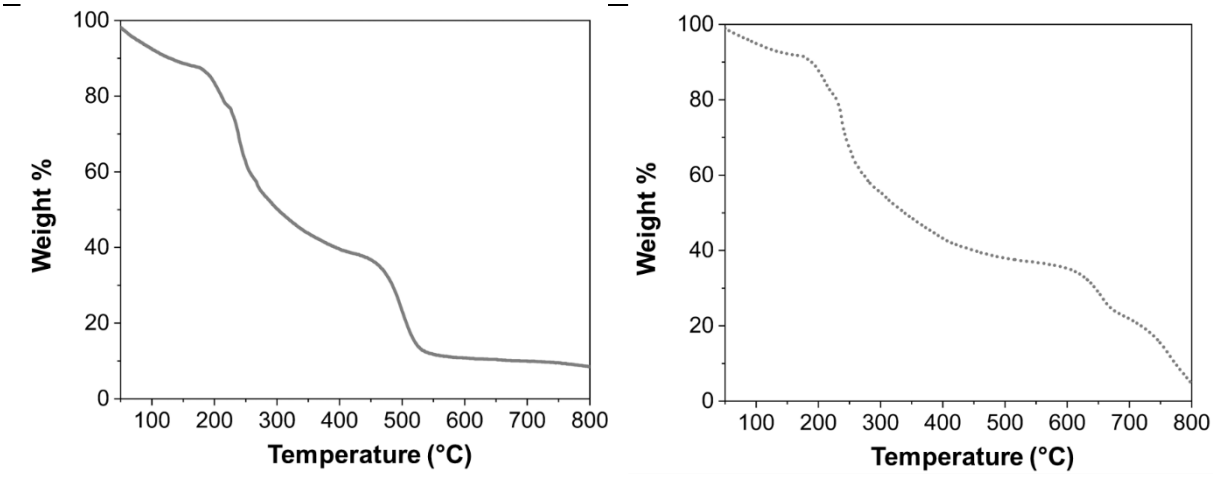

M-TYR$_{30}$-ARG$_{70}$

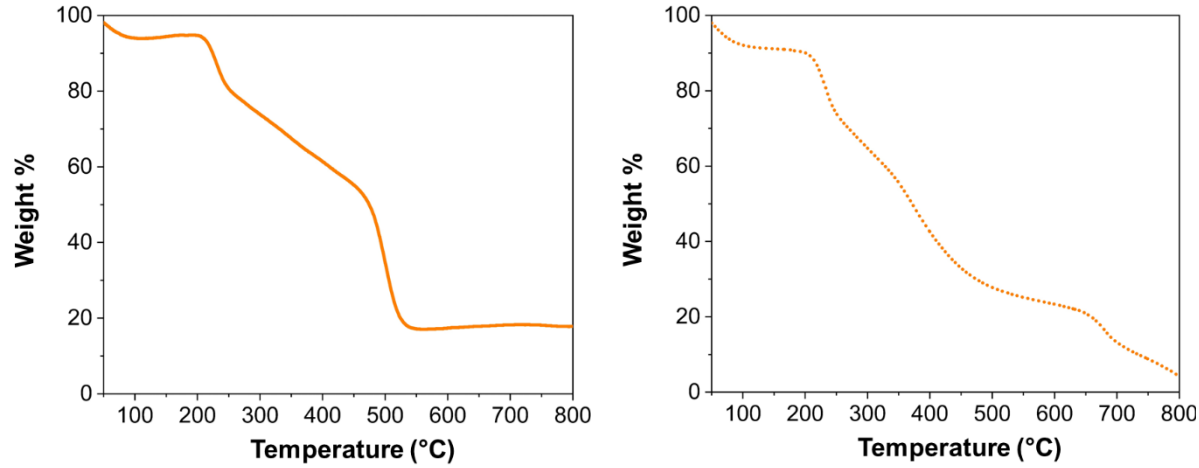

AGMA1

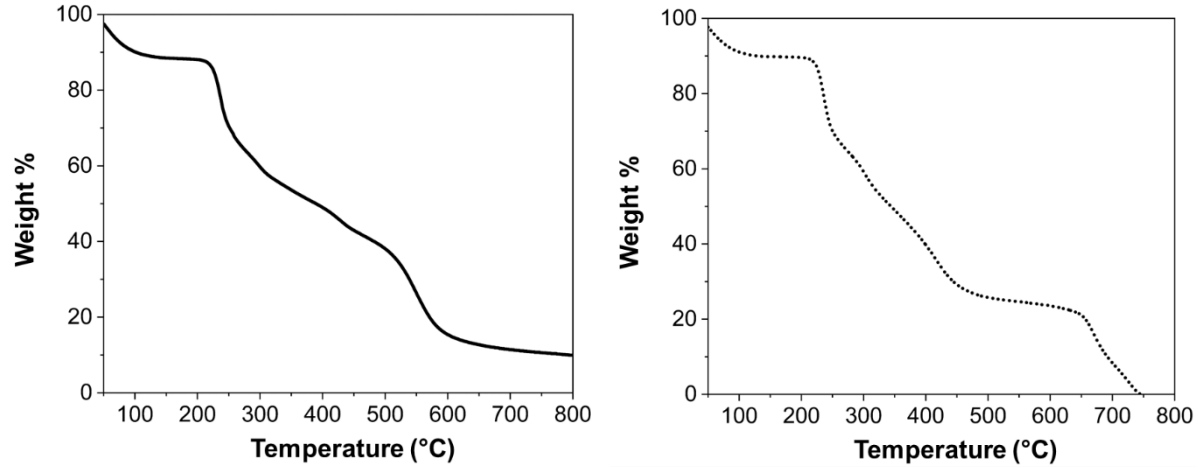

Table A3.1. Thermal data of PAAs in nitrogen and air by thermogravimetric analysis

Sample	T_{onset} [a] (°C)	$T_{max,1}$ (°C) [b]	$T_{max,2}$ (°C) [c]	RMF (%) [d]
		N_2		
M-GLY	151	270	-	12
M-ARG	149	287	-	18
M-SER	134	247	-	16
M-LEU	115	268	-	9
M-ALA	160	285	-	16
M-HIS	135	258	-	20
M-GLU	172	351	-	27
M-GLY$_{50}$-CYSS$_{50}$	189	240	651	5
M-TYR$_{30}$-ARG$_{70}$	201	310	680	4

AGMA1	128	238	670	-
AIR				
M-GLY	205	260	617	3
M-ARG	155	286	567	0.8
M-SER	126	238	541	3
M-LEU	103	259	507	6
M-ALA	158	296	552	7
M-HIS	126	256	561	0.4
M-GLU	177	350	533	4
M-GLY$_{50}$-CYSS$_{50}$	128	240	501	9
M-TYR$_{30}$-ARG$_{70}$	224	233	500	18
AGMA1	101	238	550	10

[a]Onset decomposition temperature at 10% weight loss. [b]First temperature at maximum weight loss rate. [c]Second temperature at maximum weight loss rate. [d]Residual mass fraction at 800 °C.

ANNEX 4

pH-dependent ionic species distributions of PAAs

The pK_a values of the ionizable functions of PAAs were determined by potentiometric titration as the pH values at the half-equivalent points, located in the buffer zone related to the specific function. The half-equivalent points were obtained as the half-titrant volume amounts added between consecutive inflections in the pH versus titrant volume curves. Direct determination of the pK_a values of the ionizable functions in the copolymers M-GLY_{50}-$CYSS_{50}$ and M-TYR_{30}-ARG_{70} was not possible due to solubility constraints. Speciation diagrams were generated by plotting the concentration fractions (α) of the different ionic species against pH obtained from Equations 2.2.1-14 (Section 2.2), using the *pKa* values of the PAA repeat units shown in Table 2.2.1 of the main test. The reported species distributions include: M-GLY, M-ARG, M-SER, M-ALA, M-LEU, M-HIS, M-GLU and AGMA1.

M-GLY

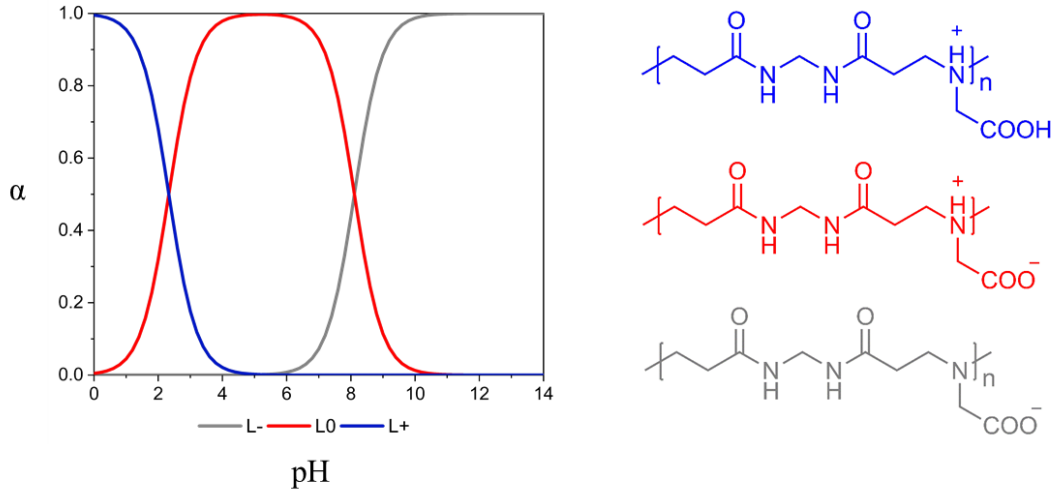

M-ARG

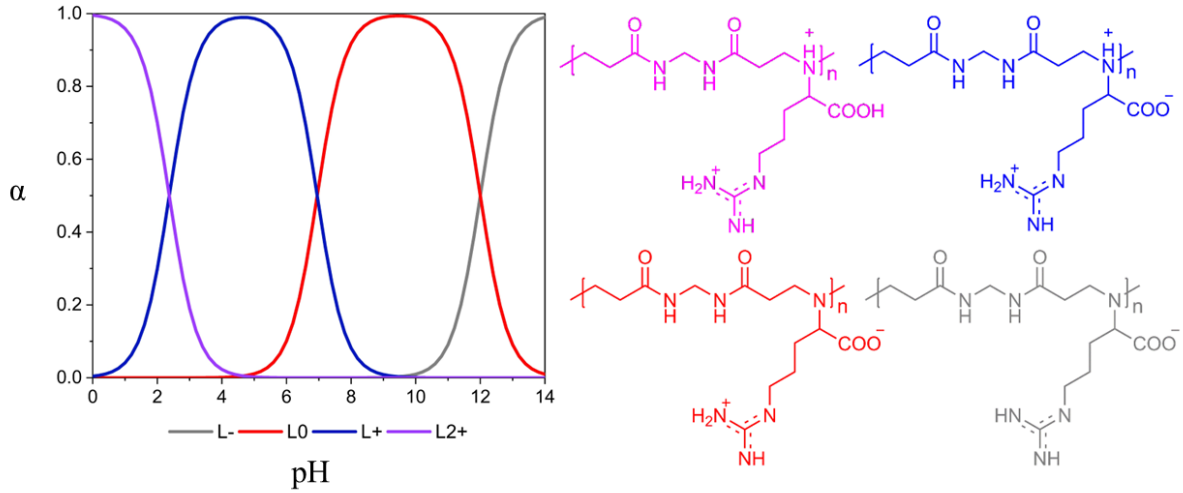

M-SER

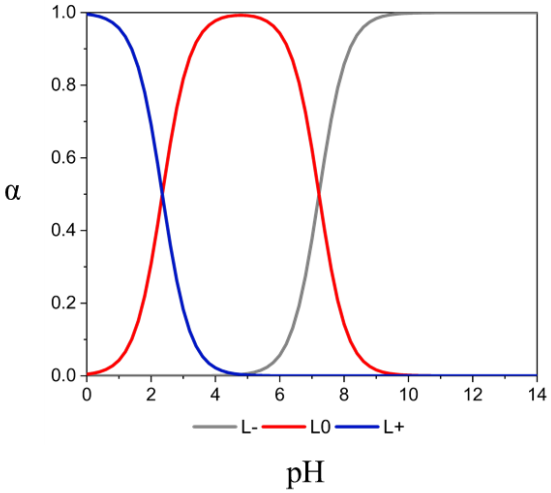

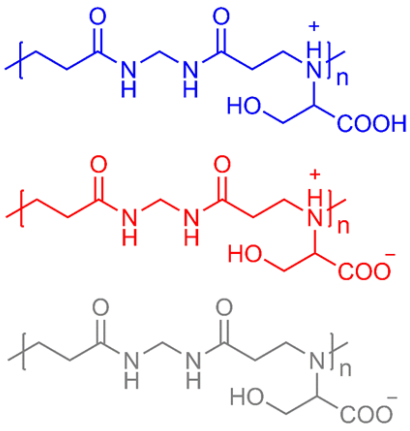

M-ALA

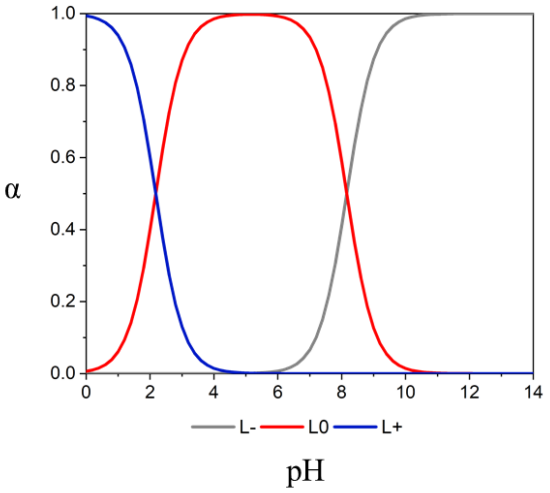

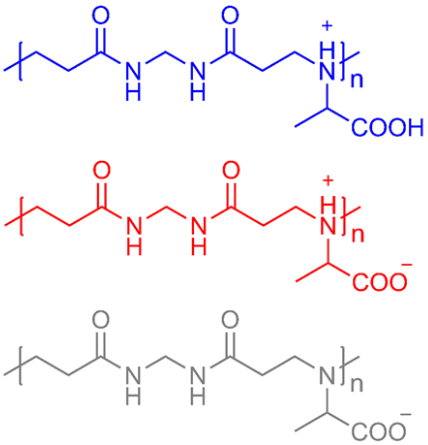

M-LEU

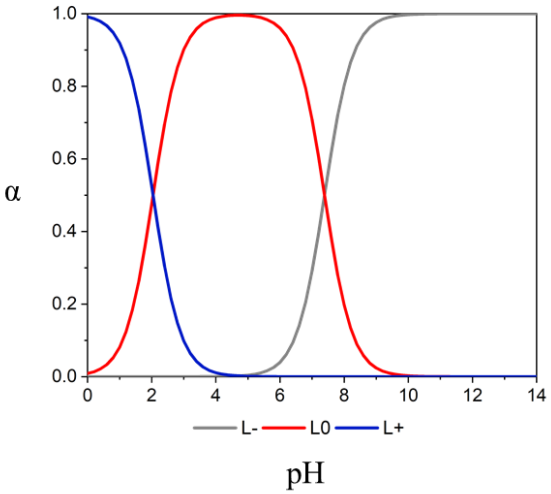

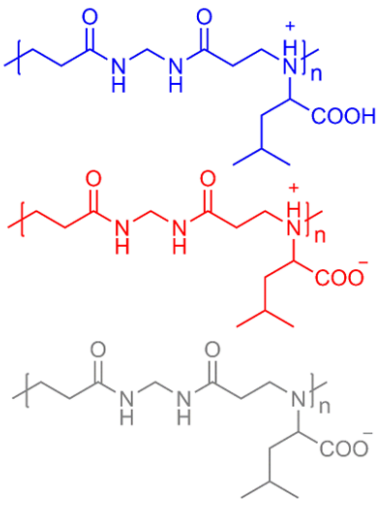

M-HIS

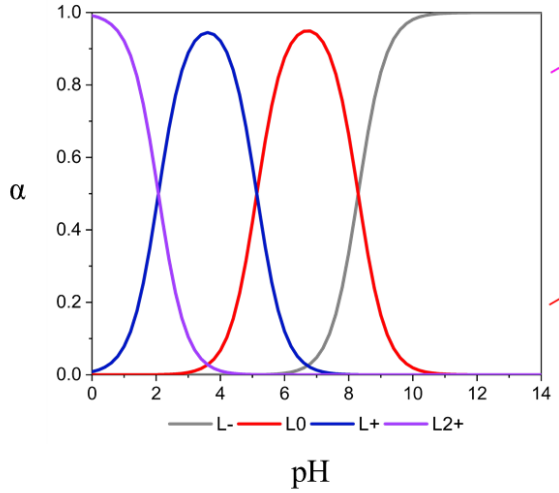

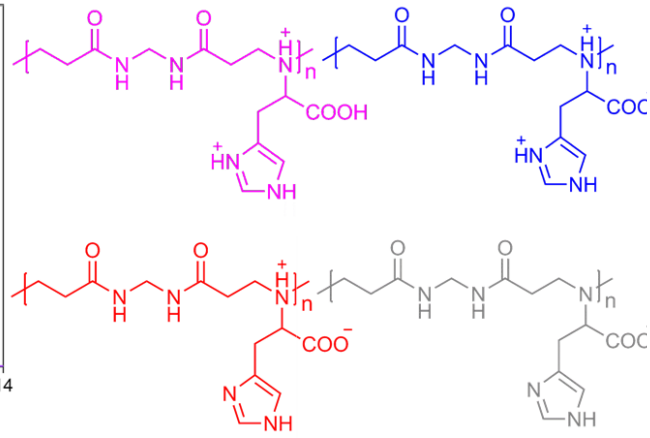

M-GLU

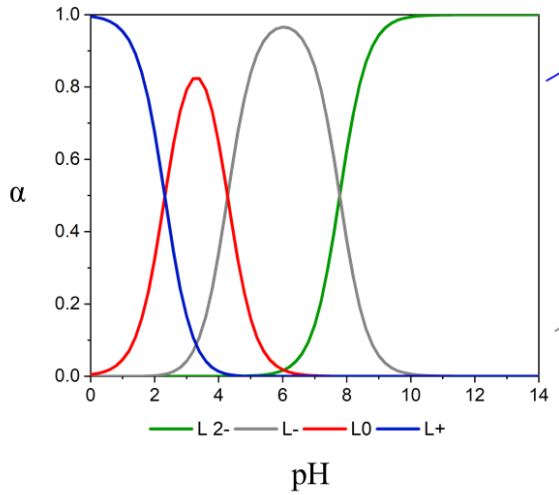

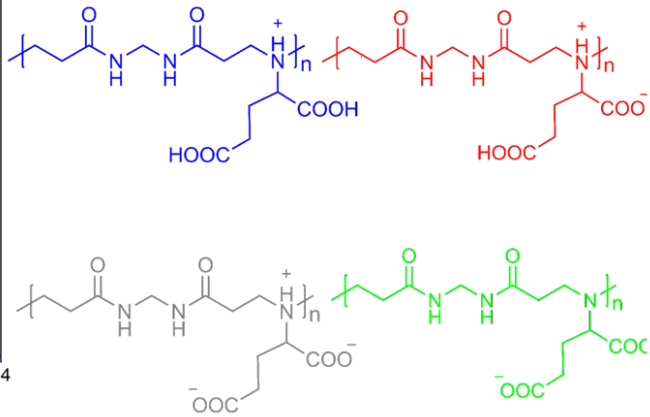

AGMA1

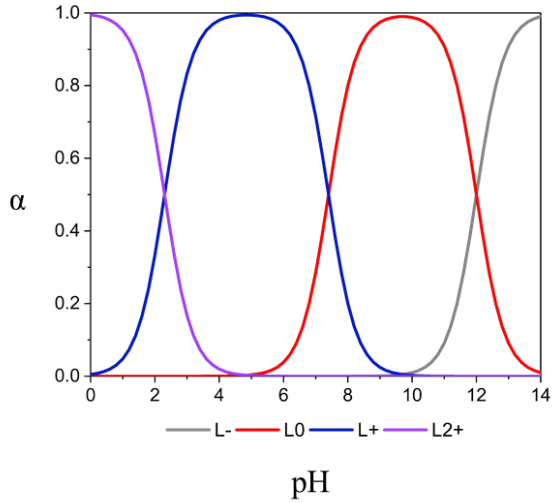

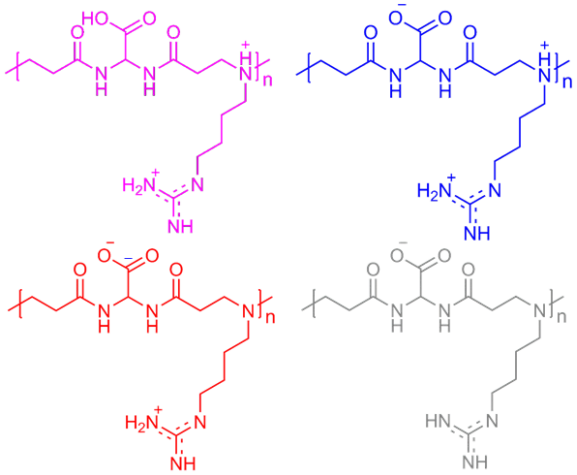

BIBLIOGRAPHY

1. Ferruti, P. Poly(amidoamine)s: Past, present, and perspectives. *Journal of Polymer Science, Part A: Polymer Chemistry* **2013**, *51*(11), 2319–2353. doi:10.1002/pola.26632.

2. Dubé, M. A.; Salehpour, S. Applying the Principles of Green Chemistry to Polymer Production Technology. *Macromolecular Reaction Engineering* **2014**, *8*(1), 7–28. doi:10.1002/mren.201300103.

3. Arioli, M.; Manfredi, A.; Alongi, J.; Ferruti, P.; Ranucci, E. Highlight on the mechanism of linear polyamidoamine degradation in water. *Polymers* **2020**, *12*(6), 1–16. doi:10.3390/POLYM12061376.

4. Ferruti, P.; Marchisio, M. A.; Duncan, R. Poly(amido-amine)s: Biomedical Applications. *Macromolecular Rapid Communications* **2002**, *23*(5–6), 332–355. doi:10.1002/1521-3927(20020401)23:5/6<332::AID-MARC332>3.0.CO;2-I.

5. Martuscelli, E.; Nicolais, L.; Riva, F.; Ferruti, P.; Provenzale, L. Synthesis and characterization of a potentially non-thrombogenic polyethylene-poly(amido-amine) graft copolymer. *Polymer* **1978**, *19*(9), 1063–1066. doi:10.1016/0032-3861(78)90148-9.

6. Lazzari, F.; Manfredi, A.; Alongi, J.; Marinotto, D.; Ferruti, P.; Ranucci, E. D-, L- and D,L-tryptophan-based polyamidoamino acids: PH-dependent structuring and fluorescent properties. *Polymers* **2019**, *11*(3). doi:10.3390/polym11030543.

7. Tonna, N.; Bianco, F.; Matteoli, M.; Cagnoli, C.; Antonucci, F.; Manfredi, A.; et al. A soluble biocompatible guanidine-containing polyamidoamine as promoter of primary brain cell adhesion and in vitro cell culturing. *Science and Technology of Advanced Materials* **2014**, *15*(4), 0–7. doi:10.1088/1468-6996/15/4/045007.

8. Ferruti, P.; Franchini, J.; Bencini, M.; Ranucci, E.; Zara, G. P.; Serpe, L.; et al. Prevailingly Cationic Agmatine-Based Amphoteric Polyamidoamine as a Nontoxic, Nonhemolytic, and "Stealthlike" DNA Complexing Agent and Transfection Promoter. *Biomacromolecules* **2007**, *8*(5), 1498–1504. doi:10.1021/bm061126c.

9. Ferruti, P.; Bianchi, S.; Ranucci, E.; Chiellini, F.; Piras, A. M. Novel agmatine-containing poly(amidoamine) hydrogels as scaffolds for tissue engineering. *Biomacromolecules* **2005**, *6*(4), 2229–2235. doi:10.1021/bm050210+.

10. Donalisio, M.; Ranucci, E.; Cagno, V.; Civra, A.; Manfredi, A.; Cavalli, R.; et al. Agmatine-Containing Poly(amidoamine)s as a Novel Class of Antiviral Macromolecules: Structural Properties and In Vitro Evaluation of Infectivity Inhibition. *Antimicrobial Agents and Chemotherapy* **2014**, *58*(10), 6315–6319. doi:10.1128/AAC.03420-14.

11. Cavalli, R.; Primo, L.; Sessa, R.; Chiaverina, G.; di Blasio, L.; Alongi, J.; et al. The AGMA1 polyamidoamine mediates the efficient delivery of siRNA. *Journal of Drug Targeting* **2017**, *25*(9–10), 891–898. doi:10.1080/1061186X.2017.1363215.

12. Ferruti, P.; Alongi, J.; Barabani, E.; Manfredi, A.; Ranucci, E. Silk/Polyamidoamine Membranes for Removing Chromium VI from Water. *Polymers* **2023**, *15*(8), 1871. doi:10.3390/polym15081871.

13. Ferruti, P.; Manzoni, S.; Richardson, S. C. W.; Duncan, R.; Pattrick, N. G.; Mendichi, R.; et al. Amphoteric Linear Poly(amido-amine)s as Endosomolytic Polymers: Correlation between Physicochemical and Biological Properties. *Macromolecules* **2000**, *33*(21), 7793–7800. doi:10.1021/ma000378h.

14. Richardson, S. C. W.; Pattrick, N. G.; Stella Man, Y. K.; Ferruti, P.; Duncan, R. Poly(Amidoamine)s as Potential Nonviral Vectors: Ability to Form Interpolyelectrolyte Complexes and to Mediate Transfection in Vitro. *Biomacromolecules* **2001**, *2*(3), 1023–1028. doi:10.1021/bm010079f.

15. Ranucci, E.; Ferruti, P.; Lattanzio, E.; Manfredi, A.; Rossi, M.; Mussini, P. R.; et al. Acid-base properties of poly(amidoamine)s. *Journal of Polymer Science Part A: Polymer Chemistry* **2009**, *47*(24), 6977–6991. doi:10.1002/pola.23737.

16. Franchini, J.; Ranucci, E.; Ferruti, P.; Rossi, M.; Cavalli, R. Synthesis, Physicochemical Properties, and Preliminary Biological Characterizations of a Novel Amphoteric Agmatine-Based Poly(amidoamine) with RGD-Like Repeating Units. *Biomacromolecules* **2006**, *7*(4), 1215–1222. doi:10.1021/bm060054m.

17. Ferruti, F.; Alongi, J.; Manfredi, A.; Ranucci, E.; Ferruti, P. Controlled synthesis of linear polyamidoamino acids. *Polymers* **2019**, *11*(8). doi:10.3390/polym11081324.

18. Manfredi, A.; Mauro, N.; Terenzi, A.; Alongi, J.; Lazzari, F.; Ganazzoli, F.; et al. Self-Ordering Secondary Structure of d - And l -Arginine-Derived Polyamidoamino Acids. *ACS Macro Letters* **2017**, *6*(9), 987–991. doi:10.1021/acsmacrolett.7b00492.

19. Lazzari, F.; Manfredi, A.; Alongi, J.; Mendichi, R.; Ganazzoli, F.; Raffaini, G.; et al. Self-structuring in water of polyamidoamino acids with hydrophobic side chains deriving from natural α-amino acids. *Polymers* **2018**, *10*(11). doi:10.3390/polym10111261.

20. Mantha, S.; Pillai, S.; Khayambashi, P.; Upadhyay, A.; Zhang, Y.; Tao, O.; et al. Smart Hydrogels in Tissue Engineering and Regenerative Medicine. *Materials* **2019**, *12*(20), 3323. doi:10.3390/ma12203323.

21. Jacchetti, E.; Emilitri, E.; Rodighiero, S.; Indrieri, M.; Gianfelice, A.; Lenardi, C.; et al. Biomimetic poly(amidoamine) hydrogels as synthetic materials for cell culture. *Journal of Nanobiotechnology* **2008**, *6*(1), 14. doi:10.1186/1477-3155-6-14.

22. Magnaghi, V.; Conte, V.; Procacci, P.; Pivato, G.; Cortese, P.; Cavalli, E.; et al. Biological performance of a novel biodegradable polyamidoamine hydrogel as guide for peripheral nerve regeneration. *Journal of Biomedical Materials Research Part A* **2011**, *98A*(1), 19–30. doi:10.1002/jbm.a.33091.

23. Li, J.; Gao, L.; Xu, R.; Ma, S.; Ma, Z.; Liu, Y.; et al. Fibers reinforced composite hydrogels with improved lubrication and load-bearing capacity. *Friction* **2022**, *10*(1), 54–67. doi:10.1007/s40544-020-0389-9.

24. Teixeira, M. O.; Antunes, J. C.; Felgueiras, H. P. Recent Advances in Fiber–Hydrogel Composites for Wound Healing and Drug Delivery Systems. *Antibiotics* **2021**, *10*(3), 248. doi:10.3390/antibiotics10030248.

25. Gualandi, C.; Bloise, N.; Mauro, N.; Ferruti, P.; Manfredi, A.; Sampaolesi, M.; et al. Poly-l-Lactic Acid Nanofiber–Polyamidoamine Hydrogel Composites: Preparation, Properties, and Preliminary Evaluation as Scaffolds for Human Pluripotent Stem Cell Culturing. *Macromolecular Bioscience* **2016**, 1533–1544. doi:10.1002/mabi.201600061.

26. Maggi, F.; Manfredi, A.; Carosio, F.; Maddalena, L.; Alongi, J.; Ferruti, P.; et al. Toughening Polyamidoamine Hydrogels through Covalent Grafting of Short Silk Fibers. *Molecules* **2022**, *27*(22), 1–15. doi:10.3390/molecules27227808.

27. Ranucci, E.; Spagnoli, G.; Ferruti, P.; Sgouras, D.; Duncan, R. Poly(Amidoamine)s with potential as drug carriers: Degradation and cellular toxicity. *Journal of Biomaterials Science, Polymer Edition* **1991**, *2*(4), 303–315. doi:10.1163/156856291X00197.

28. Richardson, S.; Ferruti, P.; Duncan, R. Poly(amidoamine)s as potential endosomolytic polymers: Evaluation in vitro and body distribution in normal and tumour-bearing animals. *Journal of Drug Targeting* **1999**, *6*(6), 391–404. doi:10.3109/10611869908996846.

29. Seymour, L.; Ulbrich, K.; Steyger, P.; Brereton, M.; Subr, V.; Strohalm, J.; et al. Tumour tropism and anti-cancer efficacy of polymer-based doxorubicin prodrugs in the treatment of subcutaneous murine B16F10 melanoma. *British Journal of Cancer* **1994**, *70*(4), 636–641. doi:10.1038/bjc.1994.363.

30. Gianasi, E.; Wasil, M.; Evagorou, E. G.; Keddle, A.; Wilson, G.; Duncan, R. HPMA copolymer platinates as novel antitumour agents: in vitro properties, pharmacokinetics and antitumour activity in vivo. *European Journal of Cancer* **1999**, *35*(6), 994–1002. doi:10.1016/S0959-8049(99)00030-1.

31. Barbucci, R.; Casolaro, M.; Ferruti, P.; Barone, V.; Leli, F.; Oliva, L. Macroinorganics. 7. Property structure relationships for polymeric bases whose monomeric units behave independently toward protonation. *Macromolecules* **1981**, *14*(5), 1203–1209. doi:10.1021/ma50006a013.

32. Ferruti, P.; Danusso, F.; Franchi, G.; Polentarutti, N.; Garattini, S. Effects of a series of new synthetic high polymers on cancer metastases. *Journal of Medicinal Chemistry* **1973**, *16*(5), 496–499. doi:10.1021/jm00263a018.

33. Ferruti, P.; Mauro, N.; Falciola, L.; Pifferi, V.; Bartoli, C.; Gazzarri, M.; et al. Amphoteric, prevailingly cationic L-arginine polymers of poly(amidoamino acid) structure: Synthesis,

acid/base properties and preliminary cytocompatibility and cell-permeating characterizations. *Macromolecular Bioscience* **2014**, *14*(3), 390–400. doi:10.1002/mabi.201300387.

34. Barbucci, R.; Casolaro, M.; Ferruti, P.; Barone, V. Macroinorganics: 8. Chelation of copper(II) ion with some new poly(amido-amines). *Polymer* **1982**, *23*(1), 148–151. doi:10.1016/0032-3861(82)90031-3.

35. Ferruti, P.; Ranucci, E.; Manfredi, A.; Mauro, N.; Ferrari, E.; Bruni, R.; et al. L-lysine and EDTA polymer mimics as resins for the quantitative and reversible removal of heavy metal ion water pollutants. *Journal of Polymer Science Part A: Polymer Chemistry* **2012**, *50*(24), 5000–5010. doi:10.1002/pola.26330.

36. Pesavento, M.; Soldi, T.; Ferruti, P.; Barbucci, R.; Benvenuti, M. Applied macroinorganics. IV. Effect of the crosslinking agent on protonation, and metal ions complexing abilities, of ion exchange resins with poly(amido–amine) structure. *Journal of Applied Polymer Science* **1983**, *28*(11), 3361–3368. doi:10.1002/app.1983.070281105.

37. Ferruti, P.; Ranucci, E.; Bianchi, S.; Falciola, L.; Mussini, P. R.; Rossi, M. Novel polyamidoamine-based hydrogel with an innovative molecular architecture as a Co 2+ -, Ni 2+ -, and Cu 2+ -sorbing material: Cyclovoltammetry and extended X-ray absorption fine structure studies. *Journal of Polymer Science Part A: Polymer Chemistry* **2006**, *44*(7), 2316–2327. doi:10.1002/pola.21349.

38. Manfredi, A.; Ranucci, E.; Morandi, S.; Mussini, P. R.; Ferruti, P. Fast and quantitative manganese sorption by polyamidoamine resins. *Journal of Polymer Science Part A: Polymer Chemistry* **2013**, *51*(4), 769–773. doi:10.1002/pola.26462.

39. Manfredi, A.; Carosio, F.; Ferruti, P.; Ranucci, E.; Alongi, J. Linear polyamidoamines as novel biocompatible phosphorus-free surface-confined intumescent flame retardants for cotton fabrics. *Polymer Degradation and Stability* **2018**, *151*(February), 52–64. doi:10.1016/j.polymdegradstab.2018.02.020.

40. Beduini, A.; Carosio, F.; Ferruti, P.; Ranucci, E.; Alongi, J. Polyamidoamines derived from natural α-amino acids as effective flame retardants for cotton. *Polymers* **2021**, *13*(21). doi:10.3390/polym13213714.

41. Hon, D. N. -S. Photooxidative degradation of cellulose: Reactions of the cellulosic free radicals with oxygen. *Journal of Polymer Science: Polymer Chemistry Edition* **1979**, *17*(2), 441–454. doi:10.1002/pol.1979.170170214.

42. Alebeid, O. K.; Zhao, T. Review on: developing UV protection for cotton fabric. *The Journal of The Textile Institute* **2017**, *108*(12), 2027–2039. doi:10.1080/00405000.2017.1311201.

43. Alongi, J.; Treccani, S.; Comite, V.; Fermo, P.; Ferruti, P.; Ranucci, E. Polyamidoamine-based photostabilizers for cotton fabrics. *Polymer Degradation and Stability* **2024**, *228*(July), 110938. doi:10.1016/j.polymdegradstab.2024.110938.

44. Agency, U. E. P. *Protocols for Short Term Toxicity Screening of Hazardous Waste Sites*; 2005.

45. Linder, G.; Greene, J.; Ratsch, H.; Nwosu, J.; Smith, S.; Wilborn, D. Seed Germination and Root Elongation Toxicity Tests in Hazardous Waste Site Evaluation: Methods Development and Applications. In *Plants for Toxicity Assessment*; ASTM International100 Barr Harbor Drive, PO Box C700, West Conshohocken, PA 19428-2959, 1990; pp 177–187. doi:10.1520/STP19062S.

46. Pokorska-Niewiada, K.; Rajkowska-Myśliwiec, M.; Protasowicki, M. Acute Lethal Toxicity of Heavy Metals to the Seeds of Plants of High Importance to Humans. *Bulletin of Environmental Contamination and Toxicology* **2018**, *101*(2), 222–228. doi:10.1007/s00128-018-2382-9.

47. Luo, Y.; Liang, J.; Zeng, G.; Chen, M.; Mo, D.; Li, G.; et al. Seed germination test for toxicity evaluation of compost: Its roles, problems and prospects. *Waste Management* **2018**, *71*, 109–114. doi:10.1016/j.wasman.2017.09.023.

48. Kader, M. A. A comparison of seed germination calculation formulae and the associated interpretation of resulting data. *Journal and proceedings of the Royal Society of New South Wales* **2005**, *138*(3–4), 65–75. doi:10.5962/p.361564.

49. Alongi, J.; Costantini, A.; Ferruti, P.; Ranucci, E. Evaluation of the eco-compatibility of polyamidoamines by means of seed germination test. *Polymer Degradation and Stability* **2022**, *197*, 109854. doi:10.1016/j.polymdegradstab.2022.109854.

50. Beduini, A.; Carosio, F.; Ferruti, P.; Ranucci, E.; Alongi, J. Sulfur-based copolymeric polyamidoamines as efficient flame-retardants for cotton. *Polymers* **2019**, *11*(11). doi:10.3390/polym11111904.

51. Emilitri, E.; Ferruti, P.; Annunziata, R.; Ranucci, E.; Rossi, M.; Falciola, L.; et al. Novel amphoteric cystine-based poly(amidoamine)s responsive to redox stimuli. *Macromolecules* **2007**, *40*(14), 4785–4793. doi:10.1021/ma062115e.

52. Levie, R. de. *How to Use Excel® in Analytical Chemistry*; Cambridge University Press, 2001.

53. Duis, K.; Junker, T.; Coors, A. Environmental fate and effects of water-soluble synthetic organic polymers used in cosmetic products. *Environmental Sciences Europe* **2021**, *33*(1), 21. doi:10.1186/s12302-021-00466-2.

54. Krogh, K. A.; Halling-Sørensen, B.; Mogensen, B. B.; Vejrup, K. V. Environmental properties and effects of nonionic surfactant adjuvants in pesticides: a review. *Chemosphere* **2003**, *50*(7), 871–901. doi:10.1016/S0045-6535(02)00648-3.

55. Kadajji, V. G.; Betageri, G. V. Water Soluble Polymers for Pharmaceutical Applications. *Polymers* **2011**, *3*(4), 1972–2009. doi:10.3390/polym3041972.

56. Julinová, M.; Vaňharová, L.; Jurča, M. Water-soluble polymeric xenobiotics – Polyvinyl alcohol and polyvinylpyrrolidon – And potential solutions to environmental issues: A brief review. *Journal of Environmental Management* **2018**, *228*, 213–222. doi:10.1016/j.jenvman.2018.09.010.

57. Levy, G. J.; Miller, W. P. Polyacrylamide adsorption and aggregate stability. *Soil and Tillage Research* **1999**, *51*(1–2), 121–128. doi:10.1016/S0167-1987(99)00048-3.

58. Nigro, L.; Magni, S.; Ortenzi, M. A.; Gazzotti, S.; Signorini, S. G.; Sbarberi, R.; et al. Assessment of behavioural effects of three water-soluble polymers in zebrafish embryos. *Science of The Total Environment* **2023**, *893*, 164843. doi:10.1016/j.scitotenv.2023.164843.

59. Sobanska, M.; Scholz, S.; Nyman, A.-M.; Cesnaitis, R.; Gutierrez Alonso, S.; Klüver, N.; et al. Applicability of the fish embryo acute toxicity (FET) test (OECD 236) in the regulatory context of Registration, Evaluation, Authorisation, and Restriction of Chemicals (REACH). *Environmental Toxicology and Chemistry* **2017**, *37*(3), 657–670. doi:10.1002/etc.4055.

60. Yang, Y.; Wang, G.; Li, G.; Ma, R.; Kong, Y.; Yuan, J. Selection of sensitive seeds for evaluation of compost maturity with the seed germination index. *Waste Management* **2021**, *136*, 238–243. doi:10.1016/j.wasman.2021.09.037.

61. Di Salvatore, M.; Carafa, A. M.; Carratù, G. Assessment of heavy metals phytotoxicity using seed germination and root elongation tests: A comparison of two growth substrates. *Chemosphere* **2008**, *73*(9), 1461–1464. doi:10.1016/j.chemosphere.2008.07.061.

62. Banks, M. K.; Schultz, K. E. Comparison of Plants for Germination Toxicity Tests in Petroleum-Contaminated Soils. *Water, Air, and Soil Pollution* **2005**, *167*(1–4), 211–219. doi:10.1007/s11270-005-8553-4.

63. Bosker, T.; Bouwman, L. J.; Brun, N. R.; Behrens, P.; Vijver, M. G. Microplastics accumulate on pores in seed capsule and delay germination and root growth of the terrestrial vascular plant Lepidium sativum. *Chemosphere* **2019**, *226*, 774–781. doi:10.1016/j.chemosphere.2019.03.163.

64. Wolny, E.; Betekhtin, A.; Rojek, M.; Braszewska-Zalewska, A.; Lusinska, J.; Hasterok, R. Germination and the Early Stages of Seedling Development in Brachypodium distachyon. *International Journal of Molecular Sciences* **2018**, *19*(10), 2916. doi:10.3390/ijms19102916.

65. Weitbrecht, K.; Müller, K.; Leubner-Metzger, G. First off the mark: early seed germination. *Journal of Experimental Botany* **2011**, *62*(10), 3289–3309. doi:10.1093/jxb/err030.

66. Müller, K.; Tintelnot, S.; Leubner-Metzger, G. Endosperm-limited Brassicaceae Seed Germination: Abscisic Acid Inhibits Embryo-induced Endosperm Weakening of Lepidium sativum (cress) and Endosperm Rupture of Cress and Arabidopsis thaliana. *Plant and Cell Physiology* **2006**, *47*(7), 864–877. doi:10.1093/pcp/pcj059.

67. Ma, Z.; Bykova, N. V.; Igamberdiev, A. U. Cell signaling mechanisms and metabolic regulation of germination and dormancy in barley seeds. *The Crop Journal* **2017**, *5*(6), 459–477. doi:10.1016/j.cj.2017.08.007.

68. US Environmental Protection Agency. *Seed Germination/Root Elongation Toxicity Test*; 1996.

69. Ko, K.-S.; Han, J.; Kong, I. C. Assessment of Arsenite, Arsenate, and Chromate Phytotoxicity Based on the Activity of Seed Germination and Growth (Root & Shoot) of Various Plant Seeds. *Human and Ecological Risk Assessment: An International Journal* **2013**, *19*(3), 742–753. doi:10.1080/10807039.2012.708273.

70. Alaguprathana, M.; Poonkothai, M.; Al-Ansari, M. M.; Al-Humaid, L.; Kim, W. Cytogenotoxicity assessment in Allium cepa roots exposed to methyl orange treated with Oedogonium subplagiostomum AP1. *Environmental Research* **2022**, *213*, 113612. doi:10.1016/j.envres.2022.113612.

71. Duncan, R.; Ferruti, P.; Sgouras, D.; Tuboku-Metzger, A.; Ranucci, E.; Bignotti, F. A Polymer-Triton X-100 Conjugate Capable of PH-Dependent Red Blood Cell Lysis: A Model System Illustrating the Possibility of Drug Delivery Within Acidic Intracellular Compartments. *Journal of Drug Targeting* **1994**, *2*(4), 341–347. doi:10.3109/10611869409015915.

72. Kuboi, T.; Fujii, K. Toxicity of Cationic Polymer Flocculants to Higher Plants. *Soil Science and Plant Nutrition* **1985**, *31*(2), 163–173. doi:10.1080/00380768.1985.10557424.

73. Hansen, A. M. B.; Brill, J. L.; Connors, K. A.; Belanger, S. E.; Baun, A.; Sanderson, H. Understanding ecotoxicological drivers and responses of freshwater green algae, Raphidocelis subcapitata, to cationic polyquaternium polymers. *Environmental Research* **2023**, *231*, 116282. doi:10.1016/j.envres.2023.116282.

74. Liwarska-Bizukojc, E. Effect of Innovative Bio-Based Plastics on Early Growth of Higher Plants. *Polymers* **2023**, *15*(2), 438. doi:10.3390/polym15020438.

75. Sobarzo-Bernal, O.; Gómez-Merino, F. C.; Alcántar-González, G.; Saucedo-Veloz, C.; Trejo-Téllez, L. I. Biostimulant Effects of Cerium on Seed Germination and Initial Growth of Tomato Seedlings. *Agronomy* **2021**, *11*(8), 1525. doi:10.3390/agronomy11081525.

76. Li, H.; Liu, Y.; Chen, Q.; Jin, L.; Peng, R. Research Progress of Zebrafish Model in Aquatic Ecotoxicology. *Water (Switzerland)* **2023**, *15*(9). doi:10.3390/w15091735.

77. Rohr, S.; Otten, C.; Abdelilah-Seyfried, S. Asymmetric involution of the myocardial field drives heart tube formation in zebrafish. *Circulation Research* **2008**, *102*(2), 12–19. doi:10.1161/CIRCRESAHA.107.165241.

78. Chen, J.; Eeden, F. J. M. Van; Warren, K. S.; Chin, A.; Nüsslein-volhard, C.; Haffter, P.; et al. Develop_124_21_4373. **1997**, *4382*, 4373–4382.

79. Liu, J.; Bressan, M.; Hassel, D.; Huisken, J.; Staudt, D.; Kikuchi, K.; et al. A dual role for ErbB2 signaling in cardiac trabeculation. *Development* **2010**, *137*(22), 3867–3875. doi:10.1242/dev.053736.

80. Han, X. B.; Yuen, K. W. Y.; Wu, R. S. S. Polybrominated diphenyl ethers affect the reproduction and development, and alter the sex ratio of zebrafish (Danio rerio). *Environmental Pollution* **2013**, *182*, 120–126. doi:10.1016/j.envpol.2013.06.045.

81. Glazer, L.; Hawkey, A. B.; Wells, C. N.; Drastal, M.; Odamah, K. A.; Behl, M.; et al. Developmental Exposure to Low Concentrations of Organophosphate Flame Retardants Causes Life-Long Behavioral Alterations in Zebrafish. *Toxicological Sciences* **2018**, *165*(2), 487–498. doi:10.1093/toxsci/kfy173.

82. Usenko, C. Y.; Abel, E. L.; Hopkins, A.; Martinez, G.; Tijerina, J.; Kudela, M.; et al. Evaluation of common use Brominated Flame Retardant (BFR) toxicity using a Zebrafish embryo model. *Toxics* **2016**, *4*(3). doi:10.3390/toxics4030021.

83. Zhang, Q.; Zheng, S.; Shi, X.; Luo, C.; Huang, W.; Lin, H.; et al. Neurodevelopmental toxicity of organophosphate flame retardant triphenyl phosphate (TPhP) on zebrafish (Danio rerio) at different life stages. *Environment International* **2023**, *172*(22), 107745. doi:10.1016/j.envint.2023.107745.

84. Jarema, K. A.; Hunter, D. L.; Shaffer, R. M.; Behl, M.; Padilla, S. Acute and developmental behavioral effects of flame retardants and related chemicals in zebrafish. *Neurotoxicology and Teratology* **2015**, *52*, 194–209. doi:10.1016/j.ntt.2015.08.010.

85. OECD. Oecd Guidelines for the Testing of Chemicals. *Guidelines for the testing of chemicals* **2004**, No. April, 1–15.

86. Chahardehi, A. M.; Arsad, H.; Lim, V. Zebrafish as a successful animal model for screening toxicity of medicinal plants. *Plants* **2020**, *9*(10), 1–35. doi:10.3390/plants9101345.

87. Wisenden, B. D.; Paulson, D. C.; Orr, M. Zebrafish embryos hatch early in response to chemical and mechanical indicators of predation risk, resulting in underdeveloped swimming ability of hatchling larvae. *Biology open* **2022**, *11*(12), 1–7. doi:10.1242/bio.059229.

88. Choe, C. P.; Choi, S. Y.; Kee, Y.; Kim, M. J.; Kim, S. H.; Lee, Y.; et al. Transgenic fluorescent zebrafish lines that have revolutionized biomedical research. *Laboratory Animal Research* **2021**, *37*(1), 1–29. doi:10.1186/s42826-021-00103-2.

89. Silva Brito, R.; Canedo, A.; Farias, D.; Rocha, T. L. Transgenic zebrafish (Danio rerio) as an emerging model system in ecotoxicology and toxicology: Historical review, recent advances, and trends. *Science of the Total Environment* **2022**, *848*(March), 157665. doi:10.1016/j.scitotenv.2022.157665.

90. Ruzicka, L.; Howe, D. G.; Ramachandran, S.; Toro, S.; Van Slyke, C. E.; Bradford, Y. M.; et al. The Zebrafish Information Network: New support for non-coding genes, richer Gene Ontology annotations and the Alliance of Genome Resources. *Nucleic Acids Research* **2019**, *47*(D1), D867–D873. doi:10.1093/nar/gky1090.

91. Pelka, K. E.; Henn, K.; Keck, A.; Sapel, B.; Braunbeck, T. Size does matter – Determination of the critical molecular size for the uptake of chemicals across the chorion of zebrafish (Danio rerio) embryos. *Aquatic Toxicology* **2017**, *185*, 1–10. doi:10.1016/j.aquatox.2016.12.015.

92. Rawson, D. M.; Zhang, T.; Kalicharan, D.; Jongebloed, W. L. Field emission scanning electron microscopy and transmission electron microscopy studies of the chorion, plasma membrane and syncytial layers of the gastrula-stage embryo of the zebrafish Brachydanio rerio: A consideration of the structural and functional. *Aquaculture Research* **2000**, *31*(3), 325–336. doi:10.1046/j.1365-2109.2000.00401.x.

93. Lazzari, F.; Manfredi, A.; Alongi, J.; Ganazzoli, F.; Vasile, F.; Raffaini, G.; et al. Hydrogen bonding in a L-glutamine-based polyamidoamino acid and its pH-dependent self-ordered coil conformation. *Polymers* **2020**, *12*(4). doi:10.3390/POLYM12040881.

94. Lazzari, F.; Manfredi, A.; Alongi, J.; Mendichi, R.; Ganazzoli, F.; Raffaini, G.; et al. Self-structuring in water of polyamidoamino acids with hydrophobic side chains deriving from natural α-amino acids. *Polymers* **2018**, *10*(11). doi:10.3390/polym10111261.

95. Manfredi, A.; Mauro, N.; Terenzi, A.; Alongi, J.; Lazzari, F.; Ganazzoli, F.; et al. Self-Ordering Secondary Structure of d - And l -Arginine-Derived Polyamidoamino Acids. *ACS Macro Letters* **2017**, *6*(9), 987–991. doi:10.1021/acsmacrolett.7b00492.

96. Schier, A. F.; Talbot, W. S. Molecular genetics of axis formation in zebrafish. *Annual Review of Genetics* **2005**, *39*, 561–613. doi:10.1146/annurev.genet.37.110801.143752.

97. Khatri, D.; Zizioli, D.; Tiso, N.; Facchinello, N.; Vezzoli, S.; Gianoncelli, A.; et al. Down-regulation of coasy, the gene associated with NBIA-VI, reduces Bmp signaling, perturbs dorso-ventral patterning and alters neuronal development in zebrafish. *Scientific Reports* **2016**, *6*(July), 1–15. doi:10.1038/srep37660.

98. Naganathan, S. R.; Oates, A. C. Patterning and mechanics of somite boundaries in zebrafish embryos. *Seminars in Cell and Developmental Biology* **2020**, *107*(April), 170–178. doi:10.1016/j.semcdb.2020.04.014.

99. Hen Chow, E. S.; Cheng, S. H. Cadmium affects muscle type development and axon growth in zebrafish embryonic somitogenesis. *Toxicological Sciences* **2003**, *73*(1), 149–159. doi:10.1093/toxsci/kfg046.

100. Basnet, R. M.; Zizioli, D.; Taweedet, S.; Finazzi, D.; Memo, M. Zebrafish larvae as a behavioral model in neuropharmacology. *Biomedicines* **2019**, *7*(1). doi:10.3390/BIOMEDICINES7010023.

101. Irons, T. D.; MacPhail, R. C.; Hunter, D. L.; Padilla, S. Acute neuroactive drug exposures alter locomotor activity in larval zebrafish. *Neurotoxicology and Teratology* **2010**, *32*(1), 84–90. doi:10.1016/j.ntt.2009.04.066.

102. Hernandez, R. E.; Galitan, L.; Cameron, J.; Goodwin, N.; Ramakrishnan, L. Delay of Initial Feeding of Zebrafish Larvae until 8 Days Postfertilization Has No Impact on Survival or Growth Through the Juvenile Stage. *Zebrafish* **2018**, *15*(5), 515–518. doi:10.1089/zeb.2018.1579.

103. Nigro, L.; Magni, S.; Ortenzi, M. A.; Gazzotti, S.; Signorini, S. G.; Sbarberi, R.; et al. Assessment of behavioural effects of three water-soluble polymers in zebrafish embryos. *Science of the Total Environment* **2023**, *893*(May), 164843. doi:10.1016/j.scitotenv.2023.164843.

104. Li, Q.; Lin, J.; Zhang, Y.; Liu, X.; Chen, X. Q.; Xu, M. Q.; et al. Differential behavioral responses of zebrafish larvae to yohimbine treatment. *Psychopharmacology* **2015**, *232*(1), 197–208. doi:10.1007/s00213-014-3656-5.

105. Fetcho, J. R.; McLean, D. L. Startle Response. *Encyclopedia of Neuroscience* **2009**, 375–379. doi:10.1016/B978-008045046-9.01973-2.

106. Colwill, R. M.; Creton, R. Imaging escape and avoidance behavior in zebrafish larvae. *Reviews in the Neurosciences* **2011**, *22*(1), 63–73. doi:10.1515/RNS.2011.008.

107. Zhu, Q.; Costentin, C.; Nocera, D. G. Chemical Science biology and photoredox chemistry †. *Chemical Science* **2023**, *00*, 6876–6881. doi:10.1039/d3sc01867a1.

108. Zizioli, D.; Zanella, I.; Mignani, L.; Degli Antoni, M.; Castelli, F.; Quiros-Roldan, E. Cabotegravir Exposure of Zebrafish (Danio rerio) Embryos Impacts on Neurodevelopment and Behavior. *International Journal of Molecular Sciences* **2023**, *24*(3). doi:10.3390/ijms24031994.

109. Kimmel, C. B.; Ballard, W. W.; Kimmel, S. R.; Ullmann, B.; Schilling, T. F. Stages of embryonic development of the zebrafish. *Developmental Dynamics* **1995**, *203*(3), 253–310. doi:10.1002/aja.1002030302.

110. Zizioli, D.; Ferretti, S.; Mignani, L.; Castelli, F.; Tiecco, G.; Zanella, I.; et al. Developmental safety of nirmatrelvir in zebrafish (Danio rerio) embryos. *Birth Defects Research* **2023**, *115*(4), 430–440. doi:10.1002/bdr2.2128.

111. Bonsignorio, D.; Perego, L.; Del Giacco, L.; Cotelli, F. Structure and macromolecular composition of the zebrafish egg chorion. *Zygote* **1996**, *4*(2), 101–108. doi:10.1017/S0967199400002975.

112. Bodewein, L.; Schmelter, F.; Di Fiore, S.; Hollert, H.; Fischer, R.; Fenske, M. Differences in toxicity of anionic and cationic PAMAM and PPI dendrimers in zebrafish embryos and cancer cell lines. *Toxicology and Applied Pharmacology* **2016**, *305*, 83–92. doi:10.1016/j.taap.2016.06.008.

113. Busquet, F.; Strecker, R.; Rawlings, J. M.; Belanger, S. E.; Braunbeck, T.; Carr, G. J.; et al. OECD validation study to assess intra- and inter-laboratory reproducibility of the zebrafish embryo toxicity test for acute aquatic toxicity testing. *Regulatory Toxicology and Pharmacology* **2014**, *69*(3), 496–511. doi:10.1016/j.yrtph.2014.05.018.

114. Sobanska, M.; Scholz, S.; Nyman, A. M.; Cesnaitis, R.; Gutierrez Alonso, S.; Klüver, N.; et al. Applicability of the fish embryo acute toxicity (FET) test (OECD 236) in the regulatory context of Registration, Evaluation, Authorisation, and Restriction of Chemicals (REACH). *Environmental Toxicology and Chemistry* **2018**, *37*(3), 657–670. doi:10.1002/etc.4055.

115. Lawson, N. D.; Weinstein, B. M. In vivo imaging of embryonic vascular development using transgenic zebrafish. *Developmental Biology* **2002**, *248*(2), 307–318. doi:10.1006/dbio.2002.0711.

116. Park, H.; Lee, J. Y.; Park, S.; Song, G.; Lim, W. Developmental toxicity of fipronil in early development of zebrafish (Danio rerio) larvae: Disrupted vascular formation with angiogenic failure and inhibited neurogenesis. *Journal of Hazardous Materials* **2020**, *385*(October 2019), 121531. doi:10.1016/j.jhazmat.2019.121531.

117. Collery, R. F.; Link, B. A. Dynamic smad-mediated BMP signaling revealed through transgenic zebrafish. *Developmental Dynamics* **2011**, *240*(3), 712–722. doi:10.1002/dvdy.22567.

118. Moro, E.; Vettori, A.; Porazzi, P.; Schiavone, M.; Rampazzo, E.; Casari, A.; et al. Generation and application of signaling pathway reporter lines in zebrafish. *Molecular Genetics and Genomics* **2013**, *288*(5–6), 231–242. doi:10.1007/s00438-013-0750-z.

119. Westerfield, M. *The Zebrafish Book: A Guide for the Laboratory Use of Zebrafish (Danio Rerio)*; 5th ed.; University of Oregon Press, Ed.; 2007.

120. Walz, W. *Zebrafish Protocols for Neurobehavioral Research*; 2004.

121. Malešič, J.; Kolar, J.; Strlič, M.; Kočar, D.; Fromageot, D.; Lemaire, J.; et al. Photo-induced degradation of cellulose. *Polymer Degradation and Stability* **2005**, *89*(1), 64–69. doi:10.1016/j.polymdegradstab.2005.01.003.

122. Merlin, A.; Fouassier, J. Photochemical investigations into cellulosic materials I. Free radical generation in cellulose by photosensitized excitation. *Die Angewandte Makromolekulare Chemie* **1980**, *86*(1), 109–121. doi:10.1002/apmc.1980.050860108.

123. Vosmanská, V.; Barb, R. A.; Kolářová, K.; Rimpelová, S.; Heitz, J.; Švorčík, V. Effect of VUV-excimer lamp treatment on cellulose fiber. *International Journal of Polymer Analysis and Characterization* **2016**, *21*(4), 337–347. doi:10.1080/1023666X.2016.1156897.

124. Hodgson, J. L.; Coote, M. L. Clarifying the Mechanism of the Denisov Cycle: How do Hindered Amine Light Stabilizers Protect Polymer Coatings from Photo-oxidative Degradation? *Macromolecules* **2010**, *43*(10), 4573–4583. doi:10.1021/ma100453d.

125. Yao, Y.-N.; Wang, Y.; Zhang, H.; Gao, Y.; Zhang, T.; Kannan, K. A review of sources, pathways, and toxic effects of human exposure to benzophenone ultraviolet light filters. *Eco-Environment & Health* **2024**, *3*(1), 30–44. doi:10.1016/j.eehl.2023.10.001.

126. Mao, J. F.; Li, W.; Ong, C. N.; He, Y.; Jong, M.-C.; Gin, K. Y.-H. Assessment of human exposure to benzophenone-type UV filters: A review. *Environment International* **2022**, *167*, 107405. doi:10.1016/j.envint.2022.107405.

127. Zhou, H.; Hu, X.; Liu, M.; Yin, D. Benzotriazole ultraviolet stabilizers in the environment: A review of analytical methods, occurrence, and human health impacts. *TrAC Trends in Analytical Chemistry* **2023**, *166*, 117170. doi:10.1016/j.trac.2023.117170.

128. Nuñez, A.; Vallecillos, L.; Marcé, R. M.; Borrull, F. Occurrence and risk assessment of benzothiazole, benzotriazole and benzenesulfonamide derivatives in airborne particulate matter from an industrial area in Spain. *Science of The Total Environment* **2020**, *708*, 135065. doi:10.1016/j.scitotenv.2019.135065.

129. Yildiz, G.; Demiryürek, A. T.; Sahin-Erdemli, I.; Kanzik, I. Comparison of antioxidant activities of aminoguanidine, methylguanidine and guanidine by luminol-enhanced chemiluminescence. *British Journal of Pharmacology* **1998**, *124*(5), 905–910. doi:10.1038/sj.bjp.0701924.

130. Wang, Y.-X.; Su, W.-C.; Wang, Q.; Lin, Y.-F.; Zhou, Y.; Lin, L.-F.; et al. Antityrosinase and antioxidant activities of guanidine compounds and effect of guanylthiourea on melanogenesis. *Process Biochemistry* **2019**, *85*, 84–96. doi:10.1016/j.procbio.2019.07.003.

131. Nauser, T.; Carreras, A. Carbon-centered radicals add reversibly to histidine – implications. *Chem. Commun.* **2014**, *50*(92), 14349–14351. doi:10.1039/C4CC05316H.

132. Zhao, Z.; Fu, C.; Zhang, Y.; Fu, A. Dimeric Histidine as a Novel Free Radical Scavenger Alleviates Non-Alcoholic Liver Injury. *Antioxidants* **2021**, *10*(10), 1529. doi:10.3390/antiox10101529.

133. Jablonsky, M.; Šima, J. Oxidative degradation of paper – A minireview. *Journal of Cultural Heritage* **2021**, *48*, 269–276. doi:10.1016/j.culher.2021.01.014.

134. Davand, R.; Rahimpour, M. R.; Hassanajili, S.; Rashedi, R. Theoretical and experimental assessment of <scp>UV</scp> resistance of <scp>high-density</scp> polyethylene: Screening and optimization of <scp>hindered amine light stabilizers</scp>. *Journal of Applied Polymer Science* **2021**, *138*(43). doi:10.1002/app.51262.

135. Vigneswaran, C.; Ananthasubramanian, M.; Kandhavadivu, P. Bioprocessing of natural fibres. In *Bioprocessing of Textiles*; Elsevier, 2014; pp 53–188. doi:10.1016/B978-93-80308-42-5.50003-2.

136. ZHAO, H.; KWAK, J.; CONRADZHANG, Z.; BROWN, H.; AREY, B.; HOLLADAY, J. Studying cellulose fiber structure by SEM, XRD, NMR and acid hydrolysis. *Carbohydrate Polymers* **2007**, *68*(2), 235–241. doi:10.1016/j.carbpol.2006.12.013.

137. Standardization, I. O. for. *ISO 2469 Paper, Board and Pulps - Measurement of Diffuse Radiance Factor (Diffuse Reflectance Factor)*; 2024.

138. Schuessler, G. Z. *No Title*. <https://zschuessler.github.io/DeltaE/learn/.>.

139. Slanzi, A.; Iannoto, G.; Rossi, B.; Zenaro, E.; Constantin, G. In vitro Models of Neurodegenerative Diseases. *Frontiers in Cell and Developmental Biology* **2020**, *8*. doi:10.3389/fcell.2020.00328.

140. Walczak, P. A.; Perez-Esteban, P.; Bassett, D. C.; Hill, E. J. Modelling the central nervous system: tissue engineering of the cellular microenvironment. *Emerging Topics in Life Sciences* **2021**, *5*(4), 507–517. doi:10.1042/ETLS20210245.

141. Mantha, S.; Pillai, S.; Khayambashi, P.; Upadhyay, A.; Zhang, Y.; Tao, O.; et al. Smart Hydrogels in Tissue Engineering and Regenerative Medicine. *Materials* **2019**, *12*(20), 3323. doi:10.3390/ma12203323.

142. Teixeira, M. O.; Antunes, J. C.; Felgueiras, H. P. Recent Advances in Fiber–Hydrogel Composites for Wound Healing and Drug Delivery Systems. *Antibiotics* **2021**, *10*(3), 248. doi:10.3390/antibiotics10030248.

143. Li, J.; Gao, L.; Xu, R.; Ma, S.; Ma, Z.; Liu, Y.; et al. Fibers reinforced composite hydrogels with improved lubrication and load-bearing capacity. *Friction* **2022**, *10*(1), 54–67. doi:10.1007/s40544-020-0389-9.

144. Xu, S.; Deng, L.; Zhang, J.; Yin, L.; Dong, A. Composites of electrospun-fibers and hydrogels: A potential solution to current challenges in biological and biomedical field. *Journal of Biomedical Materials Research Part B: Applied Biomaterials* **2016**, *104*(3), 640–656. doi:10.1002/jbm.b.33420.

145. Mariano, A.; Fasolino, I.; Dinger, N. B.; Latte Bovio, C.; Bonadies, I.; Pezzella, A.; et al. Eumelanin-Coated Aligned PLA Electrospun Microfibers to Guide SH-SY5YCells Spreading, Alignment, And Maturation. *Advanced Materials Interfaces* **2023**, *10*(9). doi:10.1002/admi.202202022.

146. Baldassarro, V. A.; Dolci, L. S.; Mangano, C.; Giardino, L.; Gualandi, C.; Focarete, M. L.; et al. In Vitro Testing of Biomaterials for Neural Repair: Focus on Cellular Systems and High-Content Analysis. *BioResearch Open Access* **2016**, *5*(1), 201–211. doi:10.1089/biores.2016.0025.

147. Fasolino, I.; Bonadies, I.; Ambrosio, L.; Raucci, M. G.; Carfagna, C.; Caso, F. M.; et al. Eumelanin Coated PLA Electrospun Micro Fibers as Bioinspired Cradle for SH-SY5Y Neuroblastoma Cells Growth and Maturation. *ACS Applied Materials & Interfaces* **2017**, *9*(46), 40070–40076. doi:10.1021/acsami.7b13257.

148. Fasolino, I.; Carvalho, E. D.; Raucci, M. G.; Bonadies, I.; Soriente, A.; Pezzella, A.; et al. Eumelanin decorated poly(lactic acid) electrospun substrates as a new strategy for spinal cord injury treatment. *Biomaterials Advances* **2023**, *146*, 213312. doi:10.1016/j.bioadv.2023.213312.

149. Park, Y. J.; Yu, D. M.; Ahn, J. H.; Choi, J.-H.; Hong, Y. T. Surface modification of polyimide films by an ethylenediamine treatment for a flexible copper clad laminate. *Macromolecular Research* **2012**, *20*(2), 168–173. doi:10.1007/s13233-012-0025-2.

150. Haddad, T.; Noel, S.; Liberelle, B.; El Ayoubi, R.; Ajji, A.; De Crescenzo, G. Fabrication and surface modification of poly lactic acid (PLA) scaffolds with epidermal growth factor for neural tissue engineering. *Biomatter* **2016**, *6*(1), e1231276. doi:10.1080/21592535.2016.1231276.

151. Mallamaci, G.; Brugnoli, B.; Mariano, A.; D'Abusco, A. S.; Piozzi, A.; Di Lisio, V.; et al. Surface modification of polyester films with polyfunctional amines: Effect on bacterial biofilm formation. *Surfaces and Interfaces* **2023**, *39*, 102924. doi:10.1016/j.surfin.2023.102924.

152. Friedman, M. Applications of the Ninhydrin Reaction for Analysis of Amino Acids, Peptides, and Proteins to Agricultural and Biomedical Sciences. *Journal of Agricultural and Food Chemistry* **2004**, *52*(3), 385–406. doi:10.1021/jf030490p.

153. Yang, J.; Li, F.; Lu, G.; Lu, Y.; Song, C.; Zhou, R.; et al. Electrospun Biodegradable Poly(L-lactic acid) Nanofiber Membranes as Highly Porous Oil Sorbent Nanomaterials. *Nanomaterials* **2022**, *12*(15), 2670. doi:10.3390/nano12152670.

154. Tarus, B. K.; Fadel, N.; Al-Oufy, A.; El-Messiry, M. Investigation of mechanical properties of electrospun poly (vinyl chloride) polymer nanoengineered composite. *Journal of Engineered Fibers and Fabrics* **2020**, *15*. doi:10.1177/1558925020982569.

155. Fiore, N. J.; Tamer-Mahoney, J. D.; Beheshti, A.; Nieland, T. J. F.; Kaplan, D. L. 3D biocomposite culture enhances differentiation of dopamine-like neurons from SH-SY5Y cells: A model for studying Parkinson's disease phenotypes. *Biomaterials* **2022**, *290*, 121858. doi:10.1016/j.biomaterials.2022.121858.

156. Ruijtenberg, S.; van den Heuvel, S. Coordinating cell proliferation and differentiation: Antagonism between cell cycle regulators and cell type-specific gene expression. *Cell Cycle* **2016**, *15*(2), 196–212. doi:10.1080/15384101.2015.1120925.

157. Li, Q.; Zhang, P.; Cai, Y. Genkwanin suppresses MPP+-induced cytotoxicity by inhibiting TLR4/MyD88/NLRP3 inflammasome pathway in a cellular model of Parkinson's disease. *NeuroToxicology* **2021**, *87*, 62–69. doi:10.1016/j.neuro.2021.08.018.

158. Lawrimore, C. J.; Crews, F. T. Ethanol, <scp>TLR</scp> 3, and <scp>TLR</scp> 4 Agonists Have Unique Innate Immune Responses in Neuron-Like <scp>SH</scp> - <scp>SY</scp> 5Y and Microglia-Like <scp>BV</scp> 2. *Alcoholism: Clinical and Experimental Research* **2017**, *41*(5), 939–954. doi:10.1111/acer.13368.

159. Qiao, C.; Zhang, L.-X.; Sun, X.-Y.; Ding, J.-H.; Lu, M.; Hu, G. Caspase-1 Deficiency Alleviates Dopaminergic Neuronal Death via Inhibiting Caspase-7/AIF Pathway in MPTP/p Mouse Model of Parkinson's Disease. *Molecular Neurobiology* **2017**, *54*(6), 4292–4302. doi:10.1007/s12035-016-9980-5.

160. Aloe, L.; Rocco, M.; Balzamino, B.; Micera, A. Nerve Growth Factor: A Focus on Neuroscience and Therapy. *Current Neuropharmacology* **2015**, *13*(3), 294–303. doi:10.2174/1570159X13666150403231920.

161. Walzl, A.; Unger, C.; Kramer, N.; Unterleuthner, D.; Scherzer, M.; Hengstschläger, M.; et al. The Resazurin Reduction Assay Can Distinguish Cytotoxic from Cytostatic Compounds in Spheroid Screening Assays. *SLAS Discovery* **2014**, *19*(7), 1047–1059. doi:10.1177/1087057114532352.

162. Zhou, P.; Weng, R.; Chen, Z.; Wang, R.; Zou, J.; Liu, X.; et al. TLR4 Signaling in MPP + -Induced Activation of BV-2 Cells. *Neural Plasticity* **2016**, *2016*, 1–9. doi:10.1155/2016/5076740.

163. B. Ranby, J. F. R. *Photodegradation, Photooxidation and Photostabilization of Polymers.*; Wiley, 1975.

164. N.S. Allen, E. *Developments in Polymer Photochemistry*; Elsevier Applied Science Publishers Ltd.

165. J.F. Rabek. *Photodegradation of Polymers*; Berlin Heidelberg : Springer-Verlag, 1996.

166. Lemaire, J.; Gardette, J.-L.; Lacoste, J.; Delprat, P.; Vaillant, D. Mechanisms of Photooxidation of Polyolefins: Prediction of Lifetime in Weathering Conditions; 1996; pp 577–598. doi:10.1021/ba-1996-0249.ch035.

167. Hamid, S. H. Fundamental and Technical Aspects of the Photooxidation of Polymers. *Handbook of Polymer Degradation* **2020**, No. 13, 697–702. doi:10.1201/9781482270181-128.

168. Carlsson, D. J.; Brousseau, R.; Zhang, C.; Wiles, D. M. Identification of Products from Polyolefin Oxidation by Derivatization Reactions; 1988; pp 376–389. doi:10.1021/bk-1988-0364.ch027.

169. Miller, W. L.; Kester, D. R. Hydrogen peroxide Measurement in Seawater by (p-Hydroxyphenyl)acetic Acid Dimerization. *Analytical Chemistry* **1988**, *60*(24), 2711–2715. doi:10.1021/ac00175a014.